

SANDIA REPORT

SAND2005-2733

Unlimited Release

Printed April 27, 2005

The Local Variational Multi-Scale Method for Turbulence Simulation

Srinivas Ramakrishnan (Rice University)

S. Scott Collis (Sandia National Laboratories)

Prepared by
Sandia National Laboratories
Albuquerque, New Mexico 87185 and Livermore, California 94550

Sandia is a multiprogram laboratory operated by Sandia Corporation,
a Lockheed Martin Company, for the United States Department of Energy's
National Nuclear Security Administration under Contract DE-AC04-94-AL85000.

Approved for public release; further dissemination unlimited.



Sandia National Laboratories

Issued by Sandia National Laboratories, operated for the United States Department of Energy by Sandia Corporation.

NOTICE: This report was prepared as an account of work sponsored by an agency of the United States Government. Neither the United States Government, nor any agency thereof, nor any of their employees, nor any of their contractors, subcontractors, or their employees, make any warranty, express or implied, or assume any legal liability or responsibility for the accuracy, completeness, or usefulness of any information, apparatus, product, or process disclosed, or represent that its use would not infringe privately owned rights. Reference herein to any specific commercial product, process, or service by trade name, trademark, manufacturer, or otherwise, does not necessarily constitute or imply its endorsement, recommendation, or favoring by the United States Government, any agency thereof, or any of their contractors or subcontractors. The views and opinions expressed herein do not necessarily state or reflect those of the United States Government, any agency thereof, or any of their contractors.

Printed in the United States of America. This report has been reproduced directly from the best available copy.

Available to DOE and DOE contractors from
U.S. Department of Energy
Office of Scientific and Technical Information
P.O. Box 62
Oak Ridge, TN 37831

Telephone: (865) 576-8401
Facsimile: (865) 576-5728
E-Mail: reports@adonis.osti.gov
Online ordering: <http://www.doe.gov/bridge>

Available to the public from
U.S. Department of Commerce
National Technical Information Service
5285 Port Royal Rd
Springfield, VA 22161

Telephone: (800) 553-6847
Facsimile: (703) 605-6900
E-Mail: orders@ntis.fedworld.gov
Online ordering: <http://www.ntis.gov/ordering.htm>



SAND2005-2733XX
Unlimited Release
Printed on April 27, 2005

The Local Variational Multi-Scale Method for Turbulence Simulation

by

Srinivas Ramakrishnan
Mechanical Engineering & Materials Science
Rice University

S. Scott Collis
Computational Mathematics & Algorithms
Sandia National Laboratories ¹

¹Sandia is a multiprogram laboratory operated by Sandia Corporation, a Lockheed-Martin Company, for the United States Department of Energy under Contract DE-AC04-94AL85000.

Abstract

Accurate and efficient turbulence simulation in complex geometries is a formidable challenge. Traditional methods are often limited by low accuracy and/or restrictions to simple geometries. We explore the merger of Discontinuous Galerkin (DG) spatial discretizations with Variational Multi-Scale (VMS) modeling, termed Local VMS (LVMS), to overcome these limitations. DG spatial discretizations support arbitrarily high-order accuracy on unstructured grids amenable for complex geometries. Furthermore, high-order, hierarchical representation within DG provides a natural framework for *a priori* scale separation crucial for VMS implementation. We show that the combined benefits of DG and VMS within the LVMS method leads to promising new approach to LES for use in complex geometries.

The efficacy of LVMS for turbulence simulation is assessed by application to fully-developed turbulent channel flow. First, a detailed spatial resolution study is undertaken to record the effects of the DG discretization on turbulence statistics. Here, the local *hp*-refinement capabilities of DG are exploited to obtain reliable low-order statistics efficiently. Likewise, resolution guidelines for simulating wall-bounded turbulence using DG are established. We also explore the influence of enforcing Dirichlet boundary conditions indirectly through numerical fluxes in DG which allows the solution to jump (slip) at the channel walls. These jumps are effective in simulating the influence of the wall commensurate with the local resolution and this feature of DG is effective in mitigating near-wall resolution requirements. In particular, we show that by locally modifying the numerical viscous flux used at the wall, we are able to regulate the near-wall slip through a penalty that leads to improved shear-stress predictions. This work, demonstrates the potential of the numerical viscous flux to act as a numerically consistent wall-model and this success warrants future research.

As in any high-order numerical method some mechanism is required to control aliasing effects due to nonlinear interactions and to ensure nonlinear stability of the method. In this context, we evaluate the merits of two approaches to de-aliasing — spectral filtering and polynomial dealiasing. While both approaches are successful, polynomial-dealiasing is found to be better suited for use in large-eddy simulation. Finally, results using LVMS are reported and show good agreement with reference direct numerical simulation thereby demonstrating the effectiveness of LVMS for wall-bounded turbulence. This success paves the way for future applications of LVMS to more complex turbulent flows.

Acknowledgments

The first author would like to thank my advisor, Dr. Scott Collis, for his constant support and guidance in the compilation of this thesis. I could not have asked for a better mentor to help me make the transition from a student to a researcher. And the very high standards set by Dr. Collis, through his conduct both in research and teaching, will serve as a reliable yardstick by which I measure my continuing professional growth.

I would also like to thank Drs. Carroll, Symes, and Spanos for their willingness to serve on my committee and for their valuable comments and suggestions.

I thank the the members of the Flow Physics and Simulation (FPS) Lab, Dr. Guoquan Chen, Dr. Alexander Dobrinsky, Dr. Kaveh Ghayour, and Zachary Smith for the opportunity to interact in various ways through which my understanding on many diverse subjects stand enhanced.

A special thanks to my friend Sunil for all his advice and support on matters both personal and professional during my stay at Rice. Shelley Johnson–Gottschalk and her family deserve a special mention for enriching my experience beyond the hedges of Rice through their warmth and hospitality. I would also like to thank Dr. G.V. Devarajan for all his support during my graduate work.

I wish to thank my wife, Sadhana, for her love and understanding during this time. Finally, as a small token of my appreciation, I dedicate this thesis to all the members of my family (Geetha, Ramakrishna, and Venkatesh).

This research has been supported in part by the Texas Advanced Technology Program under Grant numbers 003604-017-1997 and 003604-0011-2001. Computations were performed on an 82 processor Pentium IV Beowulf cluster that was purchased with the aid of NSF MRI grant 0116289-2001. The second author's work on this project has been partially supported by the ASC Algorithms: Computational Methods subprogram as well as through the Laboratory Directed Research & Development Program at Sandia.

Nomenclature

Roman Symbols

C_s	Coefficient of the SGS Smagorinsky model
c_s	Grid stretching factor
f	Body force or force distribution in the momentum equations
h	Representative mesh length scale
L	Number of modes for given p , $L = p + 1$
L_e	Multi-scale partition parameter for element e
L_x	Channel length in x
L_z	Channel width in z
N_x	Number of Elements in x
N_y	Number of Elements in y
N_z	Number of Elements modes in z
p	Pressure, polynomial order
q	Quadrature order
Re	Reynolds number
Re_τ	Reynolds number based on friction velocity u_τ
s	Spectral shift (spectral filter parameter)
\mathbf{S}	Numerical source term
\mathbf{S}, S_{ij}	Strain-rate tensor
t	Time
t^+	Viscous time, $t^+ = tu_\tau^2/\nu$

(u, v, w)	Velocity components in Cartesian coordinates
\mathbf{u}	Velocity vector
U	Exact velocity/solution space
W	Test function space
u_τ	Friction velocity, $u_\tau = (\tau_w/\rho)^{1/2}$
u^+	Velocity in viscous units, $u^+ = u/u_\tau$
(x, y, z)	Cartesian coordinates
x_i	Cartesian coordinates

Greek Symbols

δ	Half-height or mean half-height of the channel
Δ	Finite difference operator
$\tilde{\Delta}$	VMS model length scale
ϵ	Penalty factor
μ	Dynamic viscosity coefficient
ν	Kinematic viscosity coefficient, $\nu = \mu/\rho$
ν_T	Non-dimensional eddy viscosity in SGS model
Ω	Domain of a volume integral
ρ	Fluid density
τ_{ij}	Stress tensor
τ_w	Average wall shear stress

Accents, Superscripts, and Subscripts

$()_{max}$	Maximum value
$()_{rms}$	Root-mean-square value
$()^+$	Wall coordinates or viscous units
$\overline{()}$	Mean or grid-filtered variables/ Large-scales of the solution
$\tilde{()}$	Small-scales of the solution
$()'$	Unresolved-scales of motion
$\hat{()}$	Numerical fluxes

Abbreviations

BR	Bassi-Rebay numerical viscous flux
BLDG	Boundary Local Discontinuous Galerkin numerical viscous flux
DG	Discontinuous Galerkin
DNS	Direct Numerical Simulation
DYN	Dynamic LES
LDG	Local Discontinuous Galerkin numerical viscous flux
LES	Large Eddy Simulation
ℓ VMS	Local VMS
LVMS	Local VMS
PD	Polynomial Dealiasing
RANS	Reynolds Averaged Navier-Stokes
RHS	Right Hand Side
RMS	Root-Mean-Square

RK	Runge-Kutta
SF	Spectral Filter
SBLDG	Streamwise-positive BLDG numerical viscous flux
SGS	Sub-Grid Scales
TVD	Total Variational Diminishing
VMS	Variational Multi-Scale

Table of Contents

Abstract	3
Acknowledgments	5
Nomenclature	7
1 Introduction	1
1.1 Turbulence Simulation Background	2
1.1.1 Discontinuous Galerkin Methods	4
1.1.2 Variational Multi-Scale (VMS) Methods	5
1.1.3 Local Variational Multi-Scale – ℓ VMS	6
1.2 Goals and Accomplishments	8
2 Formulation and Implementation	11
2.1 Discontinuous Galerkin Method	11
2.2 ℓ VMS Formulation	16
2.3 VMS Model Description	21
2.4 Discretization and Implementation	22
2.5 Summary	23
3 Turbulent Channel Simulation	25
3.1 Turbulent Channel Flow–Preliminaries	25
3.2 Numerical Results	27
3.2.1 Low Reynolds Number	29
3.2.2 Moderate Reynolds Number	36
3.3 Discussion	39
3.4 Summary	40
4 Boundary Conditions Enforcement	87
4.1 Numerical Viscous Fluxes Definitions	87
4.2 Numerical Results	89
4.2.1 Low Reynolds Number	89
4.2.2 Moderate Reynolds Number	95

4.3	Discussion	97
4.4	Summary	100
5	Local Variational Multi-Scale — ℓVMS	129
5.1	Strategies for Non-linear Stability	129
5.1.1	Polynomial Dealiasing (PD)	130
5.1.2	Spectral Filtering (SF)	131
5.1.3	Numerical Viscous Fluxes	132
5.2	Numerical Results Preliminaries	132
5.3	Non-linear Stability – Filtering and Dealiasing	133
5.4	ℓVMS Modeling	134
5.4.1	Parameter Selection	135
5.4.2	Polynomial Dealiasing	136
5.4.3	Role of Numerical Fluxes and Spectral Filtering	137
5.4.4	Importance of Small Scales Space	138
5.4.5	Local Polynomial Enrichment	139
5.4.6	Moderate Reynolds Number	140
5.5	Summary	140
6	Discussion and Future Work	163
6.1	Conclusions	163
6.2	Future Work	164
	Bibliography	166

List of Tables

1.1	Simulation hierarchy	2
3.1	Simulation parameters and results summary for a resolution study with a $4 \times 4 \times 8$ mesh at $Re_\tau = 100$	42
3.2	Simulation parameters and results summary for a resolution study with a $8 \times 8 \times 8$ mesh at $Re_\tau = 100$	42
3.3	Simulation parameters and results summary for a resolution study with a $4 \times 8 \times 8$ at $Re_\tau = 100$	42
3.4	Simulation parameters and results summary for a resolution study with a $8 \times 8 \times 8$ at $Re_\tau = 100$	42
3.5	Simulation parameters and results summary for a resolution study with a $8 \times 8 \times 16$ at $Re_\tau = 180$	43
3.6	Simulation parameters and results summary for a resolution study with a $16 \times 16 \times 16$ mesh at $Re_\tau = 180$	43
3.7	Simulation parameters and results summary for a resolution study with a $8 \times 8 \times 18$ mesh at $Re_\tau = 395$	43
4.1	Effect of various numerical viscous fluxes for a $8 \times 4 \times 8$ mesh using $p = 3$ at $Re_\tau = 100$	101
4.2	Effect of various numerical viscous fluxes for a $4 \times 4 \times 8$ mesh using $p = 3$ at $Re_\tau = 100$	101
4.3	Effect of various numerical viscous fluxes for a $4 \times 4 \times 8$ mesh using $p = 6$ at $Re_\tau = 100$	101
4.4	Effect of numerical viscous flux for a $16 \times 4 \times 16$ mesh using $p = \{6, 5, 5, 6\}$ at $Re_\tau = 180$	102
4.5	Effect of various numerical viscous fluxes for $8 \times 8 \times 12$ mesh using $p = 4$ at $Re_\tau = 395$	102
5.1	Simulation parameters and result summary for a $4 \times 4 \times 4$ using $p = 5$ to compare spectral filtering against dealiasing at $Re_\tau = 100$	142
5.2	Simulation parameters and result summary for a $4 \times 4 \times 4$ mesh for $Re_\tau = 100$ to study non-linear stability, partition selection, and VMS modeling.	142

5.3	Simulation parameters and result summary for a $4 \times 9 \times 6$ using $p = 5$ at $Re_\tau = 395$ using ℓ VMS	142
-----	--	-----

List of Figures

1.1	Typical turbulent shear-flows illustrating large-scale coherent structures	3
2.1	Schematic of DGM discretization	13
2.2	Multi-scale partitioning of a turbulent energy spectrum and the interaction between the scales.	17
2.3	Illustration of ℓ VMS modeling capabilities for flows in complex geometries. . .	24
3.1	The planar channel configuration	26
3.2	Quadrature grid for a mesh with variable polynomial orders	26
3.3	$Re_\tau = 100$ using $p = 3$ with different mesh topologies – mean velocity and turbulence intensity profiles	44
3.4	$Re_\tau = 100$ using $p = 3$ with different mesh topologies – streamwise and spanwise spectra	45
3.5	$Re_\tau = 100$ using $p = 3$ with different mesh topologies – streamwise and spanwise spectra (u and v components)	46
3.6	$Re_\tau = 100$ using $p = 3$ with different mesh topologies – Reynolds, viscous, and total stress profiles	47
3.7	$Re_\tau = 100$ using $p = 4$ with different mesh topologies – mean velocity and turbulence intensity profiles	48
3.8	$Re_\tau = 100$ using $p = 4$ with different mesh topologies – streamwise and spanwise spectra	49
3.9	$Re_\tau = 100$ using $p = 4$ with different mesh topologies – streamwise and spanwise spectra (u component)	50
3.10	$Re_\tau = 100$ using $p = 4$ with different mesh topologies – Reynolds and viscous, and total stress profiles	51
3.11	$Re_\tau = 100$ using $p = 6$ with different mesh topologies – mean velocity and turbulence intensity profiles	52
3.12	$Re_\tau = 100$ using $p = 6$ with different mesh topologies – streamwise and spanwise spectra	53
3.13	$Re_\tau = 100$ using $p = 6$ with different mesh topologies – streamwise and spanwise spectra (u and v components)	54

3.14	$Re_\tau = 100$ using $p = 6$ with different mesh topologies – Reynolds and viscous, and total stress profiles	55
3.15	$Re_\tau = 100$ using $4 \times 4 \times 8$ mesh using two different polynomial orders – meanflow and turbulence intensity profiles	56
3.16	$Re_\tau = 100$ using $4 \times 4 \times 8$ mesh using two different polynomial orders – Reynolds, viscous, and total stress profiles	57
3.17	$Re_\tau = 100$ using $4 \times 4 \times 8$ mesh using two different polynomial orders – streamwise and spanwise directions one-dimensional energy spectra	58
3.18	Effects of numerical dissipation using different mesh and polynomial orders at $Re_\tau = 100$ – meanflow and turbulence intensity profiles	59
3.19	Effects of numerical dissipation using different mesh and polynomial orders at $Re_\tau = 100$ – Reynolds, viscous, and total stress profiles	60
3.20	Effects of numerical dissipation using different mesh and polynomial orders at $Re_\tau = 100$ – streamwise and spanwise directions one-dimensional energy spectra	61
3.21	$Re_\tau = 180$ with a $8 \times 8 \times 16$ mesh using different polynomial orders – meanflow and turbulence intensity profiles	62
3.22	$Re_\tau = 180$ with a $8 \times 8 \times 16$ mesh using different polynomial orders – streamwise and spanwise spectra	63
3.23	$Re_\tau = 180$ with a $8 \times 8 \times 16$ mesh using different polynomial orders – Reynolds and viscous stress profiles	64
3.24	$Re_\tau = 180$ with a $16 \times 16 \times 16$ mesh using different polynomial orders – meanflow and turbulence intensity profiles	65
3.25	$Re_\tau = 180$ with a $16 \times 16 \times 16$ mesh using different polynomial orders – streamwise and spanwise spectra	66
3.26	$Re_\tau = 180$ with a $16 \times 16 \times 16$ mesh using different polynomial orders – Reynolds and viscous stress profiles	67
3.27	$Re_\tau = 395$ with a $8 \times 8 \times 18$ mesh using different polynomial orders – meanflow and turbulence intensity profiles	68
3.28	$Re_\tau = 395$ with a $8 \times 8 \times 18$ mesh using different polynomial orders – streamwise and spanwise spectra	69
3.29	$Re_\tau = 395$ with a $8 \times 8 \times 18$ mesh using different polynomial orders – Reynolds and viscous stress profiles	70

3.30	Comparison of low-order statistics for $Re_\tau = 395$ and $Re_\tau = 100$ with similar relative resolution ($p = 4$)	71
3.31	Comparison of low-order statistics for $Re_\tau = 395$ and $Re_\tau = 100$ with similar relative resolution	72
3.32	$Re_\tau = 100$ with a $4 \times 8 \times 8$ mesh with different polynomial orders – meanflow and turbulence intensity profiles	73
3.33	$Re_\tau = 100$ with a $4 \times 8 \times 8$ mesh using different polynomial orders – streamwise and spanwise spectra	74
3.34	$Re_\tau = 100$ with a $4 \times 8 \times 8$ mesh using different polynomial orders – Reynolds and viscous stress profiles	75
3.35	$Re_\tau = 100$ with a $8 \times 4 \times 8$ mesh using different polynomial orders – meanflow and turbulence intensity profiles	76
3.36	$Re_\tau = 100$ with a $8 \times 4 \times 8$ mesh using different polynomial orders – streamwise and spanwise spectra	77
3.37	$Re_\tau = 100$ with a $8 \times 4 \times 8$ mesh using different polynomial orders – Reynolds, viscous, and total stress profiles	78
3.38	$Re_\tau = 100$ with a $4 \times 4 \times 8$ mesh with different polynomial orders – meanflow and turbulence intensity profiles	79
3.39	$Re_\tau = 100$ with a $4 \times 4 \times 8$ mesh with different polynomial orders – streamwise and spanwise spectra	80
3.40	$Re_\tau = 100$ with a $4 \times 4 \times 8$ mesh with different polynomial orders – Reynolds, viscous, and total stress profiles	81
3.41	$Re_\tau = 100$ with a $8 \times 8 \times 8$ mesh using different polynomial orders – meanflow and turbulence intensity profiles	82
3.42	$Re_\tau = 100$ with a $8 \times 8 \times 8$ mesh using different polynomial orders – streamwise and spanwise spectra	83
3.43	$Re_\tau = 100$ with a $8 \times 8 \times 8$ mesh using different polynomial orders – Reynolds and viscous stress profiles	84
3.44	Wall shear stress and average streamwise velocity slip at the wall	85
3.45	$Re_\tau = 100$ with a $8 \times 8 \times 8$ mesh at $p = 3$ with local h –refinement in the wall-normal direction – meanflow and turbulence intensity profiles	86
4.1	$Re_\tau = 100$ on a $8 \times 4 \times 8$ mesh using $p = 3$ with different numerical viscous fluxes – meanflow, viscous, and total stress profiles profiles	103

4.2	$Re_\tau = 100$ on a $8 \times 4 \times 8$ mesh using $p = 3$ with different numerical viscous fluxes – Reynolds stress and turbulence intensity profiles	104
4.3	$Re_\tau = 100$ on a $8 \times 4 \times 8$ mesh using $p = 3$ with different numerical viscous fluxes – streamwise and spanwise spectra	105
4.4	$Re_\tau = 100$ on a $8 \times 4 \times 8$ mesh using $p = 3$ with different numerical viscous fluxes – meanflow, viscous, and total stress profiles profiles	106
4.5	$Re_\tau = 100$ on a $8 \times 4 \times 8$ mesh using $p = 3$ with different numerical viscous fluxes – streamwise and spanwise spectra	107
4.6	$Re_\tau = 100$ on a $8 \times 4 \times 8$ mesh using $p = 3$ with different numerical viscous fluxes – Reynolds stress and turbulence intensity profiles	108
4.7	$Re_\tau = 100$ on a $4 \times 4 \times 8$ mesh using $p = 3$ with different numerical viscous fluxes – meanflow, viscous, and total stress profiles	109
4.8	$Re_\tau = 100$ on a $4 \times 4 \times 8$ mesh using $p = 3$ with different numerical viscous fluxes – Reynolds and turbulence intensity profiles	110
4.9	$Re_\tau = 100$ on a $4 \times 4 \times 8$ mesh using $p = 3$ with different numerical viscous fluxes – streamwise and spanwise spectra	111
4.10	$Re_\tau = 100$ on a $4 \times 4 \times 8$ mesh using $p = 3$ with different numerical viscous fluxes – meanflow and turbulence intensity profiles	112
4.11	$Re_\tau = 100$ on a $4 \times 4 \times 8$ mesh using $p = 3$ with different numerical viscous fluxes – streamwise and spanwise spectra	113
4.12	$Re_\tau = 100$ on a $4 \times 4 \times 8$ mesh using $p = 3$ with different numerical viscous fluxes – Reynolds, viscous, and total stress profiles	114
4.13	$Re_\tau = 100$ on a $4 \times 4 \times 8$ mesh using $p = 6$ with different numerical viscous fluxes – meanflow and turbulence intensity profiles	115
4.14	$Re_\tau = 100$ on a $4 \times 4 \times 8$ mesh using $p = 6$ with different numerical viscous fluxes – streamwise and spanwise spectra	116
4.15	$Re_\tau = 100$ on a $4 \times 4 \times 8$ mesh using $p = 6$ with different numerical viscous fluxes – Reynolds, viscous, and total stress profiles	117
4.16	$Re_\tau = 180$ on a $16 \times 4 \times 16$ mesh using $p = \{6, 5, 5, 6\}$ with SBLDG – meanflow and turbulence intensity profiles profiles	118
4.17	$Re_\tau = 180$ on a $16 \times 4 \times 16$ mesh using $p = \{6, 5, 5, 6\}$ with SBLDG – streamwise and spanwise spectra	119

4.18	$Re_\tau = 180$ on a $16 \times 4 \times 16$ mesh using $p = \{6, 5, 5, 6\}$ with SBLDG – Reynolds stress, viscous, and total stress profiles	120
4.19	Comparison of SBLDG and LDG numerical viscous flux at $Re_\tau = 395$ – mean-flow and viscous stress profiles	121
4.20	Comparison of SBLDG and LDG numerical viscous flux at $Re_\tau = 395$ – streamwise and spanwise spectra	122
4.21	Comparison of SBLDG and LDG numerical viscous flux at $Re_\tau = 395$ – Reynolds stress and turbulence intensity profiles	123
4.22	Comparison of SBLDG and LDG numerical viscous flux at $Re_\tau = 395$ – viscous and total stress	124
4.23	Advection-diffusion using various numerical viscous fluxes — $p = 0$ and $p = 2$	125
4.24	Advection-diffusion using various numerical viscous fluxes — $p = 0$ and $p = 2$	126
4.25	Effect of penalty factor for the different numerical viscous fluxes	127
4.26	BR versus ILDG using $p = 2$	128
5.1	Spectral filter transfer function for various polynomial orders	143
5.2	Non-linear stability strategies evaluation at $Re_\tau = 100$ – Meanflow and rms profiles	144
5.3	Non-linear stability strategies evaluation at $Re_\tau = 100$ – 1-D energy spectrum in the x – and z – directions	145
5.4	Non-linear stability strategies evaluation at $Re_\tau = 100$ – Reynolds, viscous and total stress profiles	146
5.5	Important length scales for partition selection in ℓ VMS	147
5.6	ℓ VMS with PD at $Re_\tau = 100$ – meanflow and rms profiles	148
5.7	ℓ VMS with PD at $Re_\tau = 100$ – 1-D energy spectrum in the x – and z – directions	149
5.8	ℓ VMS with PD at $Re_\tau = 100$ – Reynolds, viscous and total stress profiles . . .	150
5.9	ℓ VMS modeling issues – meanflow and rms profiles	151
5.10	ℓ VMS modeling issues – Reynolds, viscous and total stress profiles	152
5.11	ℓ VMS modeling issues – 1-D energy spectrum in the x – and z – directions. . .	153
5.12	Role of partition in ℓ VMS – meanflow and rms profiles	154
5.13	Role of partition in ℓ VMS – 1-D energy spectrum in the x – and z – directions. .	155
5.14	Local polynomial refinement in ℓ VMS – meanflow and rms profiles	156
5.15	Local polynomial refinement in ℓ VMS – 1-D energy spectrum in the x – and z – directions	157

5.16	Local polynomial refinement in ℓ VMS – Reynolds, viscous and total stress profiles	158
5.17	ℓ VMS at $Re_\tau = 395$ – Meanflow and rms profiles	159
5.18	ℓ VMS at $Re_\tau = 395$ – 1-D energy spectrum in the x – and z – directions at $y^+ \approx 20$ wall units	160
5.19	ℓ VMS at $Re_\tau = 395$ – Reynolds, viscous and total stress profiles	161

Chapter 1

Introduction

Mathematical modeling of physical, chemical, and biological phenomenon has become a useful complement to theoretical and experimental investigations. The culmination of advances in computational power, improved mathematical description of the aforementioned systems, and their translation to efficient and accurate solution algorithms have made numerical simulation an indispensable tool in science and engineering. In the case of turbulence, theoretical efforts are severely restricted by the non-linearity of the governing partial differential equations. Meanwhile experimental studies of turbulence are constrained by cost (time and facilities) and the limitations of instrumentation in complex geometries. Here, accurate and high fidelity numerical simulations can serve to provide much needed insight into fluid dynamics in complex flow configurations, as demonstrated in simpler geometries [1, 54].

However, numerical simulation of engineering flows that are generally turbulent continues to be a formidable challenge. Turbulence simulations are inherently expensive computationally due to the presence of a broad range of spatial and temporal scales (see Fig. 1.1). The cost of simulations that resolves all the scales of motion are on the order of Re^3 (Re is the Reynolds number that are generally greater than 10^5 for most engineering flows). A major portion of this cost, as much as 90% by some estimates [73], is a direct result of attempting to *explicitly* resolve boundary layers formed at the fluid and structure interface i.e. surface of airfoils, walls of a pipes, channels etc. due to viscous effects.

A hierarchy of common turbulence simulation approaches along with the associated features are found in Table 1.1. The high cost of DNS makes it impractical for realistic engineering flows. To date, the practical industry standard for turbulence simulation is RANS. However, the level of detail present in RANS simulations is often insufficient to satisfactorily capture the unsteady dynamics of flows in complex geometries. Further, the modeling in the RANS scenario can be very complicated since it aims to model all the scales of turbulence.

Fortunately, experimental and numerical investigations [5, 54, 55, 89] have revealed scales that are generally large (relative to the domain of interest) that are responsible for

Type	Resolved Scales	Cost	Models
Direct Numerical Simulation (DNS)	All	High	None
Large Eddy Simulation (LES)	Large	Intermediate	SGS closures
Reynolds Averaged Navier-Stokes (RANS)	Mean	Low	Variable [92]
Hybrid*	Large/Mean	Variable	SGS and/or variable [92]

Table 1.1: Turbulence simulation approaches. * Hybrid simulations generally have capabilities intermediate between RANS and LES.

the important dynamical processes in the flow. Large Eddy Simulations (LES) exploits this feature of turbulence by resolving only these large scales and modeling the remaining scales using Sub-Grid Scales (SGS) closures [36, 82]. Since the large scales form a small fraction of the scales present in the flow, it reduces the required degrees of freedom, and thus, the associated computational cost.

Recently, simulations that combine RANS and LES have been developed that build upon the merits of both approaches to achieve increased efficiency while retaining sufficient fidelity [70, 83, 86]. While these approaches show some advantages in the interim, their long term success is limited, for a number of reasons (see Section 1.1.3). The current research aims to develop a framework ℓ VMS, that merges a Discontinuous Galerkin (DG) spatial discretization with a promising new approach to LES, namely the VMS [28, 46, 47, 76, 78]. We believe that this combination has the potential for accurate and efficient turbulence simulations that overcomes the inherent limitations of both traditional and the more recent hybrid methods. Now, we present some background information before introducing the ℓ VMS framework (see Section 1.1.3).

1.1 Turbulence Simulation Background

Turbulence simulation methods such as DNS, LES, and RANS are mature areas of research precluding a comprehensive review here. Fortunately, there are a number of review articles and monographs that interested readers may consult for additional details.

A good account of the early successes in turbulence simulation, namely DNS and LES,

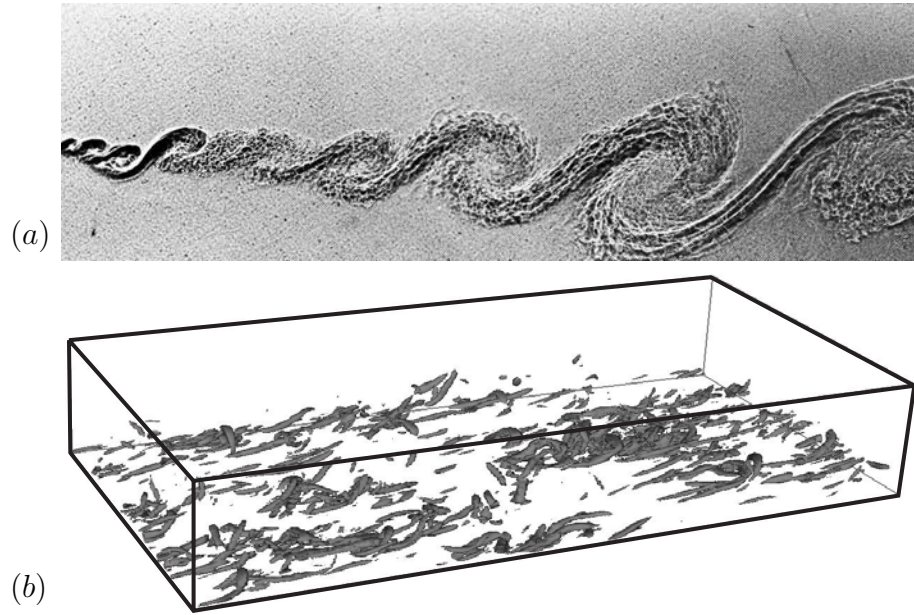


Figure 1.1: Typical turbulent shear-flows illustrating large-scale coherent structures: (a) mixing layer experiment [12], (b) direct numerical simulation of channel flow [31]. This illustration first appeared in the article by Collis [29]

can be found in the review by Rogallo and Moin [81]. A more recent update on the progress of DNS as a valuable research tool can be found in Moin and Mahesh [68] and the articles cited therein. Incidentally, the current research effort has directly benefitted from the use of the DNS databases [69] for our validation studies. Similarly, for LES, the reviews of Ferziger [36] and Lesieur and Metais [60], the monograph by Sagaut [82] provide a good introduction to the subject. By far the most famous monograph on RANS methods is by Wilcox [92] while an equally good exposition on the subject can be found in Chen and Jaw [16].

Meanwhile, estimates for resolving the inner layer i.e. the near-wall region for a boundary layer reveal that over 90% of the computational grid points are clustered in this region [73]. This statistic spurred researchers to devise methods that forego explicitly resolving the near-wall region, and instead modeling the effect of the wall in a number of ways [33, 66, 73]. These methods that all imply the well-known law of the wall [91] come under the purview of wall-modeling. The review article by Piomelli and Balaras [73] follows the developments of wall-modeling approaches and presents instances of their successful application to different flows.

Here, we begin with a brief account of the developments in discontinuous Galerkin

methods and variational multi-scale methods that have either directly and/or indirectly contributed to the current research effort.

1.1.1 Discontinuous Galerkin Methods

Discontinuous Galerkin methods have now existed for about three decades pioneered by Reed and Hill [79] for the solution of a neutron transport equation in 1973. The following year Raviart and LeSaint [59] produced the first mathematical analysis of the method. Subsequently, the method has been placed on a strong mathematical foundation for linear hyperbolic problems by the analyses of Johnson and Pitkäranta [51], Richter [80] and Bey and Oden [10].

However, the extensions of DG to non-linear convection-diffusion problems (Navier-Stokes) has been a relatively recent development. The active interest in DG for fluid dynamics can be attributed to several key advances. One critical factor is the development of DG methods for diffusion problems. Recently, Arnold *et al.* [3] presented a comparison of DG methods developed for elliptic problems where they reviewed nine such formulations that have been developed over the years. In order to make the comparisons directly, they relate the primal formulation commonly associated with interior penalty methods [2, 90] to the flux formulation common to discontinuous Galerkin methods before undertaking a unified error analysis [3]. The study finds DG methods that are consistent, stable and possessing optimal convergence rates, notable among these are the approaches of Douglas and Dupont [34], Cockburn and Shu [24], and Bassi *et al.* [8].

Next, the Runge-Kutta Discontinuous Galerkin (RKDG) method was developed starting from one-dimensional scalar systems to a general multi-dimensional conservation laws by Cockburn and Shu [22, 23, 25, 26]. This development was motivated by the need for constructing a stable and efficient DG method amenable for solving non-linear hyperbolic conservation problems. We note in passing that some of these advances benefitted from the progress in high-order methods used for solving non-linear hyperbolic conservation systems, such as Riemann solvers, TVD methods, slope limiters etc. (see Toro [88] for details).

Now, Bassi and Rebay [6] built on the RKDG method for the inviscid flux and introduced a mixed formulation for the viscous flux to extend DG to convection-diffusion problems. Later, a similar approach was followed by other researchers that resulted in the Local Discontinuous Galerkin [24] approach of Cockburn and Shu and the method of

Lomtev *et al.* [64]. The authors note that the current work builds on the work of Bassi-Rebay [6] and Cockburn and Shu [24] for the dealing with the viscous and Euler fluxes, respectively (see Chapter 2). Simultaneously, an alternative method for dealing with viscous fluxes that eliminates the need for auxiliary variables, generated by mixed formulations, was developed by Oden *et al.* [72] and applied to convection-diffusion systems [9].

The progress in DG and their developments upto 1999 can be found in Cockburn, Shu and Karniadakis [21]. The articles by Arnold *et al.* [3] and the lecture notes of Cockburn [18] provide an excellent introduction to DG methods. The essay on DG methods by Cockburn [19], an attempt to introduce DG to a wider audience, serves to highlight the salient features of DG methods in a lucid manner.

1.1.2 Variational Multi-Scale (VMS) Methods

The Variational Multi-Scale (VMS) method was first introduced by Hughes *et al.* [45, 49] to provide a robust framework for the simulation of multi-scale phenomenon encountered in computational mechanics. Subsequently, VMS was introduced as a paradigm for Large Eddy Simulation (LES) by Hughes, Mazzei and Jansen [46]. Later, by explicitly tracking all the scales of motion, Collis [28] clarified the modeling assumptions, in the context of VMS, consistent with traditional turbulence modeling.

The first implementation of VMS with a simple constant coefficient Smagorinsky model for homogeneous isotropic turbulence [47] was shown to have excellent agreement with DNS. Soon, the early success was extended to both equilibrium and non-equilibrium turbulent channel flow [48, 71]. Recently, Ramakrishnan and Collis [78] extended VMS to a discretization that does not readily support scale separation in all directions. In doing so, they applied VMS for opposition control studies in a turbulent channel where VMS is shown to have better predictive abilities compared with the dynamic model [15].

Later, by exploiting the well-known near-wall structures of turbulent channel flow, they relate the partition selection parameter (required for *a priori* scale separation in VMS) to the near-wall streak-spacing [76]. In an effort to obtain a robust VMS model, Holmen *et al.* [42] employed a dynamic procedure for selecting the Smagorinsky coefficient, that improves the sensitivity characteristics (to the model parameters) of VMS.

All VMS results mentioned thus far have used global spectral methods that restrict the applicability of the method to simple geometries. However, VMS has been extended to

general flow configurations by Jansen [50] and Koobus and Farhat [57] with some success. The former employed a low-order (cubic and lower) finite elements while the latter uses a finite volume approach. However, we believe that for realizing the full potential of VMS requires a higher order representation within the elements than that afforded in low-order finite elements. And although the spatial derivatives are computed with high-order accuracy in the finite volume approach of Koobus and Farhat [57], scale separation is not straightforward. Here, we attempt to develop and test a method that is not only high-order accurate, but also readily supports multi-scale implementations.

1.1.3 Local Variational Multi-Scale – ℓ VMS

The ℓ VMS framework, first proposed by Collis [29], aims to overcome the disadvantages of traditional approaches to turbulence simulation. The shortcomings of the latter arise due to a variety of reasons [29]: 1) Models are developed without regard for discretization. 2) Models are often tuned to match mean flow quantities. 3) They use ad hoc blending functions to couple LES and RANS regions and/or wall functions. 4) The methods often do not converge to the exact solution (DNS). 5) Spatial filters (LES) are used that have known difficulties in unstructured grids often used close to physical walls. 6) Low-order numerical methods are employed that are unsuitable for accurate prediction in unsteady flows and are known to interact adversely with subgrid scale models.

ℓ VMS explores the merger of DG and VMS [46], an approach to LES, as a suitable framework that has many desirable features while overcoming the limitations of traditional approaches outlined previously. Let us first examine the two components individually. The DG discretization is attractive for turbulence simulation for several reasons.

1. High order (spectral) accuracy on arbitrary grids
2. Local hp - refinement capability.
3. Local conservation allows the use of different models in adjoining elements.
4. Highly parallelizable for computational efficiency.
5. Boundary and interface conditions are set weakly through numerical fluxes.

Importantly, since DG methods are ideal for hyperbolic systems or nearly hyperbolic systems, it holds great potential for high Reynolds number turbulent flows. Now, the VMS [46] paradigm is desirable for the following reasons.

1. The variational formulation provides a solid mathematical foundation for turbulence modeling [28, 46];
2. Variational projection is used for scales separation allowing the extension to complex geometries straightforward – there are no commutativity or homogeneity issues like those that arise when using spatial filters (see e.g. [39, 46]);
3. The large scales have no direct model terms. Therefore, the exact solution satisfies the large-scale equations leading to a consistent method i.e. the solution converges to DNS in the limit of high resolution.
4. *A priori* scale separation allows for different modeling approximations on different scale ranges.
5. A simple constant coefficient Smagorinsky type model acting only on the smallest *resolved* scales has been shown to be effective for both the decay of homogeneous isotropic turbulence [47] and wall bounded flows [48, 71];
6. The modeled equations are considerably simpler than the dynamic subgrid-scale model [38, 62] making calculations potentially more efficient.

The DG/VMS [29] combination is particularly synergistic, since, the high-order hierarchical elements are a natural framework for *a priori* scale identification crucial for multi-scale modeling. The flexibility engendered by DG/VMS [29] combination relates to the inherent features of the individual components.

1. DG introduces locality in *physical space* that allows for a natural coupling of different fidelity models in adjacent regions in the physical domain through numerical fluxes.
2. VMS introduces locality in *spectral space* (It may be useful think in terms of Fourier Modes) that allows a natural coupling of a range of traditional approaches such as DNS, LES, and RANS on adjacent range of scales.

Overall, we obtain a method that is flexible both from a modeling and computational efficiency perspective while offering mathematical consistency, and high-order accuracy. Importantly, ℓ VMS is amenable to complex geometry crucial for application to engineering flows (see Figure 2.3).

1.2 Goals and Accomplishments

The principal goal of the current research is to evaluate the capabilities of ℓ VMS method for turbulence simulation, in particular, wall-bounded turbulence. In the process, we encounter the familiar challenges of resolution requirements related to both reliable statistics as well as non-linear stability. Additionally, in DG, all interface and boundary conditions are enforced weakly through numerical fluxes. This allows the solution jumps both at interelement interfaces as well as wall boundaries. We study the effects of the solution jump, closely related to local resolution, on the quality turbulence statistics. Further, we introduce SGS modeling through a VMS approach in an effort to reduce resolution requirements. The principal contributions of the current research effort are listed below.

1. Validation of a DG spatial discretization for wall bounded turbulence, namely fully-developed turbulent channel flow, with the aid of available DNS [14, 69] for a range of Reynolds numbers.
2. A detailed investigation of the effects of DG spatial discretization on turbulence statistics. Thereby, resolution requirements for reasonable low-order statistics in wall-bounded flows with no explicit modeling is established. In the process, the flexibility of the DG spatial discretization for local hp -refinement that can be exploited to improve the solution efficiently through a judicious distribution of the required degrees of freedom is highlighted.
3. The enforcement of Dirichlet boundary conditions through numerical viscous flux allows jumps in the solution at the channel solid walls. This feature enables reasonable wall shear stress (τ_w) predictions even with moderate resolutions in the wall-normal direction (Δy_w^+). Further, using large Δy_w^+ values result in significant solution jumps at the channel walls that lead to poor τ_w predictions. Here, modifying the numerical viscous flux to regulate the solution jumps at the wall is found to improve τ_w predictions. Thus, demonstrating the potential of the numerical viscous flux to act as a rudimentary wall-model.
4. Evaluation of two strategies, spectral filtering [61] and polynomial dealiasing [67], for reducing aliasing errors crucial for non-linear stability is undertaken. In the current work, the overall performance of polynomial dealiasing [67] is found to be better suited for SGS modeling than spectral filtering [61].

5. Implementation of a VMS [46,48] model in the current DG spatial discretization, that we term ℓ VMS, is validated for the fully-developed turbulent channel flow. Results in good agreement with reference DNS demonstrate the efficacy of ℓ VMS for wall-bounded turbulence simulation.

We present a brief outline of the remainder of the thesis. In Chapter 2, we present the details of the DG spatial discretization and a derivation of the ℓ VMS model equations. Next, in Chapter 3, we undertake a resolution study that both validates our implementation and reveals the effects the DG spatial discretization on turbulence statistics. In the process, we highlight local hp –refinement capabilities of DG that make it attractive for turbulence simulation. Chapter 4 focuses on the numerical viscous flux and their role in enforcing boundary and interface conditions that can be exploited for reducing the near-wall resolution requirements. There, we highlight the potential advantages in enforcing wall boundary conditions using numerical fluxes. Then, in chapter 5, we present numerical results for ℓ VMS while simultaneously addresssing the challenges of reduced order modeling in a high-order method. Here, we explore strategies for improving non-linear stability and their interaction with the DG spatial discretization in the context of ℓ VMS. In the same chapter, we present a discussion on the selection of ℓ VMS parameters for the turbulent channel flow that may be useful for extending ℓ VMS to other flows. Finally, in Chapter 6, we present a discussion of our results by way of summary and propose future research directions.

Chapter 2

Formulation and Implementation

In this chapter, we begin with a description of a DG spatial discretization for the Navier-Stokes equations of motion following the discussion of Collis [29, 30]. We introduce our choices for the numerical fluxes required to complete the definition of any DG discretization. Next, we give a brief overview of the VMS method based on the expositions of Hughes *et al.* [46] and Collis [28]. Then, we present the ℓ VMS model equations by introducing a VMS model in the DG the current spatial discretization. Later, we describe the model used in this work and additional details of our implementation. Finally, we end this chapter with a summary that highlights the unique features of the ℓ VMS framework that make it attractive for turbulence simulation.

2.1 Discontinuous Galerkin Method

We begin with the strong form of the compressible Navier-Stokes equations of motion.

$$\mathbf{U}_{,t} + \mathbf{F}_{i,i} - \mathbf{F}_{i,i}^v = \mathbf{S} \quad \text{in } \Omega, \quad (2.1a)$$

$$\mathbf{U}(\mathbf{x}, 0) = \mathbf{U}_0(\mathbf{x}), \quad (2.1b)$$

where $\mathbf{U} = \{\rho, \rho \mathbf{u}, \rho e\}^T$ is the vector of conserved variables, ρ is the fluid density, $\mathbf{u} = \{u, v, w\}^T$ is the fluid velocity vector, and $e = e_{int} + \frac{u_i u_i}{2}$ is the total energy per unit mass (e_{int} is the internal energy). The inviscid and viscous flux vectors in the i th coordinate direction are $\mathbf{F}_i(\mathbf{U})$ and $\mathbf{F}_i^v(\mathbf{U})$ defined as

$$\mathbf{F}_i(\mathbf{U}) = u_i \mathbf{U} + p \begin{pmatrix} 0 \\ \delta_{1i} \\ \delta_{2i} \\ \delta_{3i} \\ u_i \end{pmatrix}, \quad \mathbf{F}_i^v(\mathbf{U}) = \begin{pmatrix} 0 \\ \tau_{1i} \\ \tau_{2i} \\ \tau_{3i} \\ \tau_{ij} u_j - q_i \end{pmatrix}, \quad (2.2)$$

where p is the thermodynamic pressure, $\tau_{ij} = 2\mu S_{ij} + \lambda u_{k,k} \delta_{ij}$, the strain rate tensor $S_{ij} = \frac{1}{2}(u_{i,j} + u_{j,i})$ and λ is the bulk viscosity. Also, the heat flux, $q_i = -\kappa T_{,i}$ where κ is the molecular conductivity and T is the temperature. Any source terms present are included in \mathbf{S} .

We solve Eq. (2.1a) subject to the appropriate boundary conditions specific to the problem of interest. Also, a state equation, such as the ideal gas law to relate the thermodynamic variables and constitutive laws to define the physical properties such as viscosity and thermal conductivity as functions of the conserved variables provide closure to the system of equations [41].

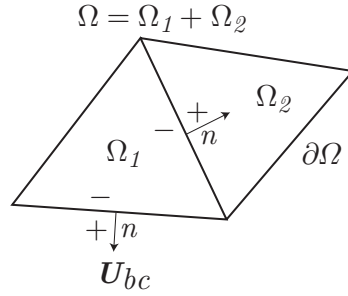
The fixed spatial domain for the problem is denoted by Ω , which is an open, connected, bounded subset of \mathbb{R}^3 , with boundary $\partial\Omega$. Let \mathcal{P}_h be a partition of the domain Ω into N subdomains Ω_e where

$$\bar{\Omega} = \bigcup_{e=1}^N \bar{\Omega}_e \quad \text{and} \quad \Omega_e \cap \Omega_f = \emptyset \quad \text{for} \quad e \neq f. \quad (2.3)$$

Now, we construct the weak form of the equations starting with the strong form of the compressible Navier–Stokes equations (2.1a). Consider a single subdomain, Ω_e , we multiply Eq. 2.1a by a weighting function, \mathbf{W} , that is continuous in Ω_e and integrate the flux terms by parts

$$\begin{aligned} & \int_{\Omega_e} \left(\mathbf{W}^T \mathbf{U}_{,t} + \mathbf{W}_{,i}^T (\mathbf{F}_i^v - \mathbf{F}_i) \right) d\mathbf{x} + \\ & \int_{\partial\Omega_e} \mathbf{W}^T (\mathbf{F}_n - \mathbf{F}_n^v) ds = \int_{\Omega_e} \mathbf{W}^T \mathbf{S} ds, \end{aligned} \quad (2.4)$$

where $\mathbf{F}_n = \mathbf{F}_i n_i$. In the standard Galerkin formulation, where the solution is continuous across the elements, the summation over all the elements in the domain would lead to the flux terms telescoping to the boundary of the spatial domain $\partial\Omega$. However, discontinuous Galerkin allows the solution and weighting functions to be discontinuous across element interfaces (see Fig. 2.1) and the coupling of the solution between adjacent elements is achieved through suitably defined numerical fluxes for both the inviscid flux (F_i) and the viscous flux (F_i^v). Since the solution is not single-valued at the element interface the numerical fluxes for the inviscid and viscous flux terms generally assume the following forms ($F_i \rightarrow \hat{\mathbf{F}}_n(\mathbf{U}^-, \mathbf{U}^+)$) and ($F_i^v \rightarrow \hat{\mathbf{F}}_i^v(\mathbf{U}^-, \mathbf{U}_{,j}^-, \mathbf{U}^+, \mathbf{U}_{,j}^+)$), respectively.

**Figure 2.1:** Schematic of DGM discretization

Now, summing over the domain and introducing the numerical fluxes, we obtain the following

$$\begin{aligned}
 B_{DG}(\mathbf{W}, \mathbf{U}) &= \sum_{e=1}^N \int_{\Omega_e} \left(\mathbf{W}^T \mathbf{U}_{,t} + \mathbf{W}_{,i}^T (\mathbf{F}_i^v - \mathbf{F}_i) \right) d\mathbf{x} + \\
 &\quad \sum_{e=1}^N \int_{\partial\Omega_e} \mathbf{W}^T \left(\hat{\mathbf{F}}_n(\mathbf{U}^-, \mathbf{U}^+) \right) ds - \\
 &\quad \sum_{e=1}^N \int_{\partial\Omega_e} \mathbf{W}^T \left(\hat{\mathbf{F}}_n^v(\mathbf{U}^-, \mathbf{U}_{,j}^-, \mathbf{U}^+, \mathbf{U}_{,j}^+) \right) ds \\
 &= \sum_{e=1}^N \int_{\Omega_e} \mathbf{W}^T \mathbf{S}, ds
 \end{aligned} \tag{2.5}$$

where the \mathbf{U}^+ and \mathbf{U}^- states are illustrated in Fig. 2.1. For a particular element on the physical boundary, $\partial\Omega$, $\mathbf{U}^+ = \mathbf{U}_{bc}$. Meanwhile, for the inter-element boundaries, \mathbf{U}^+ is obtained from the neighboring element. Thus, all boundary conditions and interface conditions are set through the numerical fluxes.

While there are a wide range of choices for both the inviscid and viscous numerical fluxes [18], we have chosen to use a Lax–Friedrichs method for the Euler flux

$$\begin{aligned}
 \hat{\mathbf{F}}_n(\mathbf{U}^-, \mathbf{U}^+) &= \frac{1}{2} \left(\mathbf{F}_n(\mathbf{U}^-) + \mathbf{F}_n(\mathbf{U}^+) \right) \\
 &\quad + \frac{1}{2} \left[\lambda_m \left(\mathbf{U}^- - \mathbf{U}^+ \right) \right],
 \end{aligned} \tag{2.6}$$

where λ_m is the maximum, in absolute value, of the eigenvalues of the Euler Jacobian $\mathbf{A}_n = \partial \mathbf{F}_n / \partial \mathbf{U}$.

For the numerical viscous flux, we use the method of Bassi and Rebay [6], that we shall refer to hereafter as the Bassi-Rebay (BR) flux. First, a “jump savvy” gradient of the state, $\sigma_j \sim \mathbf{U}_{,j}$ is computed by solving

$$\sum_{e=1}^N \int_{\Omega_e} \mathbf{W}^T \sigma_j d\mathbf{x} = - \sum_{e=1}^N \int_{\Omega_e} \mathbf{W}_{,j}^T \mathbf{U} d\mathbf{x} + \sum_{e=1}^N \int_{\partial\Omega_e} \mathbf{W}^T \widehat{\mathbf{U}}_{n_j} ds \quad \forall \mathbf{W} \in \mathcal{V}(\mathcal{P}_h) \quad (2.7)$$

for each direction, j , where

$$\widehat{\mathbf{U}} \equiv \frac{1}{2} (\mathbf{U}^- + \mathbf{U}^+). \quad (2.8)$$

The BR [6] viscous flux is then computed using

$$\widehat{\mathbf{F}}_n^v(\mathbf{U}^-, \sigma_j^-, \mathbf{U}^+, \sigma_j^+) = \frac{1}{2} (\mathbf{F}_n^v(\mathbf{U}^-, \sigma_j^-) + \mathbf{F}_n^v(\mathbf{U}^+, \sigma_j^+)). \quad (2.9)$$

While this method is known to be only “weakly stable” [3], we have not encountered any difficulties for the problems considered here and this method has been used successfully in prior studies [6]. The above flux definition, Eq. (2.8), is central to several aspects in the current work. First, in Chapter 4, we modify the above definition to study the role of the numerical fluxes in setting Dirichlet boundary conditions. Also, a VMS model, to be introduced shortly, that is an eddy viscosity model that resembles the physical diffusion term is implemented in a similar manner, with appropriate modifications consistent with a multi-scale model.

In setting boundary conditions weakly through the numerical fluxes, one must construct a state, \mathbf{U}_{bc} , that enforces the appropriate boundary conditions and Atkins [4] provides a discussion of the important issues involved in selecting \mathbf{U}_{bc} . For the Navier–Stokes calculations reported here, we use the following approach at the isothermal wall boundaries. We evaluate \mathbf{U}_{bc} separately for the convective and viscous fluxes.

Let m_i be the suitable conditions on the momentum for the Euler flux that are commonly used [4, 30]. Then the reconstructed state at a wall for the convective flux is

$$\mathbf{U}_{bc} = \left\{ \begin{array}{c} \rho^- \\ \rho^- m_1 \\ \rho^- m_2 \\ \rho^- m_3 \\ \rho^- e^- + 0.5 \rho^- (m_1^2 + m_2^2 + m_3^2) \end{array} \right\}. \quad (2.10)$$

This state enforces the no-penetration condition which is appropriate for both inviscid and viscous calculations. For the viscous flux, the no-slip condition is enforced using

$$\mathbf{U}_{bc} = \begin{Bmatrix} \rho^- \\ 0 \\ 0 \\ 0 \\ \rho^- T_w / (\gamma(\gamma - 1)M^2) \end{Bmatrix}, \quad (2.11)$$

where T_w is the prescribed wall temperature, γ is the ratio of specific heats, and M is the reference Mach number. Now, the discontinuous Galerkin problem statement can be compactly stated using (2.5), (2.6), and (2.9) as: Given $\mathbf{U}_0 = \mathbf{U}_0(\mathbf{x})$, for $t \in (0, T)$, find $\mathbf{U}(\mathbf{x}, t) \in \mathcal{V}(\mathcal{P}_h) \times H^1(0, T)$ such that $\mathbf{U}(\mathbf{x}, 0) = \mathbf{U}_0(\mathbf{x})$ and

$$B_{DG}(\mathbf{W}, \mathbf{U}) = (\mathbf{W}, \mathbf{S}) \quad \forall \mathbf{W} \in \mathcal{V}(\mathcal{P}_h), \quad (2.12)$$

where $\mathcal{V}(\mathcal{P}_h)$ is a so-called broken space [9]. If $\mathcal{V}(\mathcal{P}_h)$ is restricted to a space of continuous functions, then one recovers the classical continuous Galerkin approximation upon using the consistency properties of the numerical fluxes [18].

The DG method described above can be considered a hybrid between finite-element and finite-volume methods that has the following salient features that make it a promising method for turbulence simulation.

1. *Local* hp -refinement capabilities.
2. Spectral accuracy on arbitrary meshes.
3. Local conservation and the ability to couple different fidelity models on adjacent elements
4. In particular, the orthonormal hierarchical basis on each element is a natural framework for scale separation that is crucial for multi-scale turbulence models.

Additionally, we draw attention to the potential advantage (see Chapter 4) in setting all boundary and interelement interface conditions, in DG, through the numerical fluxes.

2.2 ℓ VMS Formulation

Before we merge the DG method with the VMS approach, let us introduce the VMS methodology following the discussion of Collis [28] for a typical domain Ω . A more detailed exposition on the method can be found in Hughes *et al.* [46] and Collis [28]. The variational form of the Navier-Stokes equations of motion can be formally represented by

$$B(\mathbf{W}, \mathbf{U} + \widetilde{\mathbf{U}} + \mathbf{U}') = (\mathbf{W}, \mathbf{F})_Q, \quad (2.13)$$

where \mathbf{W} is the vector of test functions from the same function space as the solution (\mathbf{U}) and Q is the space-time domain. Variational projection is used to separate the spatial scales in VMS instead of filtering and this obviates many of the issues related to the filtering operation [46]. The projection operation partitions the solution as $\mathbf{U} = \overline{\mathbf{U}} + \widetilde{\mathbf{U}} + \mathbf{U}'$ where $\overline{\mathbf{U}}$ are the large scales, $\widetilde{\mathbf{U}}$ are the small scales and \mathbf{U}' are the unresolved scales. Introducing the scale decomposition for the test functions, we obtain the equations corresponding to each scale range as

$$\text{Large} \quad B(\overline{\mathbf{W}}, \overline{\mathbf{U}} + \widetilde{\mathbf{U}} + \mathbf{U}') = (\overline{\mathbf{W}}, \mathbf{F})_Q, \quad (2.14)$$

$$\text{Small} \quad B(\widetilde{\mathbf{W}}, \overline{\mathbf{U}} + \widetilde{\mathbf{U}} + \mathbf{U}') = (\widetilde{\mathbf{W}}, \mathbf{F})_Q, \quad (2.15)$$

$$\text{Unresolved} \quad B(\mathbf{W}', \overline{\mathbf{U}} + \widetilde{\mathbf{U}} + \mathbf{U}') = (\mathbf{W}', \mathbf{F})_Q. \quad (2.16)$$

At this point, it is convenient to introduce definitions of the Reynolds-stress projection and cross-stress projections [28]. The projection of the unresolved Reynolds stress onto the large scales is defined as

$$R(\overline{\mathbf{W}}, \mathbf{U}') = (\nabla \overline{\mathbf{W}}, \mathbf{U}' \otimes \mathbf{U}')_Q - (\overline{\mathbf{W}}, \mathbf{n} \cdot (\mathbf{U}' \otimes \mathbf{U}'))_P, \quad (2.17)$$

where P is the lateral boundary of the space-time domain [28]. Likewise, the projection of the large/unresolved cross-stresses onto the large scales is defined as

$$C(\overline{\mathbf{W}}, \overline{\mathbf{U}}, \mathbf{U}') = (\nabla \overline{\mathbf{W}}, \overline{\mathbf{U}} \otimes \mathbf{U}' + \mathbf{U}' \otimes \overline{\mathbf{U}})_Q - (\overline{\mathbf{W}}, \mathbf{n} \cdot (\overline{\mathbf{U}} \otimes \mathbf{U}' + \mathbf{U}' \otimes \overline{\mathbf{U}}))_P. \quad (2.18)$$

It may be useful to think of each scale as a range of Fourier modes in wavespace, although other bases may be used in practice. In numerical simulations, only a finite number

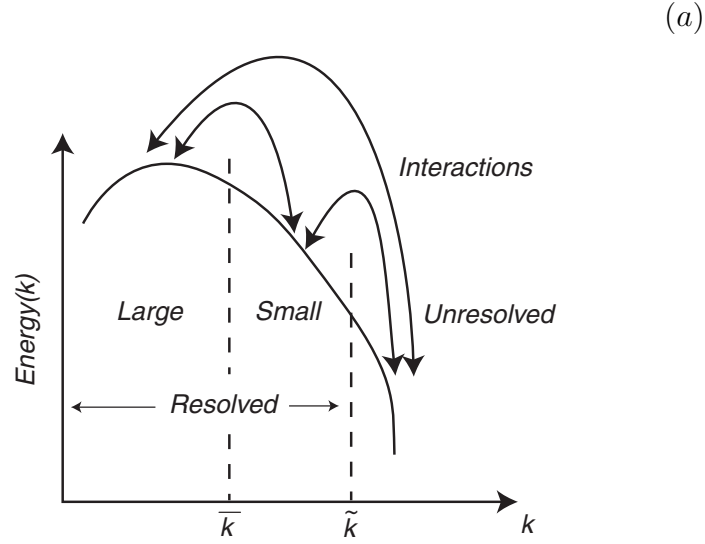


Figure 2.2: Multi-scale partitioning of a turbulent energy spectrum and the interaction between the scales.

of modes are retained leaving the smallest scales of motion unresolved. The interaction between *all* the scales in the turbulence, based on the scale decomposition introduced in VMS, can be seen in Figure 2.2 that shows a typical one-dimensional energy spectrum. The non-linear interactions of the resolved scales produce scales outside the range of resolved scales i.e. unresolved scales (\mathbf{U}') and vice-versa. The equations for the *resolved scales*, denoted by $\widetilde{\mathbf{U}} = \overline{\mathbf{U}} + \widetilde{\mathbf{U}}$, can be written as

$$B(\widetilde{\mathbf{W}}, \widetilde{\mathbf{U}}) = (\widetilde{\mathbf{W}}, \mathbf{F})_{\mathbf{Q}} + \underbrace{R(\widetilde{\mathbf{W}}, \widetilde{\mathbf{U}}) + C(\widetilde{\mathbf{W}}, \widetilde{\mathbf{U}}, \mathbf{U}') + R(\widetilde{\mathbf{W}}, \mathbf{U}') + C(\widetilde{\mathbf{W}}, \widetilde{\mathbf{U}}', \mathbf{U}')}_{\text{need to model}}, \quad (2.19)$$

where R and C are the Reynolds stress and cross stress terms that involve the unresolved scales of motion (see Hughes *et al.* [46] and Collis [28] for details). In order to obtain a solution for just the resolved scales ($\widetilde{\mathbf{U}}$) requires that the terms depending on the unresolved scales be modeled. Thus, the modeled Navier–Stokes equations are

$$B(\widetilde{\mathbf{W}}, \widetilde{\mathbf{U}}) = (\widetilde{\mathbf{W}}, \mathbf{F})_{\mathbf{Q}} + \overline{M}(\widetilde{\mathbf{W}}, \overline{\mathbf{U}})_{\mathbf{Q}} + \widetilde{M}(\widetilde{\mathbf{W}}, \widetilde{\mathbf{U}})_{\mathbf{Q}}, \quad (2.20)$$

where \overline{M} and \widetilde{M} denote the model terms acting on the large and small scales, respectively. The effect of the unresolved scales on the resolved large scales, in VMS, is considered to be negligible under the assumption of *sufficient* scale separation [28, 46, 77, 87]. Thus it

is reasonable to set $\overline{M}(\overline{\mathbf{W}}, \overline{\mathbf{U}})_{\mathbf{Q}} = 0$. Meanwhile, the influence of the unresolved scales on the small-scales must be modeled. A simple constant coefficient Smagorinsky model, acting *only* on the small-scales, has been found to be successful in prior VMS implementations [48, 71, 78].

Now, introducing the DG discretization and VMS modeling assumptions in equation (2.20), we obtain the ℓ VMS equations as

$$B_{DG}(\widetilde{\mathbf{W}}, \widetilde{\mathbf{U}}) = (\widetilde{\mathbf{W}}, \mathbf{F})_{\mathbf{Q}} + \widetilde{M}_{DG}(\widetilde{\mathbf{W}}, \widetilde{\mathbf{U}})_{\mathbf{Q}}, \quad (2.21)$$

where $\widetilde{M}_{DG}(\widetilde{\mathbf{W}}, \widetilde{\mathbf{U}})_{\mathbf{Q}}$, the model flux, that is treated in the same manner as the viscous flux (see equations (2.7), (2.8) and (2.9)) with suitable modifications consistent with the multi-scale decomposition. To be more explicit, the flux is computed using just the small scales ($\widetilde{\mathbf{U}}$), and therefore, the BR flux recast for the VMS model can be written as

$$\begin{aligned} \sum_{e=1}^N \int_{\Omega_e} \widetilde{\mathbf{W}}^T \tilde{\sigma}_j d\mathbf{x} &= - \sum_{e=1}^N \int_{\Omega_e} \widetilde{\mathbf{W}}_{,j}^T \widetilde{\mathbf{U}} d\mathbf{x} + \\ &\sum_{e=1}^N \int_{\partial\Omega_e} \widetilde{\mathbf{W}}^T \widehat{\mathbf{U}}_{n_j} ds \quad \forall \mathbf{W} \in \mathcal{V}(\mathcal{P}_h) \end{aligned} \quad (2.22)$$

for each direction, j , where

$$\widehat{\mathbf{U}} \equiv \frac{1}{2} (\widetilde{\mathbf{U}}^- + \widetilde{\mathbf{U}}^+). \quad (2.23)$$

The BR [6] viscous flux, for the VMS model, is then computed using

$$\widehat{\mathbf{F}}_n^m(\widetilde{\mathbf{U}}^-, \tilde{\sigma}_j^-, \widetilde{\mathbf{U}}^+, \tilde{\sigma}_j^+) = \frac{1}{2} (\widetilde{\mathbf{F}}_n^m(\widetilde{\mathbf{U}}^-, \tilde{\sigma}_j^-) + \widetilde{\mathbf{F}}_n^m(\widetilde{\mathbf{U}}^+, \tilde{\sigma}_j^+)). \quad (2.24)$$

It remains to define the the model term $\widetilde{M}_{DG}(\widetilde{\mathbf{W}}, \widetilde{\mathbf{U}})$ appearing the (2.21). Since we have assumed an orthogonal basis, the model represents the projection of the generalized Reynolds and cross stresses onto the small scales. For incompressible flows, this simplifies directly to the Reynolds and cross stresses. For compressible flows, there are additional terms arising from the variable density in the Reynolds stresses as well as from terms in the energy equation. For a thorough discussion of LES modeling issues in compressible flows, the interested reader is directed to the article by Martinelli *et al.* [65] that present results of *a priori* evaluation of the models developed for compressible flows.

With this background, we now merge the variational multi-scale method described

above with the DG method described earlier and present the primal formulation. We denote the boundary of the domain Ω as $\partial\Omega = \Gamma_D \cup \Gamma_N$ where Γ_D is the portion of the boundary where Dirichlet conditions are specified and Γ_N is the portion of the boundary where Neumann conditions are set. The element boundary is denoted as $\Gamma = \{\Gamma_D, \Gamma_N, \Gamma_0\}$ where Γ_0 are the inter-element boundaries. Let Ω_1 and Ω_2 be two adjacent elements; let $\Gamma_{12} = \partial\Omega_1 \cap \partial\Omega_2$; and let $\mathbf{n}^{(1)}$ and $\mathbf{n}^{(2)}$ be the corresponding outward unit normal vectors at that point. Let $\mathbf{U}^{(e)}$ and $\mathbf{F}_i^{(e)}$ be the trace of a state vector \mathbf{U} and flux vectors \mathbf{F}_i , respectively, on Γ_{12} from the interior of subdomain Ω_e . Then, we define the average $\langle \cdot \rangle$ and jump $[\cdot]$ operators on Γ_{12} as

$$[\mathbf{U}n_i] = \mathbf{U}^{(1)}n_i^{(1)} + \mathbf{U}^{(2)}n_i^{(2)}, \quad (2.25a)$$

$$[\mathbf{F}_n] = \mathbf{F}_i^{(1)}n_i^{(1)} + \mathbf{F}_i^{(2)}n_i^{(2)}, \quad (2.25b)$$

$$\langle \mathbf{U} \rangle = \frac{1}{2} (\mathbf{U}^{(1)} + \mathbf{U}^{(2)}), \quad (2.25c)$$

$$\langle \mathbf{F}_i \rangle = \frac{1}{2} (\mathbf{F}_i^{(1)} + \mathbf{F}_i^{(2)}), \quad (2.25d)$$

where $\mathbf{F}_n = \mathbf{F}_i n_i$.

With this notation, we return to equation (2.21) and introduce a discontinuous Galerkin formulation of the $B_{DG}(\mathbf{W}, \mathbf{U})$ term, defined in equation (2.12), where for simplicity the resolved scales are now simply denoted \mathbf{W}, \mathbf{U} . The primal formulation for discontinuous Galerkin applied to the Navier–Stokes equations is

$$\begin{aligned} B_{DG}(\mathbf{W}, \mathbf{U}) = & \sum_{\Omega_e} \int_{\Omega_e} \left(\mathbf{W}^T \mathbf{U}_{,t} + \mathbf{W}_{,i}^T (\mathbf{F}_i^v - \mathbf{F}_i) \right) d\mathbf{x} \\ & - \int_{\Gamma} \left([\mathbf{W}^T n_i] \langle \hat{\mathbf{F}}_i^v - \hat{\mathbf{F}}_i \rangle - \right. \\ & \quad \left. \langle (\mathbf{D}_i \mathbf{W})^T \rangle [(\hat{\mathbf{U}} - \mathbf{U})n_i] \right) ds \\ & - \int_{\Gamma_0} \left(\langle \mathbf{W}^T \rangle [\hat{\mathbf{F}}_n^v - \hat{\mathbf{F}}_n] - \right. \\ & \quad \left. [(\mathbf{D}_n \mathbf{W})^T] \langle (\hat{\mathbf{U}} - \mathbf{U})n_i \rangle \right) ds, \end{aligned} \quad (2.26)$$

where

$$\mathbf{F}_n(\mathbf{U}) = \mathbf{F}_i(\mathbf{U})n_i, \quad (2.27)$$

$$\mathbf{F}_n^v(\mathbf{U}) = \mathbf{F}_i^v(\mathbf{U})n_i = \mathbf{D}_n \mathbf{U}. \quad (2.28)$$

Quantities with a hat $\hat{\cdot}$ in (2.5) are numerical fluxes that we defined earlier (see Equations (2.6) and (2.9)). For example, The term $\hat{\mathbf{F}}_i(\mathbf{U}^-, \mathbf{U}^+)$ is an appropriate approximate Riemann flux (see [18] for a description of the various options). The particular choice of Riemann flux plays an important role in determining the dispersion/dissipation characteristics of the method [44].

Here, the ℓ VMS model takes the form of a generalized eddy diffusivity that on each subdomain, Ω_e , is given as

$$M(\tilde{\mathbf{W}}, \tilde{\mathbf{U}}) = \int_{\partial\Omega_e} \tilde{\mathbf{W}}^T \mathbf{F}_{n_e}^m(\tilde{\mathbf{U}}) ds - \int_{\Omega_e} \tilde{\mathbf{W}}_{,i}^T \mathbf{F}_i^m(\tilde{\mathbf{U}}) d\mathbf{x}, \quad (2.29)$$

where the model flux $\mathbf{F}_i^m(\tilde{\mathbf{U}})$ is of the form $\mathbf{F}_i^m(\tilde{\mathbf{U}}) = \mathbf{D}_i^m(\tilde{\mathbf{U}})\tilde{\mathbf{U}}$ and the matrix $\mathbf{D}_i^m(\tilde{\mathbf{U}})$ is possibly a nonlinear differential operator.

Extending equation (2.29) to a form compatible with discontinuous Galerkin leads to

$$M_{DG}(\tilde{\mathbf{W}}, \tilde{\mathbf{U}}) = \int_{\Gamma_0} ([\tilde{\mathbf{W}}^T] \langle \mathbf{F}_n^m(\tilde{\mathbf{U}}) \rangle) + \int_{\partial\Omega} (\tilde{\mathbf{W}}^T \mathbf{F}_n^m(\tilde{\mathbf{U}})) - \sum_{\Omega_e \in \mathcal{P}_h} \int_{\Omega_e} \tilde{\mathbf{W}}_{,i}^T \mathbf{F}_i^m(\tilde{\mathbf{U}}) d\mathbf{x}, \quad (2.30)$$

which clearly simplifies to a classical weak Galerkin approximation for continuous functions. On inter-element boundaries, an averaged flux is used while on the domain boundary one obtains a weighted integral of the modeled turbulent flux across the boundary. This last integral marks a dramatic difference between discontinuous Galerkin and standard Galerkin approximations [28, 46] on solid surfaces.

In general, the weighting functions for velocity at wall boundaries using traditional Galerkin forms are set to zero since they are assumed to satisfy the Dirichlet conditions. This precludes a means to enforce the flux of modeled turbulent stresses to be zero at solid walls. However, in discontinuous Galerkin, since all interface and boundary conditions are set through numerical fluxes, specifically boundary flux integrals, it allows the weak enforcement of zero turbulent flux at solid walls by setting the second integral in (2.30) to zero on solid surfaces. Moreover, this integral can be set to particular values on inflow

domains to represent the inflow of unresolved turbulent stress if desired.

From (2.30) we see that one can easily vary the partition between large and small scales on different subdomains. Likewise, the particular model for the turbulent flux can be altered on each domain. Thus, the model term can be written as

$$\begin{aligned}
 M_{DG}(\widetilde{\mathbf{W}}, \widetilde{\mathbf{U}}) = & \int_{\Gamma_0} ([\widetilde{\mathbf{W}}_e^T] \langle \mathbf{F}_n^{me}(\widetilde{\mathbf{U}}_e) \rangle) \\
 & + \int_{\partial\Omega} (\widetilde{\mathbf{W}}_e^T \mathbf{F}_n^{me}(\widetilde{\mathbf{U}}_e)) \\
 & - \sum_{\Omega_e \in \mathcal{P}_h} \int_{\Omega_e} \frac{\partial \widetilde{\mathbf{W}}_e}{\partial x_i}{}^T \mathbf{F}_i^{me}(\widetilde{\mathbf{U}}_e) d\mathbf{x},
 \end{aligned} \tag{2.31}$$

where the modeled turbulent flux and the solution space partitioning are dependent on the element index e . Across element boundaries, the first integral communicates the unresolved turbulent flux between neighboring elements thereby automatically converting from one partitioning to another and from one turbulent flux model to another. It is this novel capability of the ℓ VMS that makes it particularly attractive for turbulence modeling in complex flows (see Figure 2.3).

2.3 VMS Model Description

Now, we present specific choices for the models used in this work. The standard eddy diffusivity model from (2.29) can be put in this form

$$\mathbf{F}_i^m(\widetilde{\mathbf{U}}) = 2\tilde{\nu}_T \begin{bmatrix} 0 \\ (\nabla^s \widetilde{\mathbf{u}})_{:i} \\ \tilde{T}_{,i}/Pr_t \end{bmatrix}, \tag{2.32}$$

where $\nabla^s \mathbf{u}$ is the symmetric part of the gradient tensor [i.e. $(\nabla^s \mathbf{u})_{ji} = (\mathbf{u}_{i,j} + \mathbf{u}_{j,i})/2$] and $(\nabla^s \mathbf{u})_{:i}$ is the i th column of this tensor. The Smagorinsky eddy diffusivity, based on the “small-small” VMS model of Hughes *et al.* [47, 48], defined on the small-scales is

$$\tilde{\nu}_T = (C_S \tilde{\Delta})^2 |\nabla^s \widetilde{\mathbf{u}}|, \tag{2.33}$$

where C_S is the Smagorinsky coefficient that is 0.1 unless otherwise stated, $\tilde{\Delta}$ is a length scale representative of both the mesh (h) and local polynomial order (p) for the small scales defined as

$$\tilde{\Delta}^2 = (L_x L_z) / (N_x N_z (p + 1)^2), \quad (2.34)$$

where L_x and L_z are the domain sizes in the streamwise (x) and spanwise (z) directions, respectively (see Figure 3.1). Similarly, N_x and N_z are the number of elements in the streamwise and spanwise directions, respectively. We note in passing that we use a Van Driest wall damping function [36] to mitigate possible timestep restrictions arising from the use of an explicit time advancement. Next, the Pr_t is the turbulent Prandtl number that is set to a value of 1.0 for all the cases considered here. Finally, $\tilde{T}_{,i}$ is the gradient of the small-scale temperature field used to form the eddy diffusivity term to model the SGS heat flux in the energy equation. In practice, scale-similar and mixed-models appear advantageous for compressible flows [65] and VMS versions of these models can also be devised. And therefore, this is a potential course for future work.

In order to complete the description of any VMS model, we need to specify a partition of the resolved scales. In the current work, we use a two-level partition that divides the resolved scales into large- and small-scales that is specified by a modal cutoff L_e on each element. For a given polynomial order on an element $p_e > 0$, the partition bifurcates the polynomial space, in each direction, as $P_{p_e}(\Omega_e) = \{0, \dots, L_e, \dots, p_e\}$, where the modes less than L_e are considered large scales while the remaining modes including L_e form the small scales.

2.4 Discretization and Implementation

For every element $\Omega_e \in \mathcal{P}_h$ we define the finite-dimensional space $P_{p_e}(\hat{\Omega})$ of polynomials of degree $\leq p_e$ defined on a master element $\hat{\Omega}$. Then

$$P_{p_e}(\Omega_e) = \left\{ \phi \mid \phi = \hat{\phi} \mathbf{J}_{\Omega_e}^{-1}, \hat{\phi} \in P_{p_e}(\hat{\Omega}) \right\}, \quad (2.35)$$

where \mathbf{J}_{Ω_e} is the Jacobian of the transformation of element Ω_e to the master element and

$$\mathbf{V}_p(\mathcal{P}_h) = \left(\prod_{e=1}^N P_{p_e}(\Omega_e) \right)^m, \subset \mathbf{V}(\mathcal{P}_h) \quad (2.36)$$

where m is the number of conserved variables, $m = 5$.

Thus, the semi-discrete discontinuous Galerkin method is: Given $\mathbf{U}_0 = \mathbf{U}_0(\mathbf{x})$, for $t \in (0, T)$, find $\mathbf{U}_h(\mathbf{x}, t) \in \mathbf{V}_p(\mathcal{P}_h) \times H^1(0, T)$ such that

$$B_{DG}(\mathbf{W}_h, \mathbf{U}_h) = M_{DG}(\widetilde{\mathbf{W}}_h, \widetilde{\mathbf{U}}_h) + (\mathbf{W}_h, \mathbf{S}) \quad \forall \mathbf{W}_h \in \mathbf{V}_p(\mathcal{P}_h). \quad (2.37)$$

In practice, one can use a variety of polynomial bases to approximate the functions in (2.37) which offer different advantages and disadvantages. A number of options are presented in Atkins [63] including monomials, tensor products of Legendre polynomials, and warped product bases introduced by Dubiner [35]. For the VMS method, the use of orthogonal bases greatly simplifies the form of the unclosed terms in the equations. Therefore we utilize the family of orthogonal, hierarchical bases formed from tensor products of Jacobi polynomials as described in Karniadakis and Sherwin [53] which are supported in a wide range of elements types in two- and three-dimensions.

2.5 Summary

The promise of the merger of VMS and DG spatial discretization that we term Local VMS (ℓ VMS) can be attributed to the locality introduced in spectral and physical space by the former and the latter, respectively. This combination provides a framework for coupling, via numerical fluxes, different fidelity models on adjacent elements. And conceptually, this permits the use different models on different scale ranges. To be more explicit, the VMS approach to LES introduces no explicit modeling on the largest resolved scales, a feature attributed to its success [47, 48, 71, 76, 78], while a SGS scale model is active on the smallest resolved scales. This can be thought of as coupling of DNS or no-model on the large scales with a SGS model on the small scales.

Now, using DG, we extend this concept even in physical space. As an illustration of the potential of ℓ VMS, let us consider the case of a airfoil (can be any bluff body) in cross-flow at sufficiently high Reynolds number (see Figure 2.3). With the current framework, we can use hp -refinement to reduce the degrees of freedom away from the surface of the airfoil and wake. Next, one can employ ℓ VMS in the region near the surface of the airfoil to represent the boundary layer and turbulent wake (ℓ VMS_b and ℓ VMS_d in Figure 2.3). Further, in regions where turbulence is not active, the model can be turned “off” to recover

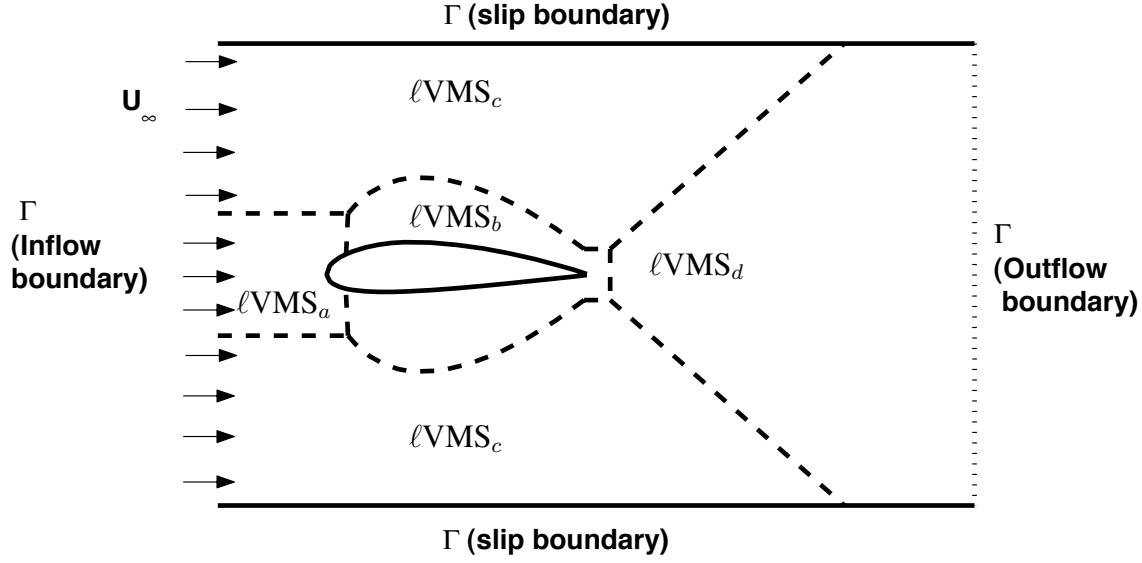


Figure 2.3: Illustration of ℓVMS modeling capabilities for flows in complex geometries: U_∞ freestream velocity; ℓVMS_a , model for laminar boundary layer; ℓVMS_b , model for a turbulent boundary layer; ℓVMS_c , model for region outside the boundary layer; ℓVMS_d , model for a turbulent wake; ---- Boundary separating different ℓVMS modeling zones.

DNS (ℓVMS_a and ℓVMS_c in Figure 2.3). This can be accomplished in VMS simply by selecting the partition (L_e) to have all the resolved scales in the large scale space.

Moreover, it is likely that the large scales for the boundary layer are different from that in the wake region (see Figure 1.1). First, using the local refinement capabilities, we select a mesh and polynomial order to sufficiently represent the features of the boundary layer and wakes. Now, ℓVMS allows the parameters such as the modal partition L_e to separate the large and small scale spaces to be specified individually on each element. And, for the flow under consideration, the important large scales in different regions of the flow are vastly different in character. Therefore, by allowing the specification of the model parameters locally based on the knowledge of physical structures in the flow, if available, can potentially lead to improved modeling of the flow. In fact, conceptually, one can even change the model in different regions in the flow. Overall, fully exploiting ℓVMS offers the flexibility needed to accurately model flows in a efficient manner even in complex geometries. As a first step towards simulations just described, we test the capabilities of the method in a fully-developed turbulent channel flow.

Chapter 3

Turbulent Channel Simulation

In this chapter, we validate our implementation by comparing numerical results for the turbulent channel flow, obtained using the DG method described in Chapter 2, with available DNS [14, 69]. In the process, we study the effects of the DG spatial discretization on the quality of turbulence statistics obtained. Also, since all interface conditions including the physical boundary conditions are enforced through the numerical fluxes, solution jumps exist even at the channel walls. Further, the solution jumps are known to be related to the local resolution [19]. Here, we focus on the solution jumps at the channel wall where the local resolution is often low and the magnitude of jumps are likely to be significant. Thus, we attempt to gain insight into the effect of this unique feature in DG on turbulence statistics. We begin with a brief description of the planar turbulent channel before proceeding to the numerical results for a range of Reynolds numbers from $Re_\tau = 100 - 395$.

3.1 Turbulent Channel Flow—Preliminaries

Consider the fully-developed turbulent flow in a plane channel with coordinates $x = x_1$ in the streamwise direction, $y = x_2$ in the wall-normal direction, and $z = x_3$ in the spanwise direction (see Figure 3.1). The reference length scale is the channel half-height δ and the reference velocity is the friction-velocity $u_\tau \equiv \sqrt{\tau_w/\rho}$ in the initial condition, where ν is the kinematic viscosity, τ_w is the shear stress at the wall (drag at the wall), and ρ is the fluid density. Thus, the reference Reynolds number is $Re_\tau \equiv u_\tau \delta / \nu$. In reporting our results, we frequently present flow quantities in wall units (or inner scaling) with $t^+ = t u_\tau^2 / \nu$, $x_i^+ = x_i u_\tau / \nu$ and $u_i^+ = u_i / u_\tau$. The flow is assumed to be periodic in the streamwise and spanwise directions where the box size is selected so that the turbulence is adequately decorrelated in both directions.

As a first step towards utilizing DG for turbulent flows, we have performed coarse grid DNS at $Re_\tau = 100$ with a centerline Mach number of $M_c = 0.3$ so that comparisons can be made directly to prior incompressible results (see e.g. [54, 69]). Following Coleman *et al.* [27], we use a cold, isothermal wall so that internal energy created by molecular dissipation

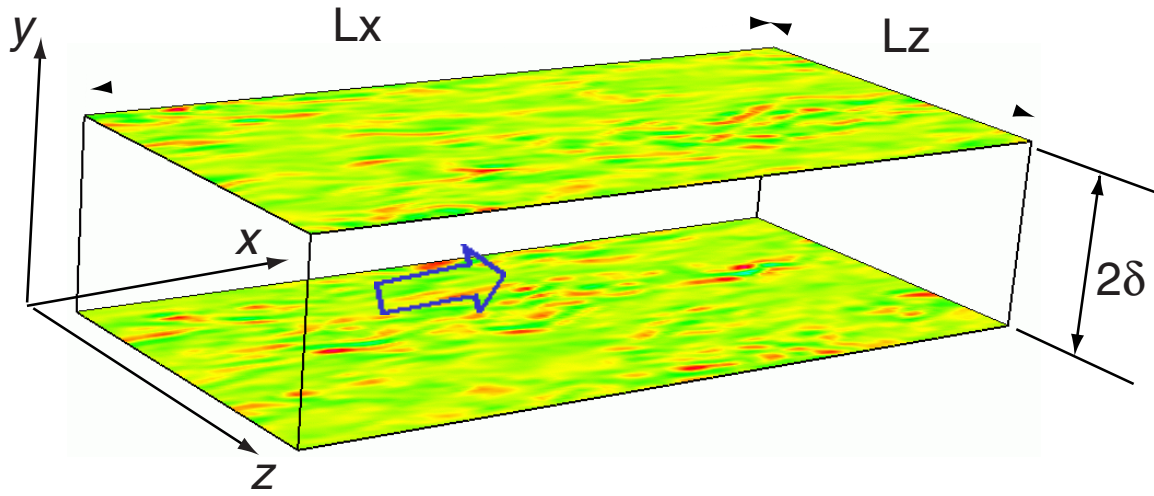


Figure 3.1: Illustration of the planar channel with the contours of wall-normal velocity obtained by Chang [14]

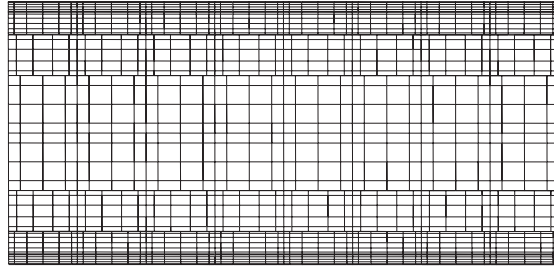


Figure 3.2: Cross-stream (z - y) quadrature grid for an $8 \times 8 \times 8$ stretched mesh with $p = \{5, 5, 4, 3\}$, this figure first appeared in the article by Collis [30]

is removed from the domain via heat transfer across the walls, allowing a statistically steady state to be achieved. While using moderate resolutions, the bulk mass flow is held constant by the addition of an x_1 -momentum source. However, at coarse resolutions additional source terms are required in both the continuity and energy equations to hold the bulk density and the average total energy constant.

The computational domain is $(4\pi, 2, 4\pi/3)$ for $Re_\tau = 100$ and $Re_\tau = 180$, while for $Re_\tau = 395$ a smaller domain of $(2\pi, 2, 2\pi/3)$ is sufficient. Exploiting the flexibility of the DG method, we use both h - and p -refinement to more efficiently resolve flow features near the wall. In particular, two types of wall-normal distributions of elements are investigated:

a uniform mesh and a stretched mesh. For the stretched mesh, the grid points are given by

$$y_j = \frac{\tanh(c_s(2j/N_y - 1))}{\tanh c_s} + 1, \quad j = 0, 1, \dots, N_y \quad (3.1)$$

where N_y is the number of elements in the wall-normal direction and c_s is the stretching factor in the range $1.0 < c_s < 2.0$. Unless explicitly stated, we use the stretched mesh.

In addition to local h -refinement using the stretched mesh, we also utilize local p -refinement by reducing the polynomial order away from the wall. Figure 3.2 shows a typical crossflow quadrature grid for the stretched mesh using 8 elements in the wall-normal direction (8×8 in the planar directions (x and z)). Moving from the bottom wall to the top wall, the element order varies like: $\{5, 5, 4, 3, 3, 4, 5, 5\}$ resulting in a total of 79,488 degrees of freedom as opposed to 110,592 for a uniform polynomial order, $p = 5$. Note that the flexibility of the DG method makes it possible to coarsen simultaneously in *all three* coordinate directions as one moves away from the wall. In all cases, we use a third-order TVD-RK time advancement with $\Delta t \leq 0.0001$. This time step is a factor of 10 smaller than that typically used in our incompressible code [32] because the incompressible code treats wall-normal viscous terms implicitly.

3.2 Numerical Results

First, we undertake a detailed resolution study at $Re_\tau = 100$ with different polynomial orders (p) using the following mesh topologies: $4 \times 4 \times 8$, $8 \times 4 \times 8$, $4 \times 8 \times 8$, and $8 \times 8 \times 8$ ($N_x \times N_y \times N_z$) where N_x , N_y , and N_z are the number of elements in the streamwise, wall-normal, and spanwise directions, respectively. The meshes are stretched in the wall-normal direction unless otherwise stated. The choice of the meshes used in this study is to highlight the effects of resolution in the planar and wall-normal directions as well as the interaction between the two.

1. For convenience in presenting the results at $Re_\tau = 100$, we refer to the following meshes, $4 \times 4 \times 8$, $8 \times 4 \times 8$, $4 \times 8 \times 8$, $8 \times 8 \times 8$, and $8 \times 8 \times 8$ uniform y -direction, as A, B, C, D, and E, respectively.
2. Also, since we consider different polynomial orders on each of the meshes above, in referring to a particular combination of a mesh using a polynomial order p , we

employ the following notation that we illustrate by example – a mesh using $4 \times 4 \times 8$ (A) with $p = 3$ will be referred to as A3 and so on.

A summary of the parameters used in the simulation along with a brief result summary for each mesh can be found in Tables 3.1, 3.2, 3.3, and 3.4. The parameters presented in the table are: p , the polynomial order; Δy_w^+ , the resolution based on the collocation grid in viscous units at the wall; d.o.f., the total number of degrees of freedom; Slip, slip in the streamwise velocity averaged over the plane ($x - z$ plane) at the wall; τ_w and $u_\tau = \sqrt{\tau_w/\rho}$, the wall shear stress and the friction velocity, respectively. Sometimes, in reporting resolutions in the wall-normal direction, we denote Δy_m^+ as the minimum height of an *element*, usually the element adjacent to the channel walls. Also, throughout the following discussion, unless otherwise stated, slip will refer to the definition give above. Primarily, when discussing the magnitude of the slip, we compare it to the maximum streamwise velocity at the center of the channel that is approximately 17, 18, and 20 for $Re_\tau = 100$, 180, and 395, respectively.

In general, we present profiles of meanflow, turbulence intensities (rms), Reynolds stress, viscous, and total (Reynolds + viscous) stress. The energy spectra in the streamwise and spanwise directions are also presented as additional indicators of resolution quality.

Before we examine the numerical simulations, it may be useful to recall the characteristic features of the fully-developed turbulent channel flow gleaned from DNS data and/or experimental observation [5, 54, 55, 69, 85].

1. The direction of the flow is streamwise (positive x direction) and the meanflow in the spanwise and wall-normal directions are negligible.
2. The physical structures in the flow have well-defined length scales: $\Delta x^+ \approx 400$, $\Delta z^+ \approx 100$ (streak spacing) and cylindrical coherent structures have radius, $r^+ \approx 15$.
3. The location of the maximum turbulence production i.e. u_{rms} peak is $y^+ \approx 20$. Therefore, a possibly important length scale in the wall-normal direction is $\Delta y^+ \leq 30$ that corresponds well with the diameter of the near-wall coherent structures.
4. Viscous effects dominate for $y^+ \leq 5$ and thereafter Reynolds stress are significant and both viscous and Reynolds stresses are comparable ($5 < y^+ < 30$). In this range, there exists a point where both viscous and inertial effects are equal that corresponds

well with the peak turbulence production ($y^+ \approx 20$). Beyond $y^+ > 30$, the inertial effects dominate and viscous effects are negligible.

3.2.1 Low Reynolds Number

Let us begin with a study using $p = 3$ for the meshes A-E at $Re_\tau = 100$. The simulation parameters and results summary for each individual mesh using different polynomial orders are reported in Tables 3.1, 3.2, 3.3, and 3.4. It is important to point out the salient features of the meshes selected that may be useful in interpreting the results presented below.

1. Cases A3, B3, and E3 share a similar near-wall resolution $\Delta y_w^+ \approx 4.3$ ($\Delta y_m^+ \approx 25$).
2. Cases A3 and C3 share the same planar resolution ($x - z$ plane).
3. Cases B3, D3, and E3 share the same planar resolution ($x - z$ plane).
4. Finally, Cases C3 and D3 have a better near-wall resolution ($\Delta y_w^+ \leq 2.5$, $\Delta y_m^+ \leq 15$) compared with A3, B3, and E3.
5. The location of the element interfaces for the bottom half the channel in the wall-normal direction (y) for the A and B meshes are as follows, $y^+ \approx \{25, 100\}$. For C and D, $y^+ \approx \{8, 25, 56, 100\}$. Finally, for the E mesh, $y^+ = \{25, 50, 75, 100\}$

The meanflow and rms profiles for A3, B3, C3, and D3 are presented in Figure 3.3. The meanflow for D3, shown in Figure 3.3(a), produces the best agreement with the reference DNS [14] while all the other cases show poor agreement with the reference. A3 and B3 severely overpredict the wall shear stress while C3 significantly underpredicts τ_w . We note here that the meanflow profile of A3 is very similar to that of B3 for $y^+ \leq 25$, but, the meanflow profile for these two cases differ significantly thereafter ($y^+ > 25$). It is important to note the presence of slip in the meanflow for all the cases considered thus far (refer to Tables 3.1, 3.2, 3.3, and 3.4 for values of slip in the meanflow). This is a unique feature of the DG solutions that allow the solution to be discontinuous at element interfaces. In the current context, the slip in the meanflow represents the difference between the imposed no-slip boundary condition and computed solution at the channel solid walls.

Now, consider the rms profiles for the above cases that is plotted in Figure 3.3(b). Again, the best overall agreement with DNS [14], for all the components of turbulence intensity, is obtained using D3. As seen with the meanflow profile, the remaining cases show poor

agreement. And, while the profiles for A3 and B3 are similar, the streamwise component of C3 is dramatically different from the latter two. However, we note the differences in the rms profiles for all the cases at $y^+ > 30$ are not as dramatic as the near-wall region ($y^+ \leq 30$). As mentioned earlier for the meanflow, there are some features on this plot that are not generally seen in traditional discretizations that enforce the Dirichlet boundary conditions strictly [14]. Note the non-zero contributions in the rms quantities at the wall ($y^+ = 0$). On the rms profiles, let us focus on the u component, A3 and B3 contain a larger slip when compared with C3 and D3. In fact, under close scrutiny one can observe that slip in u_{rms} for C3 ($\Delta y_w^+ \approx 1.4$) is less than D3 ($\Delta y_w^+ \approx 2.3$) in Figure 3.3(b).

Now, returning to the slip in the meanflow, A3, B3, and D3 have a negative value while C3 has a positive slip. Further, the absolute value of slip for A3 and B3 is considerably higher than D3. These results are indicative of an inverse relationship between the magnitude of solution jumps (see Figure 3.3(b)) and the near-wall resolution (Δy_w^+). This view is supported by the large value of slip for E3 that shares a similar near-wall resolution (Δy_w^+) with A3 and B3. It is well-known that the jumps in the DG solution are related to local resolution [19]. For the channel flow, the results above indicate that the y -direction resolution may play a dominant role in determining the amount of slip at the wall.

Also, we notice a close correspondence of significant negative slip in A3 and B3 with overpredictions in the wall shear stress (see Figure 3.44). An auxiliary trend that we draw attention to is the variation of slip with polynomial order. The slip in the streamwise velocity at the wall transitions from a relatively large negative value at A3 to positive value at A6 and subsequently to a extremely small value at A8 (refer to Table 3.1). A similar trend can be seen when going from B3 to B6 (refer to Table 3.2). While this trend is present even in the C and D meshes, the relatively high wall-normal resolution makes it less noticeable (refer to Tables 3.3 and 3.4). In fact, the slip is positive even at C3 that continues to decrease in absolute value with increasing polynomial order.

Next, we examine the energy spectra in the x - and z - directions, shown in Figures 3.4 and 3.5, for the cases under consideration. Note the streamwise spectra for A3 and C3 span a shorter range of wavenumbers (4 elements in x -direction). Let us examine Figure 3.5 and focus on the streamwise component for any visible trends. The spanwise spectra where all the cases share the same resolution may not adequately highlight trends present. Clearly, A3 and C3 that share the same planar resolution produce a similar shaped spectra but with A3 (with a larger Δy_w^+) exhibiting a distinctly higher energy content compared with C3. A

similar trend exists for B3 and D3 that is less prominent likely due to a smaller difference in Δy_w^+ compared with the difference in Δy_w^+ between A3 and C3.

Significantly, the effects of using coarse grids is clearly seen in the energy spectra. The pile up of energy, seen at the higher wavenumbers, is mainly a result of the absence of viscous dissipation scales [56]. Unfortunately, very high resolutions (DNS) are needed to adequately resolve these scales in the turbulent channel flow [69]. The general function of these scales is to dissipate the energy, transferred from the larger scales to the smaller scales through non-linear interactions, as heat. Therefore, in the absence of these scales, one can expect the large scales to have a higher energy content than usual.

Also, practical turbulence simulation using the Navier-Stokes equations of motion involve evaluation of non-linear terms using a finite representation. This operation results in aliasing errors where the overall effect of aliasing in the solution depends on the parameters of the numerical scheme [13, 58]. To be more explicit, the effect of aliasing errors is closely related to the spatial discretization [58]. While using particularly coarse grids with a low order method, aliasing errors are known to damp turbulent fluctuations [58]. On the other hand, aliasing errors employing low resolution with high order methods often render the simulation unstable [58]. At finite resolutions, these low resolution effects are handled by introducing a SGS model often in conjunction with a dealiasing mechanism [13, 67, 84]. Thus far, we have employed no dealiasing strategy and/or introduced explicit SGS modeling in any of the simulations. However, the energy spectra (see Figure 3.4) indicates the need for such mechanisms in the cases presented above (we introduce modeling and dealiasing in Chapter 5).

Finally, consider the profiles of Reynolds stress, shown in Figure 3.6(a), where D3 produces the best overall agreement with the reference [14]. Here again, we point out that the non-zero Reynolds stress contribution at the wall is a result of the current boundary conditions enforcement. Further, the largest deviation from the reference Reynolds stress profile, shown in Figure 3.6(a), is observed with A3 and B3. Since both these cases employ a large Δy_w^+ , this suggests the Reynolds stress predictions may be sensitive to the resolution in the wall-normal direction.

Meanwhile, the viscous stress profiles, shown in Figure 3.6(a), with noticeable jumps at $(y/\delta \approx 0.25$ i.e. $y^+ \approx 25)$ for A3 and B3 are indications of the low y -direction resolution employed for these cases. The relatively smoother profiles i.e. modest interelement jumps for C3 and D3, that use a better resolution in the wall-normal direction, suggest the

resolutions used in these cases are sufficient to reasonably resolve the viscous sublayer. However, the thickness of the viscous sublayer for C3 is very prominent compared with the reference consistent with the low drag predictions. Meanwhile, the viscous stress profiles for A3 and B3 are diminished compared with the reference, consistent with the high τ_w obtained for these cases. The good correspondence of D3 with the reference viscous stress and total stress profiles (D6) indicates the overall resolution (h and p) in this case is adequate to reasonably represent the near-wall region.

The ability to obtain reasonable estimates for τ_w using $\Delta y_w^+ \approx 2.3$ (D3 with $\Delta y_m^+ \approx 13$) is noteworthy. Traditional discretizations even with an explicit SGS model require $\Delta y_w^+ \leq 1.0$ [14, 15]. We believe this can be attributed, in part, to the manner of boundary conditions enforcement. The imposition of the no-slip conditions through the BR flux, allowing solution jumps, is effective in “capturing” part of the boundary layer in the jump at the channel wall. Now, we recognize that the jumps in the solution are closely related to the local residual (in the interior of the element) [19]. The presence of a large solution jump is indicative of a relatively low local resolution. In our experience with other discretizations [14, 15], we have observed that imposing hard boundary conditions with low near-wall resolutions leads to incorrect τ_w predictions, and therefore, poor low-order statistics. The strict enforcement of the no-slip conditions employing resolutions that are inadequate to sufficiently represent the viscous wall region may explain the poor τ_w predictions observed in traditional discretizations. Here, by contrast, allowing the solution to jump at the boundary, we believe, simulates the appropriate influence of wall *commensurate* with the local resolution enabling reasonable τ_w prediction even with moderate Δy_w^+ values.

Let us now consider the effect of polynomial enrichment on these meshes. A comparison of the meanflow profiles for A4, B4, C4, and D4 is presented in Figure 3.7(a). Predictably, we see an improvement in the meanflow for A4, B4, and C4. However, B4 and C4 still overpredict and underpredict the drag, respectively, while D4 shows the best agreement with the reference [14]. Meanwhile, a dramatic improvement is seen with A4 that produces a meanflow profile that nearly matches that of D4.

Next, Figure 3.7(b) shows the plot of the rms profiles, and again, improved predictions compared to the $p = 3$ simulations is observed in all the cases. The authors note difference between the rms profiles, in the near-wall region $y^+ \leq 30$, obtained using 8 (stretched) elements versus 4 (stretched) elements in the wall-normal direction. This hints at the effectiveness of hp -refinement over pure p -refinement in improving solution quality.

Now, it is interesting to note the rms profiles for A4 are nearly an average of the profiles obtained using B4 and C4. Recall that A4 shares the same Δy_w^+ as B4, and simultaneously, the planar resolution of A4 is identical to C4 (refer to Tables 3.1, 3.2, and 3.3). The better agreement of low-order statistics with DNS obtained for A4 using fewer degrees of freedom compared to B4 and C4 may be attributed to a complex interaction of planar and wall-normal direction resolution effects (we elaborate on this issue in the discussion to follow).

As before with $p = 3$, we examine the energy spectra in the x - and z - directions obtained using A4, B4, C4, and D4 that are plotted in Figure 3.8. Now, let us focus on Figure 3.9 where we plot just the u component for clarity. Note a similar trend in the energy spectra as the $p = 3$ cases. Here, the difference in resolution in the y -direction between A4 and C4 is identical to that which exists between B4 and D4. The current trend suggests that low resolutions in the wall-normal direction potentially lead to increased energy content in the resolved scales. Physically, a poorly resolved viscous wall region may result in the near-wall coherent structures that are not adequately influenced by viscous effects. This diminished viscous damping may lead to an artificially high energy content in these scales. This can translate to an overprediction of the wall shear stress, clearly seen in B4.

Interestingly, C4 with a higher y -direction resolution has a lower energy content compared to the other cases using $p = 4$, suggesting that with the current mesh and polynomial order – the overall effect of low planar resolution is a dissipative one [19, 44, 58]. Now, it is likely from these results that A4 benefits from an interaction of the planar resolution effects seen in C3 and C4 along with the wall-normal resolution effects observed in B3 and B4. Recall a noticeable departure of the meanflow profile for A3 when compared to B3 in Figure 3.3(a). The difference may be the result of difference in the planar resolution between A3 and B3. While, B4, C4, and D4 show improvements consistent with an increase in resolution, the improvements in A4 may be attributed to the arguments presented above.

Now, even with D4 that employs the highest overall resolution, the energy spectra exhibits the effects of aliasing and SGS. Meanwhile, all the stress profiles, seen in Figure 3.10, are in better agreement with the reference from $p = 3$. It is important to note that an uniform increase in the polynomial order leads to refinement in *all* three directions *simultaneously* indicated by a doubling in the number of degrees freedom when going from C3 to C4 (see Table 3.3). It is for this reason that there is a dramatic improvement in the results going from $p = 3$ to $p = 4$. Overall, the reasonable agreement with the reference obtained using D4 suggests that it has sufficient resolution in the planar and wall-normal directions to

minimize the obvious adverse effects of low resolution.

To make this discussion concrete, let consider solutions obtained with A-D using $p = 6$. A comparison of meanflow profiles for A6, B6, C6, and D6 is shown in Figure 3.11(a) where except B6, that continues to overpredict τ_w , all the cases are virtually indistinguishable from each other and in good agreement with the reference [14]. The rms profiles, shown in Figure 3.11(b), indicate excellent agreement of the profiles for C6 and D6 with the reference DNS [14]. Meanwhile, reasonable agreement with DNS is seen for A6 and B6. We note here that the jumps in the solution at the wall, significant at lower resolutions, are considerably diminished for C6 and D6 using a higher y -direction resolution. Meanwhile, the presence of jumps even at $p = 6$ for A6 and B6 confirms our earlier observation that slip at the wall is very closely related to the wall-normal resolution.

The higher energy content than the reference in the energy spectra, shown in Figure 3.12, is most likely the result of the SGS effects that are known to affect the scales closest to the grid cutoff [36, 82]. The combination of SGS and aliasing (that may be still be present) is reflected only in a mean sense seen most clearly in the difference in the meanflow profile from the reference in the core of the channel (see Figure 3.11(a)). This indicates the need for strategies to effectively counter these effects even at these resolutions. In fact, all the reference DNS [14, 69] used in the work to validate our implementation employ the 3/2-rule [13] in the planes to remove aliasing effects even though they are computed using higher resolutions than those considered in this study. Finally, the stress profiles, shown in Figure 3.14 for the all the cases except B6 are in good agreement both with each other and with the reference [14].

Thus far, through conventional wisdom and with the aid of the turbulence statistics extracted, we are able to explain the convergence of results using A, C, and D. However, the result obtained using Case B (see Figures 3.35 – 3.37) needs special attention, since we suspect the reason may be unique to the DG spatial discretization. This relates to the setting of interface conditions at interelement boundaries through the numerical fluxes. It is likely, that using a poor near-wall resolution ($\Delta y^+ \geq 1.6$ wall units) along with a relatively high planar resolution (low dissipation properties [19, 44]) leads to poor interface conditions. Notice the relatively large jump at the first interelement boundary (in the y -direction) in the viscous stress profile in Figures 3.6, 3.10, and 3.14. Although A3 experiences a similar interface condition, seen by a jump in the corresponding viscous stress profile in Figure 3.6, it is also influenced by a dissipative effect of the low planar resolution in the interior that

can explain the difference in the meanflow compared with the B3 case (see Figure 3.3(a)).

In order to clearly establish the need for strategies to account for the combined effect of SGS and aliasing errors. We present a comparison of results obtained using A4 and A8. The meanflow profile for A8 case is shown in Figure 3.15. While producing a better agreement with the reference DNS than A4, the A8 case still slightly overpredicts τ_w . As before, the rms profiles, seen in Figure 3.15(b), obtained using A8 are in excellent agreement with the reference DNS compared with the A4 case. Similarly, the Reynolds, viscous, and total stress profiles for A8 are virtually indistinguishable from the reference case. However, as seen in D6, the energy spectra at the highest wavenumbers most susceptible to the finite resolution effects contain more energy than the reference DNS [14]. This suggests the need for an active mechanism to remove the excess energy at the highest wavenumbers. Fortunately, the presence of aliasing and/or SGS effects does not have a profoundly adverse effect on the low-order statistics at these resolutions.

Given the well-known importance of spanwise resolution in wall-bounded turbulent flows [54,69], we now focus attention on the spanwise direction. The simulations discussed so far used 8 elements in the spanwise direction and reasonable solutions were obtained with $p \geq 3$, given sufficient h resolution. With 8 elements across the channel, each element is approximately 50 wall-units in width, which roughly corresponds to half the typical streak spacing [54, 55, 85]. To further explore the influence of spanwise element size, we also performed simulations on a coarse $4 \times 4 \times 4$ mesh using $p = 3$. In this case, the spanwise element size is approximately 100 wall-units which indicates that both a low- and high-speed streak are contained within one element. Consequently, the elements are larger than the near-wall vortices and our experience with DG in two-dimensional simulations indicates that high polynomial orders ($p > 7$) are required to adequately resolve a vortex within a single element. Thus, not surprisingly, this simulation was non-linearly unstable due to inadequate representation of the viscous dissipation scales.

For $p < 3$, the solutions are similar to those obtained with traditional low-order upwind finite-difference and finite-volume methods where numerical dissipation and the combined effects of low resolution tend to suppress turbulent fluctuations [44, 58]. Comparison of solutions obtained using C2, D2, C4, and D4 are plotted in Figures 3.18, 3.19, and 3.20. The meanflow profiles, plotted in Figure 3.18(a), show a significant underprediction in the drag for both C2 and D2. The rms profiles for both C2 and D2 show trends consistent with the low planar resolution similar to that observed with C3. Meanwhile, the energy spectra

and stress profiles, shown in Figures 3.19 and 3.20, exhibit solutions consistent with high levels of numerical dissipation.

Now, the dramatic reduction in numerical dissipation with increase in resolution in the streamwise direction suggests the likely source of this dissipation is the Euler flux. Since the meanflow is in the streamwise direction, it is possible that the “upwinding” effect of the Euler flux has a significant contribution in this direction similar to Streamline Upwind Petrov-Galerkin (SUPG) finite element methods [11]. Importantly, the associated numerical dissipation is significantly decreased with increase in resolution (h and/or p). Recall that we use the Lax–Friedrichs flux which is known to be highly dissipative so that these observations may be altered if a different numerical flux is used and this is an interesting area for future research. However, the key point is that for elements with $\Delta x^+ \leq 200$, $\Delta z^+ \leq 50$, and $\Delta y_w^+ \leq 2.0$ ($\Delta y_m^+ \leq 15$) using $p \geq 3$ results in solutions in reasonable agreement with DNS without indication of adverse effects of low resolution.

3.2.2 Moderate Reynolds Number

We now extend the DG spatial discretization study to higher Reynolds numbers. We first study the results for $Re_\tau = 180$ obtained using two meshes $8 \times 8 \times 16$ and $16 \times 16 \times 16$. The details of the parameters used in the the simulation can be found in Tables 3.5 and 3.6.

We examine the results obtained using $p = 3$, $p = 4$, and a variable polynomial distribution in the wall-normal direction as $p = \{5, 5, 4, 3, 3, 4, 5, 5\}$ (see Figure 3.2). Before we present the results, we note that the element interfaces using this mesh in the y -direction for one half of the channel are located at $y^+ \approx \{15, 45, 101, 180\}$. The resolution for this mesh with $\Delta x^+ \approx 280$, $\Delta z^+ \approx 47$, and $\Delta y_m^+ \leq 15$ is slightly better in all three directions compared with the A mesh at $Re_\tau = 100$. In fact, the resolutions obtained are closer to the C mesh at $Re_\tau = 100$. Thus, the meanflow and rms profiles, shown in Figure 3.21, using $p = 3$ and $p = 4$ follow a similar trend as the C mesh at $Re_\tau = 100$ (see Figure 3.32). Although, the underprediction in the τ_w does not appear to be as severe as C3 and C4 at $Re_\tau = 100$. This may be a result of improved resolution in the streamwise direction ($\Delta x^+ \approx 280 \leq 314$).

Here, we note the improvement in the rms profile, seen in Figure 3.21(b) especially for the streamwise component, while using the variable polynomial order case that uses $p = 5$ close to the wall. This feature of DG that allows us to improve local resolution can be exploited to improve efficiency. Also, from the $Re_\tau = 100$ study, local improvement of

the resolution in the near-wall region may lead to better interface conditions to the interior solution. Importantly for the channel flow, the coarsening of the grid away from the wall does not hamper the near-wall results. Although, using coarse grids the solution at the center of the channel using $p = 3$ may experience a stronger influence of the effects of under-resolution than the near-wall region.

Equally, the interface conditions, for the variable polynomial order case, will also be improved over the uniform $p = 3$ case. This is a subtlety of numerical simulation related to dominance of errors (planar versus wall-normal direction resolution effects). Fortunately, the better meanflow profile agreement with DNS for the variable polynomial order case, compared with the uniform $p = 3$ and $p = 4$ cases, suggests that improved interface conditions may have a more dominant effect, in this case, than the planar resolution effects (see Figure 3.21(a)). Similarly, the Reynolds stresses, shown in Figure 3.23(a), for all the cases are also in good agreement with the DNS [69]. Also, the variation in the viscous stress profile is not significant. Finally, the trends in the energy spectra, shown in Figure 3.22 are consistent with that observations at $Re_\tau = 100$ at similar resolutions.

Next, using the guidance of resolution estimates obtained from the $Re_\tau = 100$ resolution study, we present results at $Re_\tau = 180$ obtained with a $16 \times 16 \times 16$ mesh using $p = 3$ and $p = 4$ (see Table 3.6). The resolution in the planes using this mesh are $\Delta x^+ \approx 140$ and $\Delta z^+ \approx 47$ in the streamwise and spanwise direction, respectively. Meanwhile, the wall-normal direction resolution at the wall using $p = 3$ and $p = 4$ is $\Delta y_w^+ \approx 1.0$ and $\Delta y_w^+ \approx 0.71$ ($\Delta y_m^+ \approx 6.0$), respectively.

The meanflow and rms profiles are shown in Figure 3.24. As expected, they are in excellent agreement with the DNS [69] data, note the near-wall rms profiles at $p = 4$ are virtually indistinguishable from the reference DNS [69]. These results are similar to $Re_\tau = 100$ case using a $8 \times 8 \times 8$ stretched mesh (D3 and D4). Predictably, the energy spectra (Figure 3.25) follow the trends seen earlier at $Re_\tau = 100$ with commensurate resolutions. The Reynolds stress profile using $\Delta y_w^+ \approx 0.71$, shown in Figure 3.26, for $p = 4$ is indistinguishable from the reference DNS [69], while the $p = 3$ shows reasonable agreement with the reference. The minimal differences in the stress profiles, shown in Figure 3.26, for $p = 3$ and $p = 4$ indicates that the results are adequately converged. Here, we note the particularly good agreement with DNS [69] obtained using $p = 4$. Even with $p = 3$, the difference in total stress may be attributed to the slight peak in the Reynolds stress at $y/\delta \approx 0.1$. We note in passing that since we do not have a reference computation for the viscous stress profile, we

employ the current $p = 4$ case as reference for the $Re_\tau = 180$ results obtained using the $8 \times 8 \times 16$ mesh.

Finally, we present results at $Re_\tau = 395$, the highest Reynolds number considered in this work. A mesh is chosen ($8 \times 8 \times 18$) such that $\Delta x^+ \approx 310$, $\Delta z^+ \approx 46$, and $\Delta y_w^+ \leq 3.0$ viscous wall units. We use a higher value of grid stretching $c_s = 2.0$ in the wall-normal direction that gives us element interface locations for the lower half of the channel as $y^+ \approx \{24, 83, 205, 395\}$. Using $p = 4$ at the center of the channel gives a *minimum* collocation spacing (based on Gauss-Lobatto quadrature) as $\Delta y_c^+ \approx 22$ compared with maximum spacing at centerline ($\Delta y_c^+ \approx 6.5$) for the reference DNS of Moser, Kim, Mansour [69]. By any extent, using $p = 4$ ($\Delta y_w^+ \approx 2.8$) with this mesh amounts to an extremely coarse resolution. In fact, this resolution is comparable to the A4 case (see Table 3.1). Now, exploiting the flexibility of the DG discretization, we increase the local polynomial order such that we get a wall-normal direction polynomial order distribution as $p = \{6, 6, 5, 4, 4, 5, 6, 6\}$.

Firstly, the meanflow and rms profiles, shown in Figure 3.27, for both cases are in reasonable agreement with the reference DNS [69]. However, through local p -refinement, we notice an improvement compared with the $p = 4$ case in the rms profiles, shown in Figure 3.27(b) in the region close to the wall. Meanwhile, the Reynolds stress and viscous stress profiles (Figure 3.29) appear reasonable along with the energy spectra (Figure 3.28) for the resolutions considered. The improved total stress profile (see Figure 3.29), in the near-wall region, for the variable polynomial order demonstrates the efficacy of the local polynomial refinement in improving the accuracy of solution efficiently.

It is interesting to overlay the meanflow and rms profiles for $Re_\tau = 395$ and $Re_\tau = 100$ along with their corresponding reference solution. A comparison of the low order statistics obtained at $Re_\tau = 395$ using the current mesh with the $4 \times 4 \times 8$ mesh using $p = 4$ and $p = 6$ is shown in Figures 3.30 and 3.31. The striking similarity between the two cases at both $p = 4$ and $p = 6$ (locally) validates the resolution guidelines devised earlier using the lower Reynolds number ($Re_\tau = 100$).

3.3 Discussion

Before concluding this chapter, we comment on the DG spatial resolution effects by comparing and contrasting the effect of polynomial enrichment on the various meshes considered at $Re_\tau = 100$.

We begin with an overlay of the solutions obtained using for C3, C4, and C6 can be seen in Figures 3.32, 3.33, and 3.34. The solution is strongly influenced by the numerical dissipation introduced through the Lax-Friederichs (Euler) flux at the lower polynomial orders ($p \leq 4$). In particular, this may be due to the particularly low resolution in the x -direction. It is well-known that upwind schemes are effective in damping scales at high wavenumbers. Therefore, using a low resolution may not provide sufficient scale separation between the energy containing scales (low wavenumbers) and those susceptible to the upwinding effect. Evidence to support this view may be seen in the overall lower energy content in the streamwise energy spectra shown in Figure 3.33(a). Also, compare these results with that obtained using the A mesh where there is a sharp drop-off in the energy spectra at the highest wavenumbers, clearly seen for A3 (see Figure 3.39). By contrast, both B and D with $p \geq 3$ ensure that the planar resolution is sufficient to ensure that the effects of upwinding do not affect the dynamically important large scales (See Figures 3.36 and 3.42).

Recently, Cockburn [19], using a linear hyperbolic system, related the form of the dissipation term to particular choices of numerical fluxes in discontinuous Galerkin methods. Specifically, for a wave equation, the numerical dissipation introduced by the Lax-Friederichs flux is related to the speed of propagation and the solution jump. Given this, we can expect the dissipation in the streamwise direction to be higher for the turbulent channel flow since that is the principal direction of the meanflow. Further, at the lower resolutions the jumps are likely to be more significant. Therefore, a combination of insufficient scale separation, larger solution jumps and the direction of the meanflow leads to the resolution in the streamwise direction determining the dissipation properties of the simulation. Fortunately, the increase in resolution through polynomial order and/or mesh refinement dramatically reduces the dissipation introduced through the convective flux.

This leads us to the consistently higher energy levels observed in the spectra for A and B when compared with C and D, respectively (refer to Figures 3.39, 3.36, 3.33, and 3.42). This may be explained by the lower y resolution for A and B in the near-wall region compared with C and D. The underresolved viscous wall region results in the energy containing

eddies that are not sufficiently influenced by the physical damping due to viscous effects. Thus, the equilibrium that is achieved through an interaction of inertial and viscous effects close to the rigid walls is not faithfully represented. This leads to an artificially high energy content in the resolved scales resulting in overprediction in the wall-shear stress. Furthermore, this imbalance is exacerbated for the B mesh, that by virtue of a higher planar resolution, contains lower dissipation (see Figure 3.35 and 3.37). By contrast, the A mesh benefits from a stabilizing influence of the numerical dissipation leading to an overall better agreement with DNS (see Figure 3.38 and 3.40).

Now, an increase in the resolution in the wall-normal direction from 4 to 8 elements, that lead to improved prediction of the velocity gradients close to the wall, minimize the overprediction in the τ_w . However, the presence of numerical dissipation leads to solutions that are overdiffuse (see Figures 3.32 and 3.34). The dissipative effect that arises naturally in the discretization of the convection term is interpreted as an implicit SGS model in MILES (Monotonically Integrated LES). Thereby, eliminating the need for explicit SGS modeling [37]. This approach, currently an active area of research, is motivated by the need to reduce the computational expense associated with an explicit SGS model.

In the current work, our goal is to evaluate the efficacy of a VMS model to reduce the resolution requirements. Since the effect of an eddy viscosity SGS model is to enhance dissipation, the resolutions (h and p) chosen, in the context of modeling, should be chosen such that the influence of numerical dissipation is minimized. Fortunately, the D mesh is effective in reducing both the adverse effects of low resolutions in the x – and y –direction allowing a better convergence to the reference solution [14] with polynomial enrichment (see Figures 3.41 and 3.43). Thus, the current resolution study provides guidelines for selection of the mesh and polynomial order in the context of multi-scale modeling. In doing so, we have illustrated the advantages of local hp –refinement that can be exploited to reduce the required degrees of freedom without sacrificing accuracy.

3.4 Summary

We have highlighted the salient features of the DG spatial discretization and their role in the context of coarse grid DNS of turbulent channel flows. The effect of varying the resolution both individually in each coordinate direction, as well as, simultaneously in all the three coordinate directions are studied.

The solution jump (slip) at the boundary is related to the local resolution. In particular, the resolution in the wall-normal direction is found to be crucial in regulating the solution jumps at the wall. For particularly coarse near-wall resolutions ($\Delta y_w^+ > 4$), leads to large values of slip at the channel walls. Consequently, the results obtained are found to be in poor agreement with the reference DNS [14, 69]. Importantly, with reasonable planar resolution, a modest reduction in Δy_w^+ values lead to a reduction in the magnitude of slip and improved agreement with DNS. In general, allowing the solution to slip at the channel walls is found to mitigate the near-wall resolution requirements by capturing part of the boundary layer in the jump (see Figure 3.45).

Next, the non-linear stability of the simulation is determined by the resolution in the spanwise direction ($\Delta z^+ \leq 50$). Meanwhile, the numerical dissipation present in the discretization is found to depend on the resolution in the streamwise direction. In fact, at very low resolution, similar to traditional upwind finite volume discretizations, the numerical dissipation dominates the solution by suppressing the turbulent fluctuations. At moderate resolutions, the numerical dissipation levels are reduced, but, the solutions obtained indicate the presence of aliasing and SGS effects.

Overall, without any explicit modeling, reasonable low-order statistics are obtained here even with $\Delta x^+ \leq 150$ and $\Delta z^+ \leq 50$, and $\Delta y_m^+ \leq 15$ using $p \geq 3$. The authors note that mesh resolution guidelines developed are for the current implementation, other choices for the numerical fluxes both convective and viscous can alter these estimates. And therefore, it is a potential course for future research.

Importantly, using the turbulent channel flow, we have demonstrated the potential for producing both accurate, as well as, efficient turbulence simulations by exploiting the *local hp*-refinement capabilities of our DG implementation.

Case	p	Δy_w^+	Ndof	Slip	τ_w	u_τ
A3	3	4.35	8,192	-0.5442	1.0816	1.0379
A4	4	2.96	16,000	-0.0342	1.0018	0.9988
A5	5	2.14	27,648	0.1842	0.9760	0.9858
A6	6	1.62	43,904	0.0868	0.9818	0.9887
A8	8	1.01	93,312	-0.0055	0.9812	0.9897

Table 3.1: Simulation parameters and results summary using $4 \times 4 \times 8$ mesh for a resolution study at $Re_\tau = 100$. The element size in wall units for this mesh topology is $\Delta x^+ \approx 314$ and $\Delta z^+ \approx 52.3$ in the streamwise and spanwise directions, respectively.

Case	p	Δy_w^+	Ndof	Slip	τ_w	u_τ
B3	3	4.35	16,384	-0.7940	1.3014	1.1397
B4	4	2.96	32,000	-0.4528	1.2166	1.1020
B6	6	1.62	87,808	0.1387	1.0553	1.0264

Table 3.2: Simulation parameters and results summary using a $8 \times 4 \times 8$ mesh for a resolution study at $Re_\tau = 100$. The element size in wall units for this mesh topology is $\Delta x^+ \approx 157$ and $\Delta z^+ \approx 52.3$ in the streamwise and spanwise directions, respectively.

Case	p	Δy_w^+	Ndof	Slip	τ_w	u_τ
C2	2	2.25	6,912	-0.0183	0.6828	0.8248
C3	3	1.40	16,384	0.0063	0.7976	0.8913
C4	4	0.95	32,000	0.0023	0.8614	0.9262
C6	6	0.52	87,808	-0.0002	0.9532	0.9751

Table 3.3: Simulation parameters and results summary using a $4 \times 8 \times 8$ mesh for a resolution study at $Re_\tau = 100$. The element size in wall units for this mesh topology is $\Delta x^+ \approx 314$ and $\Delta z^+ \approx 52.3$ in the streamwise and spanwise directions, respectively.

Case	p	Δy_w^+	Ndof	Slip	τ_w	u_τ
D2	2	2.25	13,824	-0.0425	0.7984	0.8912
D3	3	2.33	32,768	-0.0350	0.9553	0.9766
D4	4	0.95	64,000	0.0060	0.9806	0.9875
D6	6	0.52	175,616	-0.0002	0.9693	0.9818
E3	3	4.32	32,768	-0.6934	1.2576	1.1204

Table 3.4: Simulation parameters and results summary using a $8 \times 8 \times 8$ mesh for a resolution study at $Re_\tau = 100$. The element size in wall units for this mesh topology is $\Delta x^+ \approx 157$ and $\Delta z^+ \approx 52.3$ in the streamwise and spanwise directions, respectively.

p	Δy_w^+	Ndof	Slip	τ_w	u_τ
3	2.52	65,536	-0.0607	0.9009	0.9482
4	1.71	128,000	0.0567	0.9403	0.9687
{5, 5, 4, 3}	1.24	158,976	0.0229	0.9555	0.9765

Table 3.5: Simulation parameters and results summary using a $8 \times 8 \times 16$ mesh for a resolution study at $Re_\tau = 180$. The element size in wall units for this mesh topology is $\Delta x^+ \approx 283$ and $\Delta z^+ \approx 47.1$ in the streamwise and spanwise directions, respectively.

p	Δy_w^+	Ndof	Slip	τ_w	u_τ
3	1.01	262,144	0.0077	0.9944	0.9962
4	0.69	512,000	0.0021	1.0025	1.0003

Table 3.6: Simulation parameters and results summary using a $16 \times 16 \times 16$ mesh for a resolution study at $Re_\tau = 180$. The element size in wall units for this mesh topology is $\Delta x^+ \approx 141$ and $\Delta z^+ \approx 47.1$ in the streamwise and spanwise directions, respectively.

p	Δy_w^+	Ndof	Slip	τ_w	u_τ
4	2.82	144,000	-0.1501	1.01	1.00
{6, 6, 5, 4}	1.46	295,776	0.1190	1.03	1.01

Table 3.7: Simulation parameters and results summary using a $8 \times 8 \times 18$ mesh for a resolution study at $Re_\tau = 395$. The element size in wall units for this mesh topology is $\Delta x^+ \approx 310$ and $\Delta z^+ \approx 46$ in the streamwise and spanwise directions, respectively.

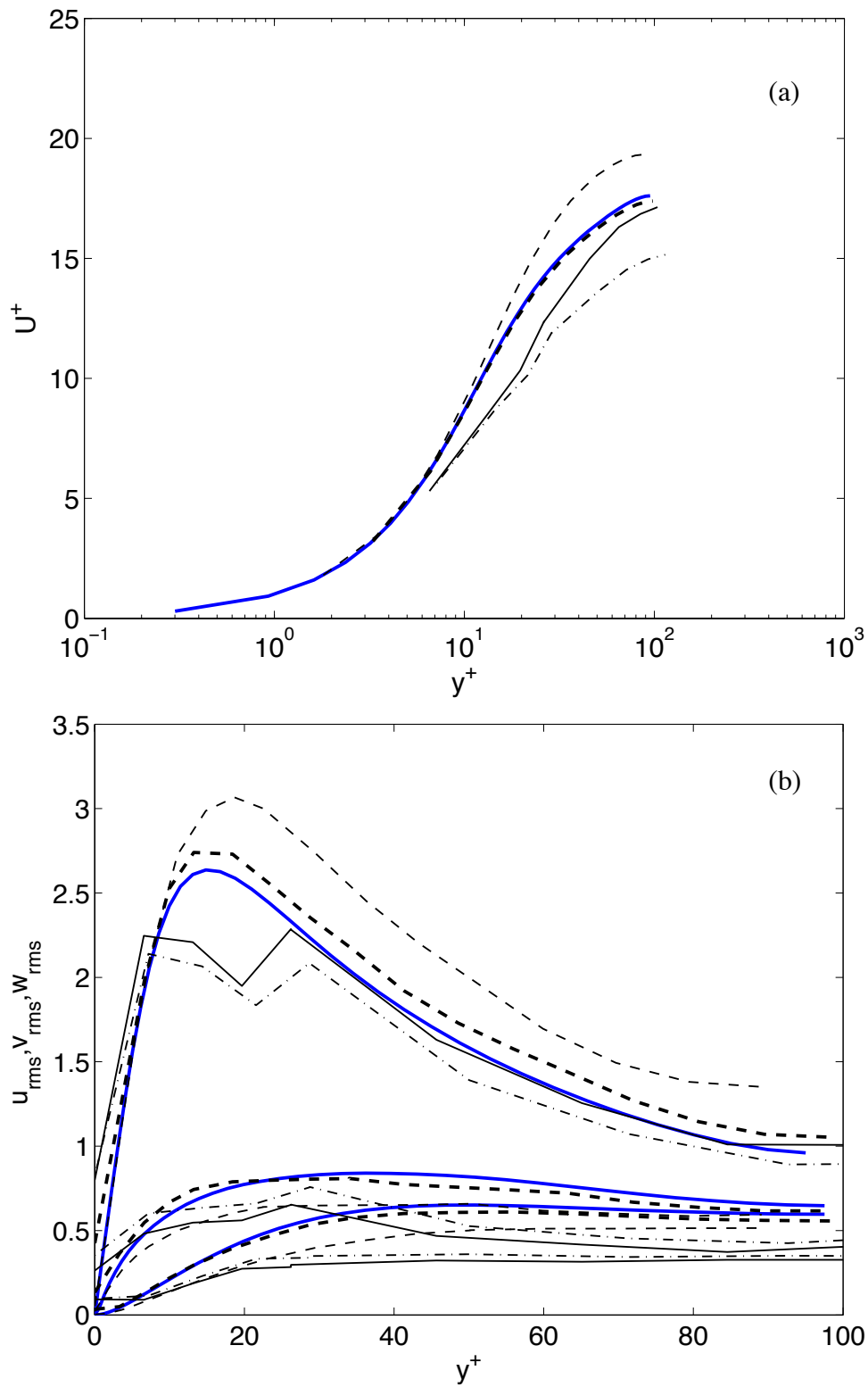


Figure 3.3: Meanflow and rms profiles for $Re_\tau = 100$ computed with different mesh topologies using $p = 3$: — DNS; — $4 \times 4 \times 8$; - - $8 \times 4 \times 8$; - · - $4 \times 8 \times 8$; · · · $8 \times 8 \times 8$.

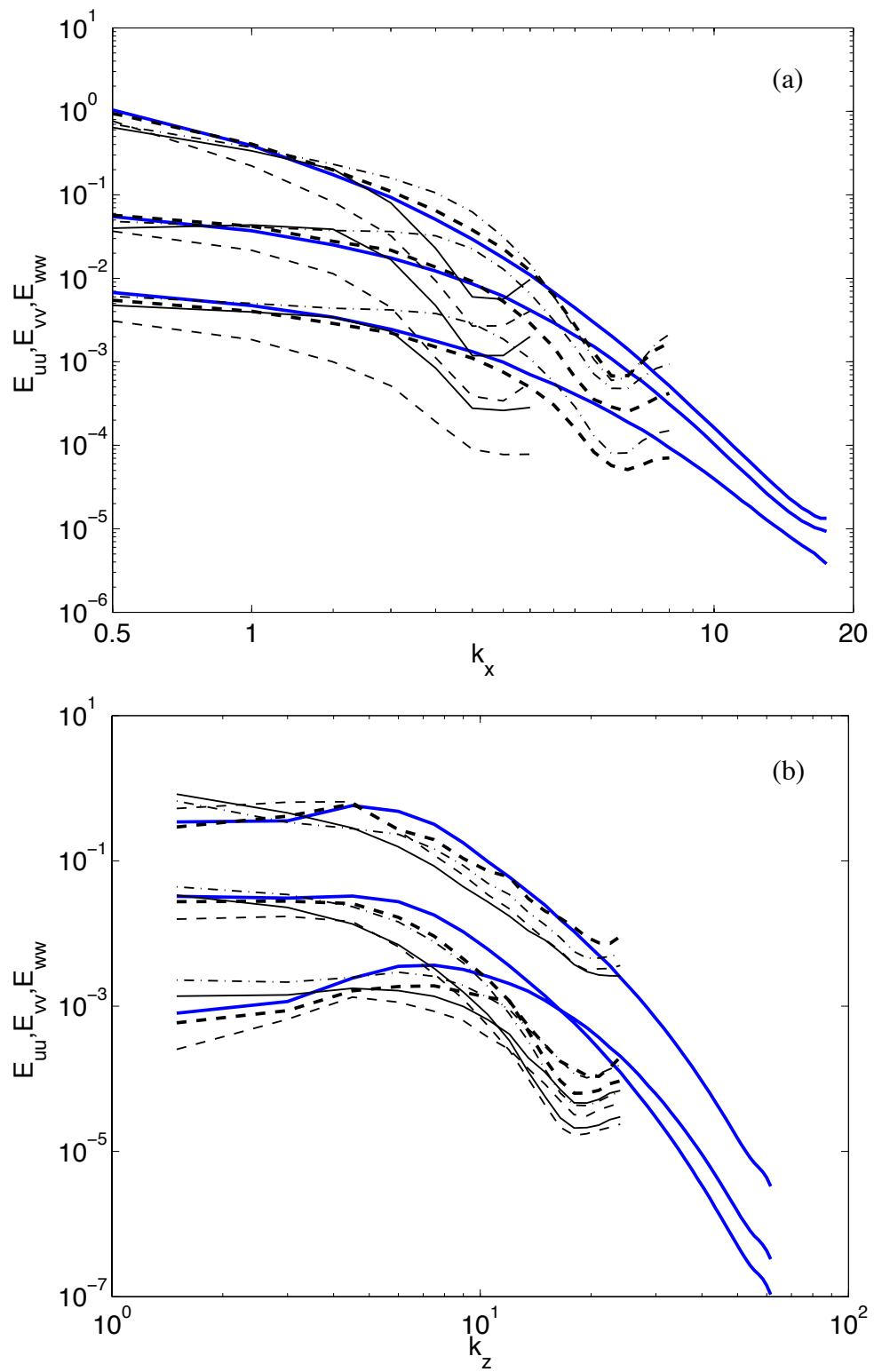


Figure 3.4: One-dimensional energy spectra in x - and z - directions for $Re_\tau = 100$ computed at $y^+ \approx 12$ with different mesh topologies using $p = 3$: — DNS; — $4 \times 4 \times 8$; - - $8 \times 4 \times 8$; . . $4 \times 8 \times 8$; - . $8 \times 8 \times 8$.

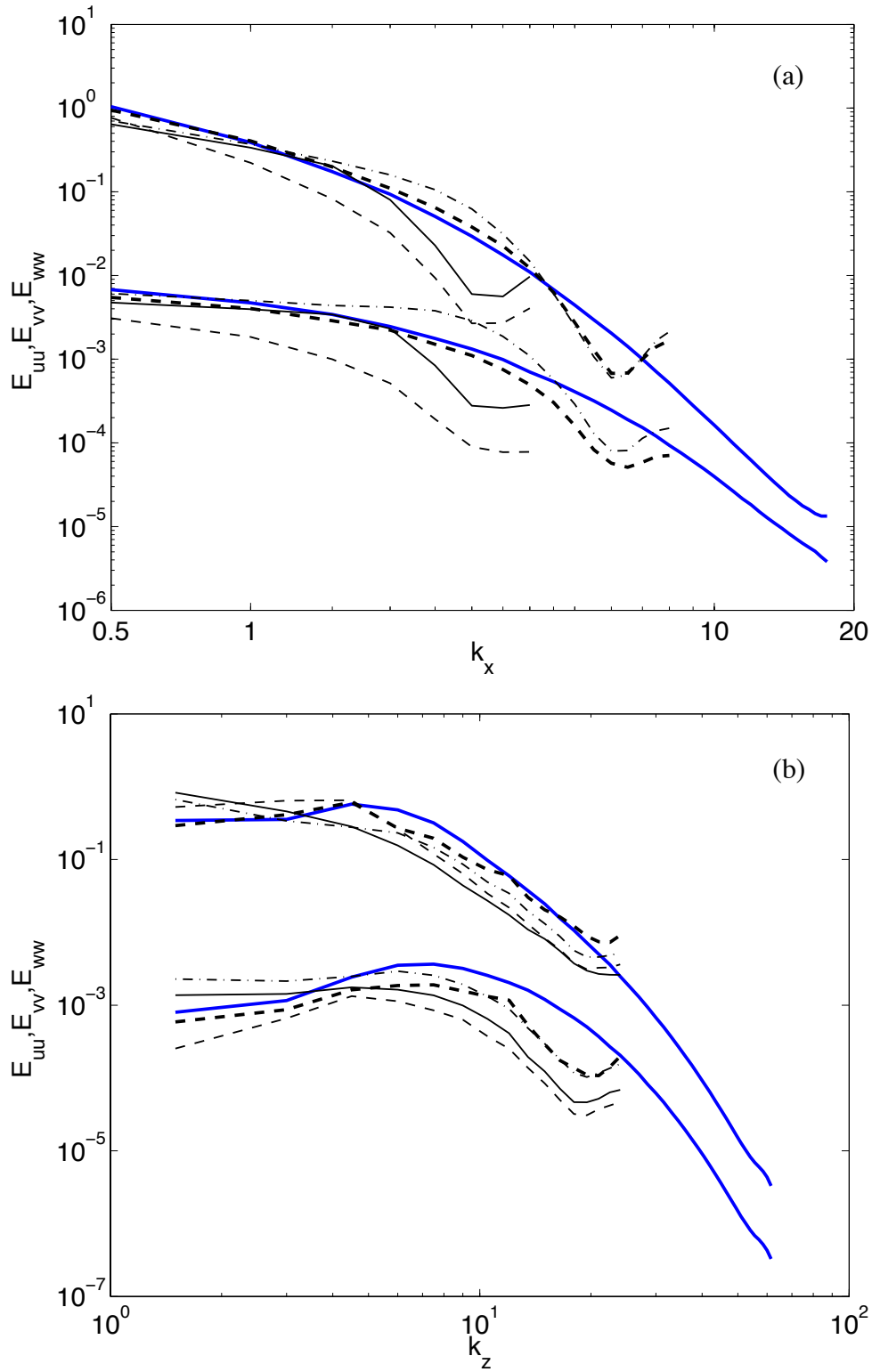


Figure 3.5: One-dimensional energy spectra in x - and z - directions (u and v components only) for $Re_\tau = 100$ computed at $y^+ \approx 12$ with different mesh topologies using $p = 3$: — DNS; — $4 \times 4 \times 8$; --- $8 \times 4 \times 8$; ---- $4 \times 8 \times 8$; -.- $8 \times 8 \times 8$.

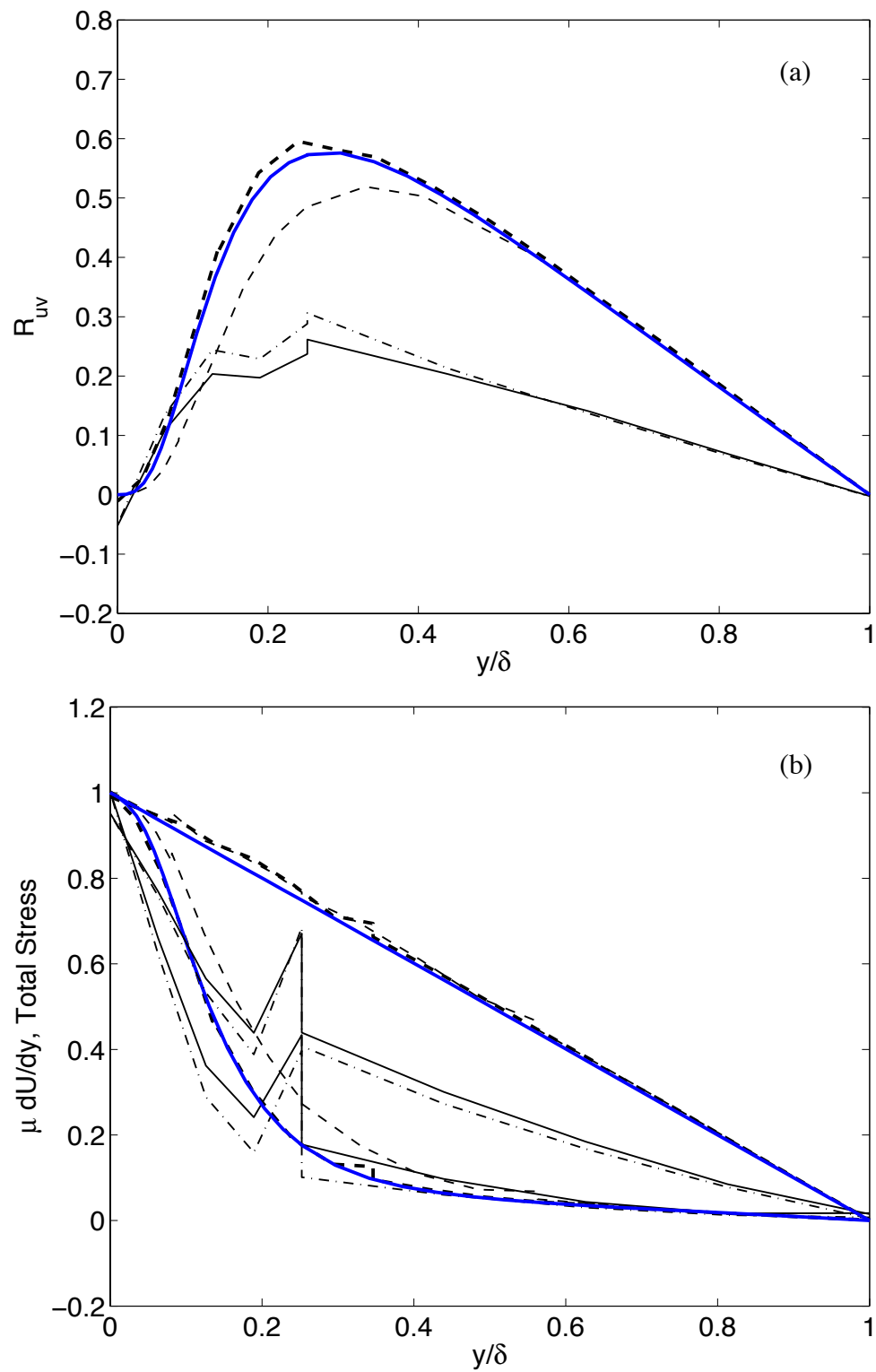


Figure 3.6: Reynolds, viscous and total stress profiles for $Re_\tau = 100$ computed with different mesh topologies using $p = 3$: — DNS; — $4 \times 4 \times 8$; - - $8 \times 4 \times 8$; - · - $4 \times 8 \times 8$; - - - $8 \times 8 \times 8$.

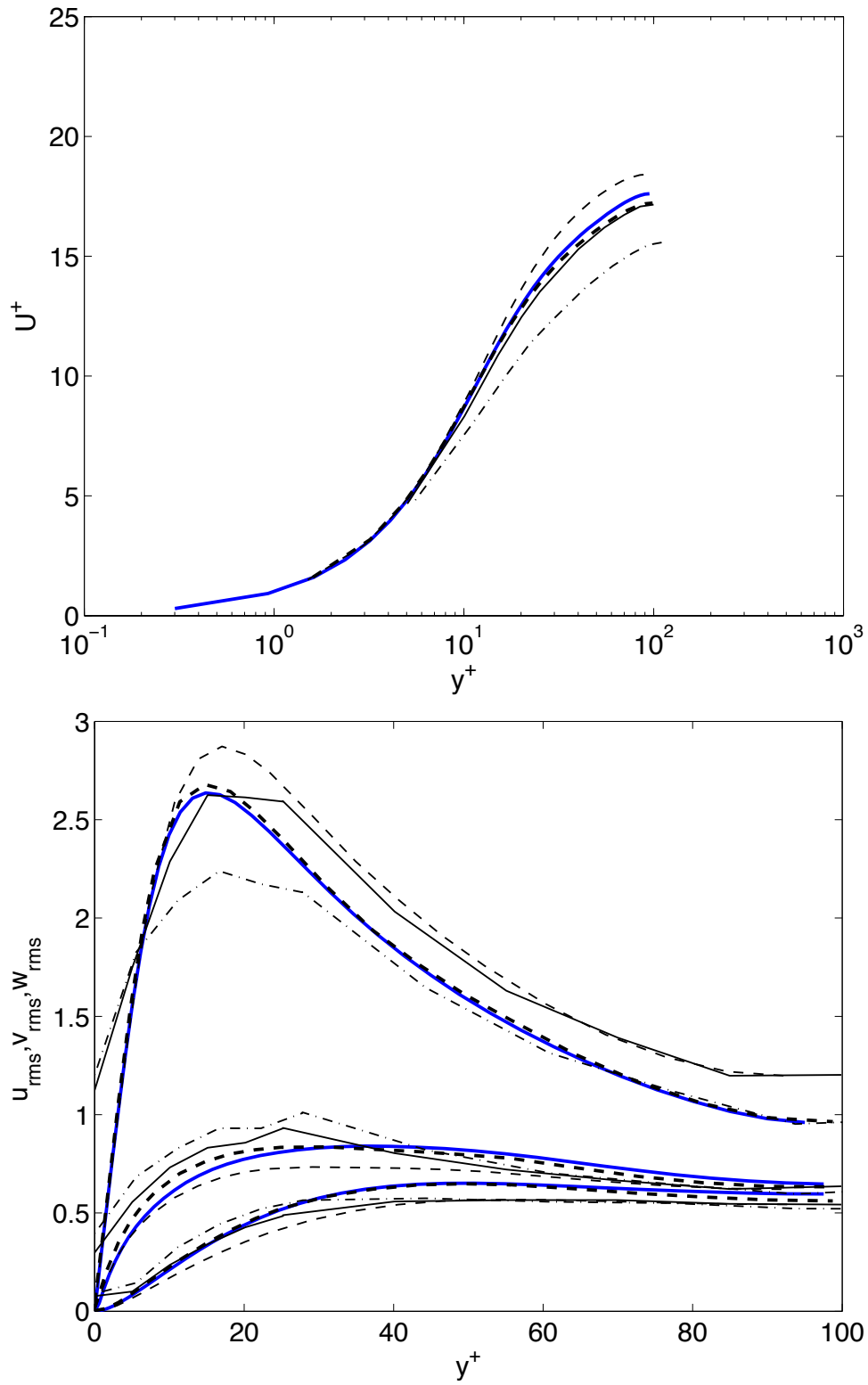


Figure 3.7: Meanflow and rms profiles for $Re_\tau = 100$ computed with different mesh topologies using $p = 4$: — DNS; — $4 \times 4 \times 8$; - - $8 \times 4 \times 8$; - · - $4 \times 8 \times 8$; - - - $8 \times 8 \times 8$.

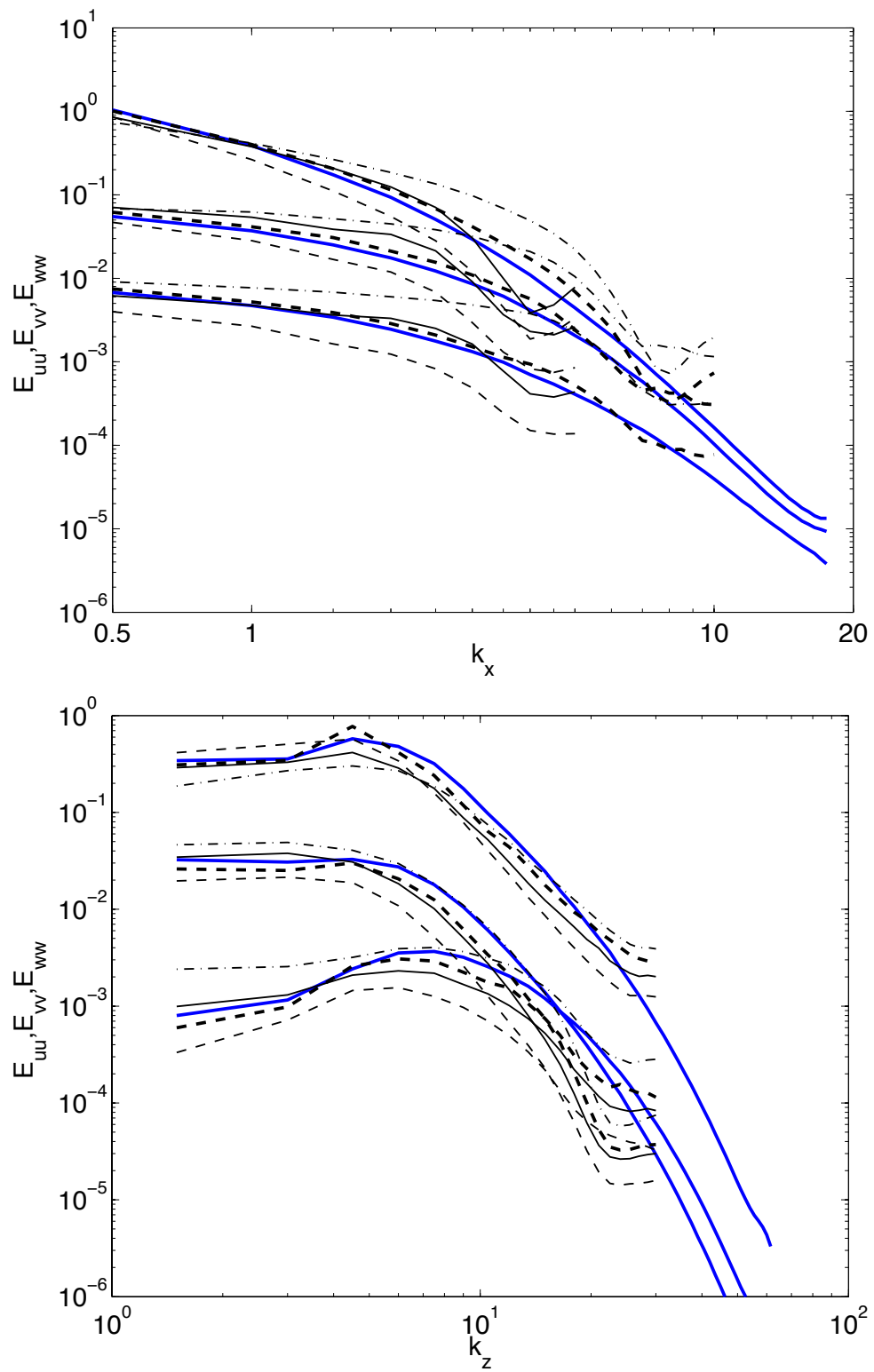


Figure 3.8: One-dimensional energy spectra in x - and z - directions for $Re_\tau = 100$ computed at $y^+ \approx 12$ with different mesh topologies using $p = 4$: — DNS; — $4 \times 4 \times 8$; - - $8 \times 4 \times 8$; . . $4 \times 8 \times 8$; - - - $8 \times 8 \times 8$.

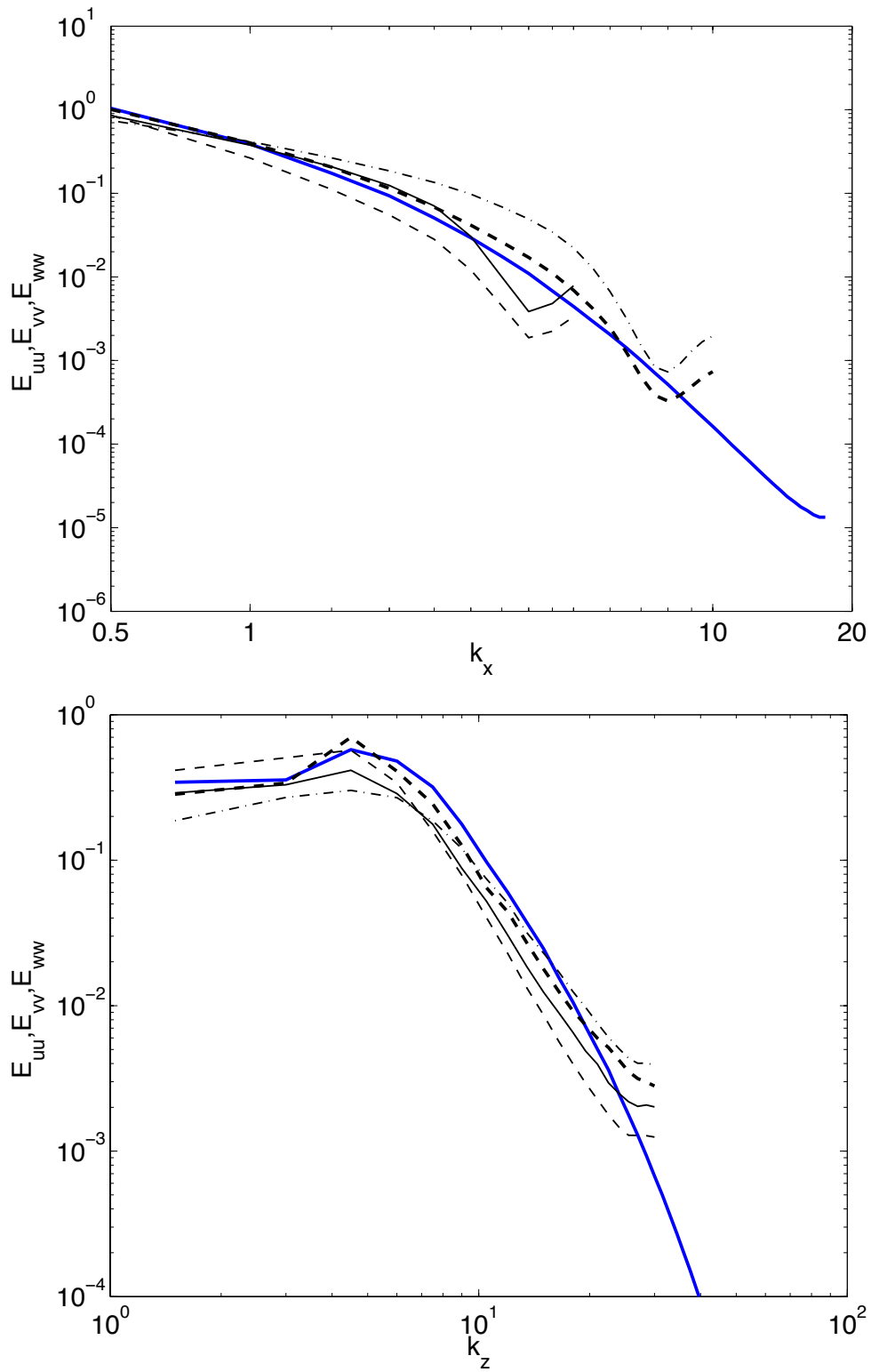


Figure 3.9: One-dimensional energy spectra in x - and z - directions (u component only) for $Re_\tau = 100$ computed at $y^+ \approx 12$ with different mesh topologies using $p = 4$: — DNS; — $4 \times 4 \times 8$; - - $8 \times 4 \times 8$; - · - $4 \times 8 \times 8$; · · · $8 \times 8 \times 8$.

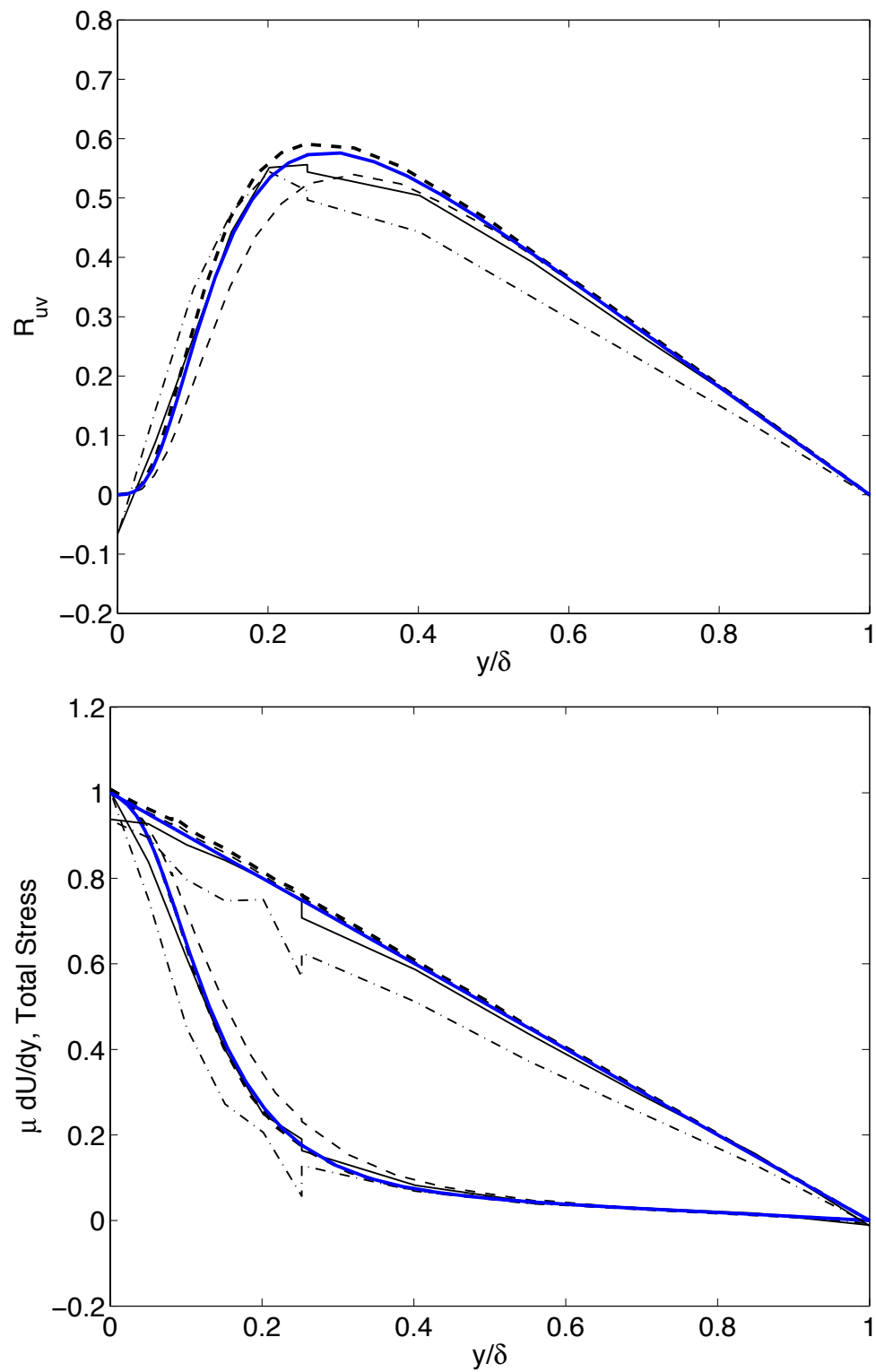


Figure 3.10: Reynolds, viscous and total stress profiles for $Re_\tau = 100$ computed with different mesh topologies using $p = 4$: — DNS; — $4 \times 4 \times 8$; - - $8 \times 4 \times 8$; - · - $4 \times 8 \times 8$; · · · $8 \times 8 \times 8$.

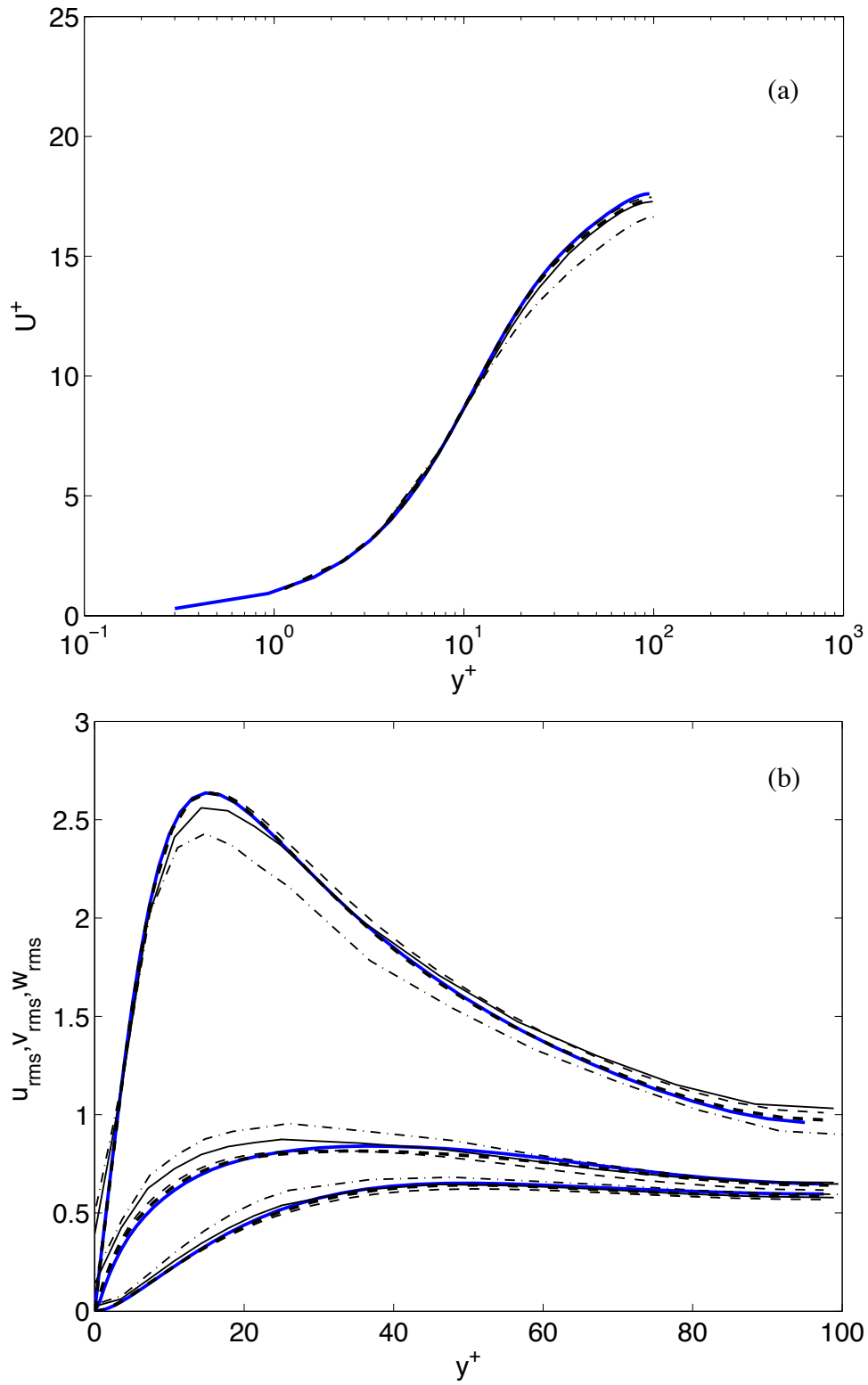


Figure 3.11: Meanflow and rms profiles for $Re_\tau = 100$ computed with different mesh topologies using $p = 6$: — DNS; — $4 \times 4 \times 8$; - - $8 \times 4 \times 8$; - - - $4 \times 8 \times 8$; - - - $8 \times 8 \times 8$.

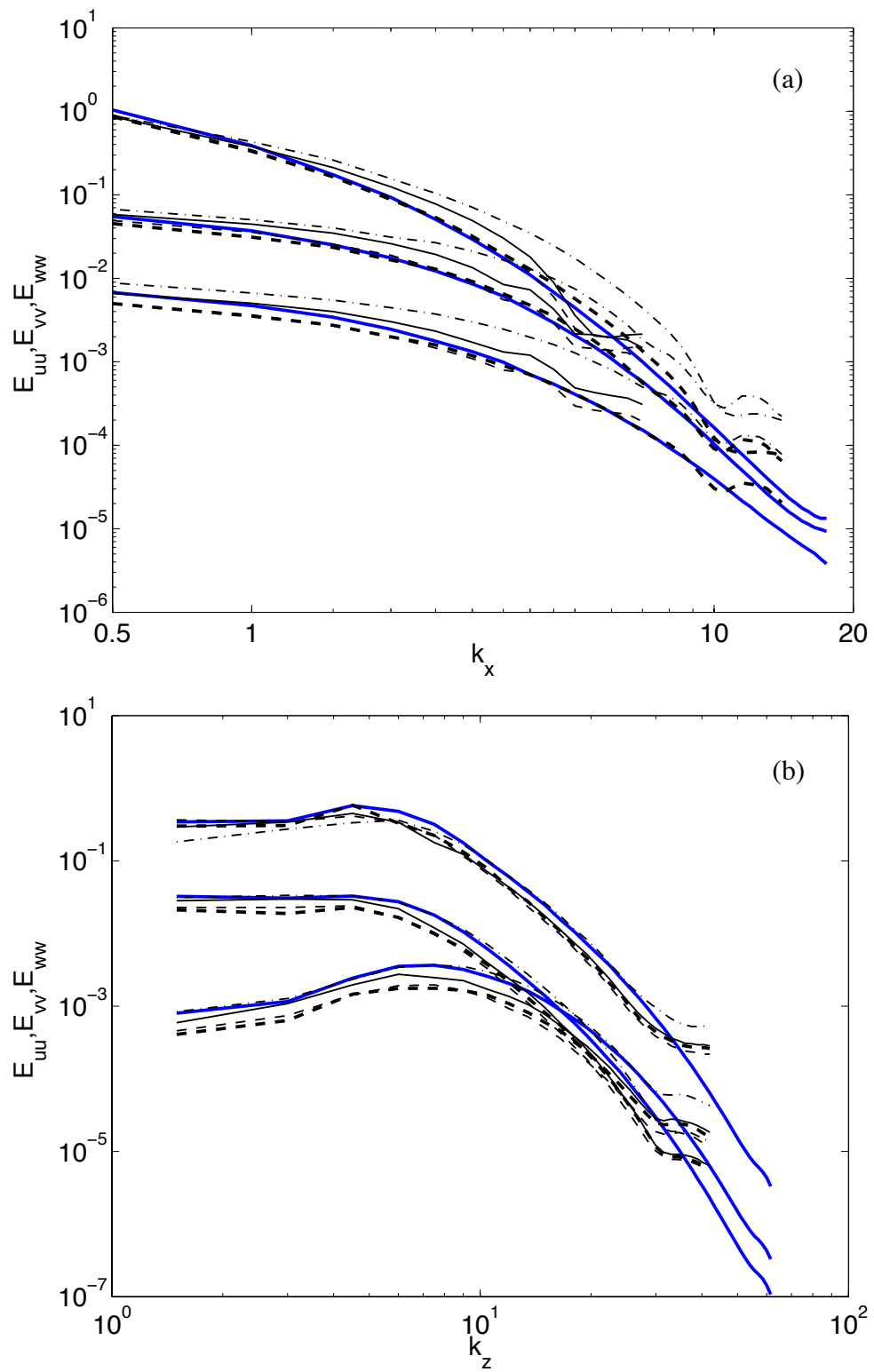


Figure 3.12: One-dimensional energy spectra in x - and z - directions for $Re_\tau = 100$ computed at $y^+ \approx 12$ with different mesh topologies using $p = 6$: — DNS; — $4 \times 4 \times 8$; - - $8 \times 4 \times 8$; . . $4 \times 8 \times 8$; - . $8 \times 8 \times 8$.

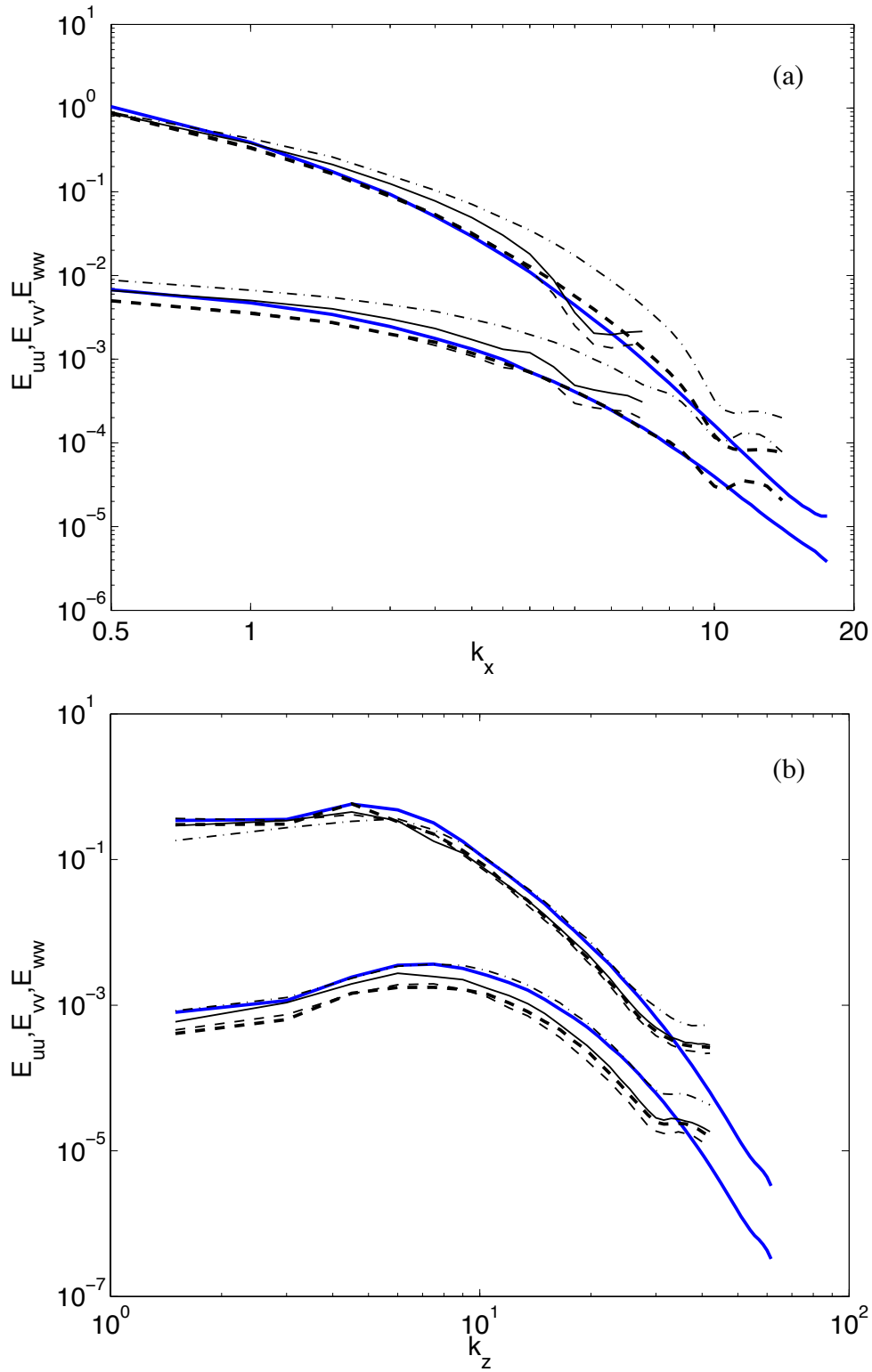


Figure 3.13: One-dimensional energy spectra in x - and z - directions (u and v components only) for $Re_\tau = 100$ computed at $y^+ \approx 12$ with different mesh topologies using $p = 6$: — DNS; — $4 \times 4 \times 8$; - - $8 \times 4 \times 8$; . . $4 \times 8 \times 8$; - . $8 \times 8 \times 8$.

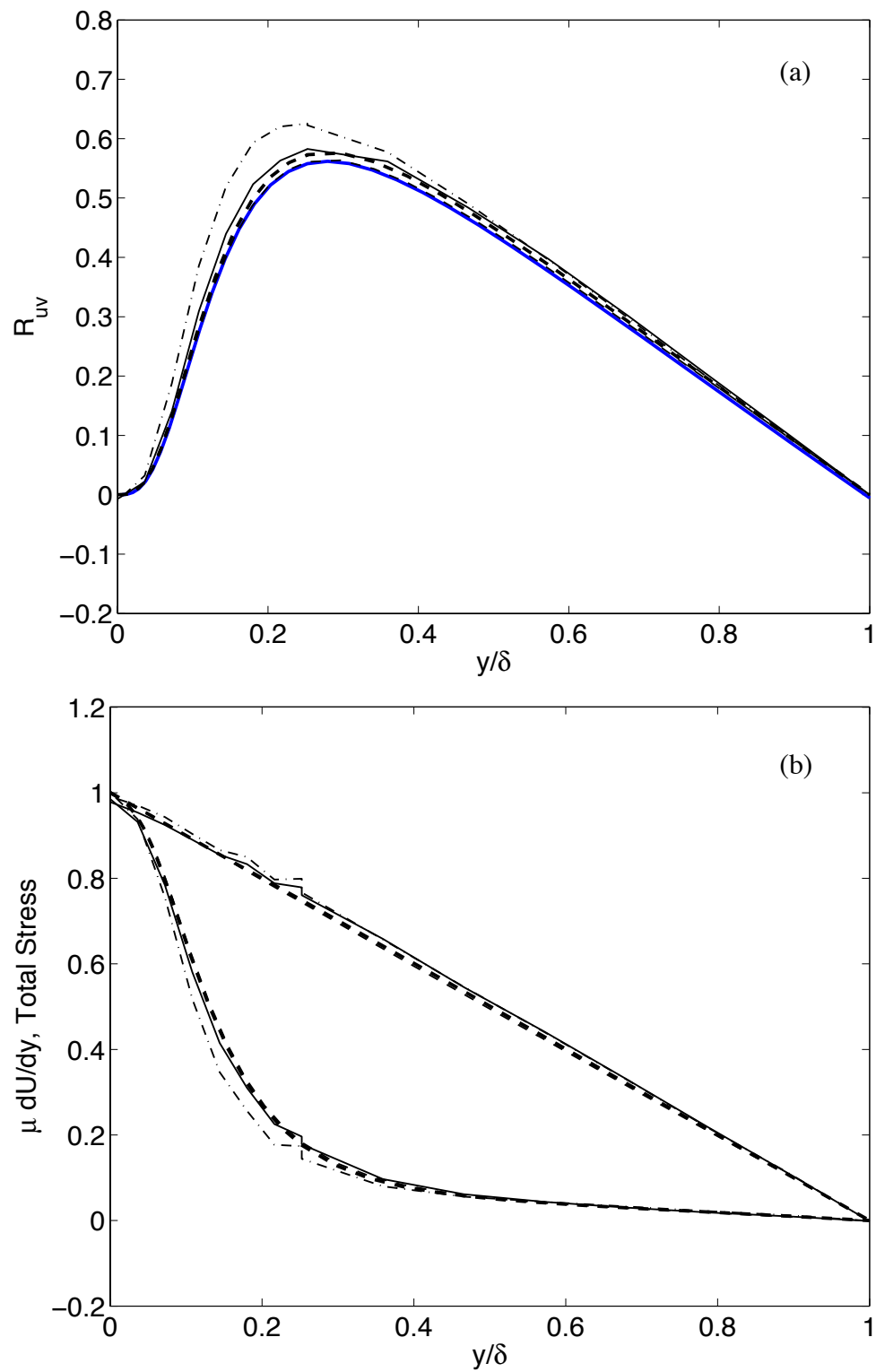


Figure 3.14: Reynolds, viscous and total stress profiles for $Re_\tau = 100$ computed with different mesh topologies using $p = 6$: — DNS; — $4 \times 4 \times 8$; - - $8 \times 4 \times 8$; - · - $4 \times 8 \times 8$; · · · $8 \times 8 \times 8$.

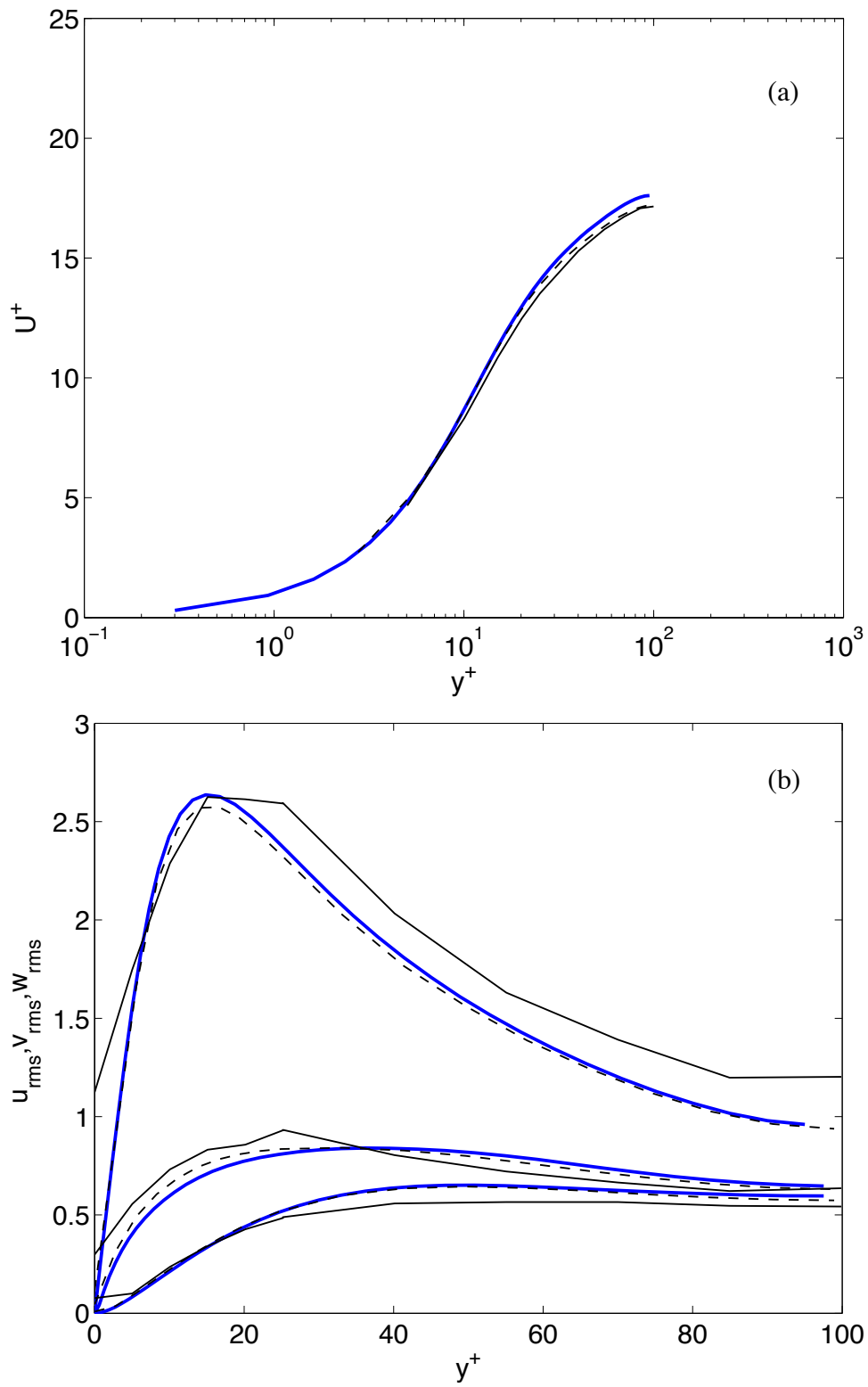


Figure 3.15: Meanflow and rms profiles for $Re_\tau = 100$ computed with a $4 \times 4 \times 8$ mesh using two different polynomial orders: — DNS; — $p = 4$; ---- $p = 8$.

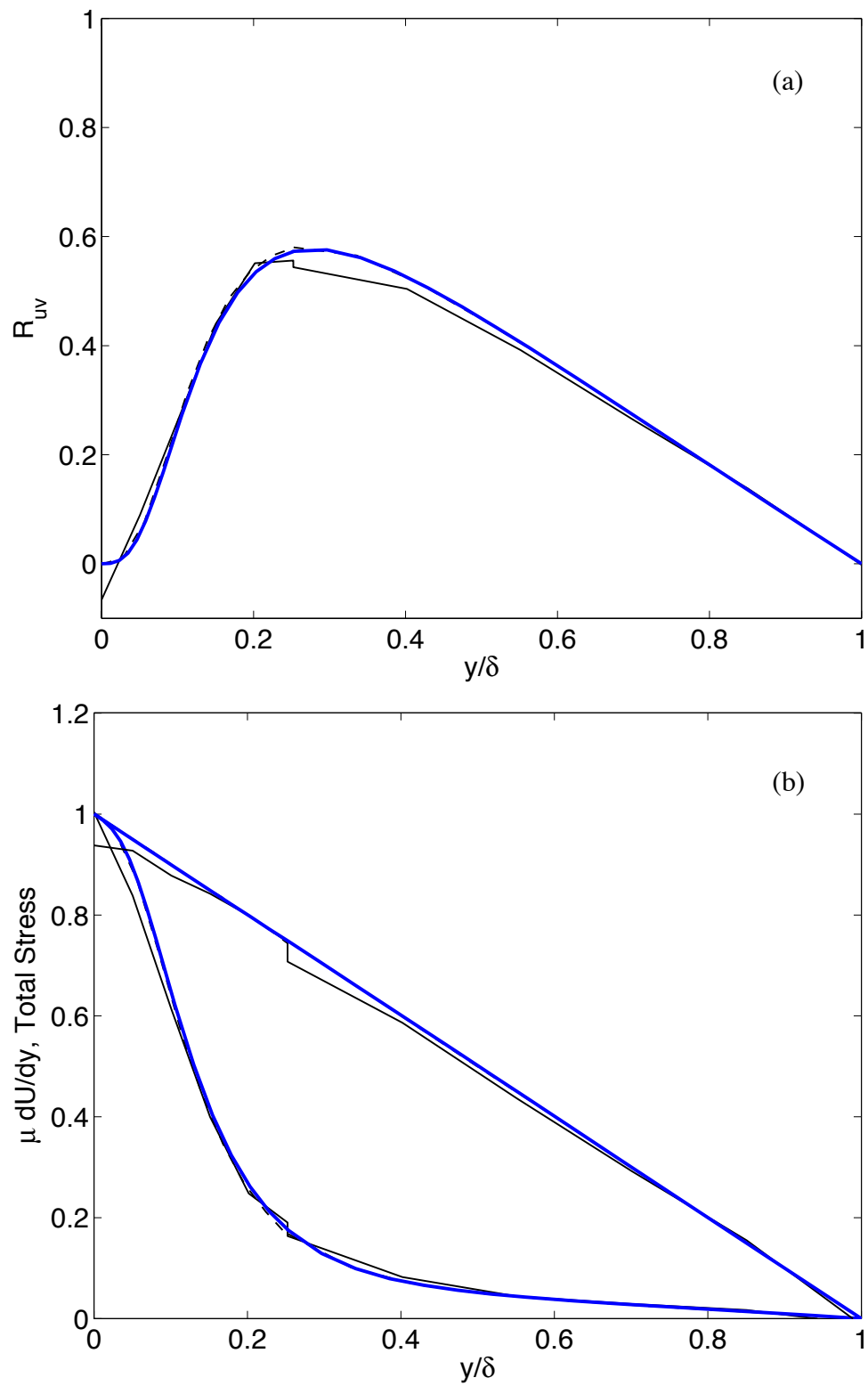


Figure 3.16: Reynolds, viscous and total stress profiles for $Re_\tau = 100$ computed with a $4 \times 4 \times 8$ mesh using two different polynomial orders: — DNS; — $p = 4$; ---- $p = 8$.

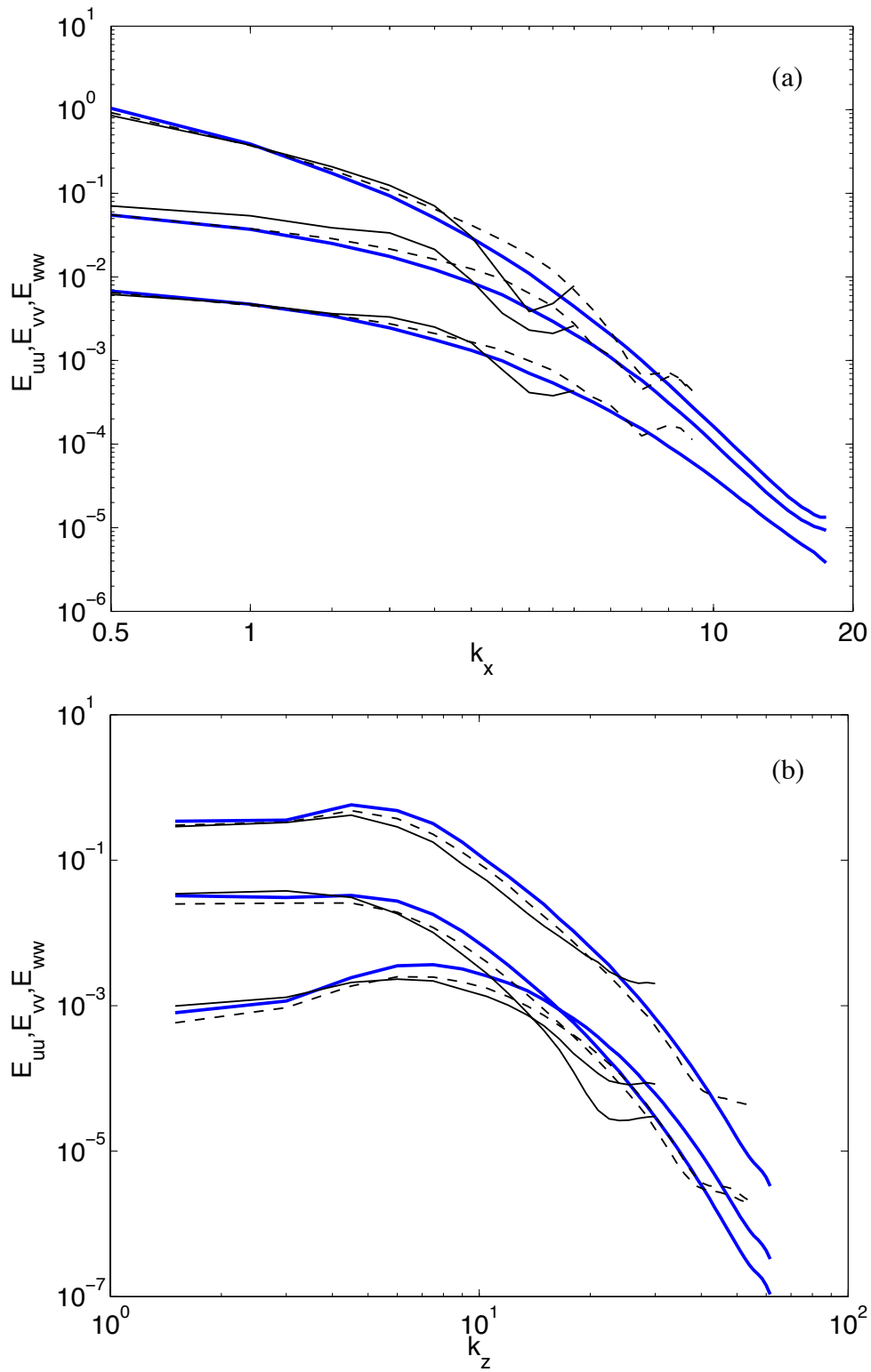


Figure 3.17: One-dimensional energy spectra in x - and z - directions for $Re_\tau = 100$ computed at $y^+ \approx 12$ for $Re_\tau = 100$ with a $4 \times 4 \times 8$ mesh using two different polynomial orders: — DNS; — $p = 4$; ---- $p = 8$.

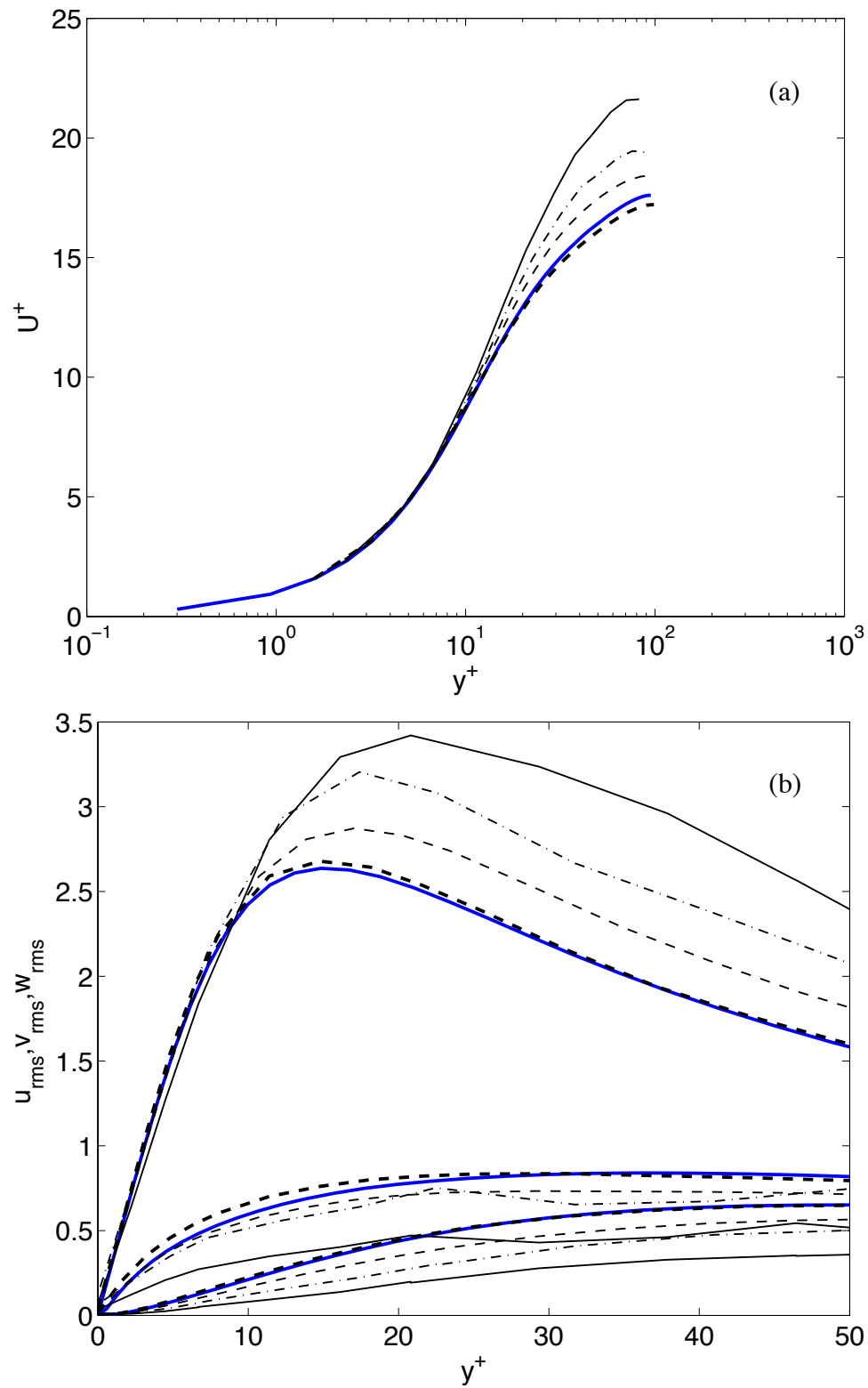


Figure 3.18: Comparison of meanflow and rms profiles for $Re_\tau = 100$ computed to illustrate the effects of numerical dissipation using different polynomial orders and mesh topologies: — DNS; — $4 \times 8 \times 8, p = 2$; ---- $4 \times 8 \times 8, p = 4$; -·- $8 \times 8 \times 8, p = 2$; ---- $8 \times 8 \times 8, p = 4$.

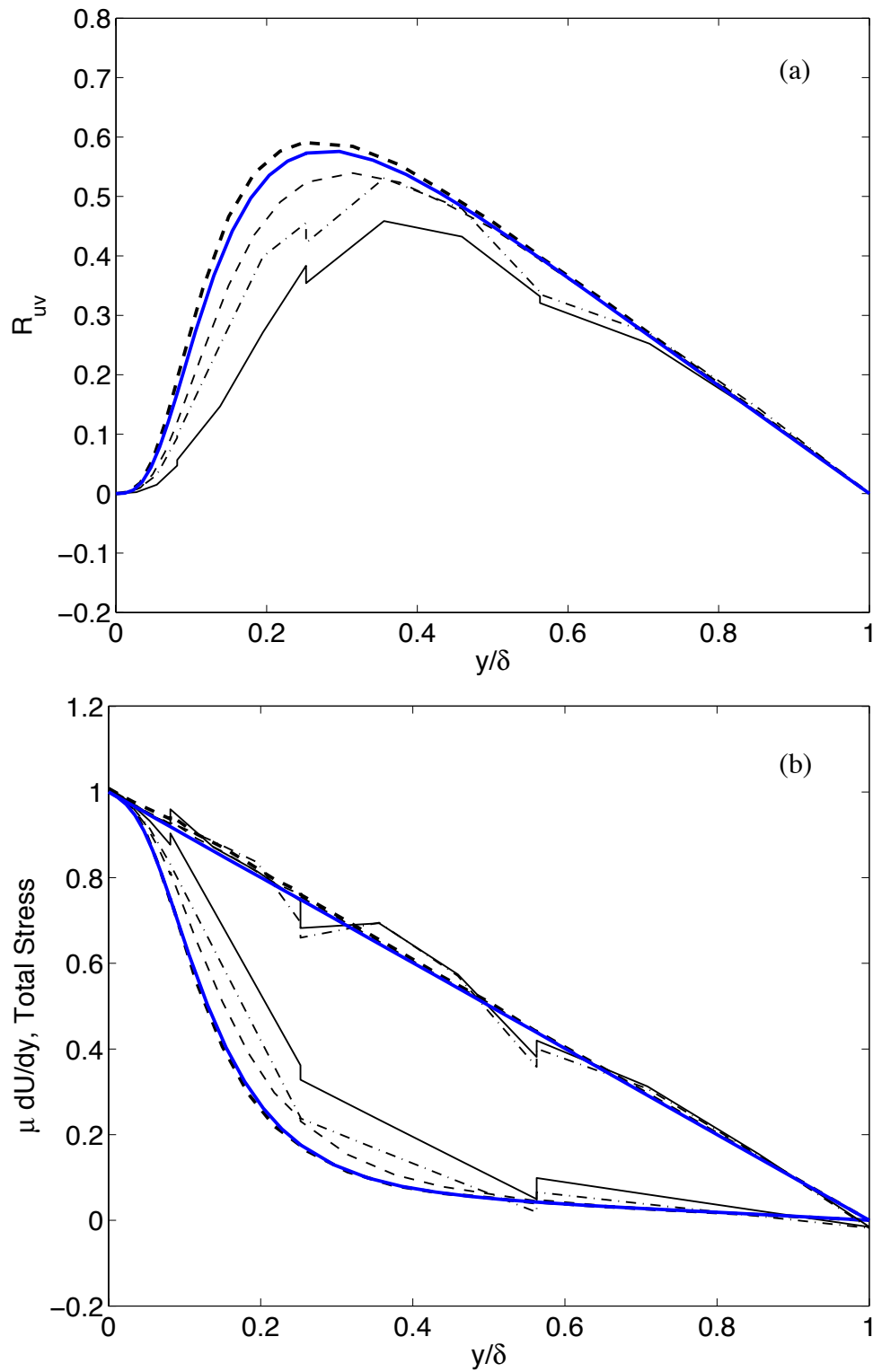


Figure 3.19: Comparison of Reynolds, viscous, and total stress profiles for $Re_\tau = 100$ computed to illustrate the effects of numerical dissipation using different polynomial orders and mesh topologies: — DNS; — $4 \times 8 \times 8, p = 2$; ---- $4 \times 8 \times 8, p = 4$; -.- $8 \times 8 \times 8, p = 2$; ---- $8 \times 8 \times 8, p = 4$.

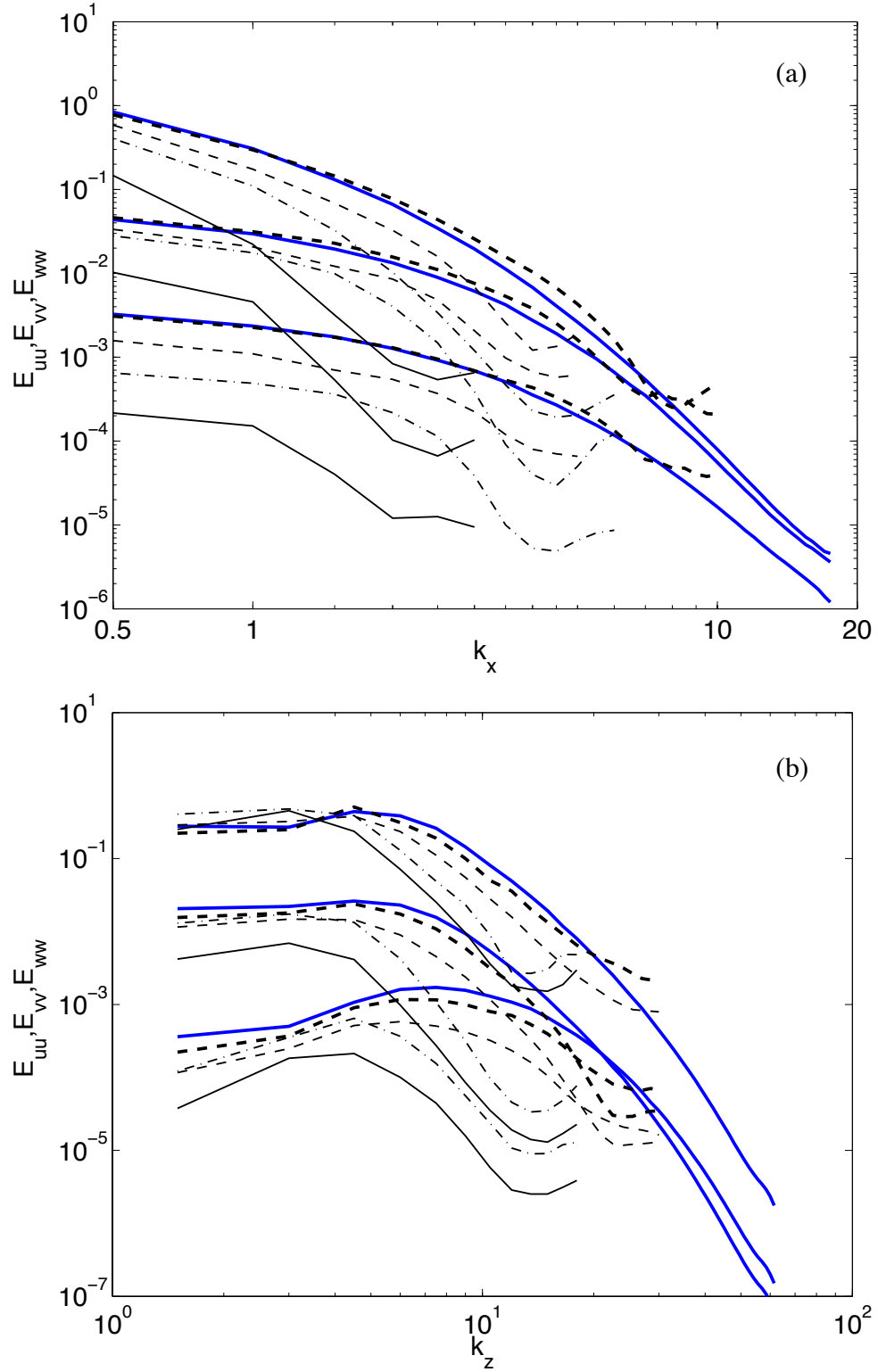


Figure 3.20: Comparison of one-dimensional energy spectra in x - and z - directions for $Re_\tau = 100$ computed at $y^+ \approx 8$ to illustrate the effects of numerical dissipation using different polynomial orders and mesh topologies: — DNS; — $4 \times 8 \times 8$, $p = 2$; ---- $4 \times 8 \times 8$, $p = 4$; —·— $8 \times 8 \times 8$, $p = 2$; ···· $8 \times 8 \times 8$, $p = 4$.

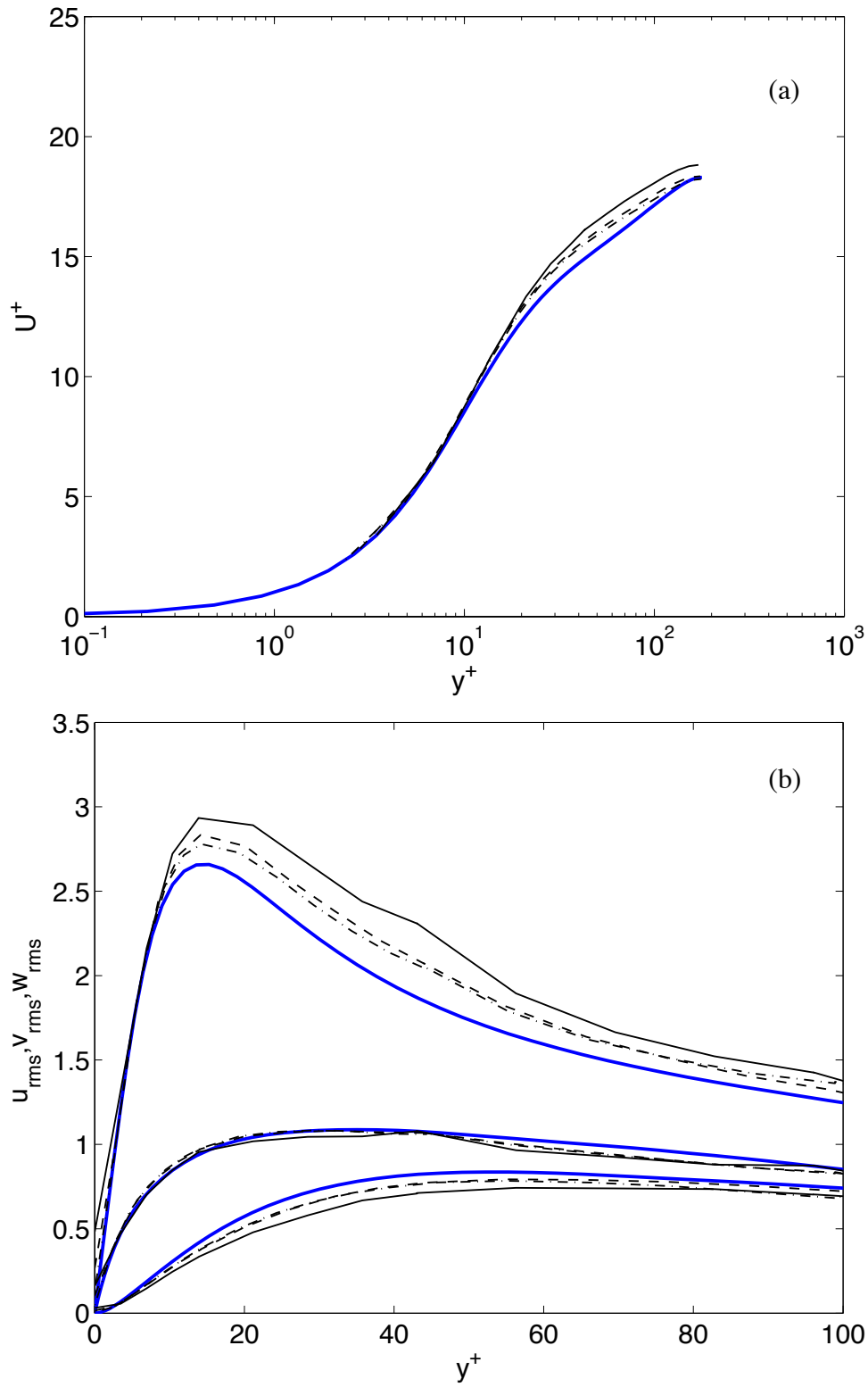


Figure 3.21: Meanflow and turbulence intensity profiles for $Re_\tau = 180$ computed with a $8 \times 8 \times 16$ mesh using different polynomial orders: — DNS; — $p = 3$; ---- $p = 4$; —·— $p = \{5, 5, 4, 3, 3, 4, 5, 5\}$.

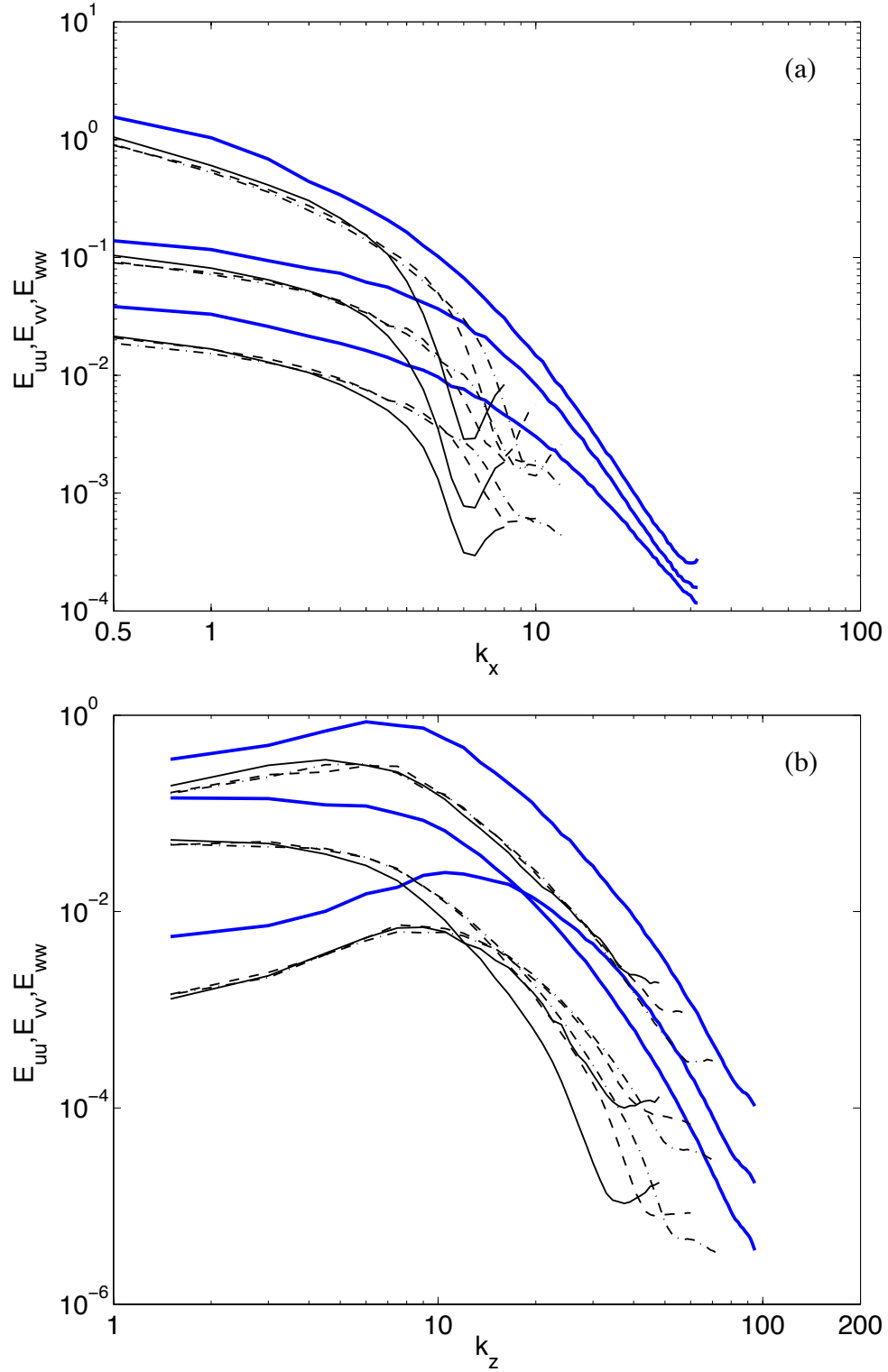


Figure 3.22: One-dimensional energy spectra in x - and z - directions for $Re_\tau = 180$ computed at $y^+ \approx 20$ with a $8 \times 8 \times 16$ mesh using different polynomial orders: — DNS; — $p = 3$; ---- $p = 4$; -·- $p = \{5, 5, 4, 3, 3, 4, 5, 5\}$.

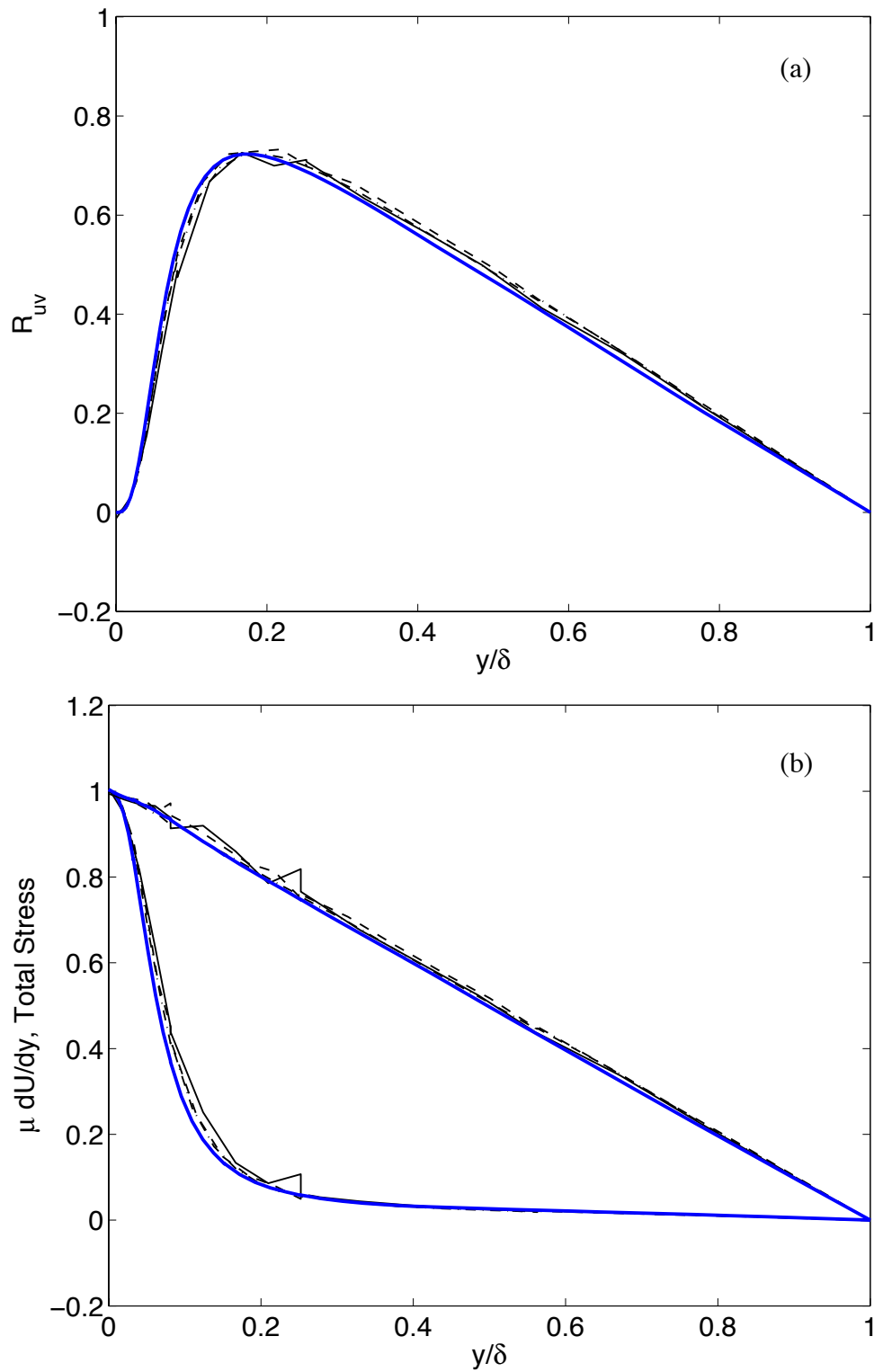


Figure 3.23: Reynolds, viscous, and total stress profiles for $Re_\tau = 180$ computed with a $8 \times 8 \times 16$ mesh using different polynomial orders: — DNS; — $p = 3$; ---- $p = 4$; —·— $p = \{5, 5, 4, 3, 3, 4, 5, 5\}$.

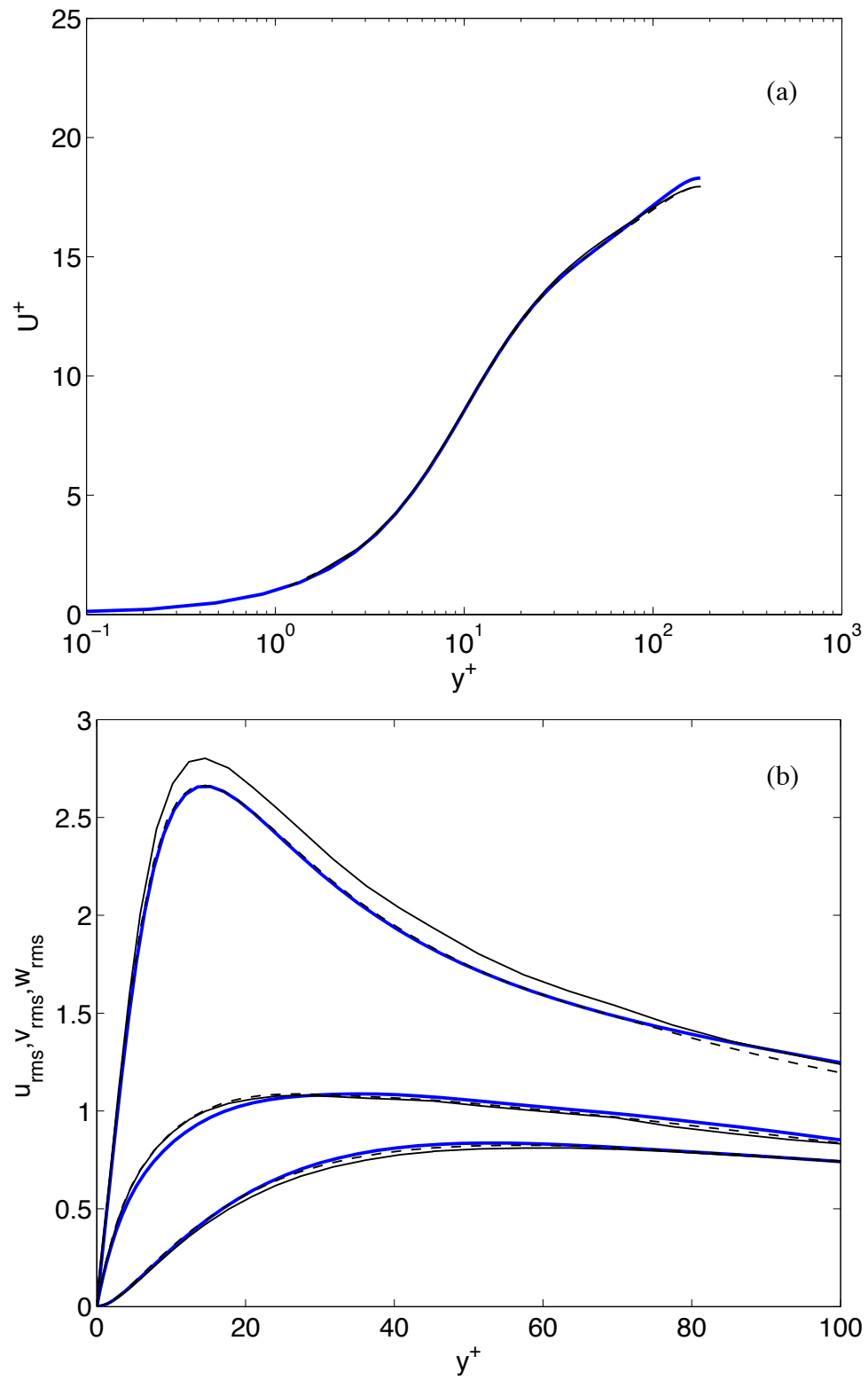


Figure 3.24: Meanflow and turbulence intensity profiles for $Re_\tau = 180$ computed with a $16 \times 16 \times 16$ mesh using different polynomial orders: — DNS; — $p = 3$; ---- $p = 4$.

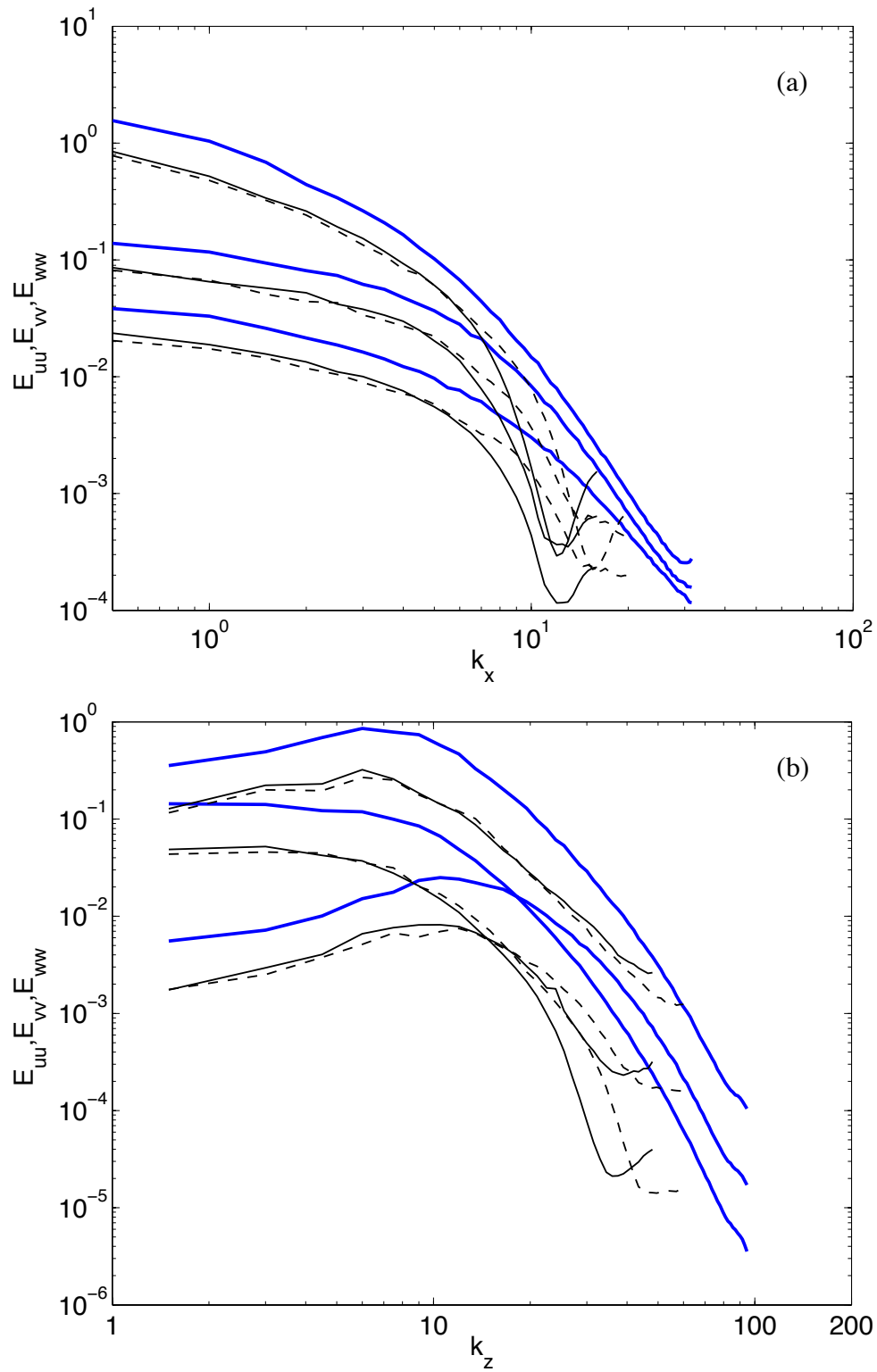


Figure 3.25: One-dimensional energy spectra in x - and z - directions for $Re_\tau = 180$ computed at $y^+ \approx 20$ with a $16 \times 16 \times 16$ mesh with different polynomial orders: — DNS; — $p = 3$; ---- $p = 4$.

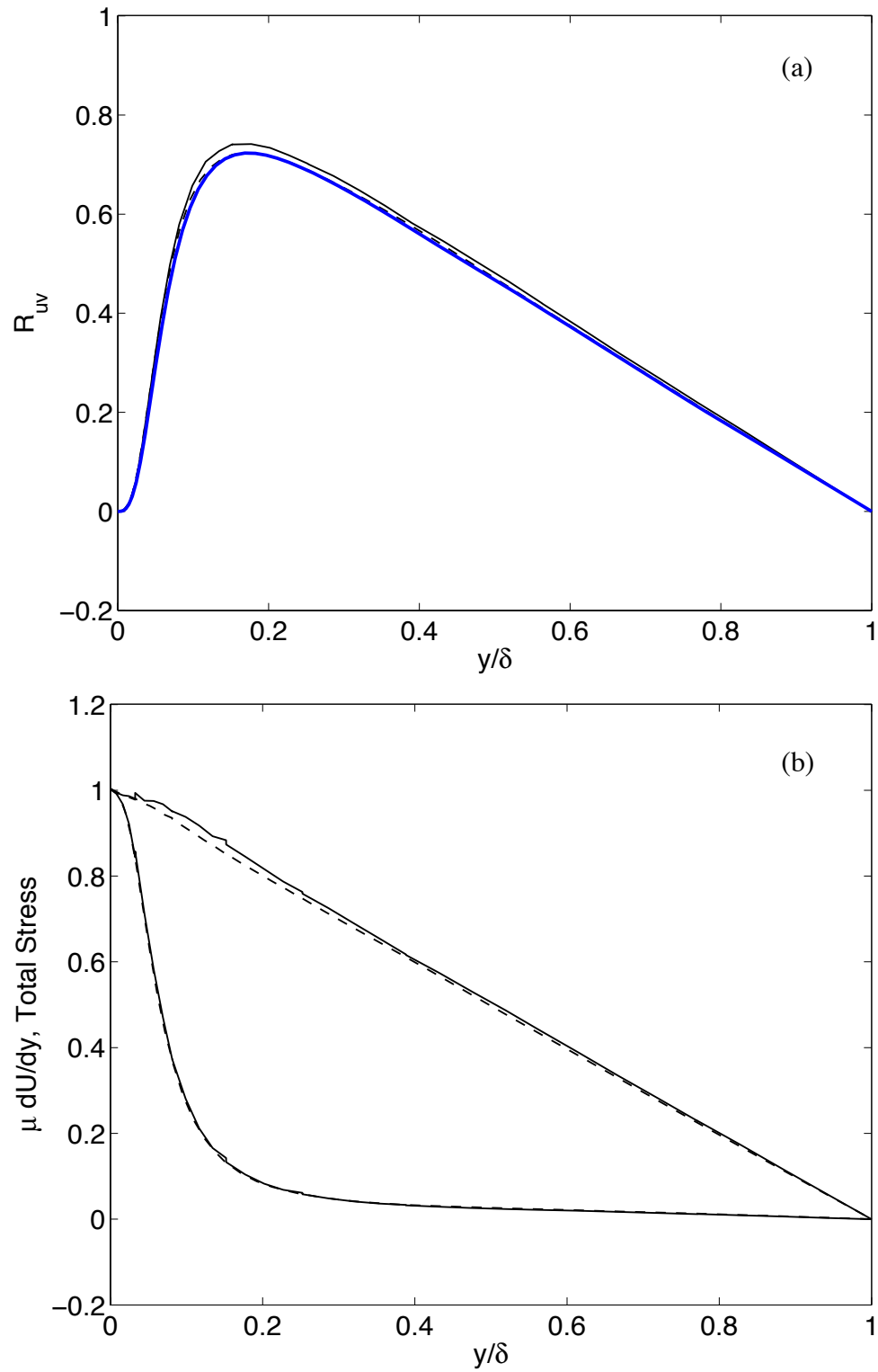


Figure 3.26: Reynolds, viscous, and total stress profiles for $Re_\tau = 180$ computed with a $16 \times 16 \times 16$ mesh using different polynomial orders: — DNS; — $p = 3$; ---- $p = 4$.

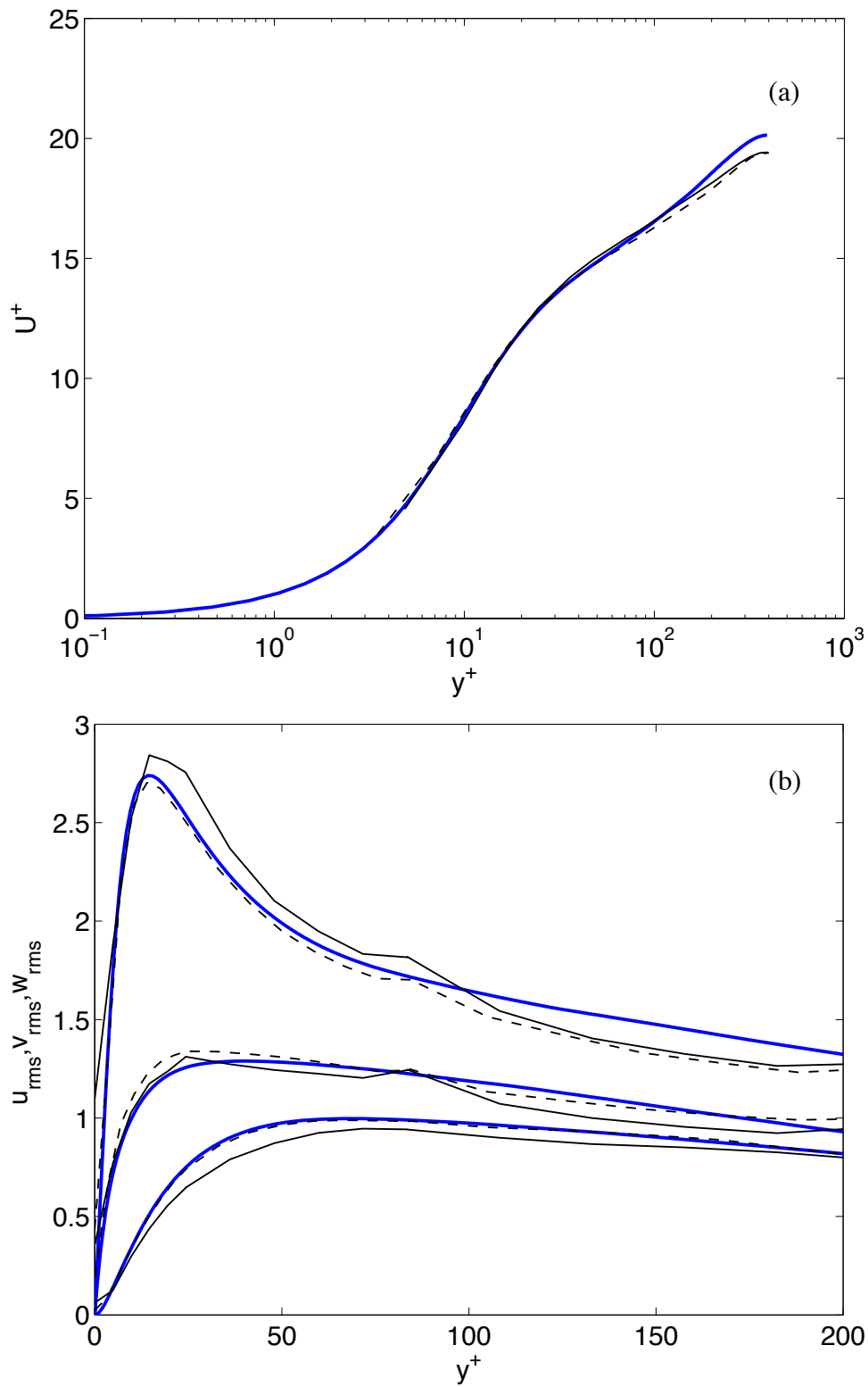


Figure 3.27: Meanflow and turbulence intensity profiles for $Re_\tau = 395$ computed with a $8 \times 8 \times 18$ mesh using different polynomial orders: — DNS; — $p = 4$; ---- $p = \{6, 6, 5, 4, 4, 5, 6, 6\}$.

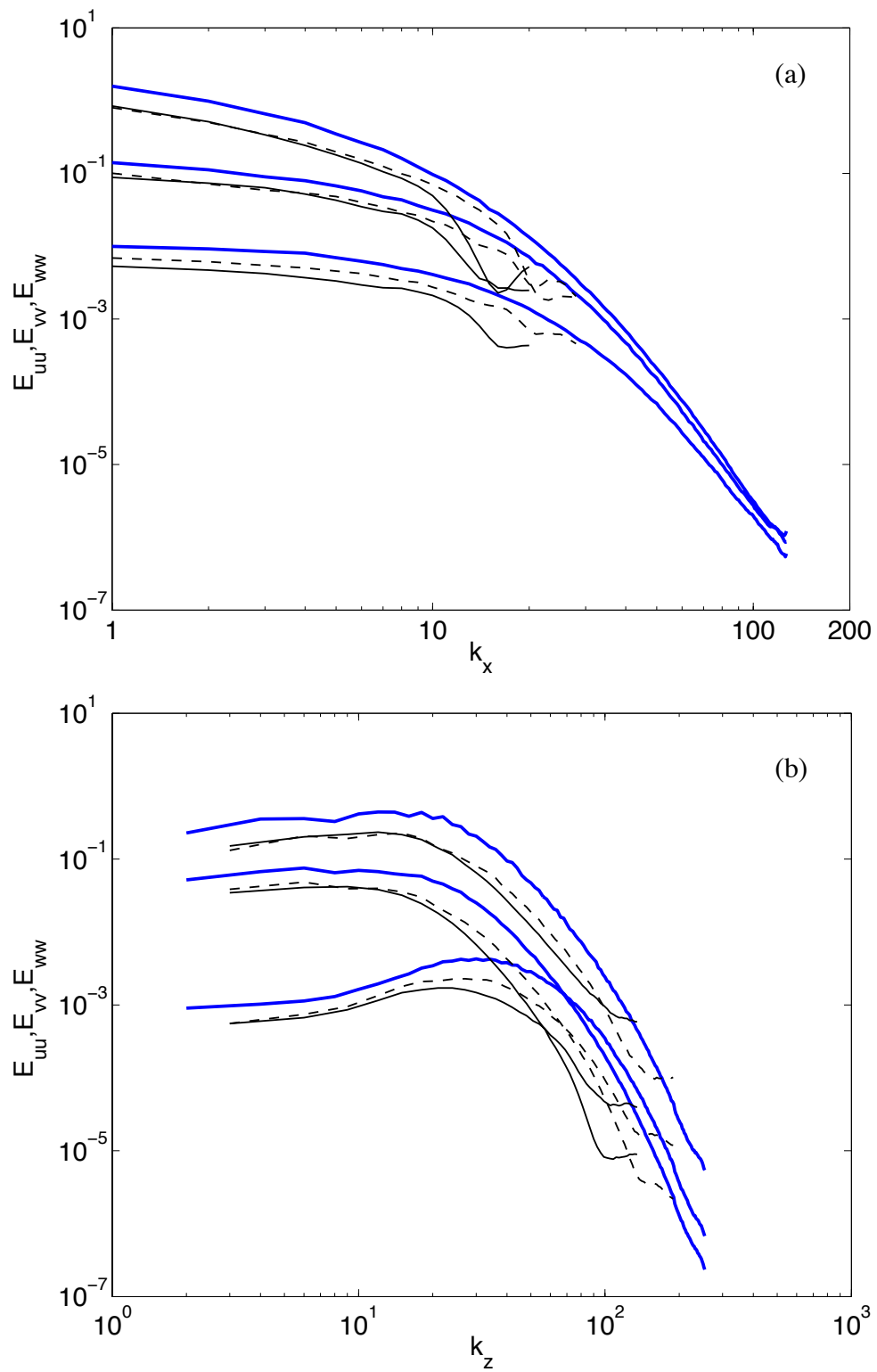


Figure 3.28: One-dimensional energy spectra in x - and z - directions for $Re_\tau = 395$ computed at $y^+ \approx 12$ with a $8 \times 8 \times 18$ mesh with different polynomial orders: — DNS; — $p = 4$; ---- $p = \{6, 6, 5, 4, 4, 5, 6, 6\}$.

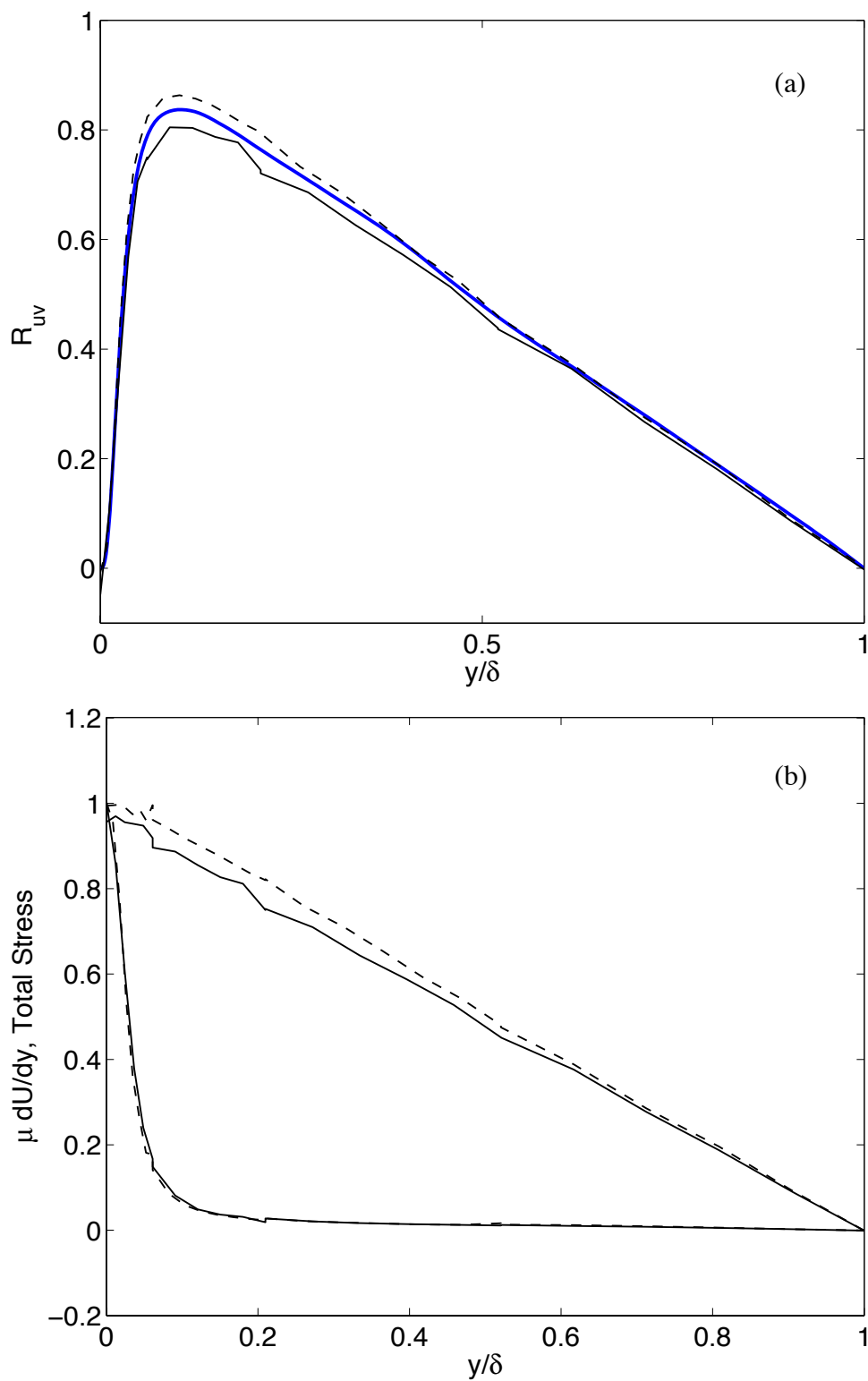


Figure 3.29: Reynolds, viscous, and total stress profiles for $Re_\tau = 395$ computed with a $8 \times 8 \times 18$ mesh using different polynomial orders: — DNS; — $p = 4$; ---- $p = \{6, 6, 5, 4, 4, 5, 6, 6\}$.

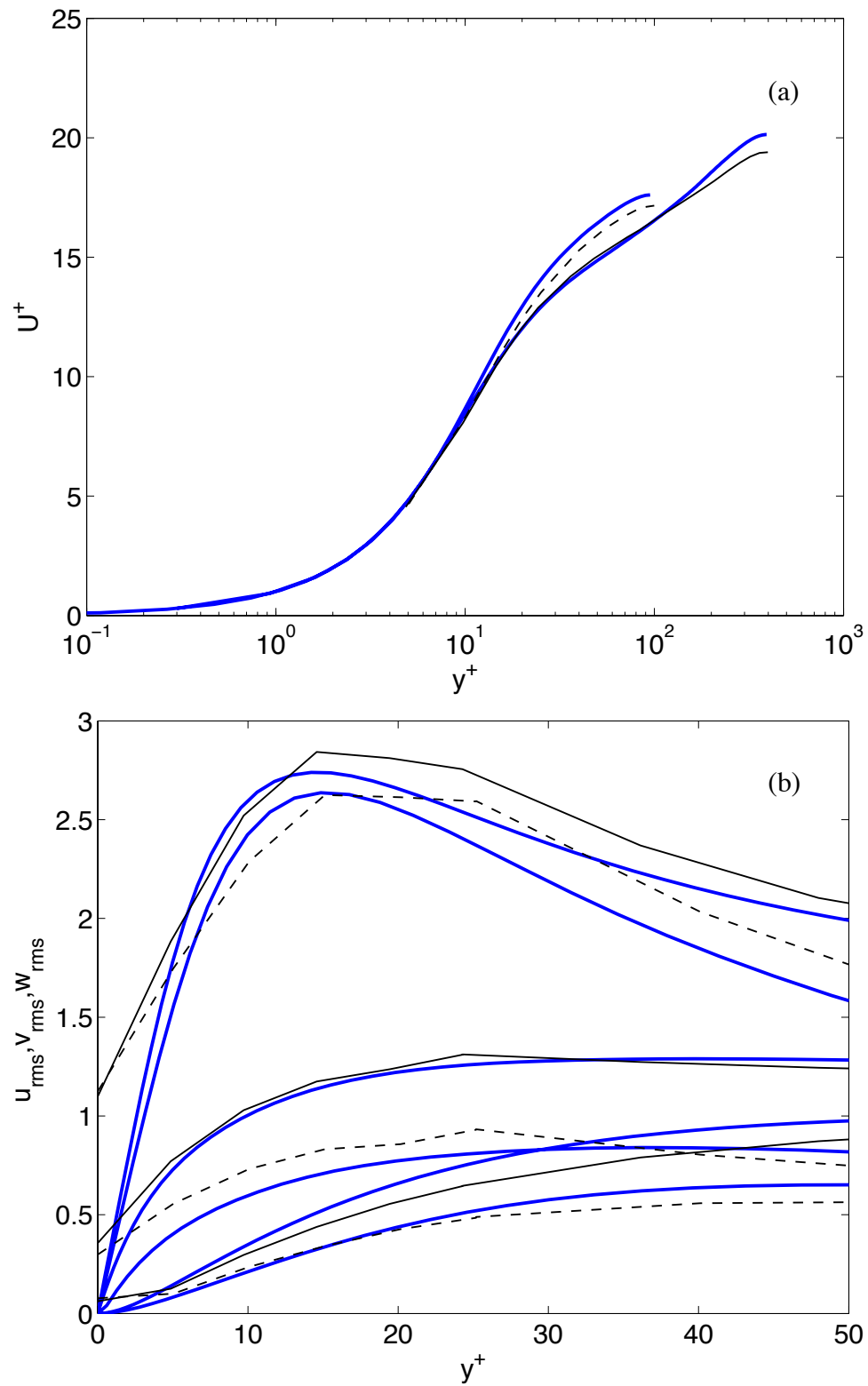


Figure 3.30: Meanflow and turbulence intensity profiles for $Re_\tau = 395$ and $Re_\tau = 100$ computed using a similar relative resolution: — DNS; — $p = 4$ at $Re_\tau = 395$; ---- $p = 4$ at $Re_\tau = 100$.

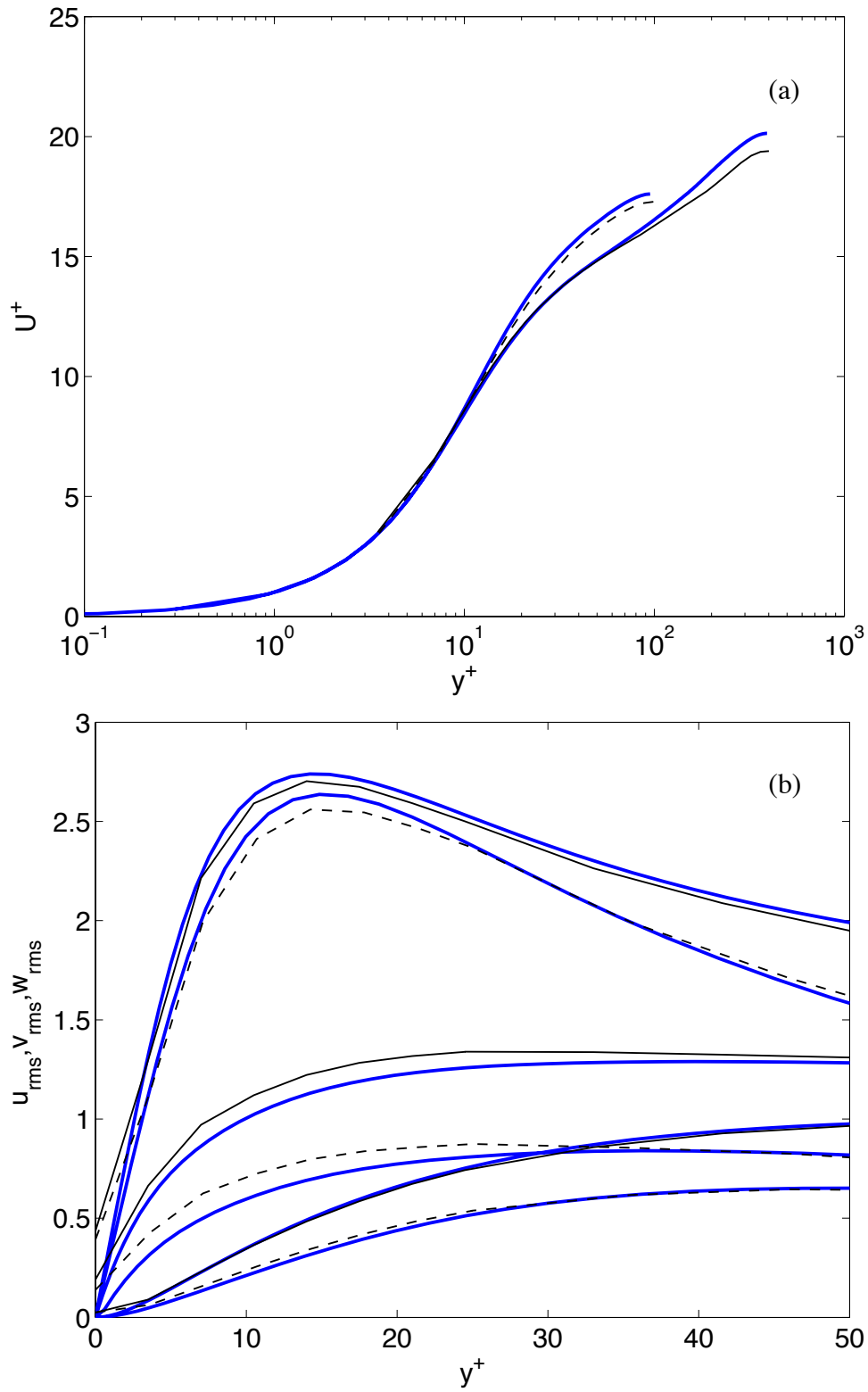


Figure 3.31: Meanflow and turbulence intensity profiles for $Re_\tau = 395$ and $Re_\tau = 100$ computed using a similar relative resolution: — DNS; — $p = \{6, 6, 5, 4, 4, 5, 6, 6\}$ at $Re_\tau = 395$; ---- $p = 6$ at $Re_\tau = 100$.

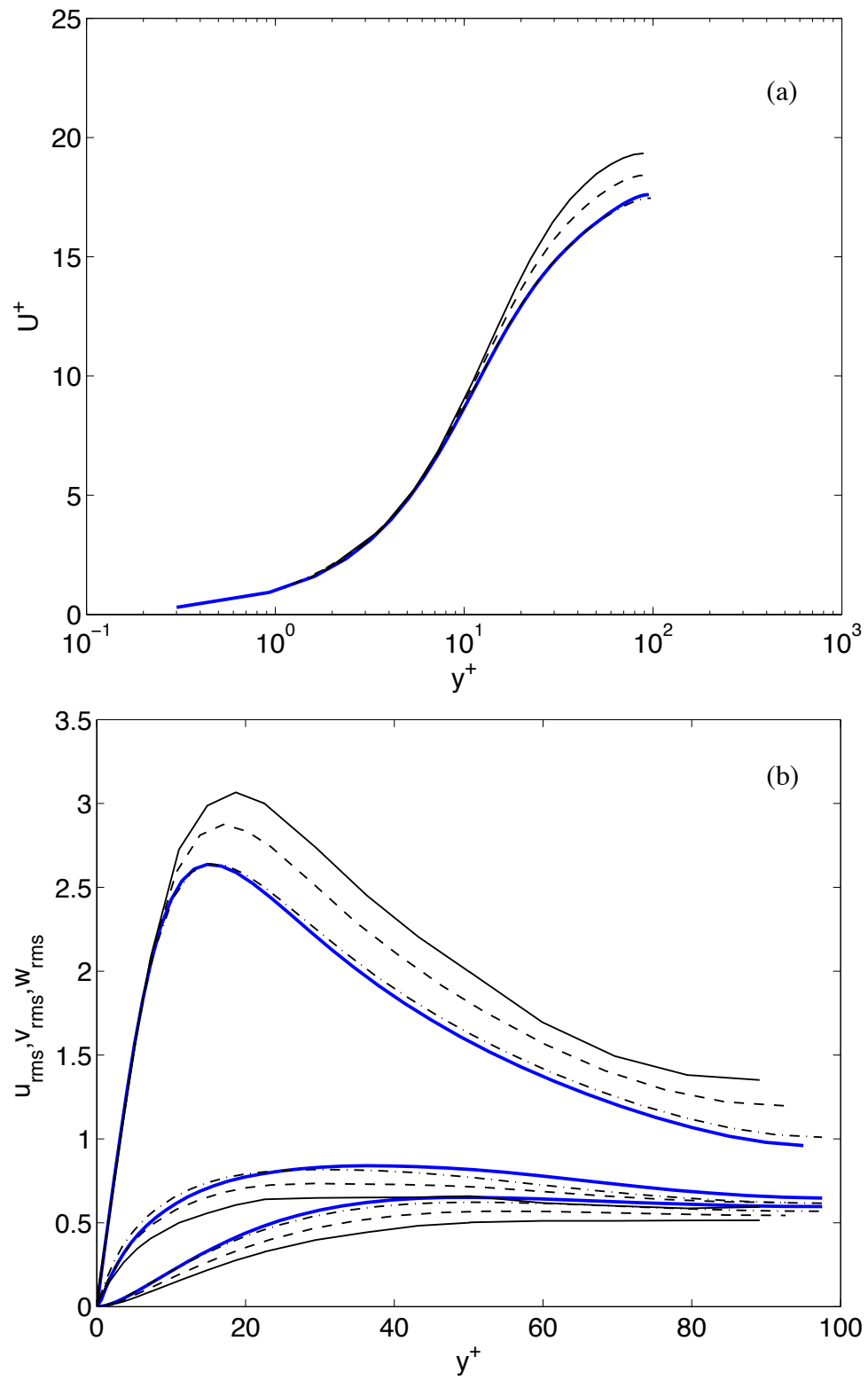


Figure 3.32: Meanflow and rms profiles for $Re_\tau = 100$ computed with a $4 \times 8 \times 8$ mesh using different polynomial orders: — DNS; — $p = 3$; ---- $p = 4$; -·-· $p = 6$.

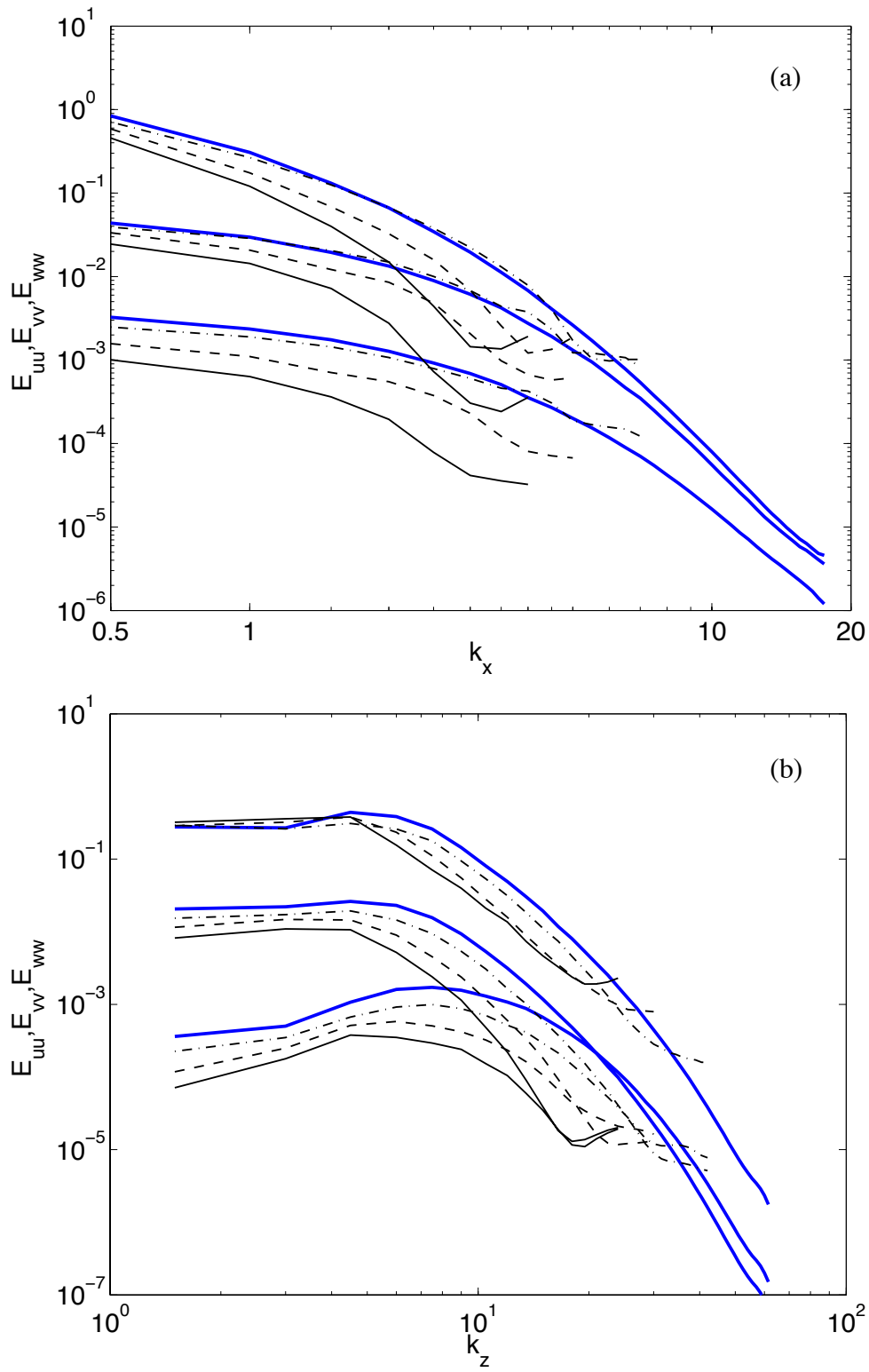


Figure 3.33: One-dimensional energy spectra in x - and z - directions for $Re_\tau = 100$ computed at $y^+ \approx 8$ with a $4 \times 8 \times 8$ mesh using different polynomial orders: — DNS; — $p = 3$; --- $p = 4$; -.- $p = 6$.

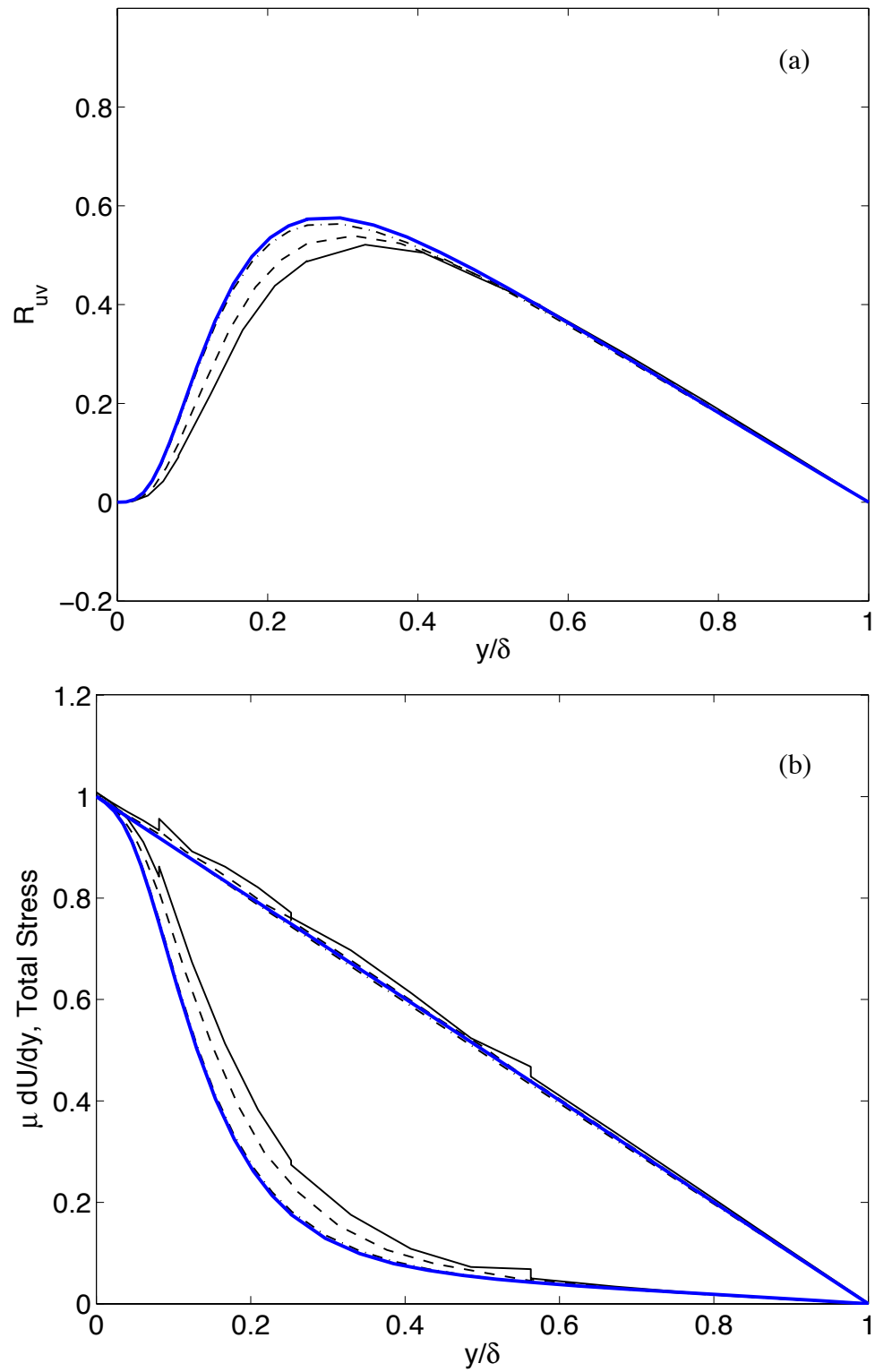


Figure 3.34: Reynolds, viscous and total stress profiles for $Re_\tau = 100$ computed with a $4 \times 8 \times 8$ mesh using different polynomial orders: — DNS; — $p = 3$; ---- $p = 4$; —·— $p = 6$.

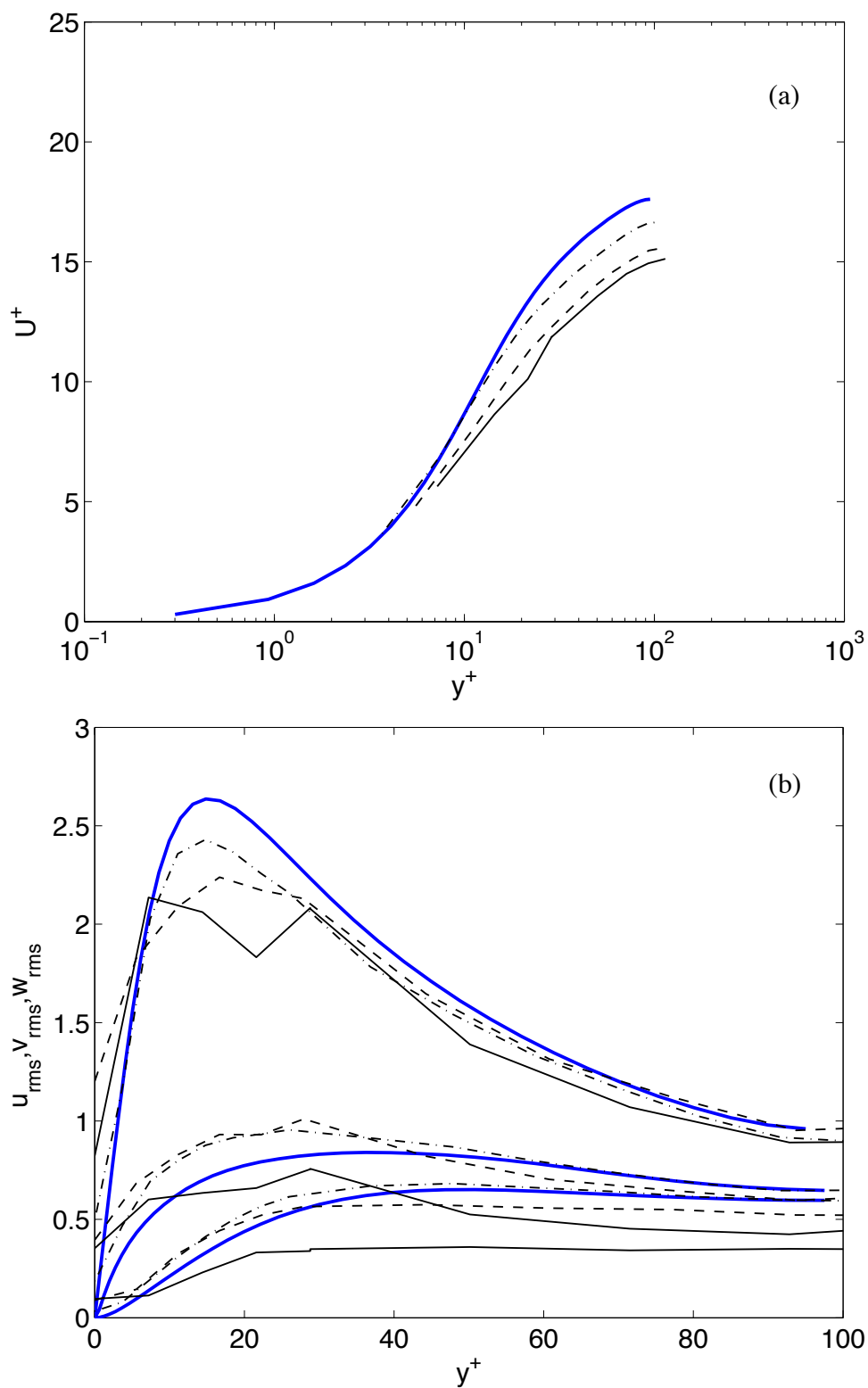


Figure 3.35: Meanflow and rms profiles for $Re_\tau = 100$ computed with a $8 \times 4 \times 8$ mesh using different polynomial orders: — DNS; — $p = 3$; ---- $p = 4$; -·- $p = 6$.

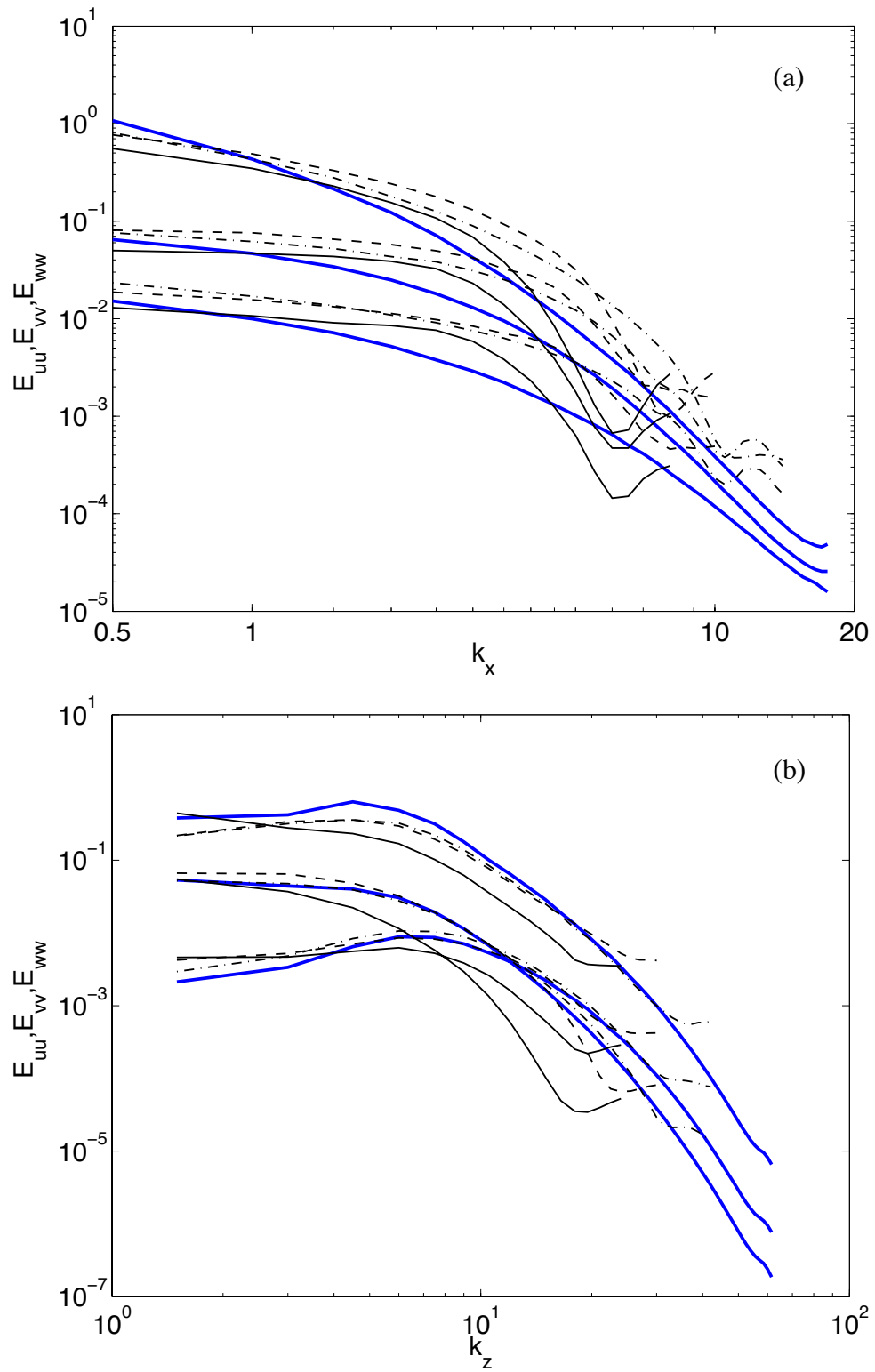


Figure 3.36: One-dimensional energy spectra in x - and z - directions for $Re_\tau = 100$ computed at $y^+ \approx 12$ with a $8 \times 4 \times 8$ mesh using different polynomial orders: — DNS; — $p = 3$; --- $p = 4$; -.- $p = 6$.

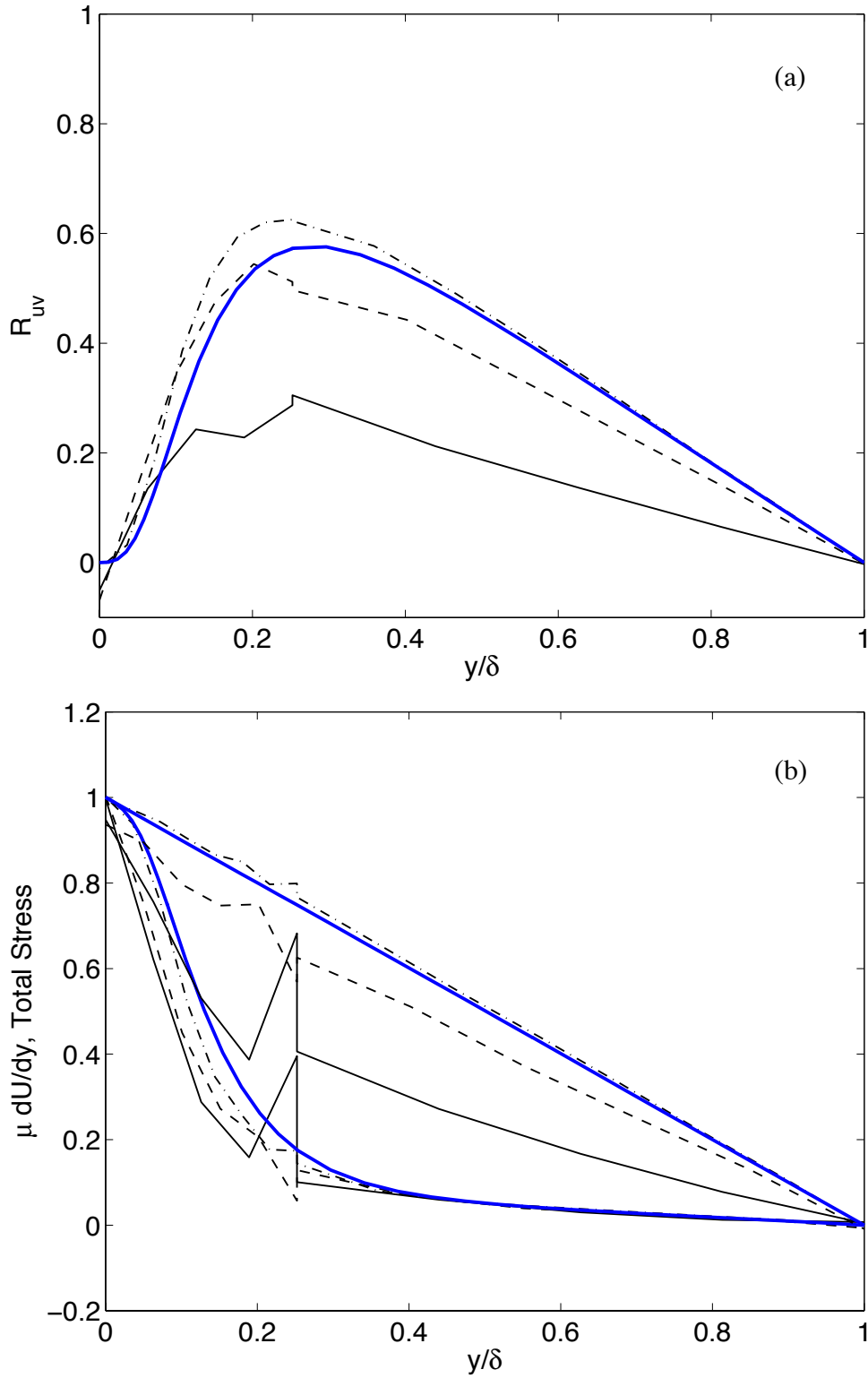


Figure 3.37: Reynolds, viscous and total stress profiles for $Re_\tau = 100$ computed with a $8 \times 4 \times 8$ mesh using different polynomial orders: — DNS; — $p = 3$; ---- $p = 4$; —·— $p = 6$.

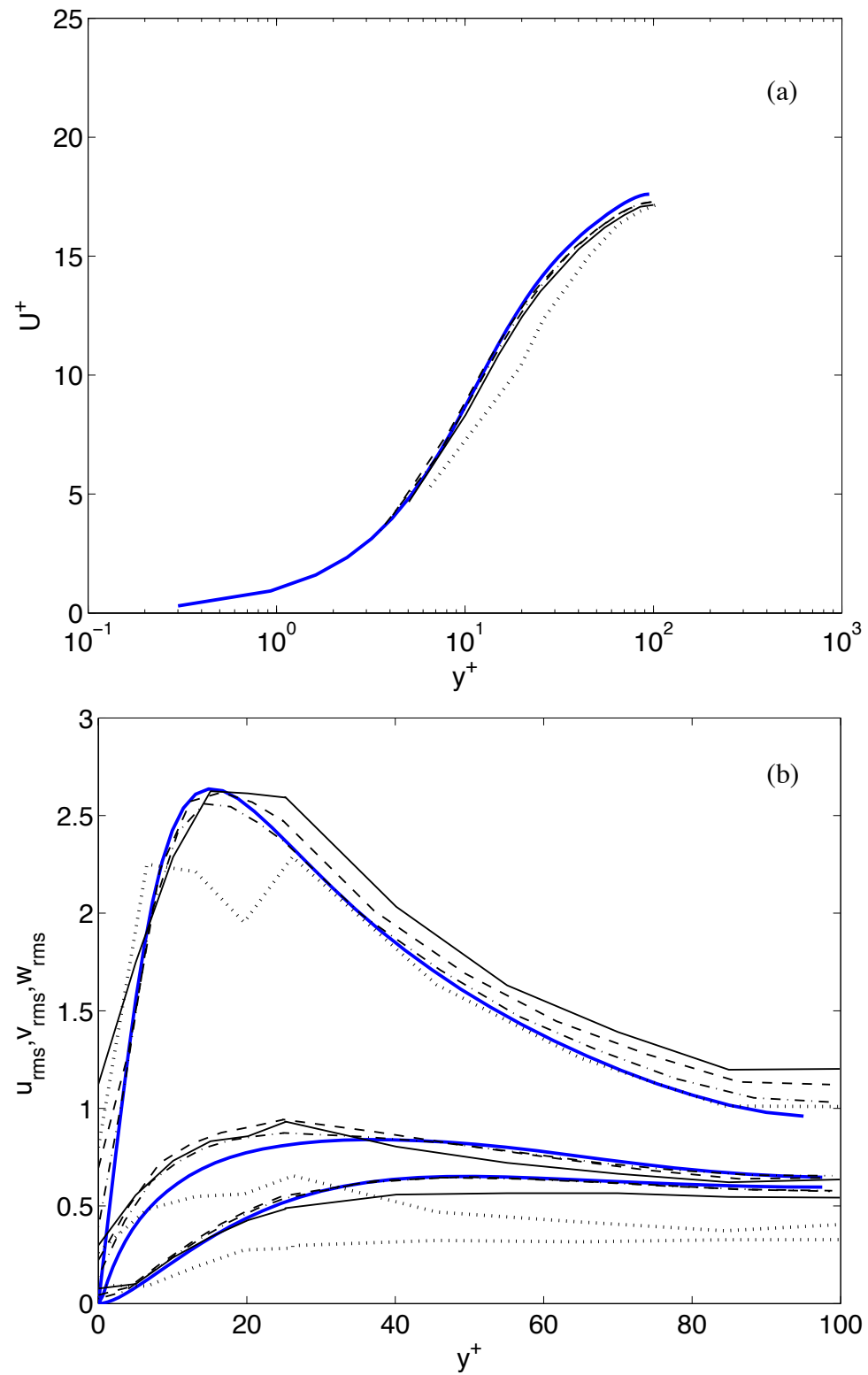


Figure 3.38: Meanflow and rms profiles for $Re_\tau = 100$ computed with a $4 \times 4 \times 8$ mesh using different polynomial orders: — DNS; $p = 3$; — $p = 4$; ---- $p = 5$; —·— $p = 6$.

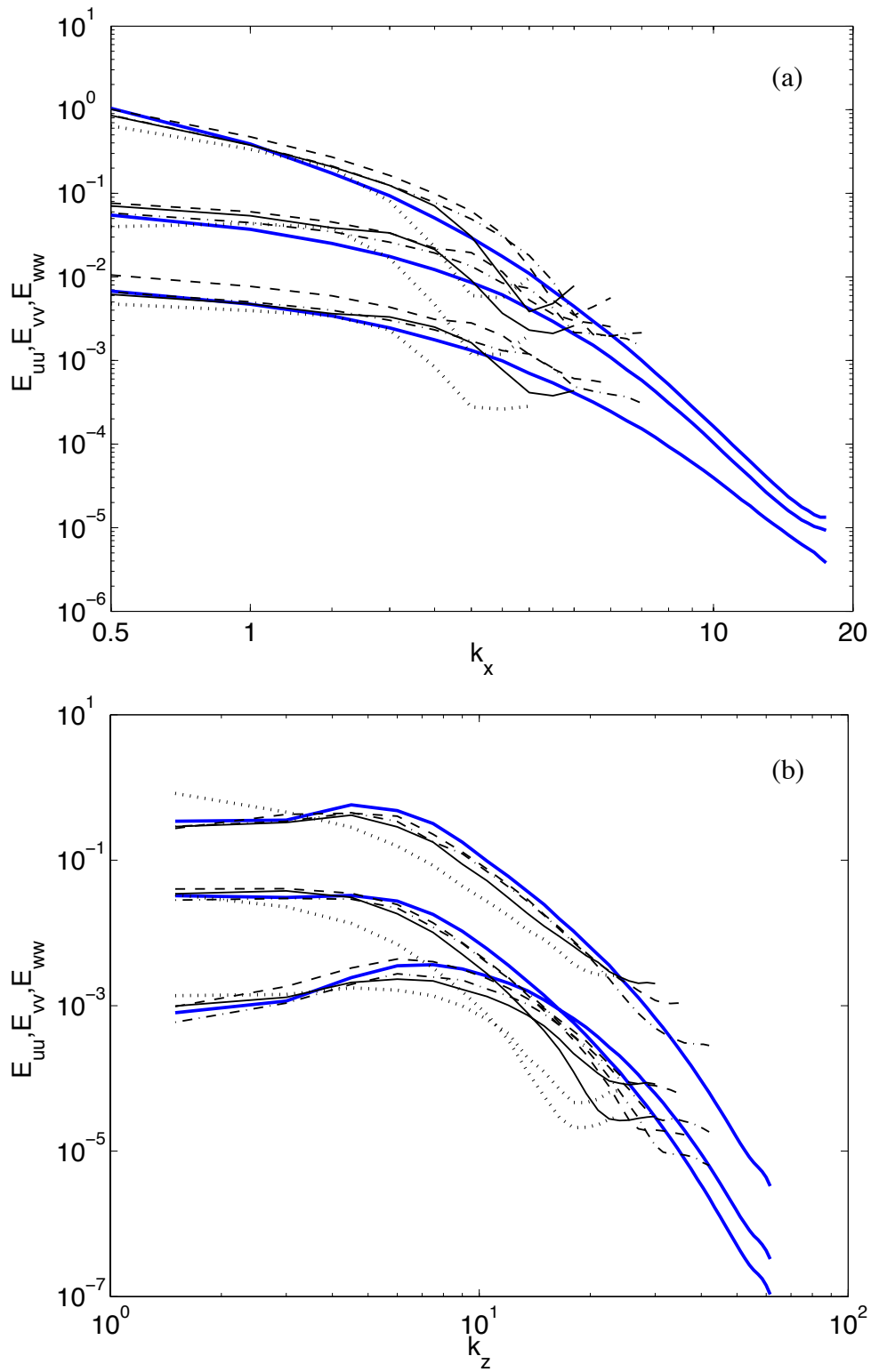


Figure 3.39: One-dimensional energy spectra in x - and z - directions for $Re_\tau = 100$ computed at $y^+ \approx 12$ for $Re_\tau = 100$ with a $4 \times 4 \times 8$ mesh using different polynomial orders: — DNS; $p = 3$; — $p = 4$; ---- $p = 5$; -.- $p = 6$.

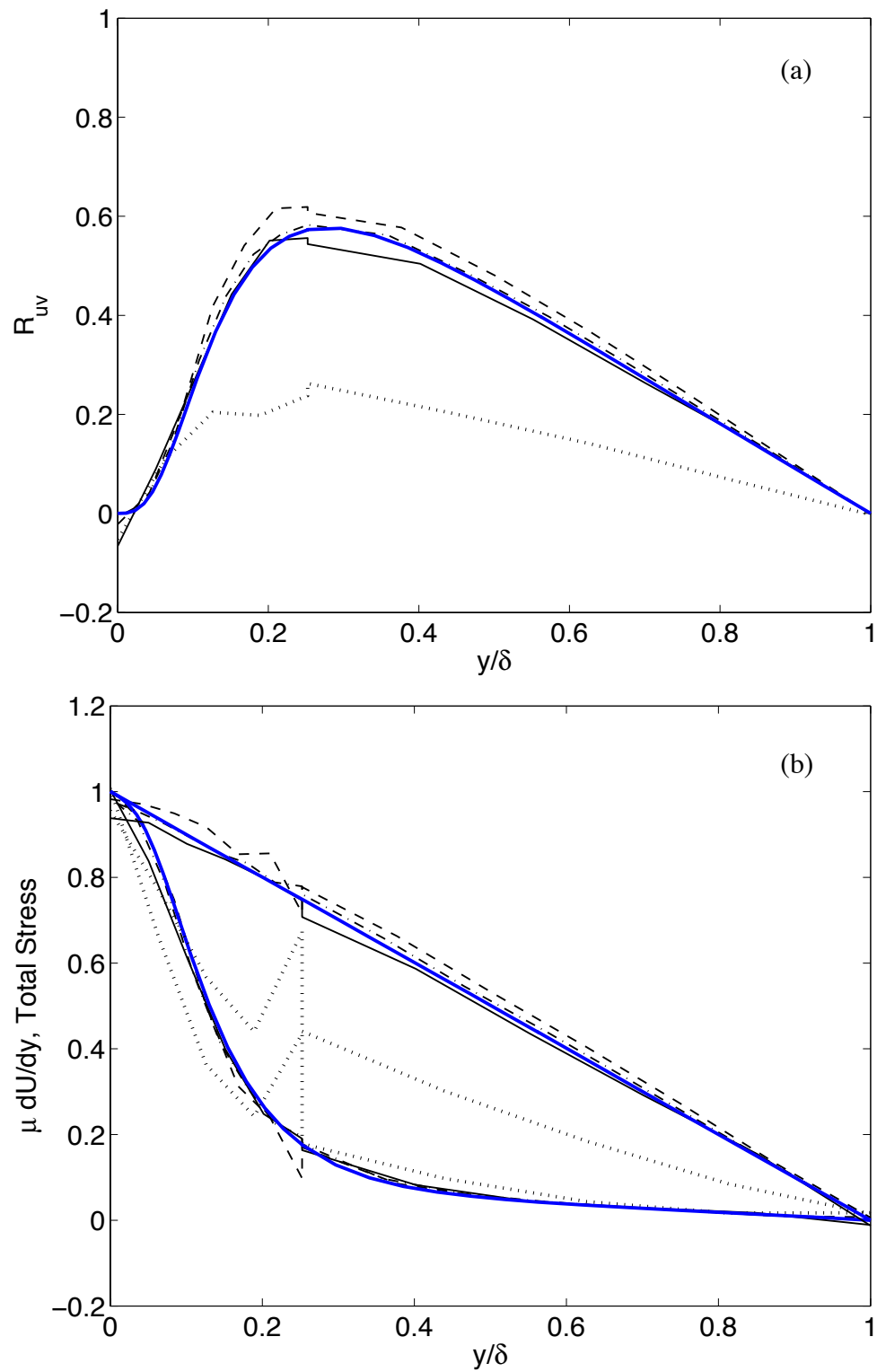


Figure 3.40: Reynolds, viscous and total stress profiles for $Re_\tau = 100$ computed with a $4 \times 4 \times 8$ mesh using different polynomial orders: — DNS; $p = 3$; — $p = 4$; ---- $p = 5$; —·— $p = 6$.

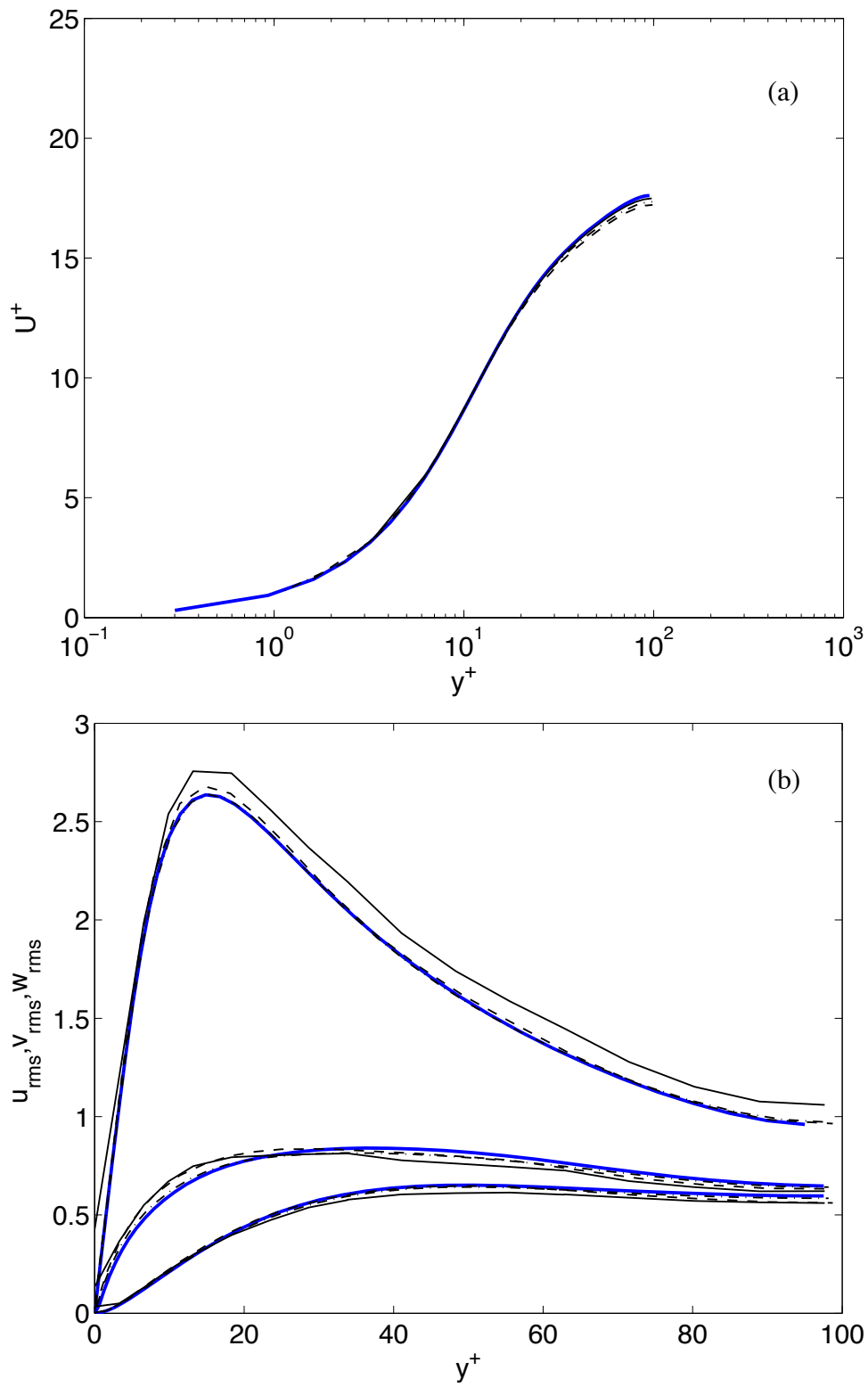


Figure 3.41: Meanflow and rms profiles for $Re_\tau = 100$ computed with a $8 \times 8 \times 8$ mesh using different polynomial orders: — DNS; — $p = 3$; ---- $p = 4$; —·— $p = 6$.

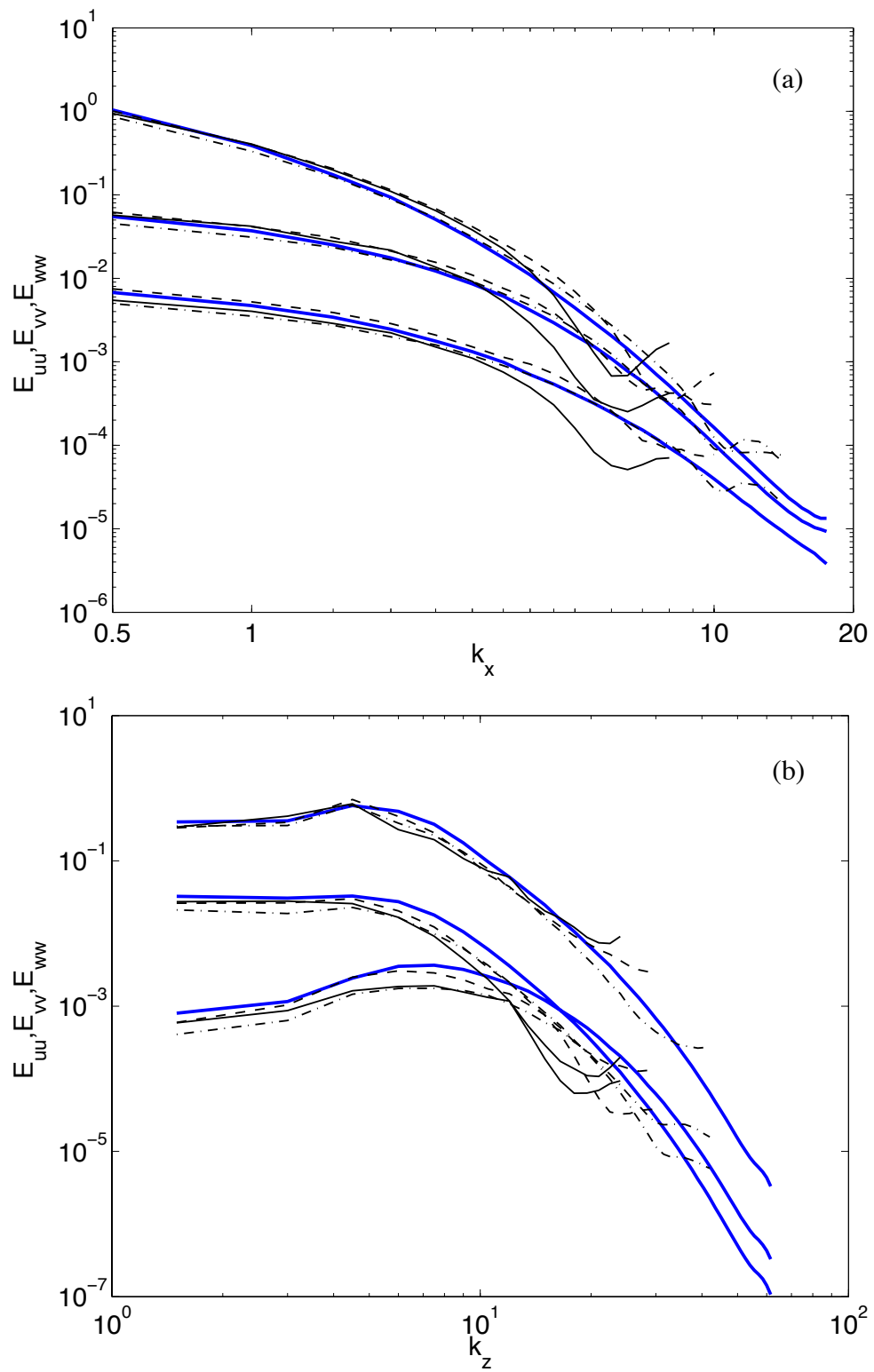


Figure 3.42: One-dimensional energy spectra in x - and z - directions for $Re_\tau = 100$ computed at $y^+ \approx 12$ with a $8 \times 8 \times 8$ mesh using different polynomial orders: — DNS; — $p = 3$; ---- $p = 4$; -.- $p = 6$.

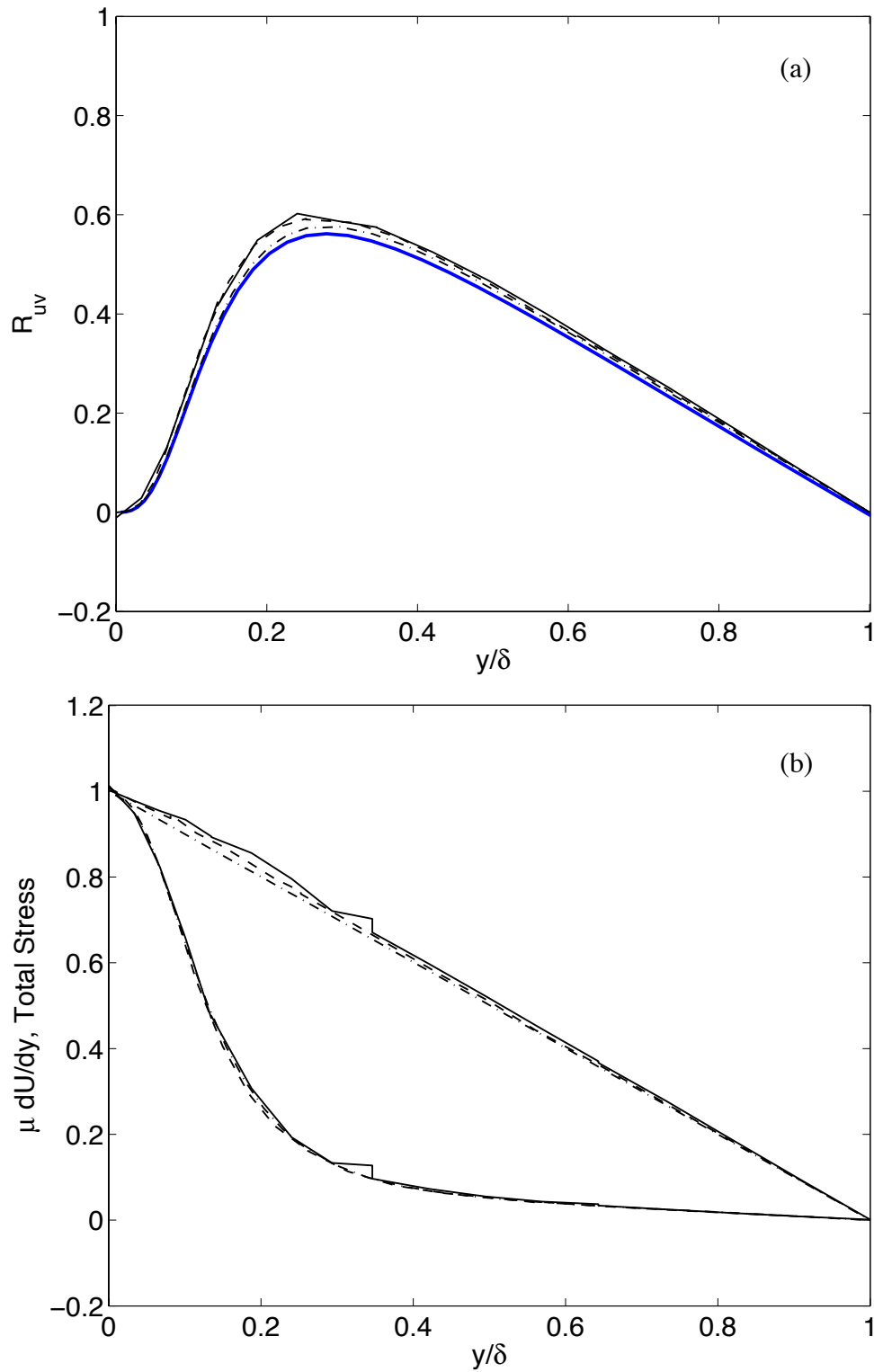


Figure 3.43: Reynolds, viscous and total stress profiles for $Re_\tau = 100$ computed with a $8 \times 8 \times 8$ mesh using different polynomial orders: — DNS; — $p = 3$; ---- $p = 4$; —·— $p = 6$.

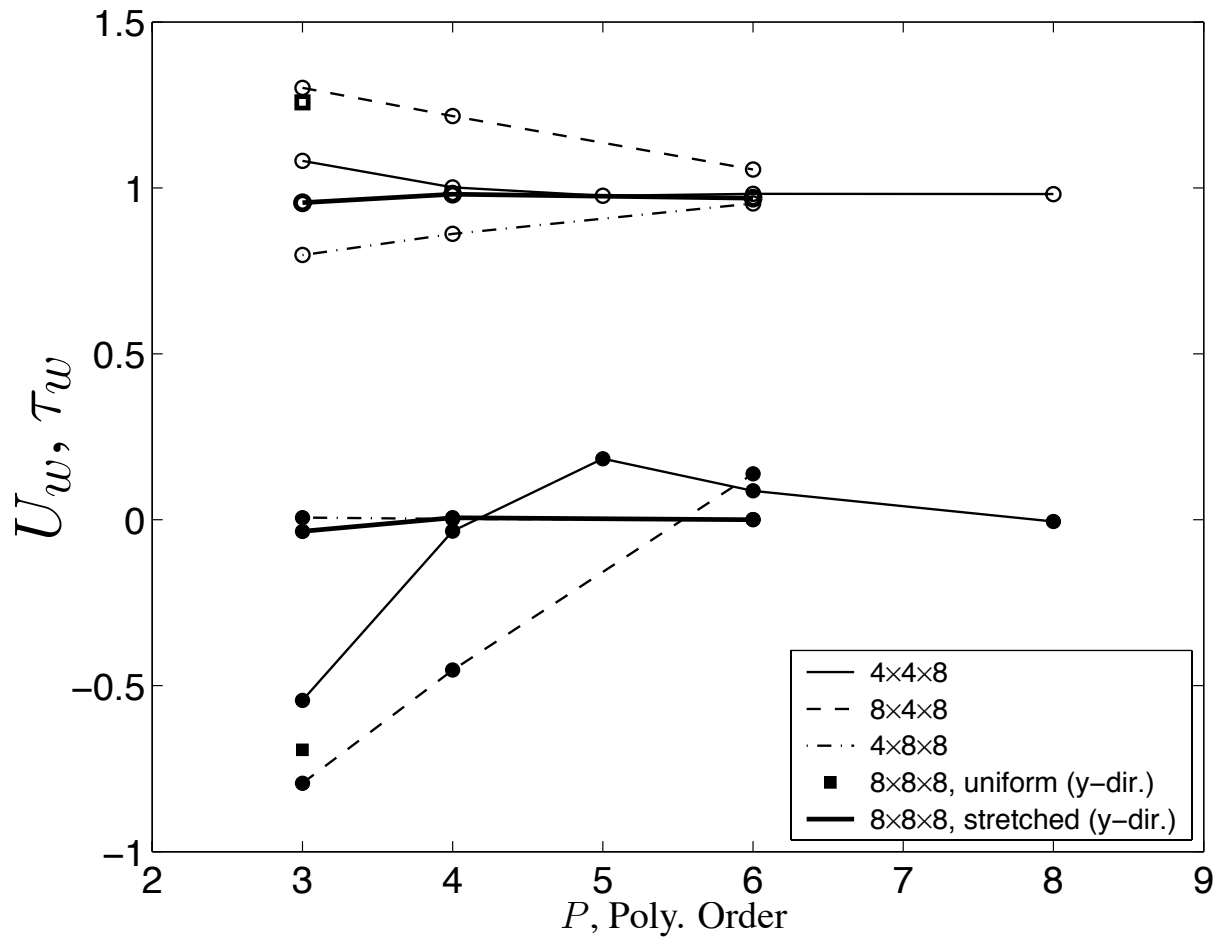


Figure 3.44: Wall shear stress and average streamwise velocity slip (at the wall) variation with polynomial orders for different meshes at $Re_\tau = 100$. The filled symbols (\bullet , \blacksquare) are planar averaged streamwise velocity slip at the channel walls (U_w , slip) while the open symbols (\circ , \square) are the time-averaged wall shear stress (τ_w).

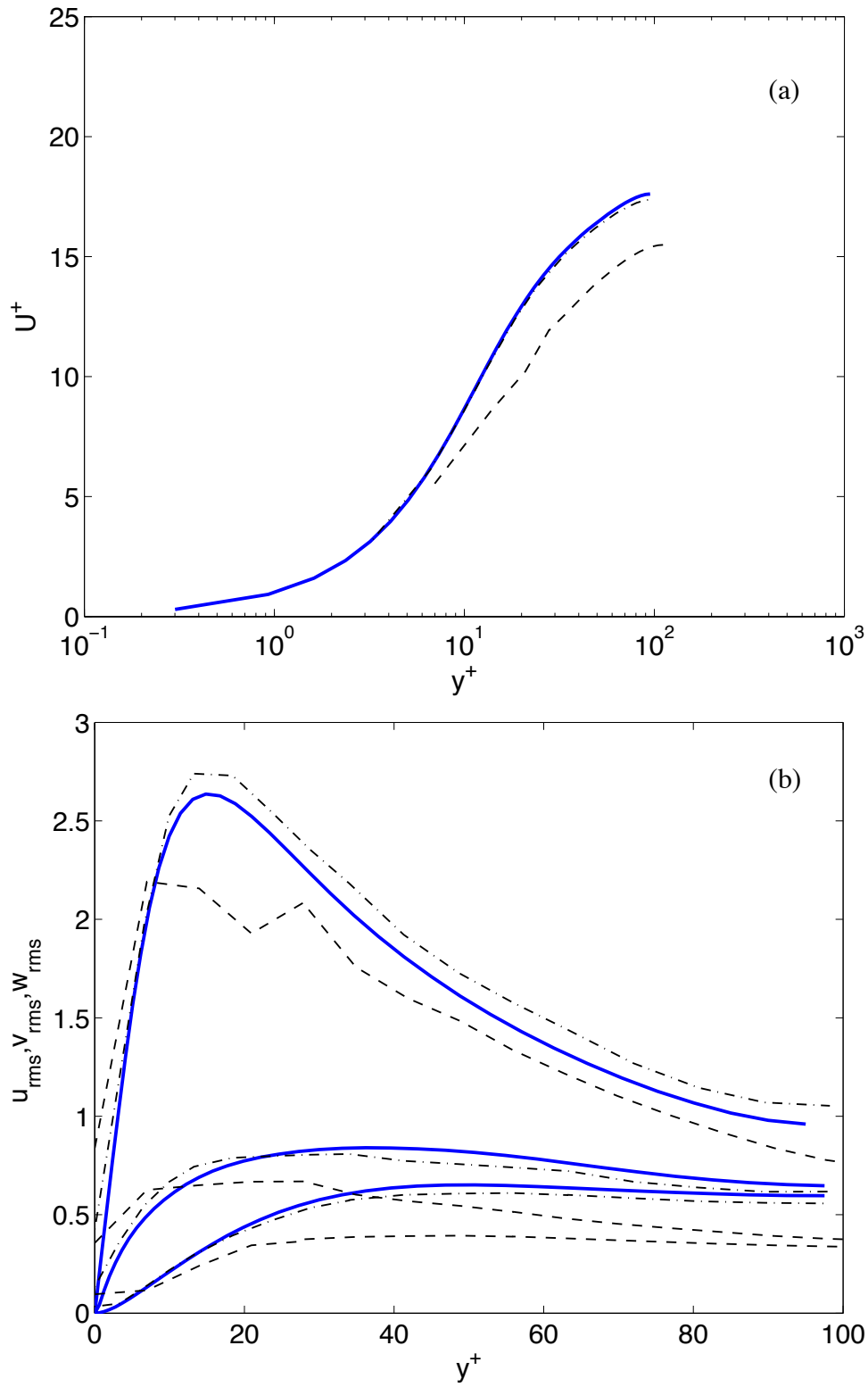


Figure 3.45: Meanflow and turbulence intensities profiles for $Re_\tau = 100$ computed using a $8 \times 8 \times 8$ mesh at $p = 3$ with local h -refinement in the wall-normal direction: — DNS; ---- Uniform; —·— Stretched with $c_s = 1.25$.

Chapter 4

Boundary Conditions Enforcement

The enforcement of wall boundary conditions weakly through numerical viscous fluxes is observed to allow the solution to jump at the channel walls (physical boundary interface). Also, we have noticed that the jumps in the solution at the element interfaces (the physical boundary included) are closely related to the local resolution. Specifically, as wall-normal direction resolution increases, the magnitude of these jumps is observed to decrease. Here, we pursue a computationally efficient means for regulating slip in lieu of resolution increase. In this chapter, we explore the use of a penalty that acts directly on these jumps through the numerical viscous flux.

First, we begin with the definitions of the the numerical viscous flux for this purpose. Later, we present numerical results to illustrate the effects of introducing penalties on the jumps at both the physical boundaries as well as interelement boundaries. As usual, we place particular emphasis on the jumps at the physical boundaries where the jumps are generally more prominent.

4.1 Numerical Viscous Fluxes Definitions

The Bassi–Rebay viscous flux allows the interface conditions to be imposed weakly i.e. allowing the jumps in the solution at interelement boundaries. Since *all* the interface conditions are enforced in this way, the Dirichlet conditions at the channel walls i.e. the no-slip condition is only satisfied in a weak sense. In Chapter 3, we have seen that using extremely coarse near-wall resolutions in the y –direction, with the current approach, can lead to a relatively large negative slip in the streamwise velocity at the wall. Recall that the direction of the flow in the channel is in the streamwise direction (in the positive direction). Therefore, a large negative value of the streamwise velocity (planar averaged) at the wall is an indication of a local reversal in the meanflow at the wall. This has the potential at even coarser resolutions (LES setting) to alter the near-wall dynamics that can adversely affect reliable prediction of turbulence statistics.

Therefore, we propose to modify the Bassi–Rebay numerical viscous flux (refer to

Eq. 2.9), to a form similar to the Local Discontinuous Galerkin [3, 20], that provides a means to control the magnitude of jumps at the interelement boundaries.

$$\hat{\mathbf{F}}_n^v(\mathbf{U}^-, \sigma_j^-, \mathbf{U}^+, \sigma_j^+) = \frac{1}{2} \left(\mathbf{F}_n^v(\mathbf{U}^-, \sigma_j^-) + \mathbf{F}_n^v(\mathbf{U}^+, \sigma_j^+) \right) + \epsilon (\mathbf{U}^+ - \mathbf{U}^-) \quad (4.1)$$

where $\epsilon > 0$ is a penalty factor. When the penalty factor is set to zero the Bassi-Rebay numerical viscous flux introduced earlier (see Eq. 2.9) is recovered. With the penalty parameter set to a large value, the solution is forced to satisfy the imposed wall-boundary conditions. In practice, while evaluating the numerical flux at the wall (refer Eq. 2.11) \mathbf{U}^+ corresponds to \mathbf{U}_{bc} . Thus, any deviation from the Dirichlet conditions is penalized using the above flux definition and the degree depends on the magnitude of the penalty. Further, we can use this flux to reduce the solution jumps at the interior interelement interfaces.

Now, the authors emphasize that even with slip at the channel walls, reasonable turbulence statistics can be obtained using DG (see Figure 3.44). Also, the weak enforcement of Dirichlet conditions mitigates the high resolution requirements in the wall-normal direction, permitting the use of rather large Δy_w^+ compared with traditional discretizations [14, 15]. Now, in general, a large negative slip in the streamwise velocity at the wall coincides with overprediction of the wall shear stress. In fact, we notice a trend towards a positive streamwise slip with an increase in resolution (this is also indicative of reasonable slip in the other velocity components at the wall). In order to counter the effects of negative slip, we modify the penalized Bassi-Rebay flux introduced above (refer to Eq. 4.1) for the streamwise momentum equation such that the u slip is constrained to be positive as

$$\hat{\mathbf{F}}_n^v(\mathbf{U}^-, \sigma_j^-, \mathbf{U}^+, \sigma_j^+) = \frac{1}{2} \left(\mathbf{F}_n^v(\mathbf{U}^-, \sigma_j^-) + \mathbf{F}_n^v(\mathbf{U}^+, \sigma_j^+) \right) + \Upsilon(\mathbf{U}^+, \mathbf{U}^-, \epsilon) \quad (4.2)$$

where

$$\Upsilon(\mathbf{U}^+, \mathbf{U}^-, \epsilon) = \begin{cases} 0, & \text{if } \mathbf{U}^- \geq 0 \\ \epsilon (\mathbf{U}^+ - \mathbf{U}^-), & \text{otherwise} \end{cases} \quad (4.3)$$

and $\epsilon > 0$ is a penalty factor as before. The above numerical viscous flux, devised to allow only positive jumps in the streamwise velocity at the wall, serves to illustrate the potential of the numerical viscous fluxes to act as a wall-model [73]. In fact, since part of the viscous sublayer is captured by the jump in the solution, we believe that the standard Bassi-Rebay flux (refer to Eq. 2.9) indeed is a wall-model, albeit a less effective one at $\Delta y_w^+ \geq 3$ viscous wall units. We hope to improve the capabilities, in this capacity, using the modifications

proposed above.

Currently, we introduce four major scenarios using the above definitions that we employ in our study.

1. Default to standard Bassi-Rebay (BR) that uses no penalty ($\epsilon = 0$)
2. Introduce a penalty in all the solution components at the wall boundaries that we term Boundary Local Discontinuous Galerkin (BLDG) method.
3. Introduce a penalty in all the solution components at the wall boundaries, except the streamwise momentum equation where we constrain the streamwise velocity to be positive that we term Streamwise-positive BLDG (SBLDG) method.
4. Introduce a penalty in all the solution components at *all* the interelement interfaces and physical boundaries that we term simply as LDG method.

Therefore, in terms of degree of penalization, the fluxes may be ranked in ascending order as BR, SBLDG, BLDG, and LDG, respectively. Also, for convenience, hereafter we drop the reference to flux, for example, BR should be interpreted/read as BR flux.

4.2 Numerical Results

Similar to the validation study (Chapter 3), for reasons of limited computational resources, we focus primarily on the results at $Re_\tau = 100$. However, we present some results at $Re_\tau = 180$ and $Re_\tau = 395$ to corroborate the observations at $Re_\tau = 100$. Note that in order to completely define the penalty based numerical viscous fluxes, we need to specify a value for the penalty factor ϵ . It is required that $\epsilon > 0$, we usually pick the value of $\epsilon \geq 1/h_w$, where h_w is the extent i.e. height of the element at the boundary in the wall-normal direction (y -direction).

4.2.1 Low Reynolds Number

We begin our study by revisiting the case with a $8 \times 4 \times 8$ mesh using $p = 3$ and introducing the modifications to the numerical viscous flux outlined above (refer to Equations 4.1 and 4.2). The simulation parameters along with resulting τ_w predictions can be seen in Table 4.1. Recall that while the planar resolution is sufficient to get reasonable low-order

statistics, as seen in the $8 \times 8 \times 8$ mesh using $p = 3$ in Figure 3.41, the particularly coarse wall-normal direction ($\Delta y_w^+ \approx 4.3$) resolution leads to poor τ_w predictions (refer to Table 3.2).

Similar to the resolution study in the previous chapter, we present the profiles of mean-flow, viscous stress, Reynolds stress, total stress, rms, and energy spectra. For the case under consideration, plots of these statistics can be seen in Figure 4.1, 4.2, and 4.3.

A comparison of the meanflow profiles obtained using BR, SBLDG-BR, SBLDG, and LDG, using $\epsilon = 100.0 > 1/h_w$, is shown in Figure 4.1(a). The value of the penalty factor is chosen to better illustrate the effects of introducing a penalty. Just to clarify, SBLDG-BR and SBLDG refer to cases where the components (at the channel walls) *except the streamwise momentum* employ BR and BLDG, respectively. Note the improvement in the meanflow profile compared with BR for all the penalty fluxes considered here. As we shall see later, BLDG produces results that are very similar to the LDG case.

In Table 4.1, note the large difference in the magnitude of the streamwise velocity slip between the SBLDG and LDG cases. By contrast, the meanflow profiles (see Figure 4.1(a)) for both the cases are remarkably similar and are in better agreement with the reference compared to the BR case. Now, the noticeable difference between SBLDG-BR and SBLDG indicates that slip in the other components at the wall (v and w) also play a major role in affecting drag predictions. Now, the similar results obtained with SBLDG and LDG (BLDG) further reinforces the importance of regulating slip in the other momentum components (v and w) for reasonable τ_w predictions. Additionally, it suggests that penalizing just the negative component of the streamwise slip at the solid walls is sufficient.

Moreover, we also note that the wall shear stress predictions for BLDG and LDG are slightly higher than the SBLDG case (refer to Table 4.1). Importantly, using penalty fluxes represents a computationally efficient manner, as opposed to increasing the local resolution, to obtain reasonable low-order statistics at coarse resolutions that can be exploited in the context of LES. Furthermore, this provides a consistent approach through the use of a numerical viscous flux to better represent the dynamics of the near-wall region using coarse resolutions in the wall-normal direction. Essentially, this is the function of a wall-model [73], thus revealing the potential of the numerical viscous flux to serve in this capacity.

An examination of the viscous stress profile, shown in Figure 4.1(b), reveals a noticeable trend. For this plot, we use the $8 \times 8 \times 8$ stretched mesh using $p = 6$ with BR as

reference that better resolves the viscous wall region. Firstly, the introduction of penalization has an overall desirable effect on the viscous stress profiles, seen in Figure 4.1(b), and the extent is related to the degree of the penalization. This is seen in the significant difference between the SBLDG-BR and SBLDG case. Further, the similarity of the LDG case and SBLDG highlights the importance of the regulating solution jump at the solid walls for more reasonable turbulence statistics. To be more explicit, at this resolution, the jumps at the channel walls appear to more significant than the jumps in the interior region of the channel. At this point, we again note that the shear stress prediction for the LDG case is slightly higher than that obtained using SBLDG (We comment on these differences towards the end of this chapter). Also, we note an improved total stress profile for the SBLDG and LDG compared with SBLDG-BR and BR cases (see Figure 4.1). As we shall see, this is due in large part to a betterment in the Reynolds stress profile.

There is also a noticeable improvement in the rms and Reynolds stress profiles, shown in Figure 4.2, with the introduction of the penalty fluxes. Note the efficacy of the penalty fluxes in reducing the slip at the wall (seen clearly for the streamwise component of the LDG case in Figure 4.2(b)). However, away from the wall all the penalty fluxes produce turbulence intensities that are very similar. And while both SBLDG and SBLDG-BR show a closer correspondence with the reference [14] than BR, the agreement of SBLDG is particularly good. This suggests that the correlation between the streamwise velocity and wall-normal velocity benefits from the penalization of the jump in the wall-normal component of velocity at the wall. This further supports the view that slip in *all* the components of momentum *at the wall* play an active role in affecting the solution. In fact, it is the combination of allowing the slip to be positive in the streamwise direction and penalizing any slip in the other components that may allow for the most accurate shear stress prediction. And, the slight increase in the shear stress predictions for BLDG and LDG may be a direct result of penalizing the positive slip in the streamwise direction. BLDG and LDG likely constrain the solution at the wall more than the SBLDG approach.

Now, the improvement seen with SBLDG, BLDG, and LDG are not surprising since slip at the wall have particular interpretations. Slip in the wall-normal component is akin to introducing suction and blowing at the wall. Turbulence control studies in the channel that introduce suction and blowing at the wall have been known to significantly affect the drag at the wall [15, 17, 40, 75]. Likewise, slip in the spanwise direction can be interpreted as an imposed wall motion that is also known to affect the drag predictions in the channel [52]. It

is likely that the introduction of a penalty on the solution jump at the wall minimizes these effects and thereby leads to improved drag predictions. Moreover, since an increase in resolution leads to smaller jumps in the solution, the adverse effects associated with large magnitudes of solution jumps are minimized with reasonable Δy_w^+ . Therefore, at these resolutions, wall boundary conditions enforcement through BR likely suffice for reliable τ_w predictions (see Chapter 3).

Next, the energy spectra in the streamwise and spanwise directions can be seen in Figure 4.3. Notice a clear trend towards a decreasing energy content in the medium to high resolved wavenumbers as the degree of penalization is increased from BR to LDG in the streamwise component of the streamwise energy spectra. The near-wall dynamics are likely improved through the corrective mechanism introduced to suitably regulate the slip at the channel walls based on the physics in the flow. Further, the large scale coherent structures i.e. low wavenumber scales are known to be affected by the geometry (see Figure 1.1). Since the information regarding the geometry is communicated through the boundary conditions, a better enforcement of the wall boundary conditions using large Δy_w^+ has a desirable effect on the dynamically important scales [5, 43, 55, 85]. It is also possible that penalization may introduce some dissipation in the scheme [19]. In any event, this potentially leads to a more reasonable cascade [36, 43, 74, 87] of energy from the large to small scales. Evidence to support this view is found in the improvement seen for the streamwise component of the streamwise energy spectra shown in Figure 4.3(a).

Overall, the introduction of the penalty fluxes partially accounts for the low resolution in the wall-normal direction. However, the spectra, though improved, still exhibit signs of low planar resolution, namely, the combined effects of SGS and aliasing errors (see Figure 4.3). As a result, the wall shear stress is still overpredicted, however to a lesser degree compared with the BR case. Here, a SGS scale model that enhances dissipation in the resolved scales and/or a mechanism (such as filtering or dealiasing) for removing the excess energy from these scales is likely needed to further improve the solution.

In order to reinforce the influence of the jumps at the wall in determining the quality of the solution, we directly compare the LDG results shown above with a BLDG using the same parameters (see Table 4.1). The similarity of the results, seen in Figures 4.4, 4.5, and 4.6 serves to justify our focus on the wall-boundary conditions enforcement in improving wall shear stress predictions and thereby leading to better overall solution quality using the current planar resolution.

As a continuation of the discussion in the previous chapter on the role of the discretization on turbulence statistics, we repeat the study presented above, but now using the $4 \times 4 \times 8$ mesh with $p = 3$ (refer to Table 4.2). Recall that we argued that a mixture of low planar resolution and low resolution in the wall-normal direction using BR leads to remarkably “accurate” predictions using this mesh (at $p \geq 4$) through comparison with results obtained other mesh topologies ($4 \times 8 \times 8$, $8 \times 4 \times 8$, and $8 \times 8 \times 8$).

The meanflow and viscous stress profiles using BR, SBLDG, BLDG, and LDG for this mesh is shown in Figure 4.7. Note the similarity of the meanflow predictions with the penalty fluxes, seen in Figure 4.7(a) with that obtained for the $4 \times 8 \times 8$ mesh using $p = 3$ (see Figure 3.3). As a result of minimizing the impact of excessive slip on the wall shear stress prediction, the dissipative influence of low planar (streamwise) resolution, on the solution is revealed. These observations lend further credence to the validation study conducted earlier (see Chapter 3) while simultaneously suggesting the effectiveness of the penalty approach in minimizing overprediction in τ_w arising from the use of coarse resolutions (Δy_w^+) in the wall-normal direction.

As observed earlier with the $8 \times 4 \times 8$ mesh using $p = 3$, the Reynolds stress and rms profiles, seen in Figure 4.7(b), are conspicuously in better agreement with DNS [14] than the BR. Similar to the meanflow, the u_{rms} profile obtained resembles the profile obtained using the $4 \times 8 \times 8$ mesh with $p = 3$ (see Figure 3.3(b)). Meanwhile, the spanwise component is similar to the $8 \times 4 \times 8$ results obtained earlier (see Figure 4.2(b)). The peak in the spanwise turbulence intensity in the near-wall region common to both the $4 \times 4 \times 8$ and $8 \times 4 \times 8$ may be attributed to low resolution in the wall-normal direction. And finally, the energy spectra show trends that are consistent with those observed for the $8 \times 4 \times 8$ mesh using $p = 3$ with the introduction of jump penalty. These results indicate that while the penalty provides a means to compensate for low resolution in the wall-normal direction, appropriate selection of planar resolution is required to obtain good low-order statistics.

Again, we draw attention to the similarity of the results using the penalty approach (SBLDG, BLDG, and LDG) that reveal the importance of managing solution jump *at the solid walls* in improving turbulence statistics for the resolutions considered thus far. Also, we make a note of the increase in the wall shear stress predictions for the BLDG and LDG compared with SBLDG (refer to Table 4.2). This trend suggests that penalizing *all* slip in the streamwise direction tends to increase wall shear stress predictions. This trend is consistent with those observed in other discretizations that strictly enforce wall boundary

conditions while using low wall-normal resolution [15]. These results suggest a potential advantage of SBLDG over BLDG and LDG.

We intend to provide a detailed discussion of this issue immediately following the numerical results at higher Reynolds numbers. There, we relate the observations of this study with results obtained using a model advection diffusion problem where the effects of penalty have a more direction interpretation. Now, Figures 4.10, 4.11, and 4.12 serve to further illustrate the role of slip in v and w , respectively, in increasing τ_w predictions for the $4 \times 4 \times 8$ mesh consistent with prior observations using the $8 \times 4 \times 8$ mesh. Simultaneously, the results demonstrate the efficacy of the penalty fluxes to counter this effect.

Let us now study the effects of introducing the penalty approach at a relatively higher resolution. For this purpose, we use the same $4 \times 4 \times 8$ mesh but with a higher polynomial order, $p = 6$, where the obvious effects of low resolution are minimized. The results obtained using BR, SBLDG-BR, BLDG, and LDG are shown in Figures 4.13, 4.14, and 4.15. The results are also summarized in Table 4.3. Note that we use a smaller value (jumps in the solution are smaller) for the penalty factor, $\epsilon = 10.0 > 1/h_w$ in this study.

Plots of the meanflow and rms profiles in Figure 4.13 are all in good agreement both with each other and the reference DNS [14]. The energy spectra, shown in Figure 4.14, for each individual case is virtually indistinguishable and in much better agreement with the reference [14], compared with the $p = 3$ case using the same mesh (see Figure 4.9). This is especially true for the spanwise direction energy spectra where we use 8 elements (see Figure 4.14(b)).

The Reynolds stress profiles, shown in Figure 4.15(a), similar to the energy spectra are again virtually indistinguishable except for the SBLDG-BR case that has a slightly higher peak value in the correlation compared with the reference DNS [14]. This suggests that the effect of the jump in the unpenalized wall-normal velocity at the wall still exerts a significant influence on the Reynolds stress estimates. Although, this is a higher resolution compared to the $p = 3$ case with the same mesh, the resulting $\Delta y_w^+ \approx 1.6$ is still fairly large. It is likely that BR permits a natural interaction between the fluctuating streamwise and wall-normal components of slip that is effective in simulating the influence of the wall for obtaining a reasonable Reynolds stress profile. Meanwhile, by introducing a penalty through SBLDG-BR, we introduce a bias that may not be appropriate at this resolution. Meanwhile, the remaining two cases show better profiles since all the components are penalized equally at the solid walls.

Finally, the viscous stress profiles, shown in Figure 4.15(b), for all the cases are in reasonable agreement with the reference DG solution at a higher resolution. Thus, the total stress profiles, also shown in the same plot, for all the cases are in good agreement with the reference except SBLDG-BR. This difference may be attributed to the difference in the Reynolds stress profiles compared to the remaining cases. Overall, the negligible differences in the solution with the introduction of penalty suggests that the utility of jump regulation at higher resolutions may be limited.

4.2.2 Moderate Reynolds Number

Before we provide a detailed discussion of the significance of the results obtained using the penalty fluxes, we present results at $Re_\tau = 180$ and 395 using the SBLDG flux that illustrates the effectiveness of this approach at higher Reynolds numbers.

First, let us consider the case at $Re_\tau = 180$ case with a $16 \times 4 \times 16$ mesh using a polynomial distribution in the wall-normal direction as $p = \{6, 5, 5, 6\}$ (refer to Table 4.4). The resulting resolution is $\Delta x^+ \approx 141$ and $\Delta z^+ \approx 47$ in the streamwise and spanwise directions, respectively. Meanwhile, the minimum resolution in the wall-normal direction based on the collocation grid $\Delta y_w^+ \approx 2.9$ ($\Delta y_m^+ \approx 45$). Thus, the first interelement interface in the wall-normal direction is at a $y^+ \approx 45$ implying the next element spanning the remainder of the channel half height is approximately 145 viscous wall units high. However, the planar resolution in both the streamwise and spanwise directions are chosen to be sufficiently high to minimize the effects of aliasing.

We include the $16 \times 16 \times 16$ mesh using $p = 4$ (refer to Table 3.6) from the validation study in Chapter 3 for comparison. Again, we use a penalty factor, $\epsilon = 100.0 > 1/h_w$ that is shown to be effective for $Re_\tau = 100$ at similar Δy_w^+ values. Unfortunately, we do not have a BR case for direct comparison, however, the relative resolution in the planes of the current mesh is similar to the $8 \times 4 \times 8$ using $p = 6$ at $Re_\tau = 100$ (see Table 3.2 and Figures 3.35, 3.36, and 3.37). Importantly, recall that the $Re_\tau = 100$ case leads to significant overprediction in τ_w in spite of using a higher resolution in the wall-normal direction compared to the current $Re_\tau = 180$ case.

A plot of the meanflow profile using SBLDG, seen in Figure 4.16(a), is in excellent agreement with both the reference DNS [69] and the DG reference solution. And, while the near-wall turbulence intensities are poorly predicted due to an extremely coarse wall-normal resolution, as seen before at $Re_\tau = 100$, the agreement in the core of the channel is

good. Although, we are using a lower polynomial order in the outer layer, namely $p = 5$, the relative resolution for this particular region of the flow is likely better than the near-wall region that results in a more reasonable agreement of the rms profiles ($y^+ > 50$) with the DNS [69]. This hints at the potential of local hp -refinement for suitable distribution of the required degrees of freedom to ensure efficiency.

Meanwhile, the streamwise direction energy spectra compared with the DG solution using $p = 4$ are generally in good agreement, at least in the lower wavenumbers. As before, the high resolution in the spanwise direction ensures good agreement between the spanwise energy spectra for both DG solutions. The Reynolds stress profile for the SBLDG case is reasonable compared with the DG reference that uses a higher resolution in the wall-normal direction and is indistinguishable from the reference [69]. The viscous stress profile, seen in Figure 4.18(b), is in good correspondence overall with the reference DG solution. The total stress, on the same plot, produces a profile that reflects the overprediction in the Reynolds stress (see Figures 4.18(a) and 4.18(b)).

Let us now consider a case at $Re_\tau = 395$ with a $8 \times 8 \times 12$ mesh using $p = 4$. The current domain size, smaller than the reference DNS [69], is $(\pi, 2.0, \pi/2)$ in the usual notation. This gives a resolution similar to the resolution for $8 \times 4 \times 8$ using $p = 4$ at $Re_\tau = 100$ ($\Delta x^+ \approx 155$, $\Delta z^+ \approx 51$ and $\Delta y_w^+ \approx 2.8(\Delta y_m^+ \approx 25)$). Here, we present a comparison of the results obtained with SBLDG and LDG using a $\epsilon = 1.0 \leq 1/h_w$ (this is a departure from the earlier cases that have always used $\epsilon \geq 1/h_w$). Notice the similar value of the *planar averaged* slip at the wall (refer to Table 4.5). First, the absolute values are modest, but negative in this planar averaged sense since the penalty factor was chosen to be small. Remarkably, both fluxes share the same nature of slip – negative. The value of slip for SBLDG is less than LDG since it is biased towards reducing negative slip in the streamwise direction.

Given this information, we expect the results for these two cases to be similar. Comparison plots of the profiles of meanflow and rms are compared with reference DNS [69] are shown in Figure 4.19. First, the overall agreement with the reference is good for both cases and importantly with each other. This is reasonable in light of the similar values of slip at the channel walls. Still, the value of τ_w is greater for the LDG, consistent with prior observations. Next, the rms profiles are both in reasonable agreement with the reference. Note, the difference in the wall value of the streamwise turbulence intensity. This is again a reflection of the bias towards penalizing negative slip for SBLDG.

Meanwhile, the energy spectra, seen in Figure 4.20, are virtually indistinguishable from one another with expected effects of due to the absence of the viscous dissipation scales. Now, unlike the previous statistics, the Reynolds stress profiles for the LDG are clearly in better agreement with the reference DNS [69] than the SBLDG case. Meanwhile, the viscous stress profiles, for both cases, are in reasonable agreement with the higher resolution DG solution (note the jump in the viscous stress profile at the first interelement interface even at this high resolution (see Table 3.7)). However, the jump at the element interface is less for the LDG compared with the SBLDG. We expect a difference here since the LDG has an active penalty influence here. Now, let us consider this in the context of the total stress profile that is plotted in Figure 4.22. Immediately, we clearly see that total stress for LDG is in much better agreement with the higher resolution DG solution than SBLDG. In fact, further away from the wall it is indistinguishable from the reference using $p = \{6, 6, 5, 4, 4, 5, 6, 6\}$ where it shares the same local resolution. By contrast, the SBLDG underpredicts the total stress throughout the channel half height. A major portion of this difference can be clearly attributed to the Reynolds stress (see Figure 4.21(a)). This result indicates the potential advantage in including a modest penalty even on the interior element interfaces at extremely coarse resolutions that we are likely to encounter in LES. Now, in the section to follow, we discuss the results presented here with the aid of simple advection-diffusion problem where the effects of penalty fluxes are transparent.

4.3 Discussion

Recently, Collis [29], using the current DG implementation to solve a simple steady advection-diffusion equation, found that using a weak (BR) boundary enforcement is clearly advantageous. Further, in our past experience with simulation codes that strictly enforce Dirichlet boundary conditions [14, 15, 76], coarse y -direction resolution leads to unusually high turbulence production and high drag predictions. Given this, the ability to obtain reasonable solutions with particularly coarse wall-normal resolution ($\Delta y_w^+ \approx 4.3$) can be attributed at least in part to the manner of the current wall boundary conditions enforcement. This statement is substantiated by the results presented above that clearly indicate the effectiveness of appropriately regulating slip at the wall in obtaining improved wall shear stress predictions. Although LDG and BLDG have a more constraining effect on slip, it is important to stress that they still permit a jump albeit significantly diminished.

To make this discussion more concrete, we apply the various penalty fluxes described in Section 4.1 to the problem considered by Collis [29]. Before we present these results, we give a brief description of this model problem. The simple steady advection-diffusion problem using a forcing $f = 1$ is given as

$$u_{,x} = 1 + \nu u_{,xx} \quad (4.4)$$

with boundary conditions $u(0) = u(1) = 0$ and diffusivity $\nu = 0.01$.

Figure 4.23 shows results computed using a discontinuous Galerkin discretization with four elements using $p = 0$ (see 4.23a) and $p = 2$ (see 4.23b), respectively using BR, BLDG, and LDG using $\epsilon = 100.0$. The BR solution obtained using $p = 0$ is a special case where the solution and jump are closely linked, in fact, at the physical boundary the solution jump at the boundary and the interior solution are exactly equivalent. Now, the BLDG flux effectively damps the solution jump, using a relatively high ϵ (see Figure 4.23(a)) and thereby the solution in the interior of the element at the boundary that further affects the solution in the interior of the domain. The LDG flux effectively damps the entire solution as it acts on all the jumps i.e. on the entire solution. With the aid of this special case, we see a direct correspondence between the jumps in the solution and interior solution that highlights the relation that exists between the residual in the interior solution and the solution jump at the element boundaries [19].

Importantly, at $p = 2$, shown in Figure 4.23(b), we see that the effect of using BLDG is to introduce oscillations in the interior solution that is consistent with the observations of Collis [29] using a hard enforcement of the boundary conditions. While the oscillations, close to the sharp gradient on the right hand side boundary, are largely confined to the first two elements, using the LDG method we see that the LDG affects all the elements in the domain. By contrast, the BR flux that is unpenalized “captures” the sharp gradient in the solution with a jump at the boundary and the effect on the adjacent elements is minimized compared with BLDG and LDG. We believe that the success of the SBLDG in the three-dimensional case can be attributed to similar behavior as the BR flux here.

Now, BLDG and LDG while regulating slip, likely constrain all components of the solution at the channel wall approaching a hard boundary enforcement. This may explain the observed increase in the shear stress predictions at the wall for these cases (refer to Table 4.1 and 4.2). And these are consistent with the observations using discretizations that strictly enforce the Dirichlet boundary conditions [14, 15].

Meanwhile, SBLDG by allowing the flow to slip (which is related to the interior residual [19]) tends to constrain the interior solution commensurate with the local resolution thereby potentially leading to more reliable τ_w estimates. It is for this reason that we believe the SBLDG approach to enforcing wall-boundary conditions may be considered effective in mimicking the function of a wall-model. Note, the oscillations close to the wall using the penalty fluxes in the total stress profiles, seen in Figures 4.1, 4.4, 4.7, 4.10, 4.15, 4.18, and 4.22, are consistent with the observations here. Importantly, these oscillations are largely confined within the element at the boundary even for the LDG case suggesting that for the simulations considered thus far the slip at interelement boundaries, though present, is not significant except perhaps for the $Re_\tau = 395$ simulation. This suggests that a combination of SBLDG at the wall and LDG (with a conservative ϵ) may have potential advantages at very coarse resolutions (see an illustration of this in the advection-diffusion problem with a flux we term ILDG in Figure 4.26).

Before we conclude this chapter, we observe that action of the penalty has a straightforward interpretation in the steady advection-diffusion equation. Principally, this is due to the direct relation that exists between the residual in the interior of the element and the solution jumps [19]. Thus, modifying the jump at the boundary (element interfaces) has a noticeable impact on the solution, especially in one-dimension.

However, the three-dimensional unsteady Navier-Stokes equations does not permit such a simple interpretation. And while the introduction of penalty on the solution jumps may introduce oscillations in the solution (see Figures 4.1, 4.4, 4.7, 4.10, 4.15, 4.18, and 4.22), it does not render the solution useless. On the contrary, there is an improvement in the turbulence statistics using large Δy_w^+ .

In fact, we have observed an improvement in the non-linear stability of simulations with the introduction of the penalty fluxes. Specifically, using the $4 \times 4 \times 4$ with $p = 3$ at $Re_\tau = 100$, the solution shows improved stability with $\epsilon = 100.0$ for SBLDG, BLDG, and LDG compared with BR. Further, the improvement in stability is directly proportional to the degree of penalization introduced. This suggests that improved non-linear stability may relate to the dissipation introduced through the penalization [19]. However, the introduction of the penalty is not sufficient to *ensure* non-linear stability and we address this issue in more detail in the following chapter.

4.4 Summary

Thus far, we have seen that the inclusion of a penalty, for the meshes considered upto this point, enables the numerical viscous flux to better enforce the wall boundary conditions. As a consequence, the near-wall dynamics are more faithfully modeled when compared with the BR approach at very coarse resolutions ($\Delta y_w^+ > 2$). Thereby, we have seen improved wall shear stress predictions even with low resolutions in the wall-normal direction. In the process, the overall quality of all the statistics considered have shown a better agreement with reference computations.

It is well-known that the choice of the numerical fluxes can affect accuracy, stability, and consistency of the method [3, 44]. The results presented here certainly demonstrate, in the practical setting of a turbulent channel, the effect of the numerical fluxes on accuracy. Also, the higher resolution case with $4 \times 4 \times 8$ mesh using $p = 6$ demonstrates the consistency and convergence of the various fluxes as resolution is increased (jumps are reduced). The minimal differences at higher resolutions using consistent numerical fluxes was also observed by Bassi and Rebay [7] for compressible fluid flow.

It is important to note there may be a potential advantage in using LDG with a modest value of ϵ (see Figure 4.22). A corresponding one-dimensional version, that we term ILDG, that uses LDG in the interior element interfaces and BR at the physical boundaries produces results that are remarkably similar to BR in Figure 4.26. Currently, the overall performance of the SBLDG in improving results and the potential difficulty in selecting values of ϵ for the interior interelement interfaces, makes SBLDG the flux of choice in the remainder of this thesis.

Thus far, we have exploited *just the inherent features* of the current DG spatial discretization to obtain reasonable low-order statistics at moderate resolutions. In fact, the penalty fluxes serve as computationally efficient manner to improve low-order statistics that partially account for the reduced wall-normal resolution. Now, we hope to build on this framework by introducing a VMS model to further reduce the required degrees of freedom. More importantly, this will introduce additional flexibility for obtaining reliable turbulence statistics at even lower resolutions that holds promise for achieving dramatic savings in overall computational cost.

Flux Type	Slip	τ_w	u_τ
BR	-0.7916	1.2179	1.1025
SBLDG-BR	0.2596	1.1291	1.0615
SBLDG	0.2668	0.9748	0.9867
BLDG	-0.0011	0.9781	0.9884
LDG	-0.0011	0.9974	0.9980

Table 4.1: Parameters and results summary for a $8 \times 4 \times 8$ mesh using $p = 3$ at $Re_\tau = 100$ using different numerical viscous flux with a penalty factor $\epsilon = 100.0$. The element size in wall units for this mesh topology is $\Delta x^+ \approx 157$ and $\Delta z^+ \approx 52.3$ in the streamwise and spanwise directions, respectively. Also, using $p = 3$, the near-wall resolution based on the collocation grid is $\Delta y_w^+ \approx 4.35$.

Flux Type	Slip	τ_w	u_τ
BR	-0.5442	1.0670	1.0308
SBLDG-BR	0.2244	0.9391	0.9668
SBLDG	0.2299	0.8575	0.9242
BLDG	-0.0007	0.8827	0.9377
LDG	-0.0007	0.8755	0.9338

Table 4.2: Parameters and results summary for a $4 \times 4 \times 8$ mesh using $p = 3$ at $Re_\tau = 100$ using different numerical viscous flux with a penalty factor $\epsilon = 10.0$. The element size in wall units for this mesh topology is $\Delta x^+ \approx 314$ and $\Delta z^+ \approx 52.3$ in the streamwise and spanwise directions, respectively. Also, using $p = 3$, the near-wall resolution based on the collocation grid is $\Delta y_w^+ \approx 4.35$.

Flux Type	Slip	τ_w	u_τ
BR	0.0867	0.9851	0.9904
SBLDG-BR	0.1806	0.9692	0.9823
BLDG	0.0018	0.9753	0.9853
LDG	0.0018	0.9805	0.9880

Table 4.3: Parameters and results summary for a $4 \times 4 \times 8$ mesh using $p = 6$ at $Re_\tau = 100$ using different numerical viscous flux. The element size in wall units for this mesh topology is $\Delta x^+ \approx 314$ and $\Delta z^+ \approx 52.3$ in the streamwise and spanwise directions, respectively. Also, using $p = 6$, the near-wall resolution based on the collocation grid is $\Delta y_w^+ \approx 1.62$.

Flux Type	Slip	τ_w	u_τ
SBLDG	0.8482	1.006	1.002
BR*	0.0020	1.001	1.000

Table 4.4: Simulations and result summary for a $16 \times 4 \times 16$ mesh using $p = \{6, 5, 5, 6\}$ at $Re_\tau = 180$ using different numerical viscous fluxes. The element size in wall units for this mesh topology is $\Delta x^+ \approx 141$ and $\Delta z^+ \approx 47$ in the streamwise and spanwise directions, respectively. Also, using $p = 4$, the near-wall resolution based on the collocation grid is $\Delta y_w^+ \approx 2.8$ ($\Delta y_m^+ \approx 45$). The * indicates that this is a higher overall resolution DG DNS with a $16 \times 16 \times 16$ mesh using $p = 4$

Flux Type	Slip	τ_w	u_τ
SBLDG	-0.03584	0.9977	0.9983
LDG	-0.03647	1.0144	1.014

Table 4.5: Parameters and results summary for a $8 \times 8 \times 12$ mesh using $p = 4$ at $Re_\tau = 395$ using different numerical viscous fluxes. The element size in wall units for this mesh topology is $\Delta x^+ \approx 155$ and $\Delta z^+ \approx 51$ in the streamwise and spanwise directions, respectively. Also, using $p = 4$, the near-wall resolution based on the collocation grid is $\Delta y_w^+ \approx 2.8$ ($\Delta y_m^+ \approx 25$).

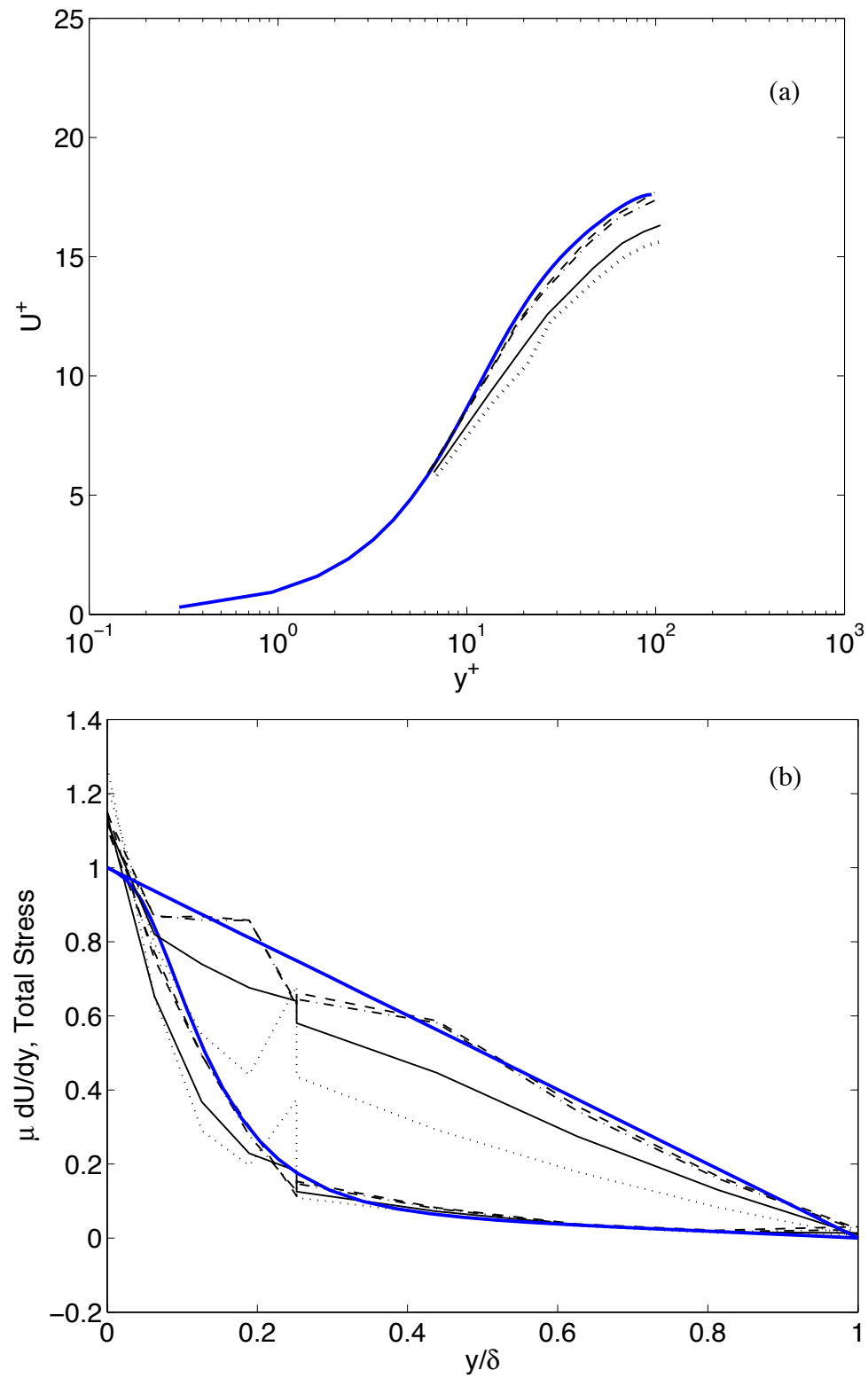


Figure 4.1: Effect of different numerical viscous fluxes on meanflow and viscous stress profiles for $Re_\tau = 100$ computed on a $8 \times 4 \times 8$ mesh using $p = 3$: — DNS; BR; — SBLDG-BR; ---- SBLDG; -.- LDG.

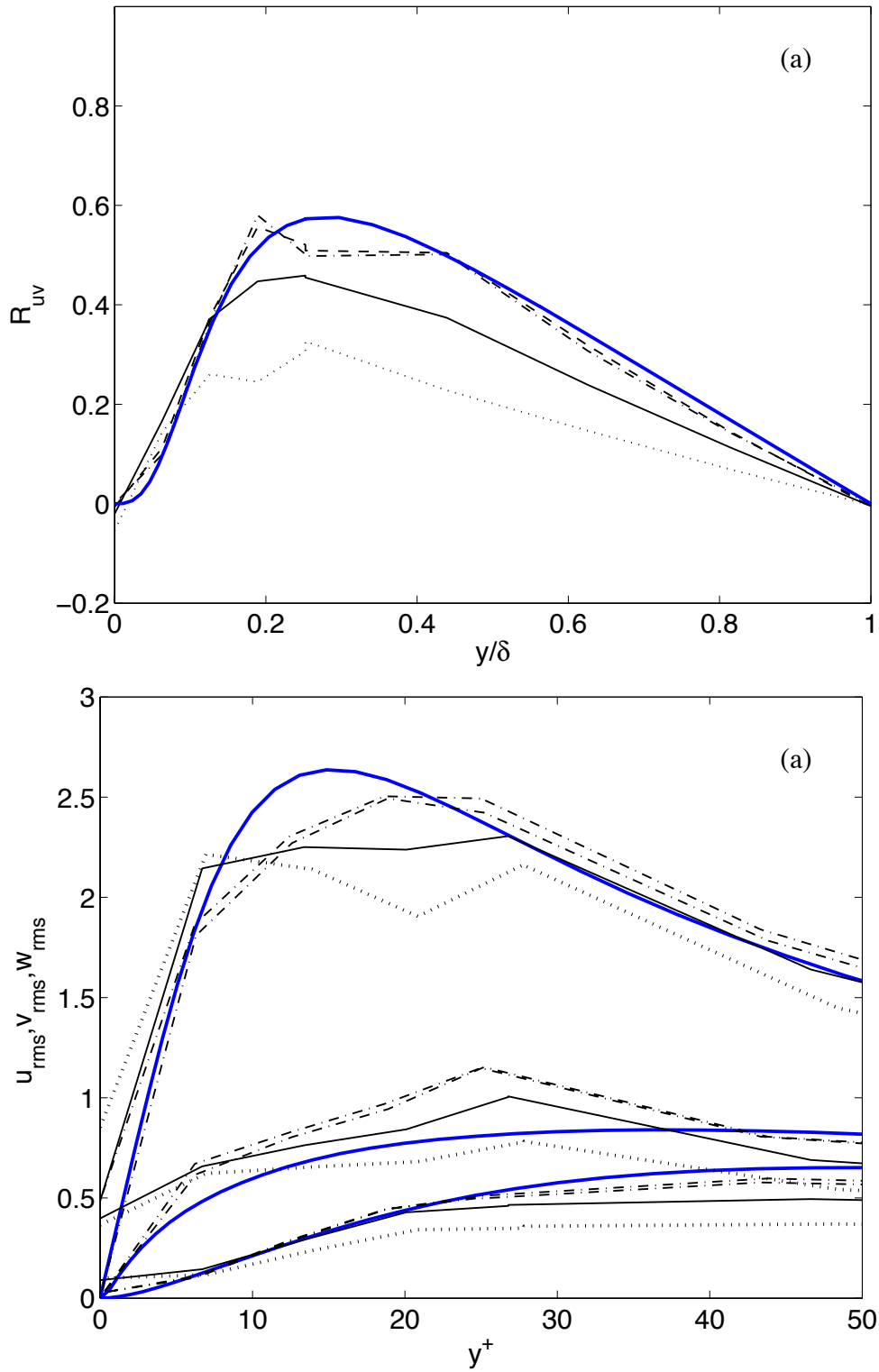


Figure 4.2: Effect of different numerical viscous fluxes on Reynolds stress and turbulence intensity profiles for $Re_\tau = 100$ computed on a $8 \times 4 \times 8$ mesh using $p = 3$: — DNS; BR; — SBLDG-BR; ---- SBLDG; -.- LDG.

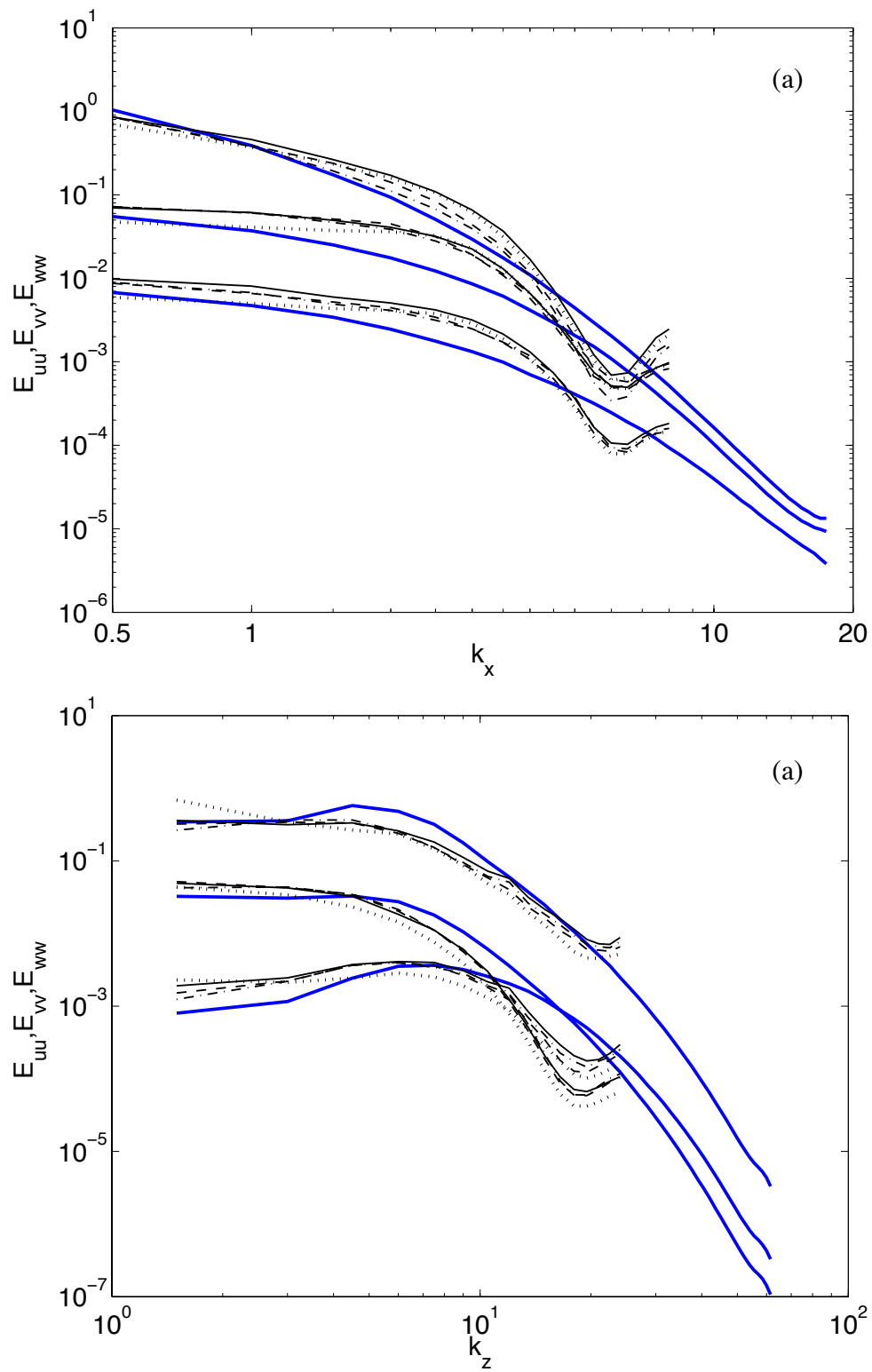


Figure 4.3: Effect of different numerical viscous fluxes on streamwise and spanwise spectra for $Re_\tau = 100$ computed on a $8 \times 4 \times 8$ mesh using $p = 3$: — DNS; BR; — SBLDG-BR; ---- SBLDG; -.- LDG.

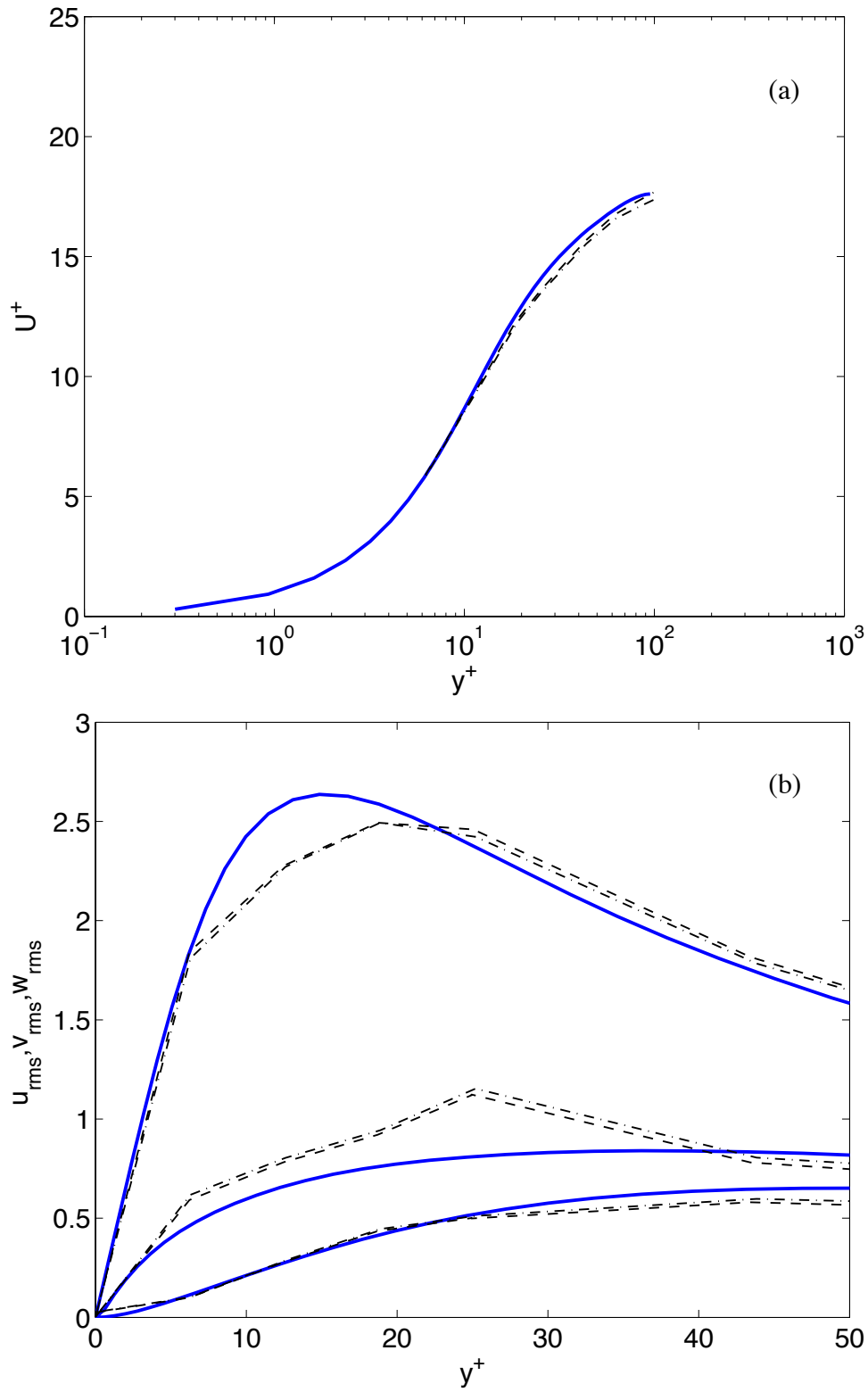


Figure 4.4: Effect of different numerical viscous fluxes on meanflow and viscous stress profiles for $Re_\tau = 100$ computed on a $8 \times 4 \times 8$ mesh using $p = 3$: — DNS; BR; ---- SBLDG; —·— LDG.

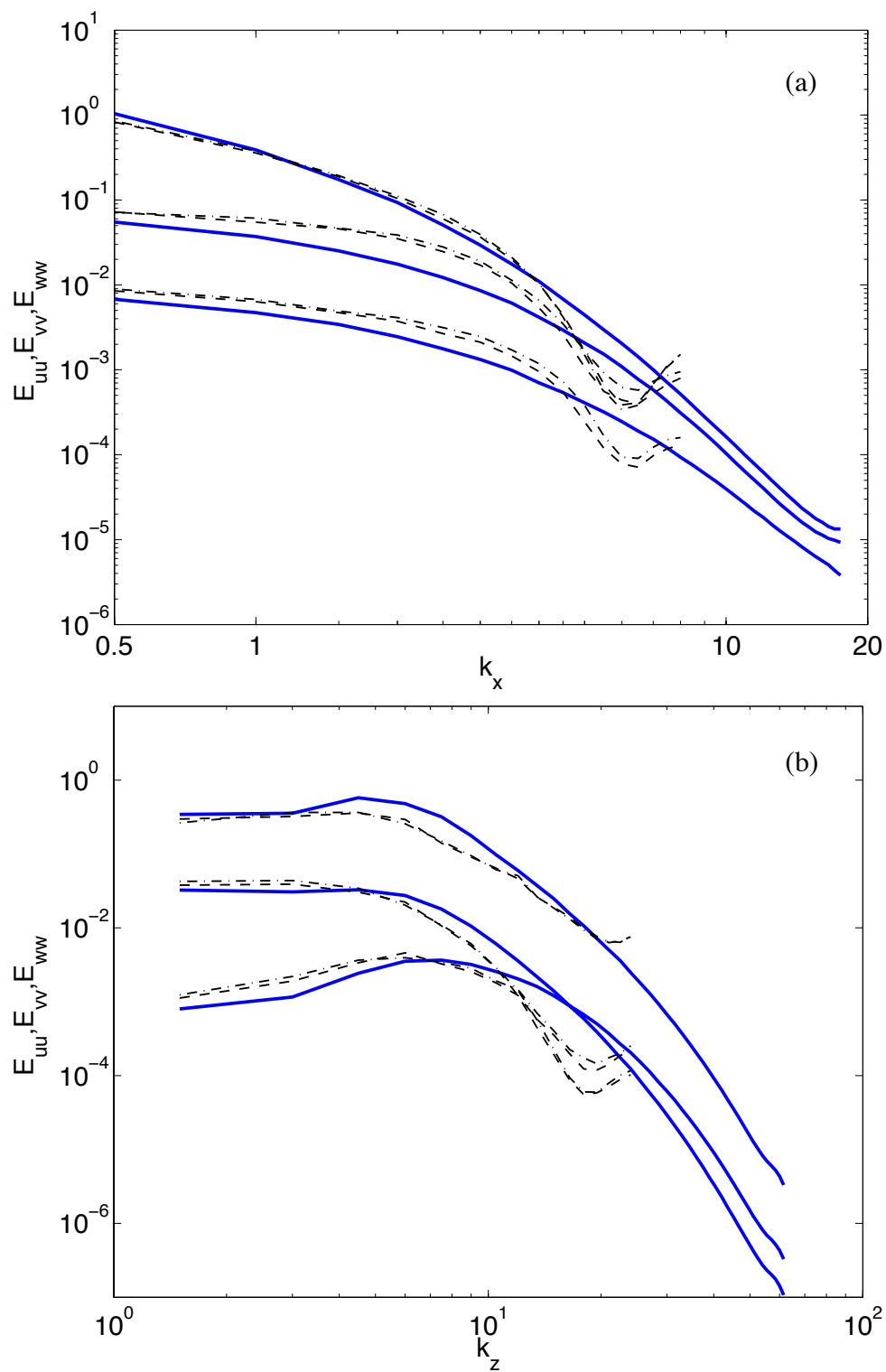


Figure 4.5: Effect of different numerical viscous fluxes on streamwise and spanwise spectra for $Re_\tau = 100$ computed on a $8 \times 4 \times 8$ mesh using $p = 3$: — DNS; ---- SBLDG; —·— LDG.

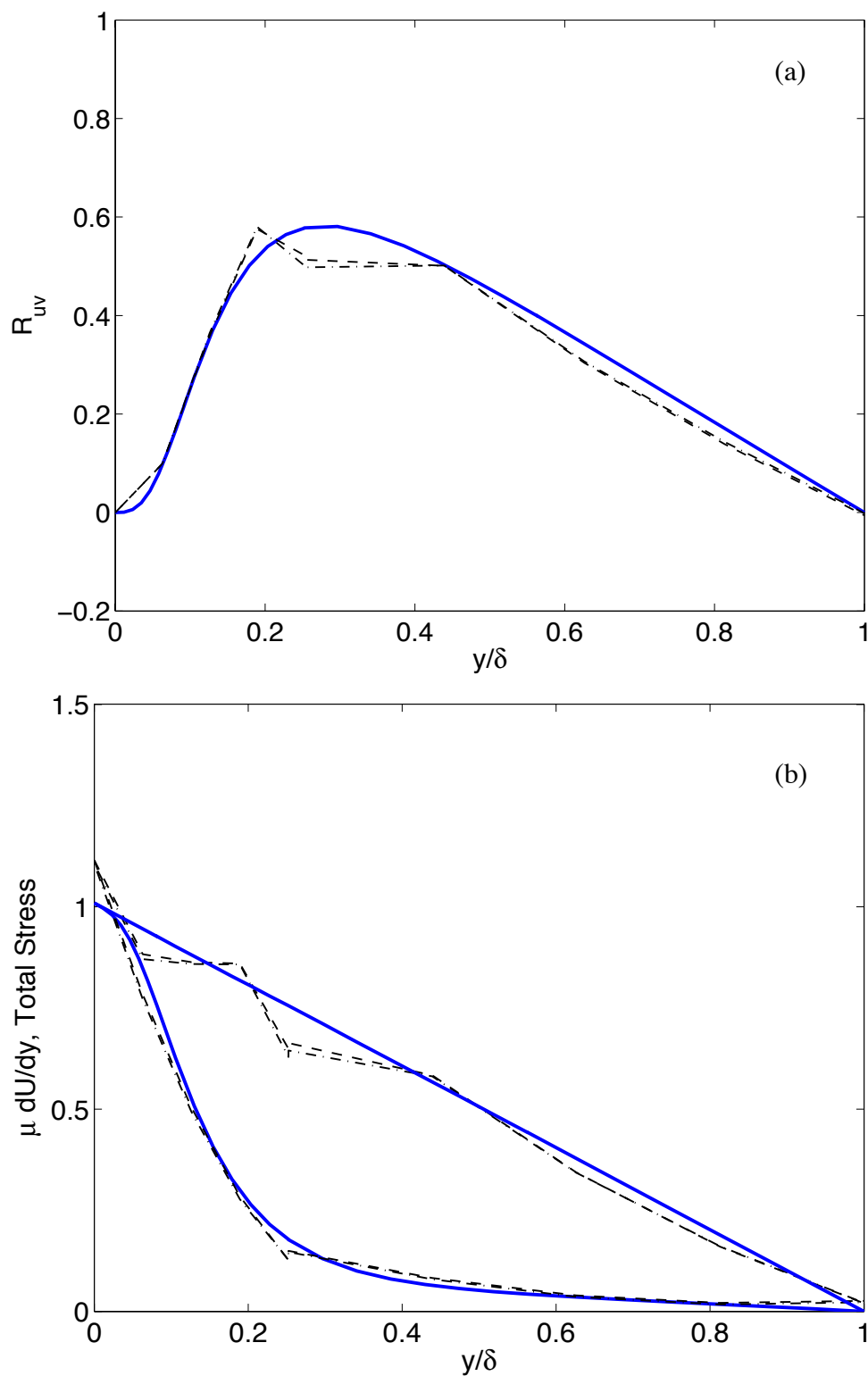


Figure 4.6: Effect of different numerical viscous fluxes on Reynolds stress and turbulence intensity profiles for $Re_\tau = 100$ computed on a $8 \times 4 \times 8$ mesh using $p = 3$: — DNS; ---- BLDG; -.- LDG.

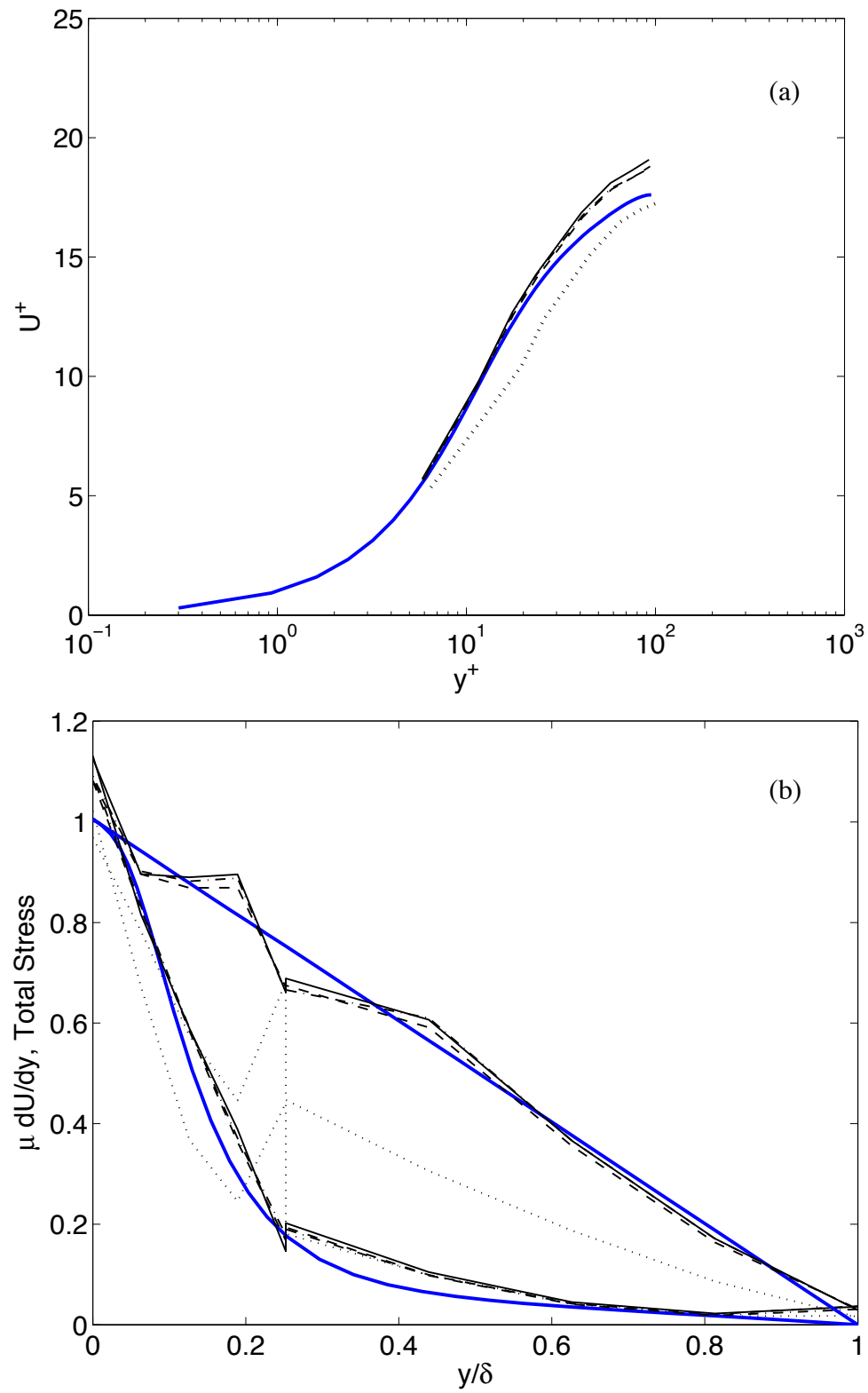


Figure 4.7: Effect of different numerical viscous fluxes on meanflow and turbulence intensity profiles for $Re_\tau = 100$ computed on a $4 \times 4 \times 8$ mesh using $p = 3$: — DNS; BR; — SBLDG; ---- BLDG; —·— LDG.

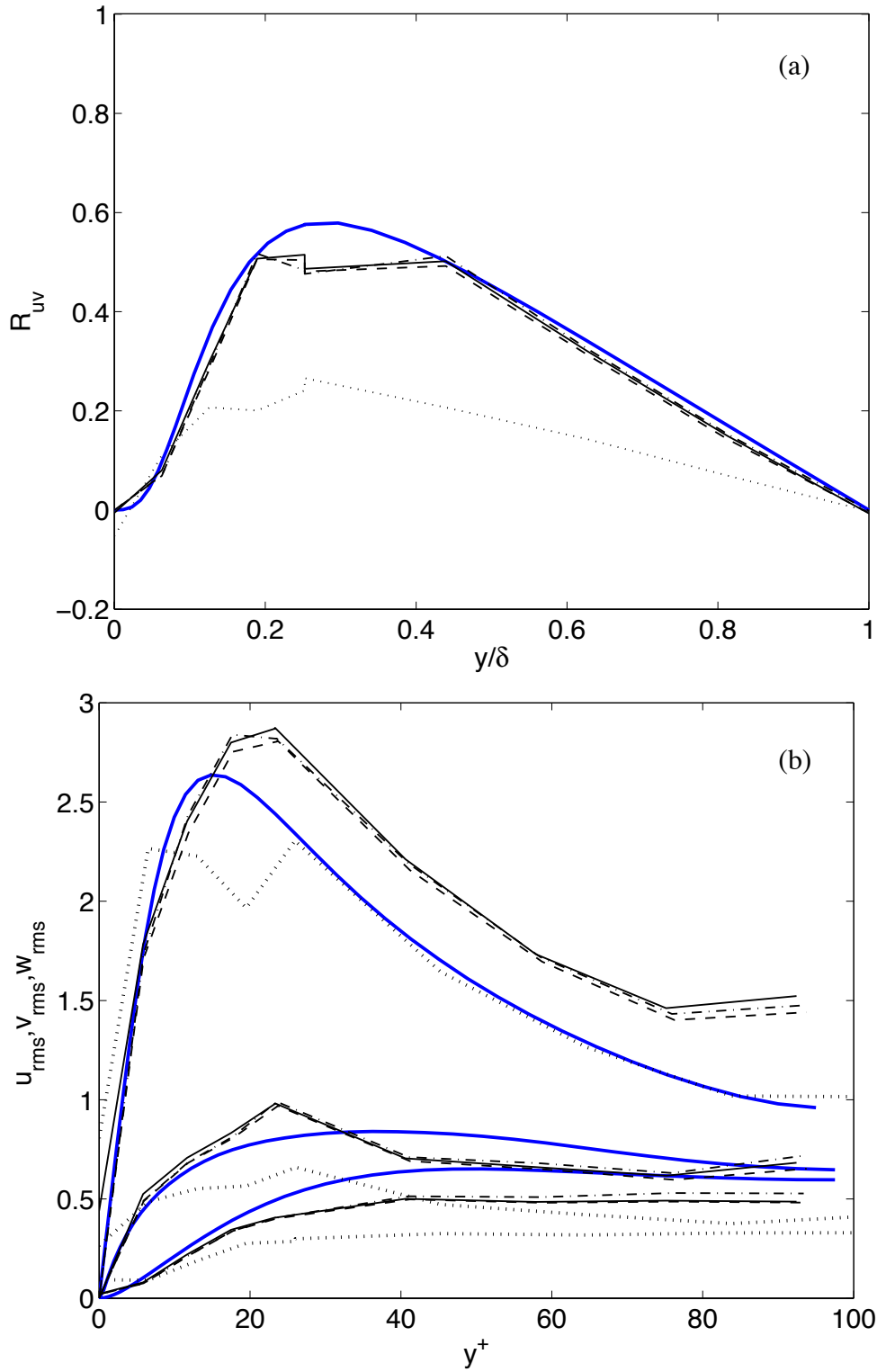


Figure 4.8: Effect of different numerical viscous fluxes on Reynolds and viscous stress for $Re_\tau = 100$ computed on a $4 \times 4 \times 8$ mesh using $p = 3$: — DNS; BR; — SBLDG; ---- BLDG; -.- LDG.

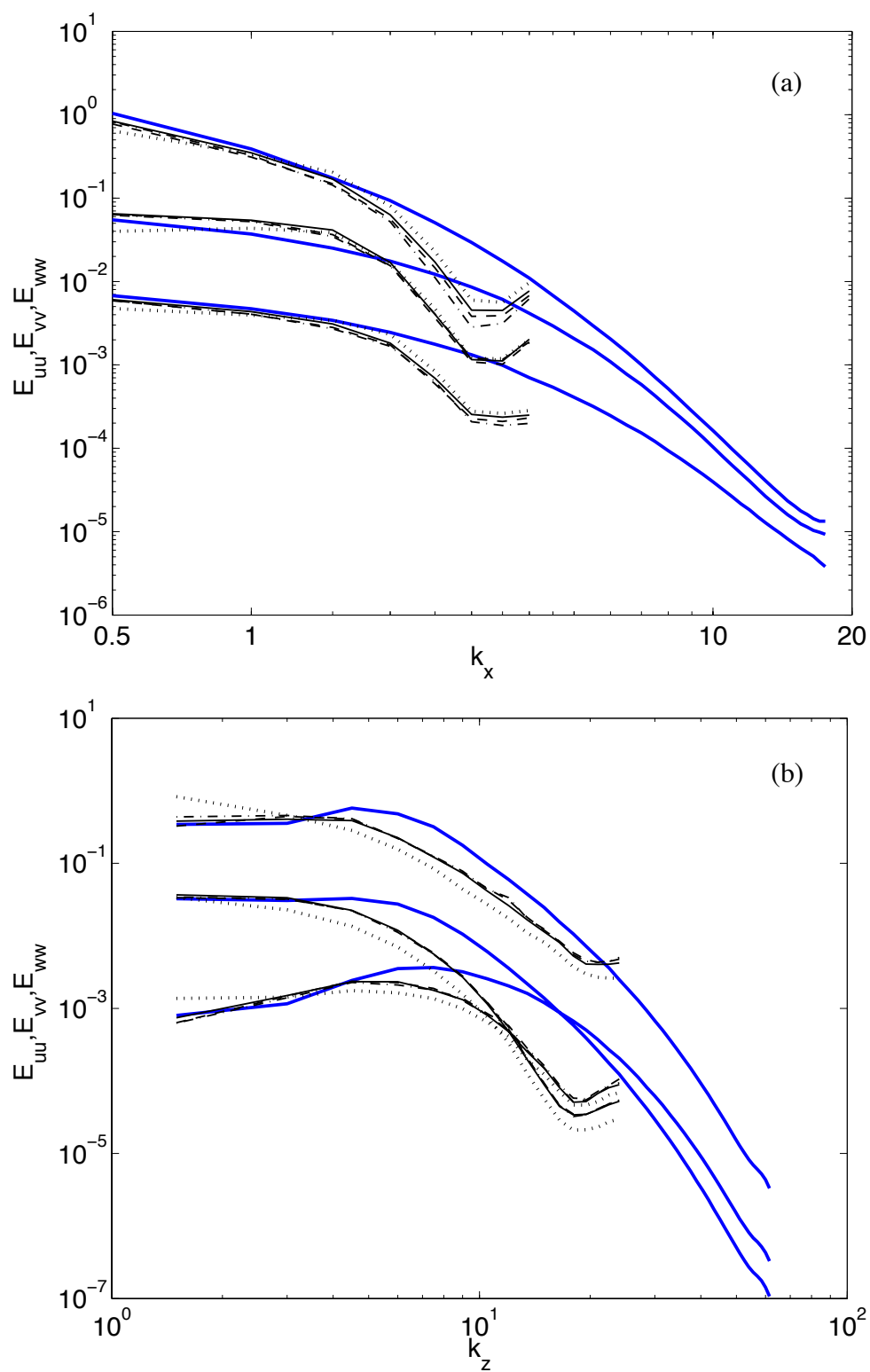


Figure 4.9: Effect of different numerical viscous fluxes on streamwise and spanwise spectra for $Re_\tau = 100$ computed on a $4 \times 4 \times 8$ mesh using $p = 3$: — DNS; BR; — SBLDG; ---- BLDG; —·— LDG.

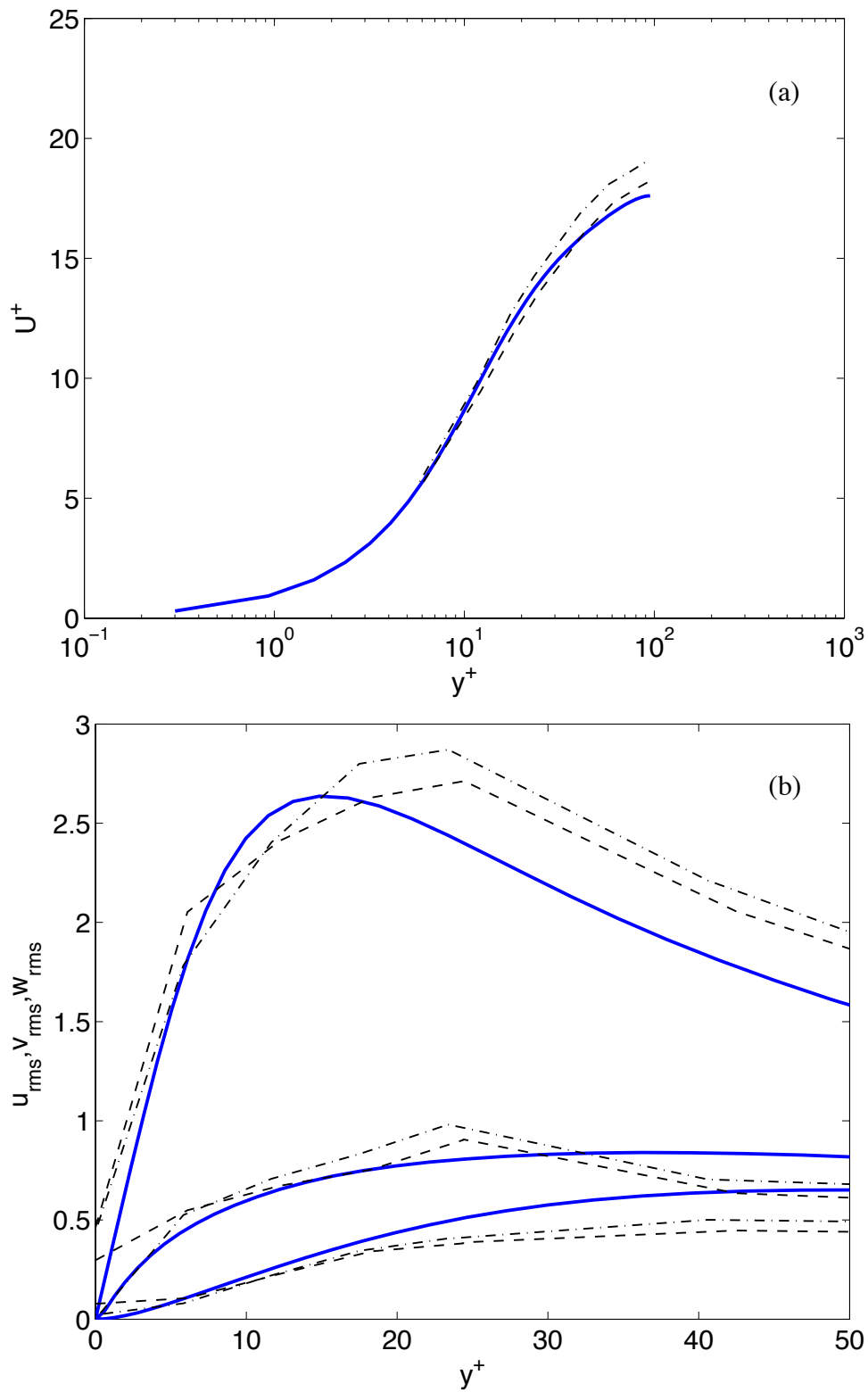


Figure 4.10: Effect of different numerical viscous fluxes on meanflow and turbulence intensity profiles for $Re_\tau = 100$ computed on a $4 \times 4 \times 8$ mesh using $p = 3$: — DNS; ---- SBLDG-BR; -.- SBLDG.

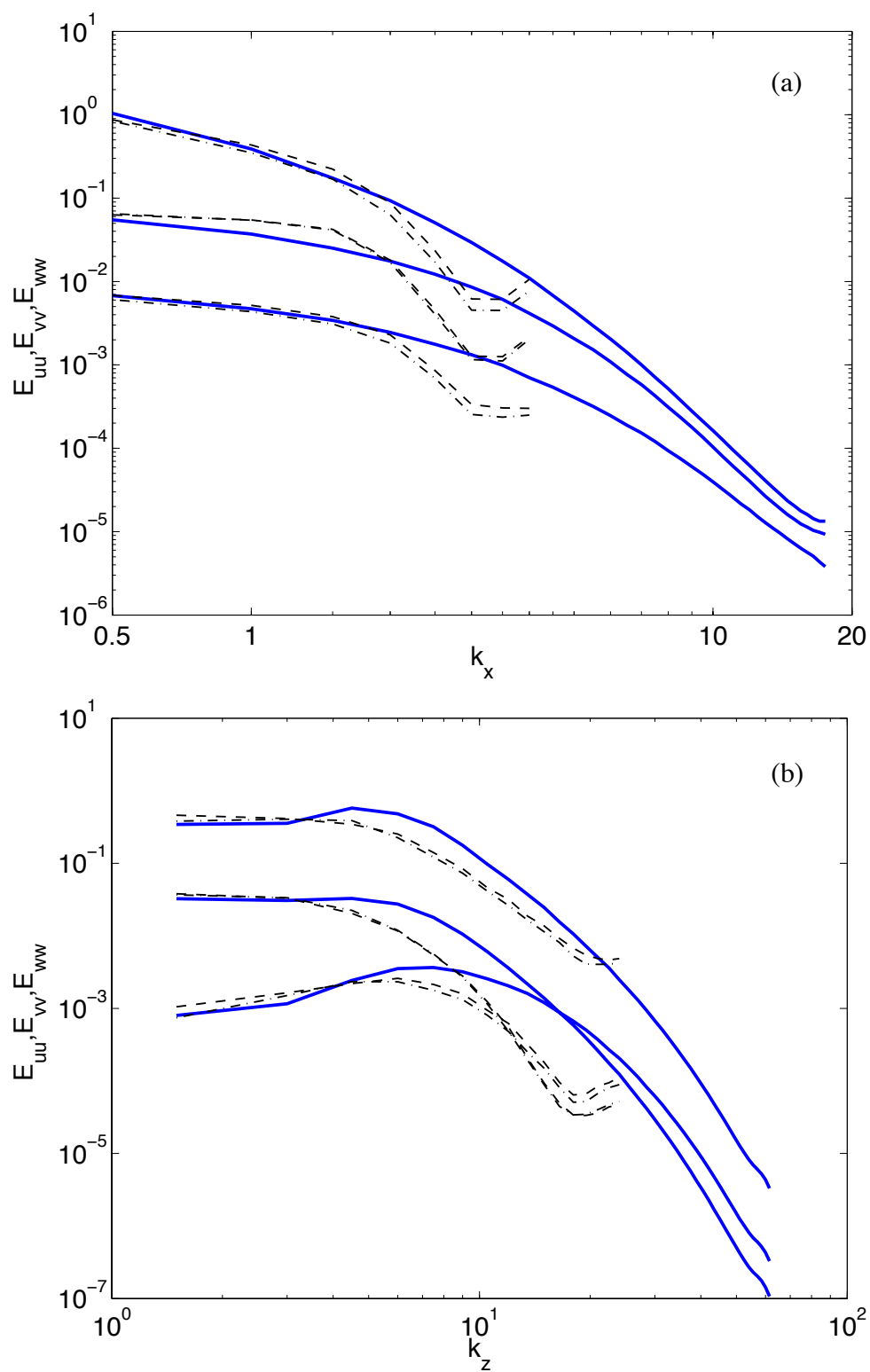


Figure 4.11: Effect of different numerical viscous fluxes on streamwise and spanwise spectra for $Re_\tau = 100$ computed on a $4 \times 4 \times 8$ mesh using $p = 3$: — DNS; ---- SBLDG-BR; -.- SBLDG.

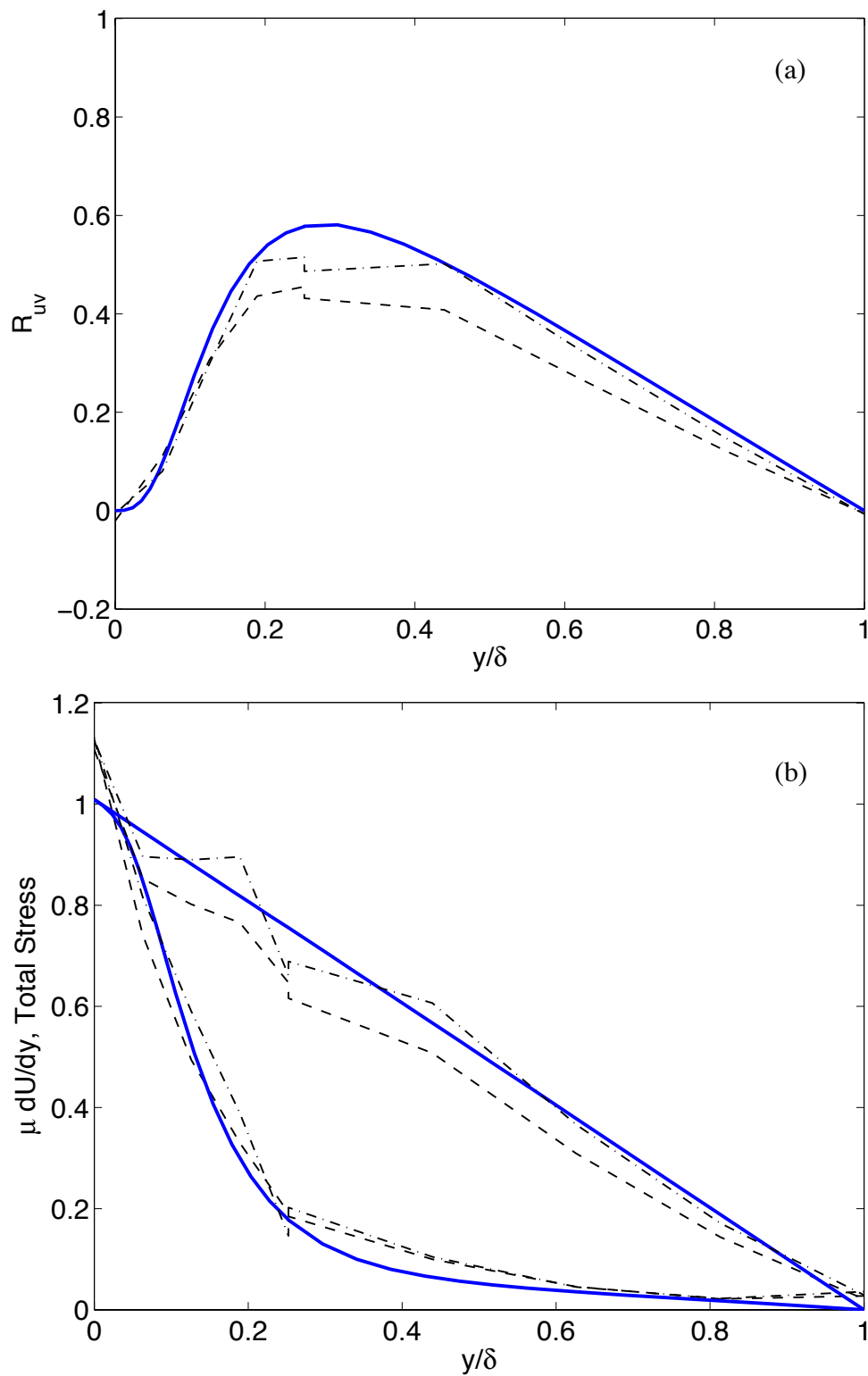


Figure 4.12: Effect of different numerical viscous fluxes on Reynolds, viscous, and total stress profiles for $Re_\tau = 100$ computed on a $4 \times 4 \times 8$ mesh using $p = 3$: — DNS; ---- SBLDG-BR; -.- SBLDG.

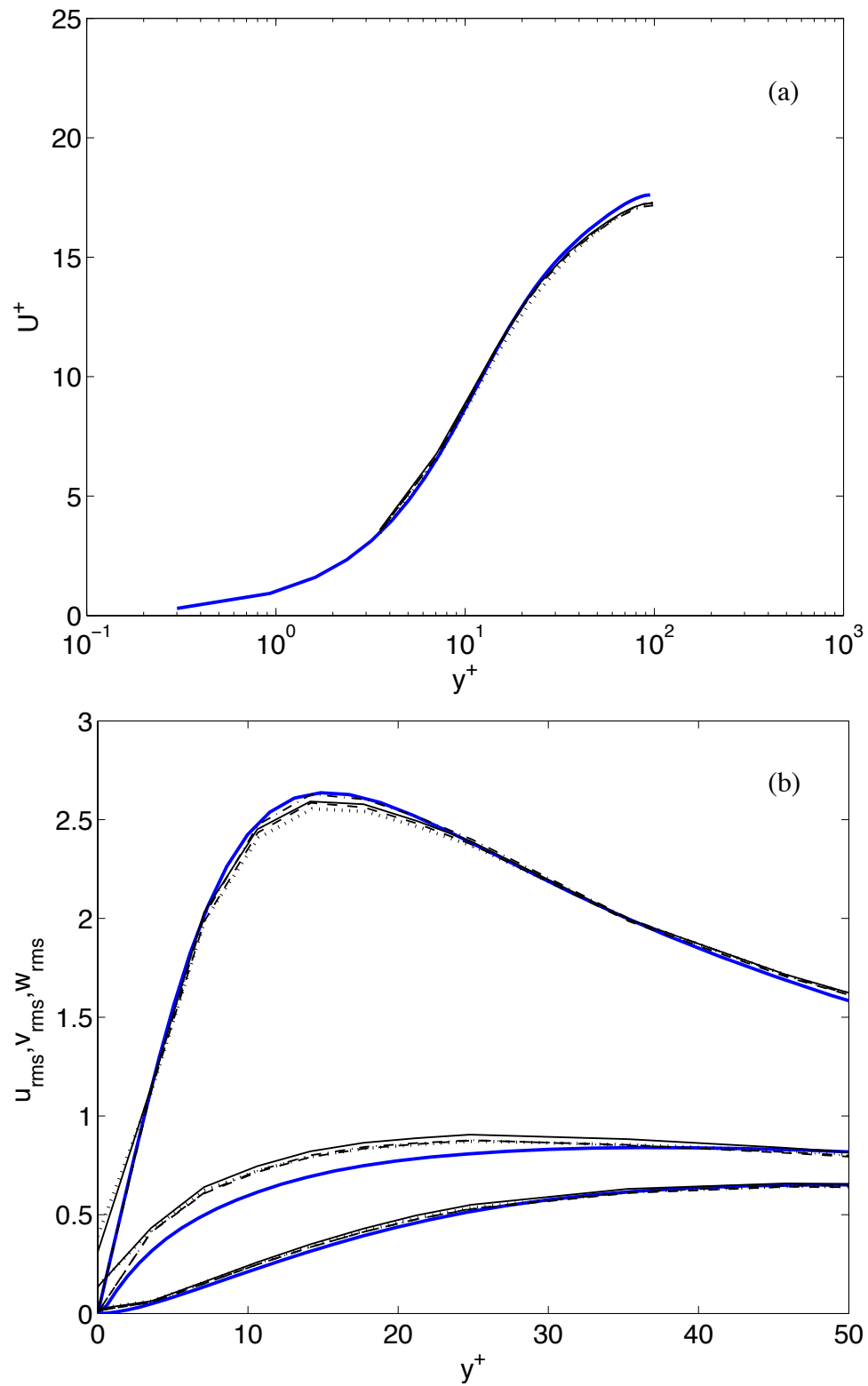


Figure 4.13: Effect of different numerical viscous fluxes on meanflow and turbulence intensity profiles for $Re_\tau = 100$ computed on a $4 \times 4 \times 8$ mesh using $p = 6$: — DNS; BR; — SBLDG-BR; ---- BLDG; -.- LDG.

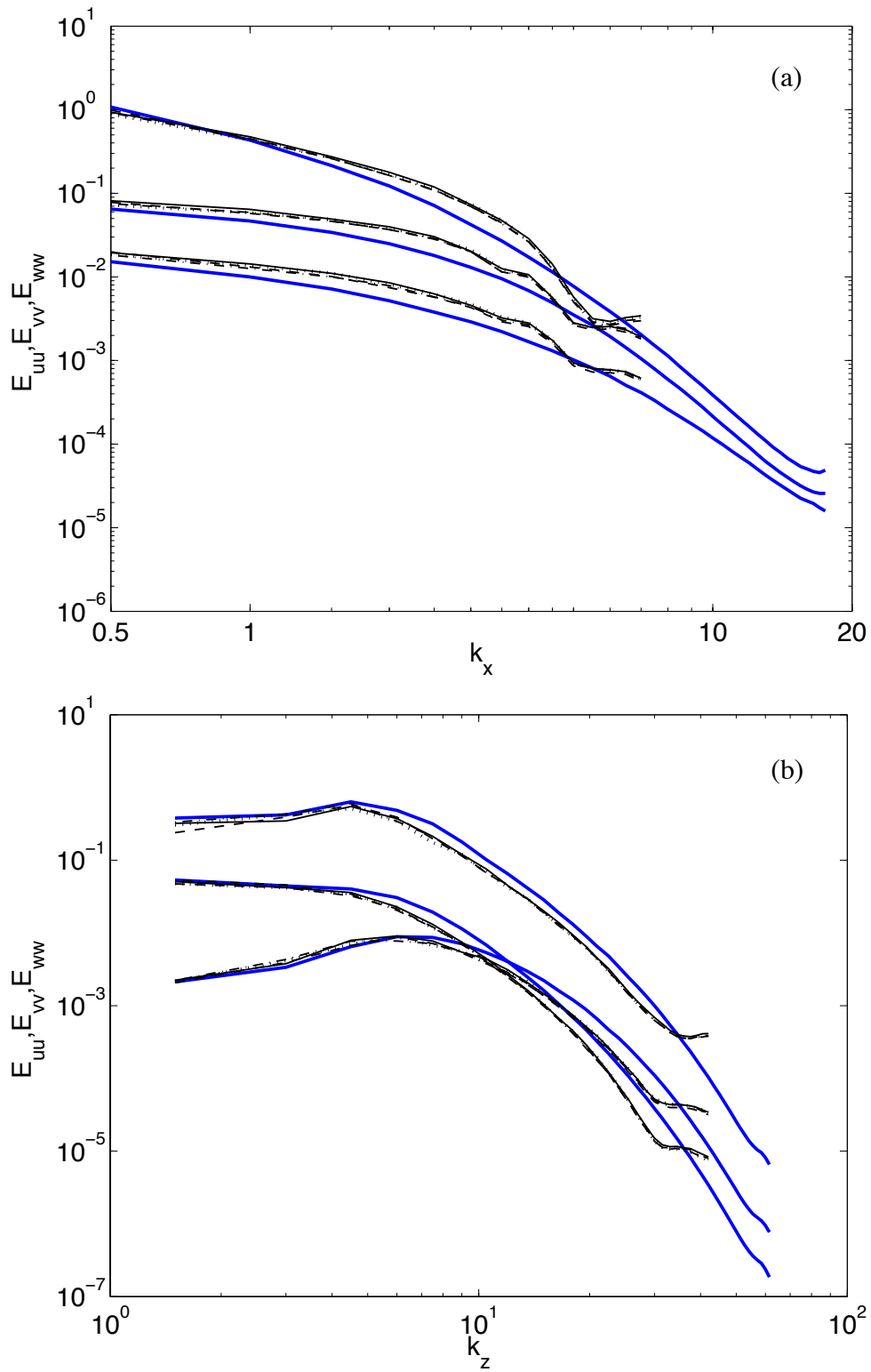


Figure 4.14: Effect of different numerical viscous fluxes on streamwise and spanwise spectra for $Re_\tau = 100$ computed on a $4 \times 4 \times 8$ mesh using $p = 6$: — DNS; BR; — SBLDG-BR; ---- BLDG; -.- LDG.

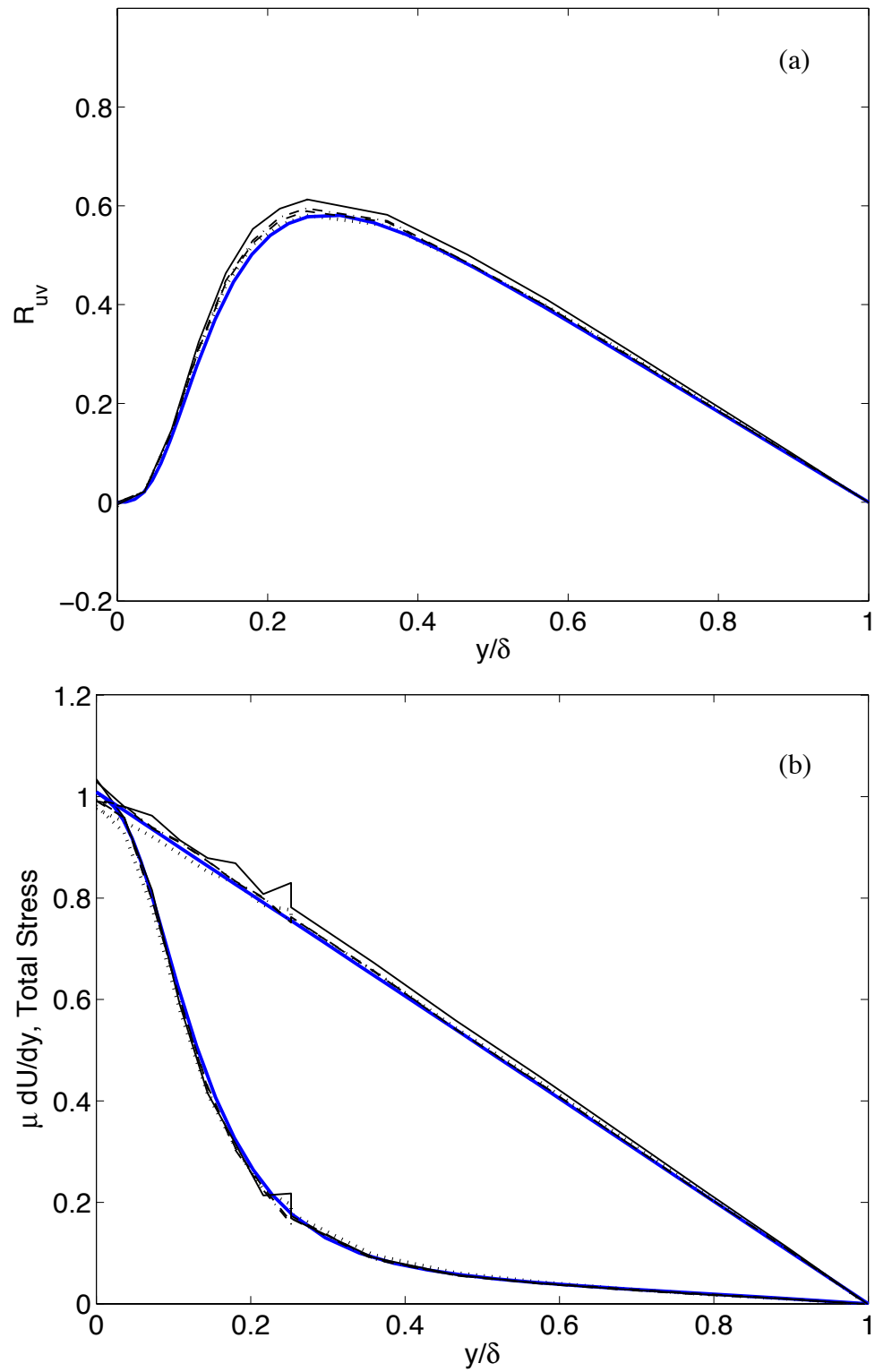


Figure 4.15: Effect of different numerical viscous fluxes on Reynolds and viscous stress for $Re_\tau = 100$ computed on a $4 \times 4 \times 8$ mesh using $p = 6$: — DNS; BR; — SBLDG-BR; ---- BLDG; — LDG.

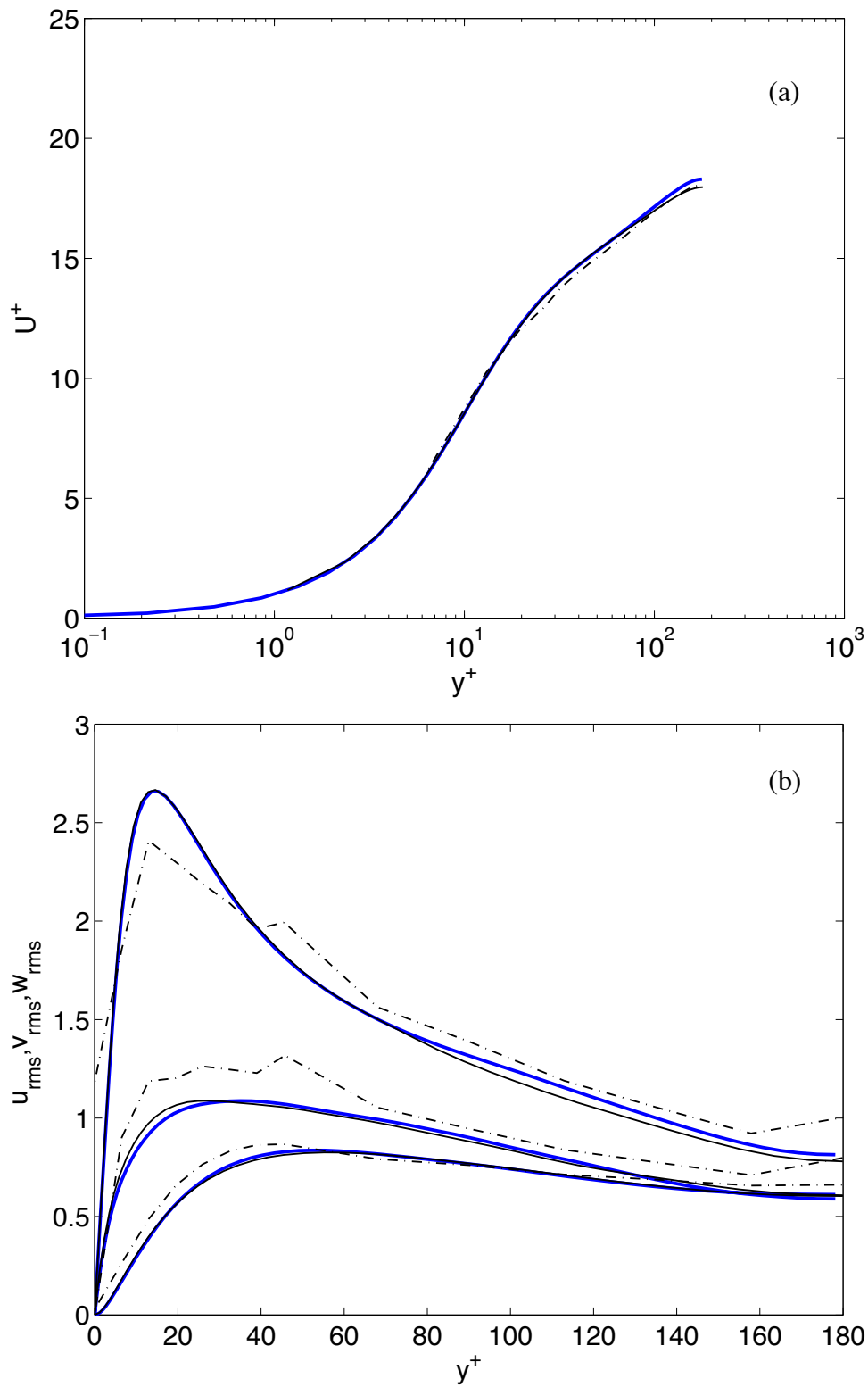


Figure 4.16: Effect of SBLDG numerical viscous flux on meanflow and turbulence intensity profiles for $Re_\tau = 180$ computed on a $16 \times 4 \times 16$ mesh using $p = \{6, 5, 5, 6\}$: — DNS; — $16 \times 16 \times 16$ using $p = 4$ with BR; - - - SBLDG.

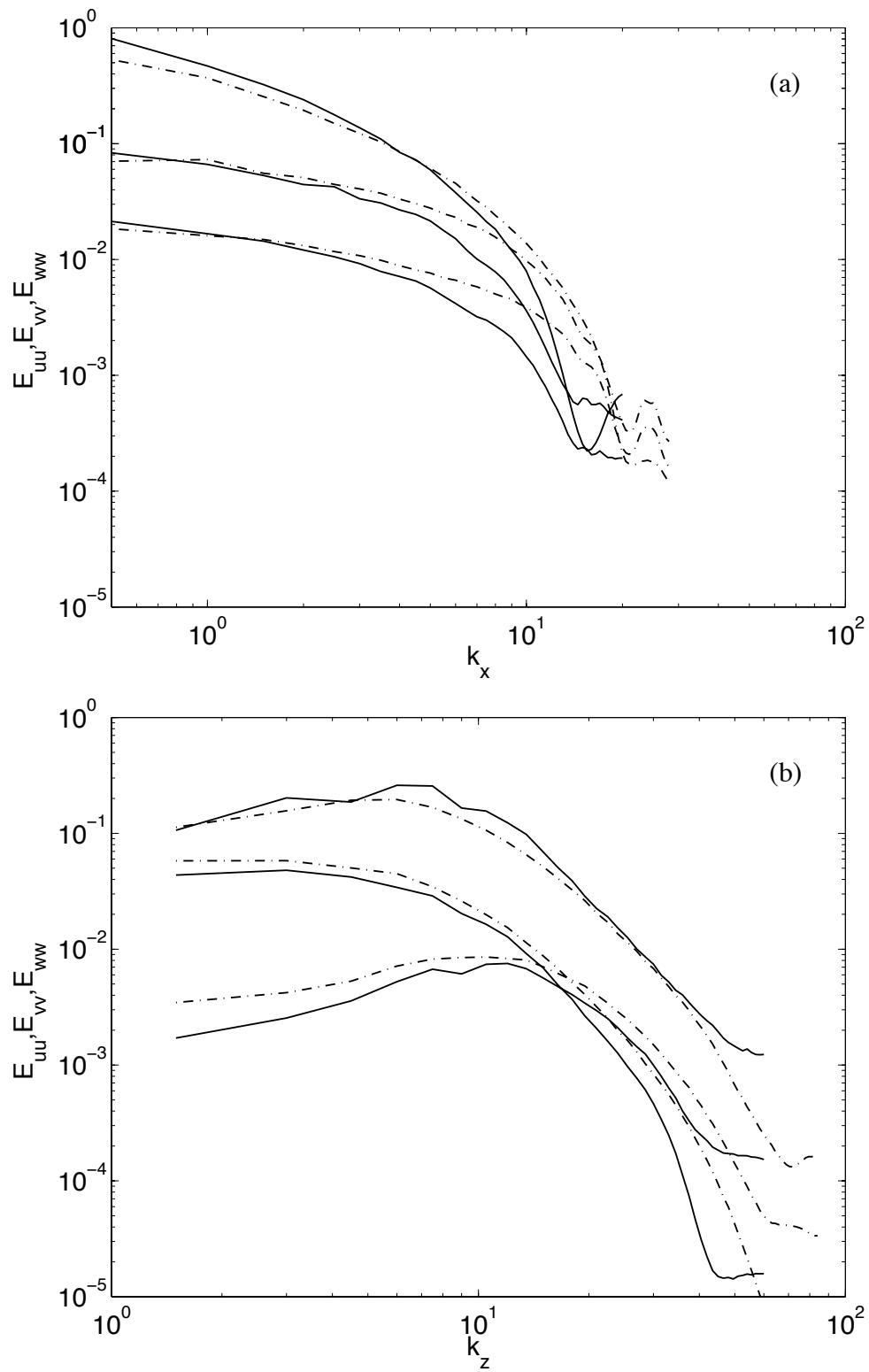


Figure 4.17: Effect of SBLDG numerical viscous flux on streamwise and spanwise spectra for $Re_\tau = 180$ computed on a $16 \times 4 \times 16$ mesh using $p = \{6, 5, 5, 6\}$: — DNS; — $16 \times 16 \times 16$ using $p = 4$ with BR; — SBLDG.

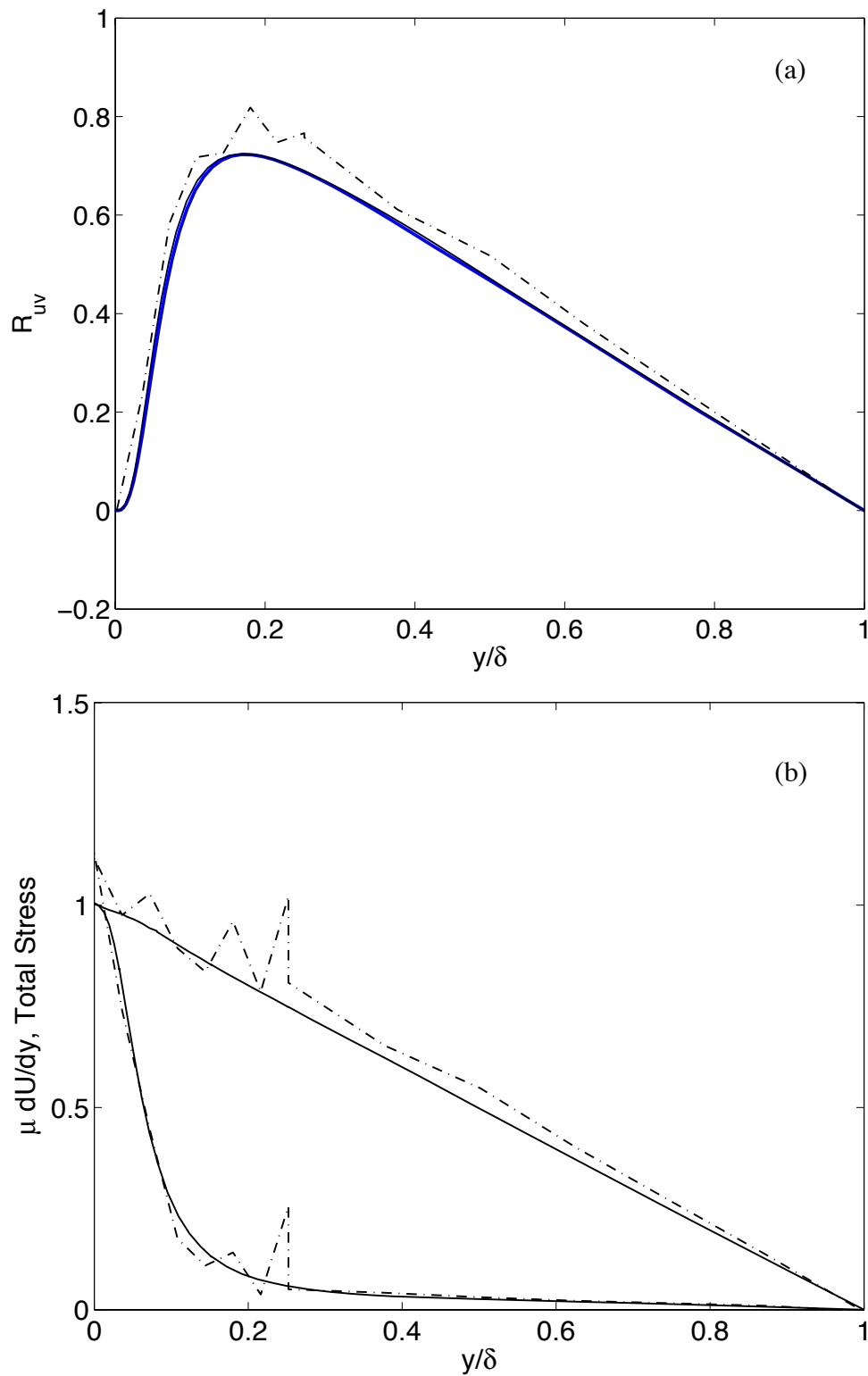


Figure 4.18: Effect of SBLDG numerical viscous flux on Reynolds , viscous, and total stress profiles for $Re_\tau = 180$ computed on a $16 \times 4 \times 16$ mesh using $p = \{6, 5, 5, 6\}$: — DNS; — — $16 \times 16 \times 16$ using $p = 4$ with BR; ··· SBLDG.

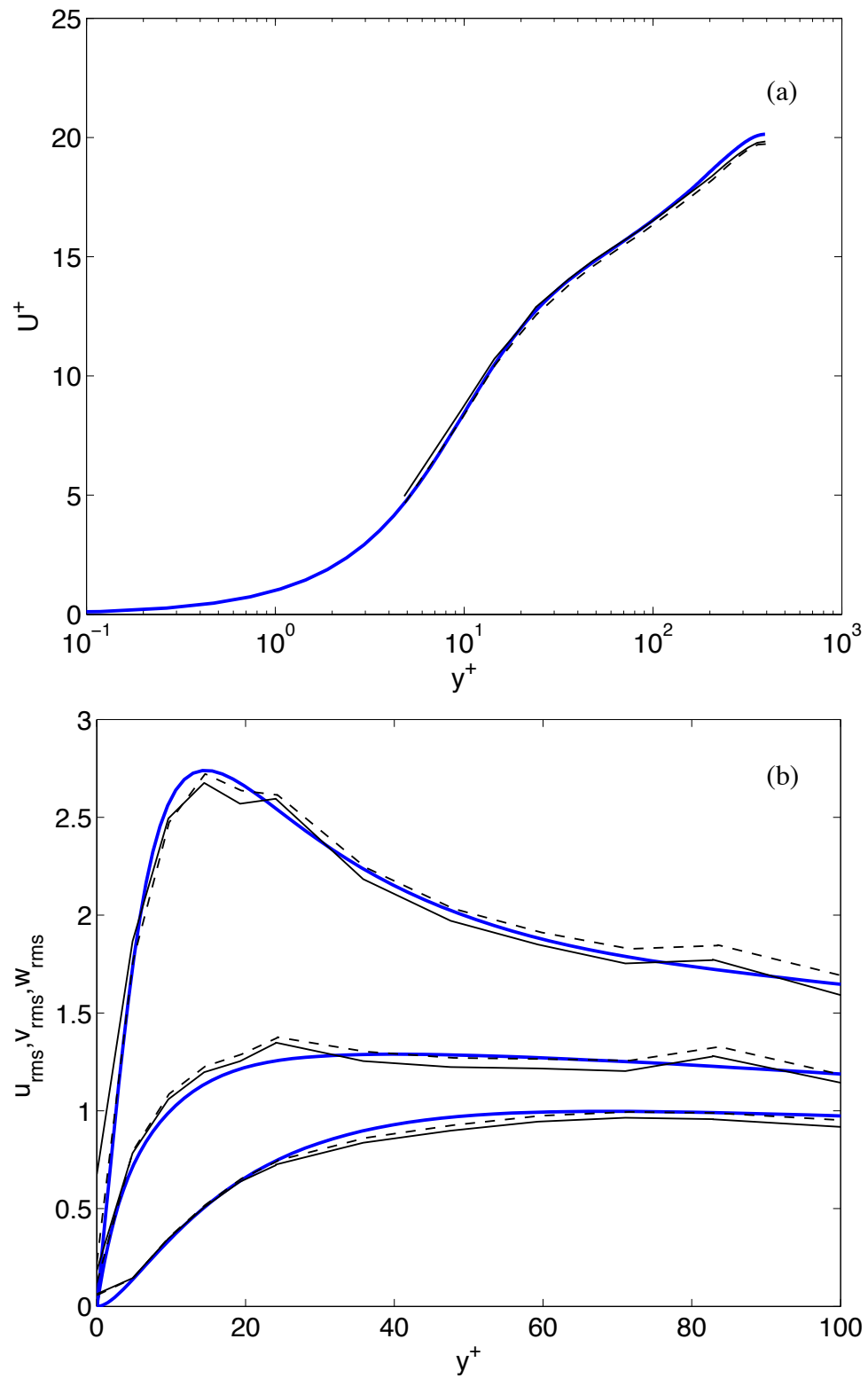


Figure 4.19: Effect of numerical viscous fluxes on meanflow and viscous stress profiles for $Re_\tau = 395$ computed on a $8 \times 8 \times 12$ mesh using $p = 4$: — DNS; — SBLDG; ---- LDG.

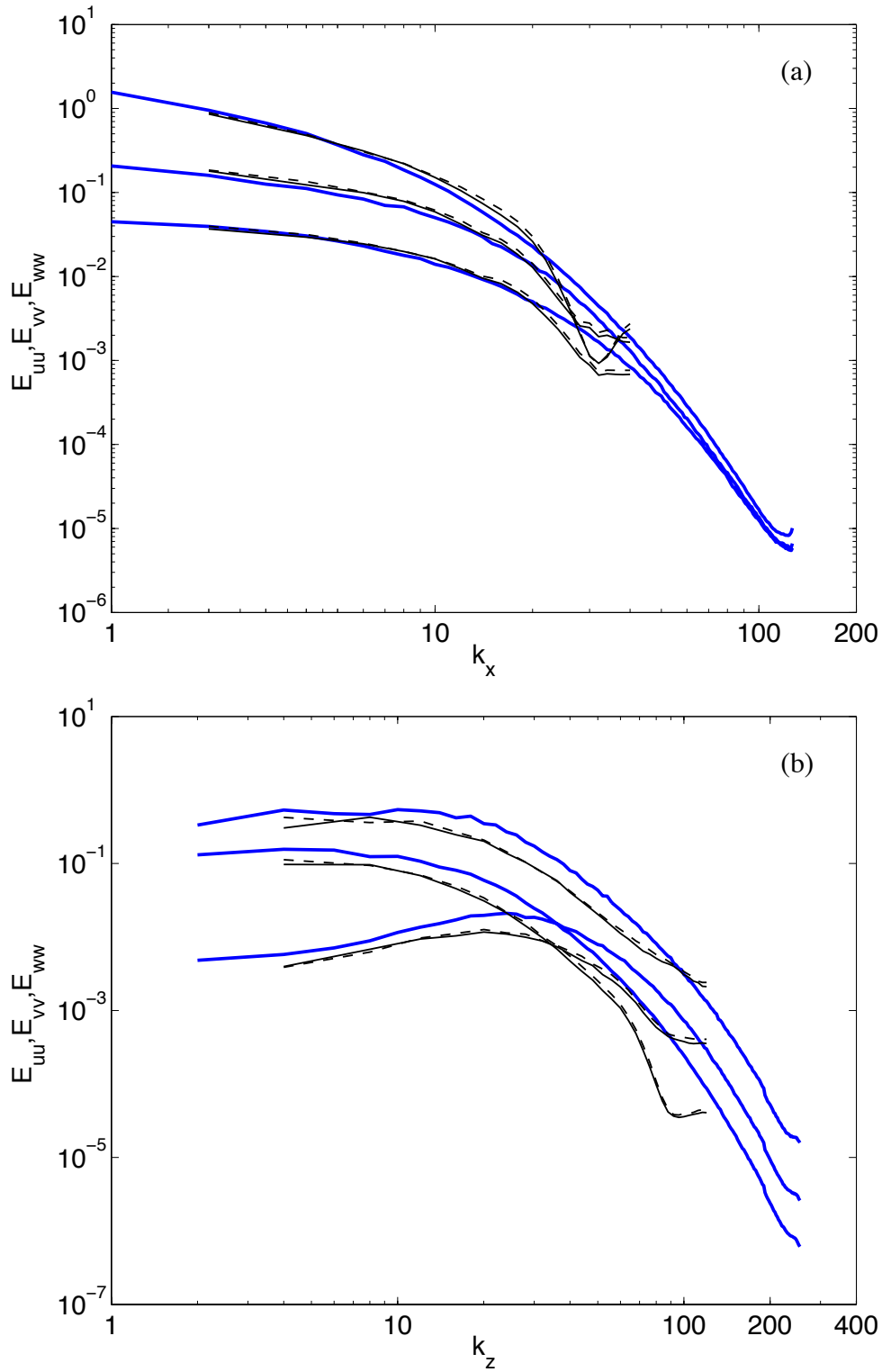


Figure 4.20: Effect of different numerical viscous fluxes on streamwise and spanwise spectra computed at $y^+ \approx 20$ for $Re_\tau = 395$ computed on a $8 \times 8 \times 12$ mesh using $p = 4$: — DNS; — SBLDG; ---- LDG.

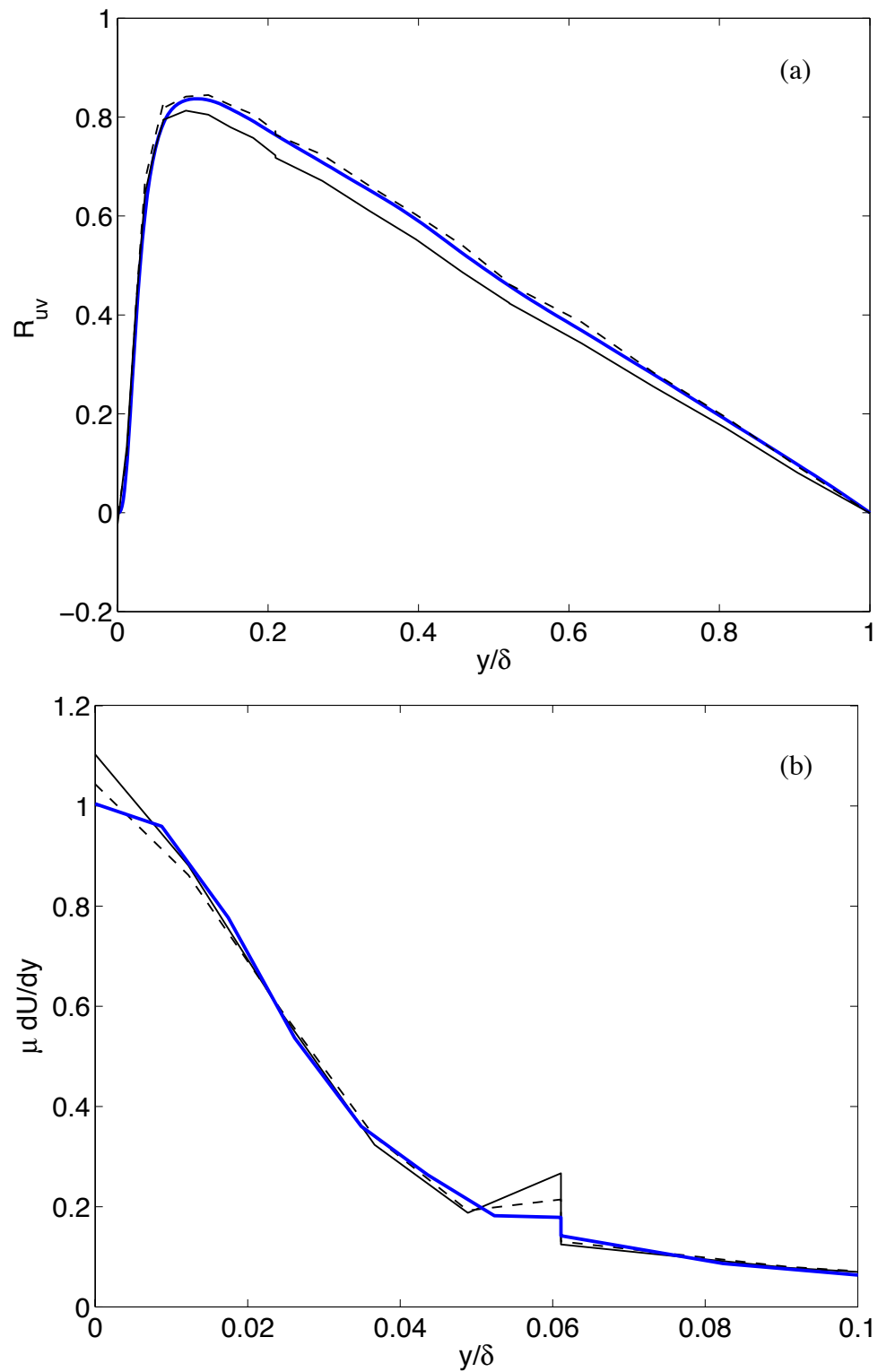


Figure 4.21: Effect of different numerical viscous fluxes on Reynolds stress and turbulence intensity profiles for $Re_\tau = 395$ computed on a $8 \times 8 \times 12$ mesh using $p = 4$: (a) — DNS; — SBLDG; ---- LDG. (b) — DG with BR flux on a $8 \times 8 \times 18$ using $\{6, 6, 5, 4, 4, 5, 6, 6\}$; — SBLDG; ---- LDG.

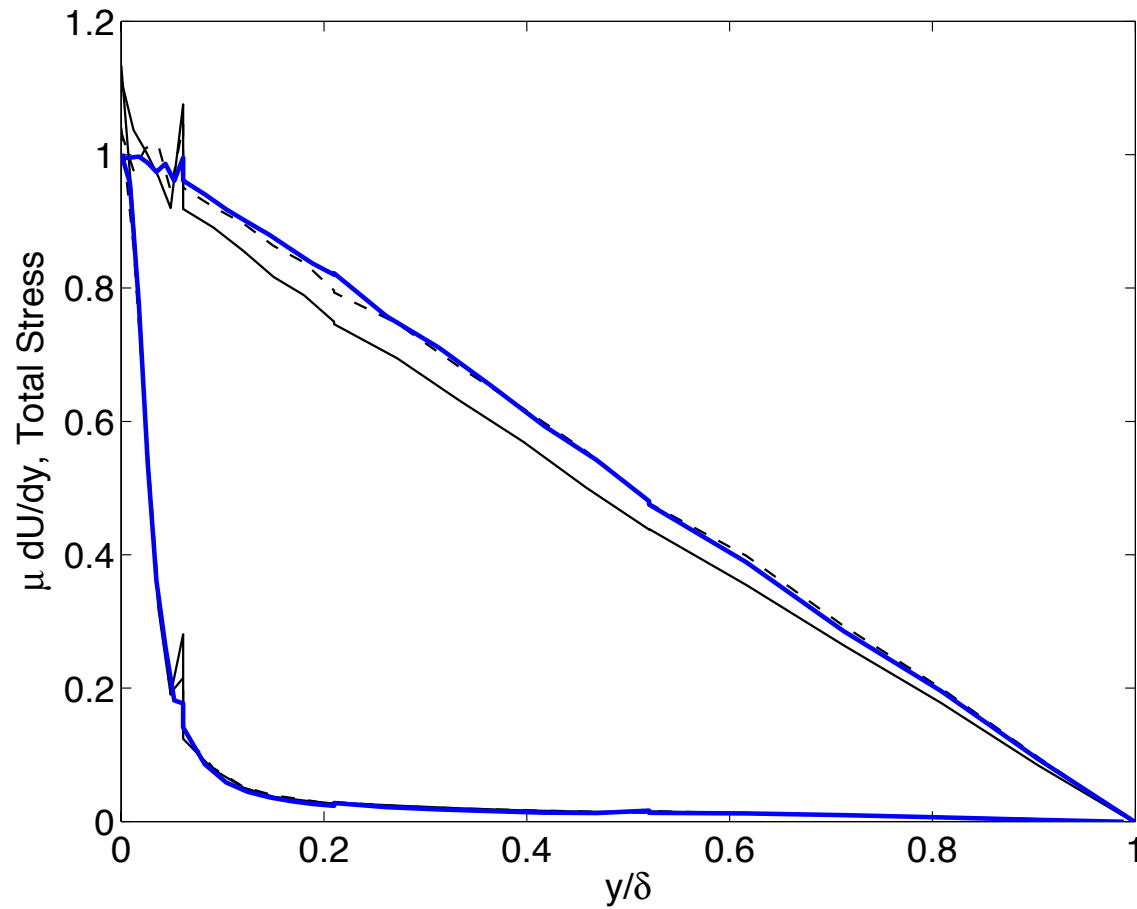


Figure 4.22: Effect of different numerical viscous fluxes on viscous and total stress for $Re_\tau = 395$ computed on a $8 \times 8 \times 12$ mesh using $p = 4$: — DG with BR flux on a $8 \times 8 \times 18$ using $\{6, 6, 5, 4, 4, 5, 6, 6\}$; — SBLDG; ---- LDG.

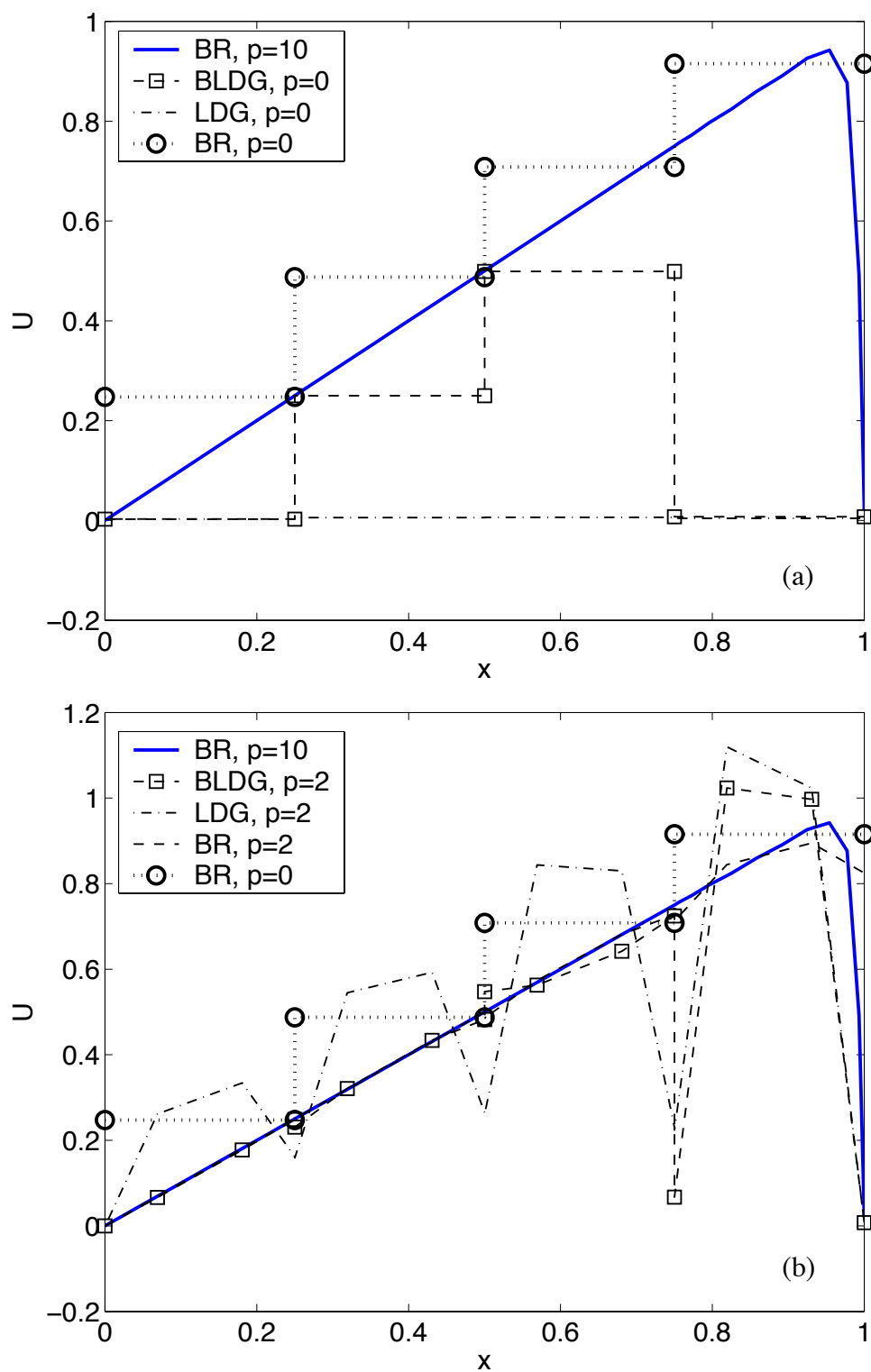


Figure 4.23: A comparison of the solution for different numerical viscous fluxes using $\epsilon = 100.0$ using two polynomial orders. (a) $p = 0$; (b) $p = 2$. The $p = 10$ DG solution obtained using BR flux is used as reference.

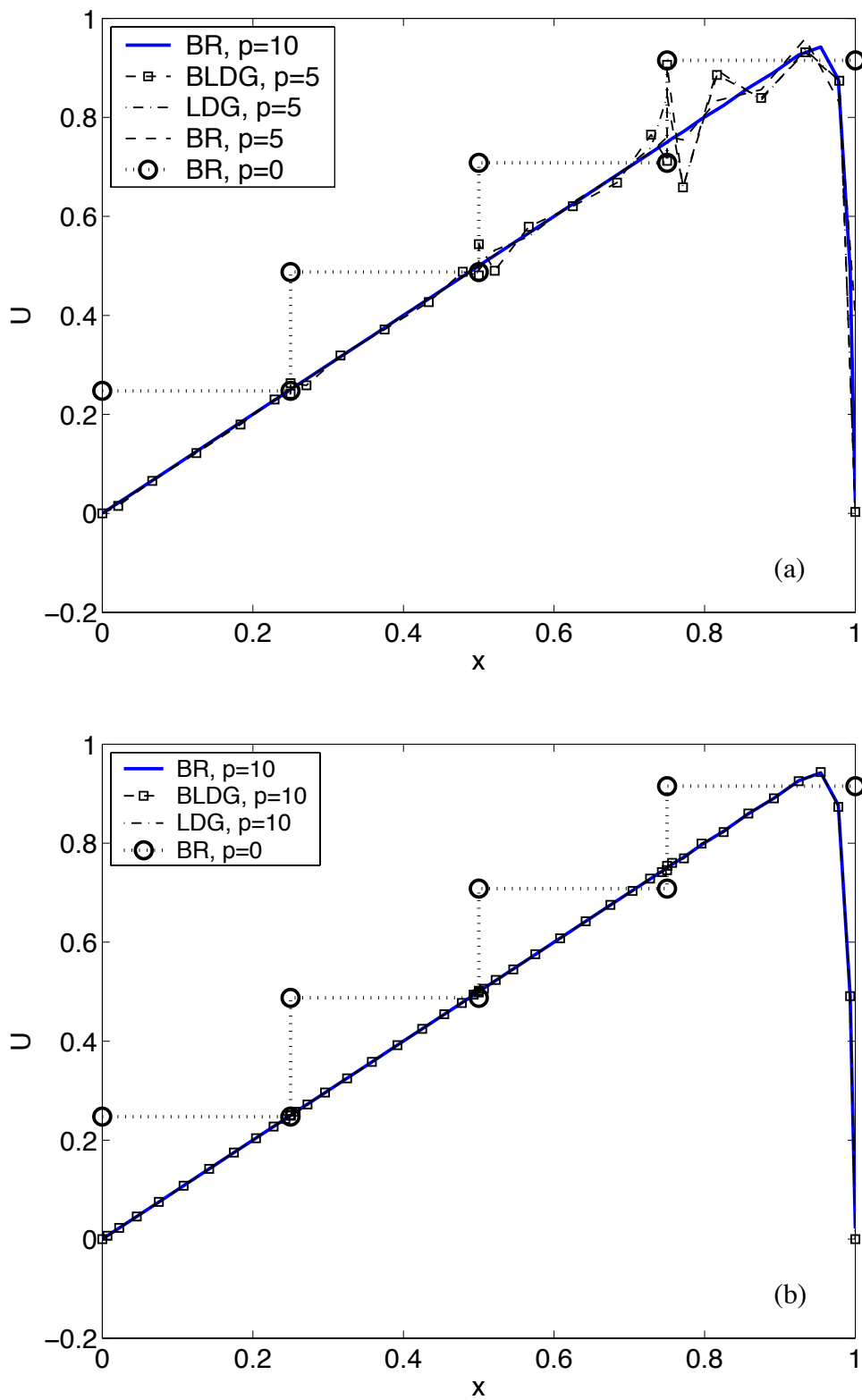


Figure 4.24: A comparison of the solution for different numerical viscous fluxes using $\epsilon = 100.0$ using high resolution. (a) $p = 5$; (b) $p = 10$.

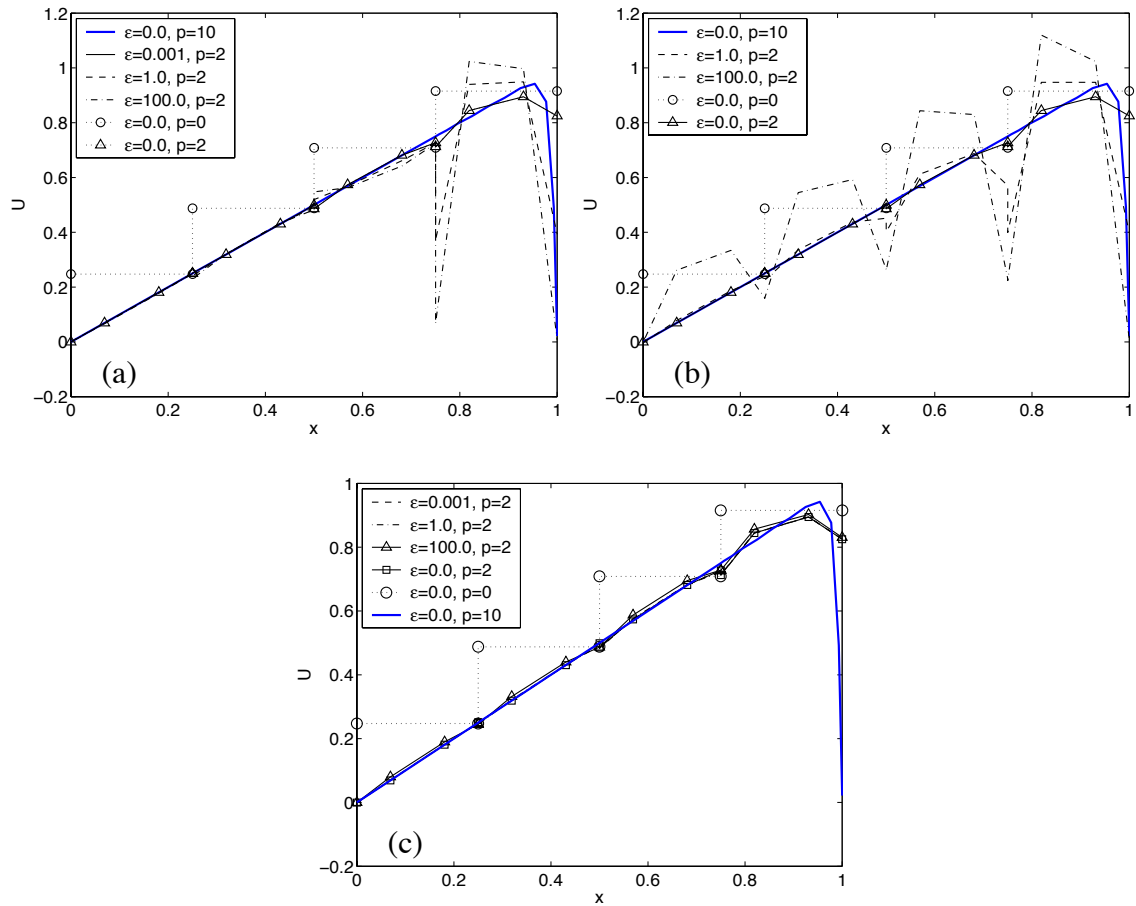


Figure 4.25: The effect of variation of ϵ on the solution for the different penalty based fluxes: (a) BLDG; (b) LDG (a) ILDG. ILDG is a special case of the LDG flux that uses BR at the physical boundaries.

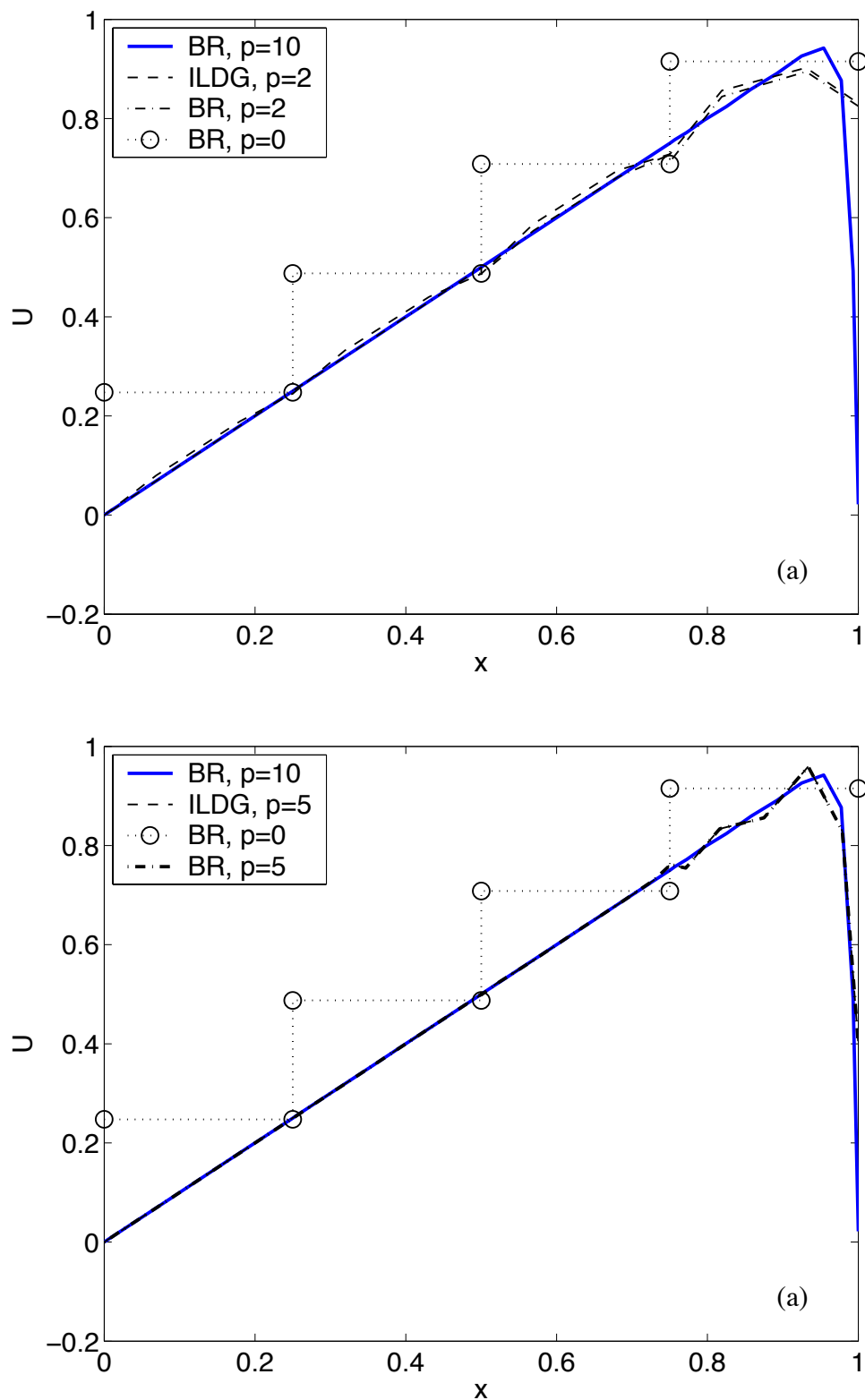


Figure 4.26: A comparison of the solution using ILDG with BR at two different polynomial orders. (a) $p = 2$;(b) $p = 5$.

Chapter 5

Local Variational Multi-Scale — ℓVMS

In this chapter, we develop strategies for SGS modeling by implementing a VMS model in the current DG spatial discretization. During the course of the spatial resolution study in Chapter 3, we mentioned the importance of sufficient resolution in the spanwise direction to ensure non-linear stability. Therefore, we first address this issue using two approaches, namely, spectral filtering [61] and polynomial dealiasing [67]. Next, we introduce the VMS model, described in Chapter 2, to account for SGS effects. Simultaneously, we comment on the role of the numerical viscous fluxes studied in Chapter 4 in the context of ℓVMS . Following the pattern in earlier chapters, we explore these methods at $Re_\tau = 100$ before we extending them to higher Reynolds numbers.

5.1 Strategies for Non-linear Stability

We observed the presence of aliasing [13, 58] and SGS effects, clearly seen by the pile up of energy at the high wavenumbers in the energy spectra. Fortunately, the *relatively* high resolution in the cases considered so far ensures that the solutions remain stable. In particular, the spanwise resolution appears to be crucial for maintaining non-linear stability. By having sufficient resolution in this direction, the fatal effects of low resolution are minimized.

Ideally, in the context of LES, one coarsens the mesh in all three coordinate directions. Further, since the effective number of degrees of freedom are reduced, we can expect a heightening of the effects of aliasing and SGS. Therefore, viable options to counter these effects needs to be established.

A SGS model, that enhances dissipation in the resolved scales can improve the non-linear stability of a simulation. However, a VMS model that acts only on the smallest resolved scales may not provide sufficient dissipation to *ensure* non-linear stability. On the other hand, a traditional constant coefficient Smagorinsky model that acts on all the resolved scales may be effective in producing stable calculations. However, conventional wisdom suggests that the dissipation introduced by the Smagorinsky model may lead to

excessive damping of the turbulent fluctuations [48, 76].

5.1.1 Polynomial Dealiasing (PD)

Recently, Kirby and Karniadakis [67] developed algorithms to successfully reduce aliasing in the context of one-dimensional Burgers equation using a DG discretization. They employ over-integration (super-collocation) coupled with a Galerkin projection to dealias the solution. They demonstrate the effectiveness of PD for incompressible channel flow at $Re_\tau = 395$ using a Galerkin spectral/ hp element method [67]. While this particular approach is new, a common strategy employed for dealiasing in global spectral methods is the $3/2$ -rule [13]. This approach is widely used to dealias simulations that have a quadratic non-linearity such as the convection term in the incompressible Navier-Stokes equations.

Along the same lines, Kirby and Karniadakis [67] advocate the use of a super-collocation method for dealiasing. This involves employing a greater number of quadrature points (q) than the number of modes (L) used to represent the solution. Specifically, they suggest that for a quadratic non-linearity, one should use a value of $3L/2$, similar to the $3/2$ -rule [13]. Currently, in the results presented thus far, we use a quadrature order, in each direction, as $q = L + 1$ that ensures that element integrals evaluations are sufficiently accurate for obtaining convergence with smooth solutions.

The PD approach of Kirby and Karniadakis [67] involves an *increase* in the computational cost. However, the results obtained by Kirby and Karniadakis [67], using a model one-dimensional Burgers problem, suggests that the increase is required just for the convection term that may potentially offset the cost factor. In fact, for channel flow simulations, the $3/2$ -rule is applied only in the planes ($x - z$ plane) [13]. Here, as a first attempt towards dealiasing using this approach [67], we apply a super-collocation approach for both the convection and diffusion terms in all three coordinate directions.

A potential advantage of using polynomial dealiasing is increased accuracy since all the integral evaluations are done using a higher quadrature order. Importantly, PD has no foreseeable adverse impact on the the solution. While the disadvantage is an increase in the computational cost. Now, it is important to note that, in VMS, modeling is confined to the smallest resolved scales [28, 46]. As a result, there is no direct mechanism present to remove aliasing errors that equally affect all the resolved scales including the large scales. Importantly, a major feature attributed to the success of prior VMS implementations is the preservation of accuracy of the large resolved scales by having no explicit model acting

on them. The authors are not aware of any VMS implementation that has not employed dealiasing. Therefore, preventing the adverse effects of aliasing errors on the large scales is necessary to obtain results that are comparable with prior VMS implementations [47, 48, 71, 76, 78].

5.1.2 Spectral Filtering (SF)

The Boyd-Vandeven Spectral Filter (SF) was used by Levin and colleagues [61] in a spectral element method for ocean modeling. They apply filtering on the vorticity and divergence fields to achieve non-linear stability. Here, we apply the same SF to the residual after each TVD-RK substep. The SF is described below.

$$\sigma(i/L, s) = \begin{cases} 1, & \text{if } i < s \\ \frac{1}{2} \operatorname{erfc}(2\sqrt{L}\chi(\theta)(|\theta| - \frac{1}{2})), \theta = \frac{i-s}{L-s} & \text{if } s \leq i \leq L \end{cases} \quad (5.1)$$

and

$$\chi(\theta) = \begin{cases} 1, & \text{if } \theta = \frac{1}{2} \\ \sqrt{-\frac{\log(1-4\Omega^2)}{4\Omega^2}}, \Omega(\theta) = |\theta| - \frac{1}{2} & \text{elsewhere} \end{cases}, \quad (5.2)$$

where i is a index for the modes ($0 \leq i \leq L$) and $L = p + 1$. The spectral shift parameter s biases the filtering action towards the higher modes (See Levin *et al.* [61] for additional details). The transfer function in modal space can be seen in Figure 5.1 for various polynomial orders. The mechanism by which aliasing errors are managed using this approach is by enhancing the dissipation (filtering) in the smallest resolved scales (or high wavenumbers in spectral space). Thus, preventing the energy from accumulating on the smallest scales.

The potential advantages of spectral filtering are

1. Enhancing dissipation at the high wavenumbers improves non-linear stability.
2. The transfer function in three-dimensional can be constructed using a tensor product approach allows for a natural implementation of the spectral filter in the current framework.
3. The spectral shift, s , reduces the impact of filtering on the large scales that is similar in spirit to the VMS model.
4. This is a computationally efficient option compared with polynomial dealiasing [67].

A potential disadvantage of this approach is reduced accuracy. Also, there is no *a priori* rationale for picking the filter parameters.

5.1.3 Numerical Viscous Fluxes

The importance of boundary enforcement using the numerical fluxes was shown to have significant impact on the accuracy of the wall shear stress predictions, particularly while using coarse grids ($\Delta y_w^+ \geq 2$). The energy spectra and viscous stress profiles, with the introduction of jump penalty, showed improvements consistent with enhanced dissipation. While PD and SF are strategies that address non-linear stability directly, the potential of penalty numerical fluxes in improving non-linear stability in the context of ℓ VMS is also explored here. This is significant since the computational overhead incurred with the introduction of a solution jump penalty is negligible.

5.2 Numerical Results Preliminaries

The introduction of SF, PD, numerical fluxes, and ℓ VMS individually and in combination lead to number of parameters. For quick reference, we describe these parameters (although they may have been defined before) and introduce/recall the symbols used to represent them.

1. p , the polynomial order.
2. q , the quadrature order for a given p , this is an important parameter since a value of $q > p + 2 \equiv L$ is considered a super-collocation method that commonly referred to as Polynomial Dealiasing (PD) [67], where L is the number of modes $L = p + 1$.
3. L_e , partition parameter that divides the modal space of an element (e) such that $P_{p_e}(\Omega_e) = \{0, \dots, L_e, \dots, p\}$ in each direction. Thus, modes less than L_e are considered large scales while the remaining modes including L_e form the small scales.
4. s , the spectral shift for the Spectral Filter (SF) [61] is similar to L_e . Therefore, modes less than s are not directly affected by the filter, while the modes including s are influenced by the action of filtering.
5. $\epsilon > 0$ is the penalty factor that has the same meaning as before in Chapter 4. Incidentally, we set $\epsilon = 0.0$ to recover the BR numerical viscous flux [6].

6. For simplicity, we use a Smagorinsky coefficient, $C_s = 0.1$ for all the cases presented here that has been successful in other VMS implementations [47, 48, 71, 76, 78].
7. Slip refers to the planar averaged mean streamwise velocity at the wall i.e solution jump in the streamwise velocity at the channel wall.

The total number of simulation parameters present here, for reasons of limited computational resources, prevents an extensive study at Reynolds number greater than $Re_\tau = 100$. Therefore, we explore the use of the parameters listed above in the context of ℓ VMS at this lower Reynolds and then present cases at higher Reynolds number to corroborate the observations at the lower Reynolds number. Also, unless explicitly stated the numerical viscous flux is BR [6].

5.3 Non-linear Stability – Filtering and Dealiasing

We begin with a $4 \times 4 \times 4$ mesh using $p = 5$ that gives a planar resolution in wall units as $\Delta x^+ \approx 314$ and $\Delta z^+ \approx 104$ with a minimum near-wall resolution based on the collocation grid $\Delta y_w^+ \approx 2.14$ ($\Delta y_m^+ \approx 25$). As mentioned in Chapter 3, using $p = 3$ with this mesh the simulation is non-linearly unstable and that applies even at $p = 5$. Recall that doubling the number of elements from 4 to 8 ($\Delta z^+ \approx 50$) in the spanwise direction resulted in stable computations even with $p = 3$.

Now, Figures 5.2, 5.3, and 5.4 show the profiles of meanflow, rms, streamwise and spanwise direction spectra, Reynolds stress, and an overlay of the viscous and total stress profiles for the simulations listed in Table 5.1. This study evaluates the effectiveness of PD [67] and SF [61] for ensuring non-linear stability. Firstly, using $s = 3$ is sufficient to ensure stability for long time computation. Using $s = 1$, we introduce filtering on a wider range of scales that results in a greater underprediction of τ_w compared with $s = 3$ (see Figure 5.2(a)). To evaluate the efficacy of PD, using the same mesh and polynomial order, we increase the quadrature order from $q = 7$ to $q = 10$. Although this is one quadrature order greater than $3L/2$ for illustrative purposes, we have confirmed that a value of $3L/2$ is sufficient to ensure non-linear stability.

The meanflow profile for PD, shown in Figure 5.2(a) results in a slight overprediction of drag compared with the reference [14]. Now, a comparison of the rms profiles, seen in Figure 5.2(b), shows an overall better agreement with reference DNS [14] for PD with

respect to the two SF simulations. It is important to point out that we compute all our statistics on the collocation grid. Therefore, the spectra for the cases that employ PD span a wider number of wavenumbers. First, we note that using this resolution, the artificial accumulation of energy at the highest wavenumbers is reduced (see Figure 5.3). Note the good correspondence of the energy spectra for both PD and SF with $s = 3$ in the largest scales i.e. low wavenumbers. Meanwhile, the dissipative effect of spectral filtering is confirmed by the lower energy in the spectra for $s = 1$ with respect to the other two cases shown in Figure 5.3.

Importantly, both approaches are successful in reducing aliasing errors sufficiently that lead to stable computations. However, solutions obtained using PD [67] show improved low-order predictions that suggests a potential advantage when compared to spectral filtering [61]. Meanwhile, the Reynolds stress and total stress, shown in Figure 5.4, for all the cases show reasonable agreement with the reference [14]. Finally, the viscous stress profiles for cases employing filtering, shown in Figure 5.4(b), have a noticeably more prominent viscous sublayer compared to super-collocation method. This further supports the claim that the action of spectral filtering is dissipative in nature.

These results demonstrate the suitability of PD as an effective strategy for enhancing stability whilst simultaneously isolating SGS effects. This is seen by the higher energy content in the spectra, clearly observed in the u component of x -direction energy spectra shown in Figure 5.3(a). Meanwhile, even with $s = 3$, required to ensure stability, the dissipation introduced by spectral filtering makes the role SGS modeling unclear.

Later in this chapter, we explore a strategy, involving the use of jump penalized viscous numerical fluxes (see Chapter 4), that allows the use of a milder spectral filter i.e. a larger spectral shift (s) to control aliasing errors in the context of ℓ VMS. This approach is attractive as the computational cost associated with spectral filtering [61] is lower than that for polynomial dealiasing [67].

5.4 ℓ VMS Modeling

Before we present results with SGS modeling, it is important to discuss parameter selection in the context of ℓ VMS.

5.4.1 Parameter Selection

The improved non-linear stability achieved through PD allows a greater flexibility in the choice of the mesh and polynomial order. Additionally in ℓ VMS, the partition L_e that separates the resolved scales as large and small is required. This is a crucial parameter that determines the accuracy of VMS simulations [47, 48, 76, 78].

First, we select the mesh and polynomial order based on the resolution study conducted in Chapter 3 that accounts for the inherent dissipation present in the spatial discretization [19, 44]. From Chapter 3, at $Re_\tau = 100$ a 4×8 planar mesh with $p > 4$ is needed to ensure both non-linear stability and low numerical dissipation. Here, we have demonstrated that a 4×4 planar mesh using $p = 5$ with PD is sufficient to produce results with no perceivable adverse effects of numerical dissipation.

Further, the resulting element sizes in viscous wall units in the x - and z -directions correspond to well-known length scales of the physical structures in the flow [54, 55, 85]. Plots of near-wall streamwise and spanwise direction velocity correlations for $Re_\tau = 100$ extracted from a $8 \times 8 \times 8$ mesh using $p = 6$ simulation are shown in Figure 5.5. The correlations for all three velocity components are considerably diminished by $x^+ \approx 400$ and $z^+ \approx 100$ (mean streak spacing) in the streamwise and spanwise directions, respectively [54, 55, 85]. Also, notice the sharp drop-off in the correlation at $x^+ \approx 200$ and $z^+ \approx 50$.

Recently, Ramakrishnan and Collis [76, 78] successfully used these length scales to identify the large scales in their VMS implementation. The numerical discretization in their study employed a Fourier basis in the planar directions that allows a transparent interpretation of modes and the associated physical length scales, leading to a surgical identification of the large and small scales. Analogous to their approach, we select $L_e = 2$ that constrains the first two modes (constant and linear) in each direction of an individual element to represent the large scales and the remaining modes form the small scales. This ensures that the constant mode that corresponds to the individual element size is in the large scale space. Meanwhile, the linear mode that divides the element is representative of the length scales where the x - and z - direction velocity correlations show a sharp drop-off (see Figure 5.5). In doing so, we largely ensure that length scales $\Delta x^+ \geq 200$ and $\Delta z^+ \geq 50$ that relate to the near-wall coherent structures form the large scales.

Finally, the elements in the wall-normal direction are stretched such that the first element size in the wall-normal direction is $\Delta y_m^+ \approx 25$. This length scale matches the diameter

of a typical near-wall structure [54, 55, 85]. Ramakrishnan and Collis [78] apply scale separation in just the planar directions in lieu of all three coordinate directions introduced in the original implementation by Hughes *et al.* [48]. Results of similar quality obtained by the two approaches suggest that scale separation in the wall-normal direction does not greatly influence the solution. Here, we follow the original implementation of Hughes *et al.* [48] that likely results in a larger small scale space than that obtained in the implementation of Ramakrishnan and Collis [78]. Finally, we observe that with $L_e = 2$ in the near-wall region, we ensure that $\Delta y^+ \approx 25$ corresponding to the constant mode, related to the size of the coherent structures, lies in the large scale space.

5.4.2 Polynomial Dealiasing

A comparison of the results obtained using SF with $s = 3$, PD, and ℓVMS -PD is presented in Figures 5.6, 5.7, and 5.8. The simulation parameters and results are found in Table 5.1.

The introduction of the VMS model leads to improved low-order statistics that can be seen in Figure 5.6. The model dissipation, accounting for the SGS scales, leads to a mean-flow profile, shown in Figure 5.6(a), that is in better agreement with the reference [14]. Similarly, the rms profiles, seen in Figure 5.6(b), for ℓVMS -PD are in good correspondence with DNS [14] compared with just PD. Consequently, there is a reduction in the peaks of the u and w components of the rms profiles for the former when compared to the latter.

The energy spectra, shown in Figure 5.7, reveals that an overall better agreement with the reference [14] is achieved through enhanced model dissipation at the higher wavenumbers. The multi-scale model introduces modeling in the range of scales most affected by SGS i.e. the smallest resolved scales. The enhanced model dissipation in the high wavenumbers coupled with dealiasing prevent the accumulation of energy in the resolved scales. Thereby, the interactions between the *resolved* large and small scales are improved. Thus, although there is no direct modeling on the large scales, the large scales influence the effect of modeling through the non-linear interactions leading to improved predictions. This provides insight into the mechanism of multi-scale modeling that is clearly superior to traditional approaches that introduces explicit modeling on *all the resolved scales* [77].

Incidentally, we note that the overall dissipative effect of the VMS model with PD (ℓVMS -PD) is less compared to the SF with $s = 3$. Finally, the stress profiles, shown in Figure 5.8, exhibit trends consistent with the introduction of model dissipation. Thus, demonstrating

the effectiveness of VMS modeling with polynomial dealiasing for a DG spatial discretization.

5.4.3 Role of Numerical Fluxes and Spectral Filtering

Let us again consider the $Re_\tau = 100$ case employing a $4 \times 4 \times 4$ mesh using $p = 5$. We examine the results obtained with the cases listed below to highlight the role of L_e , viscous numerical fluxes, and spectral filtering in ℓ VMS modeling.

1. Standard constant coefficient Smagorinsky with wall-damping i.e. ℓ VMS with $L_e = 0$.
2. ℓ VMS with $L_e = 1$.
3. ℓ VMS with $L_e = 2$ and SBLDG.
4. ℓ VMS with $L_e = 2$ using $s = 4$ and SBLDG.

A summary of the simulation parameters and results are recorded in Table 5.2.

Firstly, the meanflow profile, seen in Figure 5.9(a), indicates that the standard Smagorinsky model is highly dissipative, as expected. Although not shown here, we note that the other statistics for the Smagorinsky model exhibit signs consistent with the excessive damping of turbulent fluctuations. Here, we reiterate that the constant coefficient Smagorinsky is a limiting case of ℓ VMS with $L_e = 0$ i.e. *all* the resolved scales are in the small scale space (where the explicit SGS model is active). Next, using BR, we obtain stable computation with ℓ VMS only when $L_e \leq 1$. Meanwhile, we achieve stability with ℓ VMS using $L_e = 2$ by choosing SBLDG in lieu of BR. Finally, we introduce a mild SF ($s = 4$) in the above case to account for the presence of aliasing.

The ℓ VMS and BR combination, that requires $L_e = 1$, results in an underprediction in τ_w (see Figure 5.9(a)). The choice of the partition $L_e = 1$ allows the model acts directly on the dynamically important large scales. Recall that using large Δy_w^+ leads to a higher energy content in the spectra, attributed to the slip at the channel walls. Therefore, it is likely that enhancing model dissipation on the energy containing scales is required to improve stability. However, this results in an excessive damping of the turbulent fluctuations. Importantly, the improvement in the meanflow profile for ℓ VMS with $L_e = 1$ over the traditional Smagorinsky model demonstrates the superiority of the VMS modeling paradigm.

Simultaneously, the importance of the L_e in determining the accuracy of the large scales and thereby the quality of the results obtained is highlighted.

Clearly, the enhanced stability with SBLDG may be attributed to the introduction of the jump penalty. The enhanced stability of SBLDG with ℓ VMS suggests that introduction of the jump penalty has a stabilizing influence on the dynamically important large scales. This is not surprising since the largest resolved scales are affected by the geometry of the domain through the boundary conditions. Therefore, the penalty imposed on the fluctuating slip at the channel walls through the viscous numerical flux may have a beneficial effect on the large scales. As mentioned earlier, the penalization potentially introduces dissipation [19] in the numerical scheme and this could also improve the stability of the simulation.

Now, the ℓ VMS-SBLDG with $L_e = 2$ results in a slight overprediction in drag (see Figure 5.9(a)). Now, on the same plot, note that introducing a mild SF ($s = 4$) enhances dissipation that results in a slight underprediction in the wall shear stress. The differences in the rms and stress profiles for the above cases, seen in Figures 5.9(b) and 5.10, reflect the effects of enhancing dissipation through modeling and spectral filtering.

As usual, an examination of the energy spectra, seen in Figure 5.11, provides additional insight into effect of the modeling in ℓ VMS. Using $L_e = 1$, where the model directly affects a wider range of scales than the cases with SBLDG, the spectra shows a lower energy content than the reference [14]. Thus, providing further evidence of the adverse effects of introducing model dissipation on the large scale structures in the flow. By contrast, the ℓ VMS-SBLDG without filtering is not able to fully account for aliasing errors resulting in a higher energy content than the reference [14]. However, enhancing the dissipation at the highest wavenumbers (smallest resolved scales) through a SF with $s = 4$ leads to an overall better agreement of the energy dynamics with the reference [14]. These results reinforce the need for an effective dealiasing strategy with ℓ VMS. Also, the success of the current modeling strategy is significant since it is computationally more efficient compared with the ℓ VMS-PD combination.

5.4.4 Importance of Small Scales Space

We have demonstrated the importance of the partition (L_e) in isolating the energy containing scales, in other words, ensuring a sufficient large scales space. Let us now examine the effect of varying the partition from $L_e = 2$ to $L_e = 3$, effectively reducing the small scales space, using SBLDG with the current mesh and polynomial order (refer to Table 5.2).

The meanflow profile, seen in Figure 5.12(a), shows that reducing the small scale space leads to a significant overprediction in τ_w . The rms profiles, particularly in the spanwise and wall-normal components, show a significantly higher peak for $L_e = 3$ when compared with the cases employing $L_e = 2$. As usual, the effects of reducing model dissipation are most clearly observed in the energy spectra plotted in Figure 5.13. Note the progressive increase in the energy content of the streamwise component, shown in Figure 5.13(a), starting from $L_e = 2$ with filtering to $L_e = 3$ without filtering. Further, the difference in the energy content between $L_e = 2$ and $L_e = 3$ appears to be of the same magnitude as the difference that exists between the $L_e = 2$ case with and without filtering.

It is important to understand that a change in the partition of just one mode leads to reduction in the small scale space in *all* three directions and across *all* the elements. From a modeling perspective, a diminished small scale space increases the effect of the unresolved scales on the resolved large scales. Simultaneously, the explicit modeling is confined to shorter range of scales. Another subtle feature of multi-scale modeling is the indirect effect of modeling on the large scales through the nonlinear interactions between all the resolved scales. Also, it is likely that the effects of aliasing are more pronounced for $L_e = 3$. It is for all the above reasons that we witness a dramatic change in the solution going from $L_e = 2$ to $L_e = 3$.

5.4.5 Local Polynomial Enrichment

Now, exploiting the capabilities of ℓVMS we introduce local polynomial refinement. Let us vary the polynomial order from a uniform $p = 5$ to $p = \{6, 5, 5, 6\}$ at $Re_\tau = 100$. The simulation parameters and results are found in Table 5.2. We retain the same partition $L_e = 2$ that corresponds to the important length scales in the flow [76, 77]. And similarly, we employ the same spectral shift $s = 4$ for direct comparison with the uniform $p = 5$ case.

Immediately, we observe an improvement in the meanflow and rms profiles, shown in Figure 5.14, for the variable polynomial order case with respect to the uniform $p = 5$ case. Moreover, the highest resolved wavenumbers in the energy spectra, shown in Figure 5.15, appear to have benefitted from the increased resolution i.e. a wider small scale space. In VMS, the greater scale separation reduces the impact of the unresolved scales on the largest resolved scales [76, 77]. Consequently, the accuracy of the large scales are improved leading to better predictions. Further, the local p -refinement at the channel walls leads to

better prediction of the velocity gradients due to a smaller Δy_w^+ . Thus, the stress profiles, shown in Figure 5.16, for the variable polynomial order show better correspondence with the reference [14] (clearly observed in the total stress profile in Figure 5.16(b)).

The efficacy of local polynomial refinement in improving the solution efficiently using ℓ VMS illustrates the potential of the current framework for accurate and efficient simulation of wall-bounded turbulence. Moreover, in general configurations (see Figure 2.3), the ability to change the partition (L_e) along with the local hp -refinement holds promise for surgical modeling of turbulent flows in complex geometries.

5.4.6 Moderate Reynolds Number

Finally, we extend ℓ VMS to a higher Reynolds number, namely, $Re_\tau = 395$. The details of the simulation are listed in Table 5.3. The domain size is chosen such that with $p = 5$, we can employ the same partition and spectral shift as the $Re_\tau = 100$ case. Specifically, the mesh and domain size are $(4 \times 9 \times 6)$ and $(\pi, 2, \pi/2)$ in the x , y , and z directions, respectively.

The meanflow profile, shown in Figure 5.17(a), is in reasonable agreement with DNS [69]. However, the combination of the VMS model, SF, and the inherent dissipation at the current resolution lead to a slight underprediction in the wall shear stress similar to the $Re_\tau = 100$ case. Perhaps, local polynomial refinement in the near-wall region will improve the τ_w prediction, as observed with the $Re_\tau = 100$ above. Meanwhile, the rms profiles, energy spectra and stress profiles, shown respectively in Figures 5.17(b), 5.18, and 5.19, all show reasonable agreement with the reference [69].

The similarity in the quality of results obtained at this Reynolds number to that observed with $Re_\tau = 100$ illustrates the effectiveness of parameter selection developed here. Simultaneously, preliminary resolution guidelines for obtaining reliable low-order statistics for wall-bounded turbulence using ℓ VMS are established.

5.5 Summary

The introduction of ℓ VMS in the DG method developed in Chapter 3 and 4 leads to an overall reduction in computational cost in terms of required degrees of freedom. Also, in order to ensure the non-linear stability of the computations, we have studied two approaches: spectral filtering [61] and polynomial dealiasing [67]. Both approaches, using appropriate

parameters, lead to stable calculations. Spectral filtering is found to be a computationally efficient approach to minimize the effects of aliasing while PD involves increasing the quadrature order. In fact, the combination of SBLDG and spectral filtering provides a computationally efficient strategy for modeling in ℓ VMS. Unfortunately, this approach introduces a number of parameters (s, ϵ) in addition to the model parameters that need to be specified. Further, the selection of these parameters for general flow configurations will require numerical experimentation. Meanwhile, the ℓ VMS-PD combination requires just one additional well-defined parameter ($q = 3L/2$), leading to an overall simpler modeling strategy. Moreover, we note that results obtained using a combination of PD with ℓ VMS are in particularly good agreement with reference DNS.

In ℓ VMS, we choose the element sizes according to the size of the near-wall turbulent structures. This allows for partition selection (L_e) to be based on the important length scales present in the flow. This approach to partition selection, known to be successful for turbulent channel flows [76, 77], is reaffirmed here.

Overall, the locality of the DG/VMS framework allows improved predictions through an efficient distribution of the required degrees of freedom. Here, we have successfully exploited this capability for the turbulent channel flow. This feature of ℓ VMS along with the ability to specify model parameters independently on each element holds promise for accurate and efficient turbulence simulation in complex geometries. Thus, exploring the potential of ℓ VMS by fully exploiting its capabilities will be a logical extension for future work.

Model	p	q	s	L_e	Slip	τ_w	u_τ
SF	5	7	1	-	0.1319	0.8487	0.9207
SF	5	7	3	-	0.1590	0.8708	0.9325
PD	5	10	-	-	0.2011	0.9558	0.9770
ℓVMS -PD	5	10	-	2	0.1816	0.9142	0.9554

Table 5.1: Simulation parameters and result summary for a $4 \times 4 \times 4$ using $p = 5$ to compare spectral filtering against dealiasing $Re_\tau = 100$. The element size in wall units for this mesh topology is $\Delta x^+ \approx 314$ and $\Delta z^+ \approx 104.3$ in the streamwise and spanwise directions, respectively. The minimum wall-normal direction resolution based on the standard collocation grid is $\Delta y_w^+ \approx 2.14$ ($\Delta y_m^+ \approx 25$).

Model	Flux	p	q	ϵ	s	L_e	Slip	τ_w	u_τ
SMAG	BR	5	7	0.0	-	0	-0.0827	0.7586	0.8706
ℓVMS	BR	5	7	0.0	-	1	0.1321	0.8559	0.9246
ℓVMS	SBLDG	5	7	100.0	-	2	0.3525	0.9548	0.9762
ℓVMS -SF	SBLDG	5	7	100.0	4	2	0.2216	0.9037	0.9498
ℓVMS	SBLDG	5	7	100.0	-	3	0.4108	1.0501	1.0237
ℓVMS -SF	SBLDG	$\{6, 5\}$	$\{8, 7\}$	10.0	4	2	0.1408	0.9300	0.9636

Table 5.2: Simulation parameters and result summary for a $4 \times 4 \times 4$ mesh using $p = 5$ for $Re_\tau = 100$ to study non-linear stability, partition selection and VMS modeling.

Model	Flux	p	q	ϵ	s	L_e	Slip	τ_w	u_τ
ℓVMS -SF	SBLDG	5	7	10.0	4	2	0.3690	0.93462	0.9663

Table 5.3: A result at $Re_\tau = 395$ to demonstrate the applicability of the guidelines developed at $Re_\tau = 100$ with ℓVMS for higher Reynolds numbers. A $4 \times 9 \times 6$ mesh used in this study gives a planar resolution $\Delta x^+ \approx 310$ and $\Delta z^+ \approx 103$ viscous wall units. Meanwhile the minimum near-wall resolution is the y -direction is $\Delta y_w^+ \approx 2.305$. These parameters are selected to match the $4 \times 4 \times 4$ case at $Re_\tau = 100$ using $p = 5$.

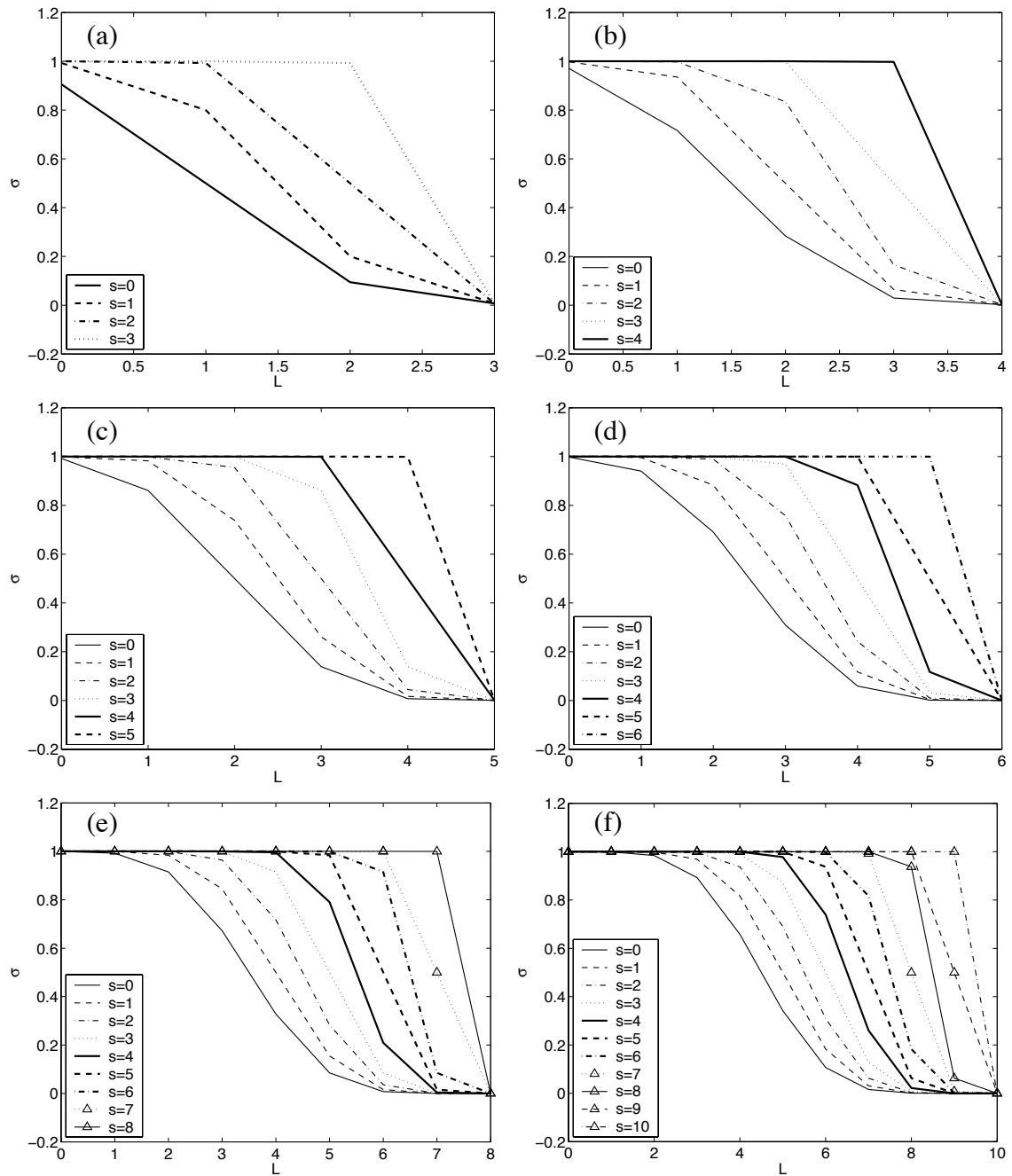


Figure 5.1: Spectral filter transfer functions for different polynomial orders. (a) $p = 3$. (b) $p = 4$. (c) $p = 5$. (d) $p = 6$. (e) $p = 8$. (f) $p = 10$. s is the spectral shift parameter.

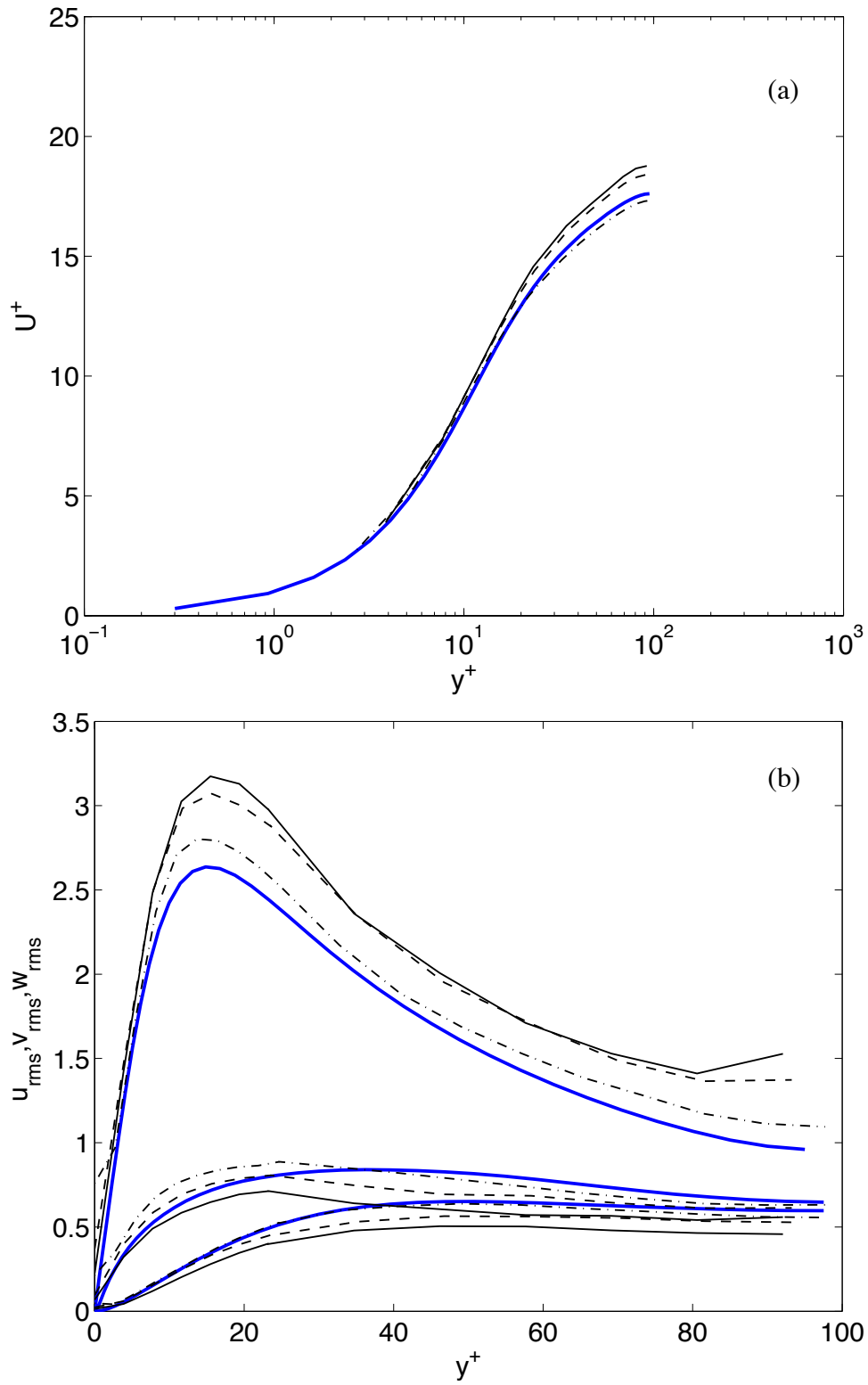


Figure 5.2: Meanflow and rms profiles for $Re_\tau = 100$ computed with a $4 \times 4 \times 4$ mesh using $p = 5$ at $Re_\tau = 100$ with SF [61] and PD [67]: — DNS; — $s = 1$; ---- $s = 3$; —·— $q = 10$.

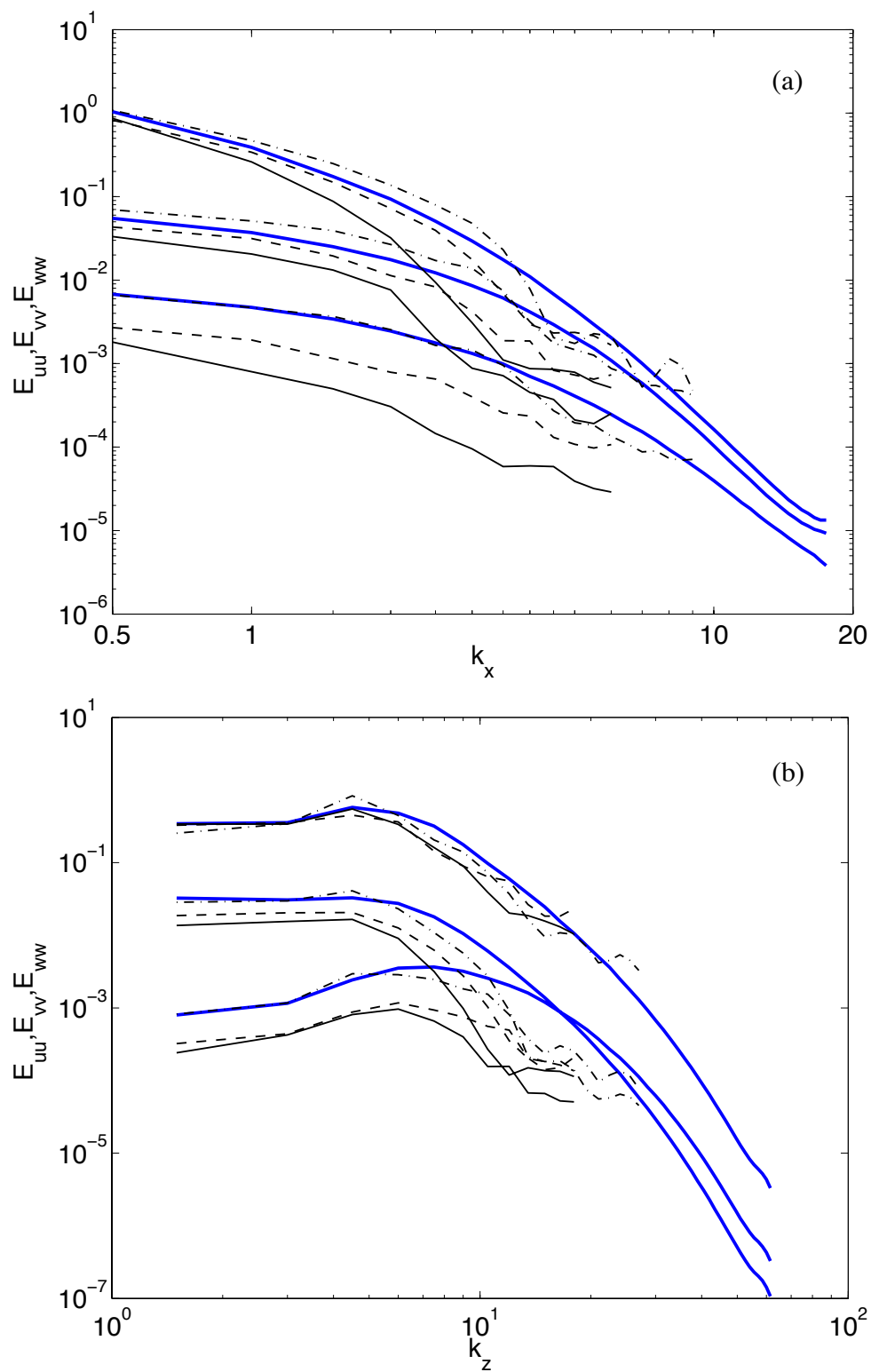


Figure 5.3: 1-D energy spectrum in the x - and z - directions at $y^+ \approx 12$ wall units for $Re_\tau = 100$ computed with a $4 \times 4 \times 4$ mesh using $p = 5$ at $Re_\tau = 100$ with SF [61] and PD [67]: — DNS; — $s = 1$; ---- $s = 3$; -.- $q = 10$.

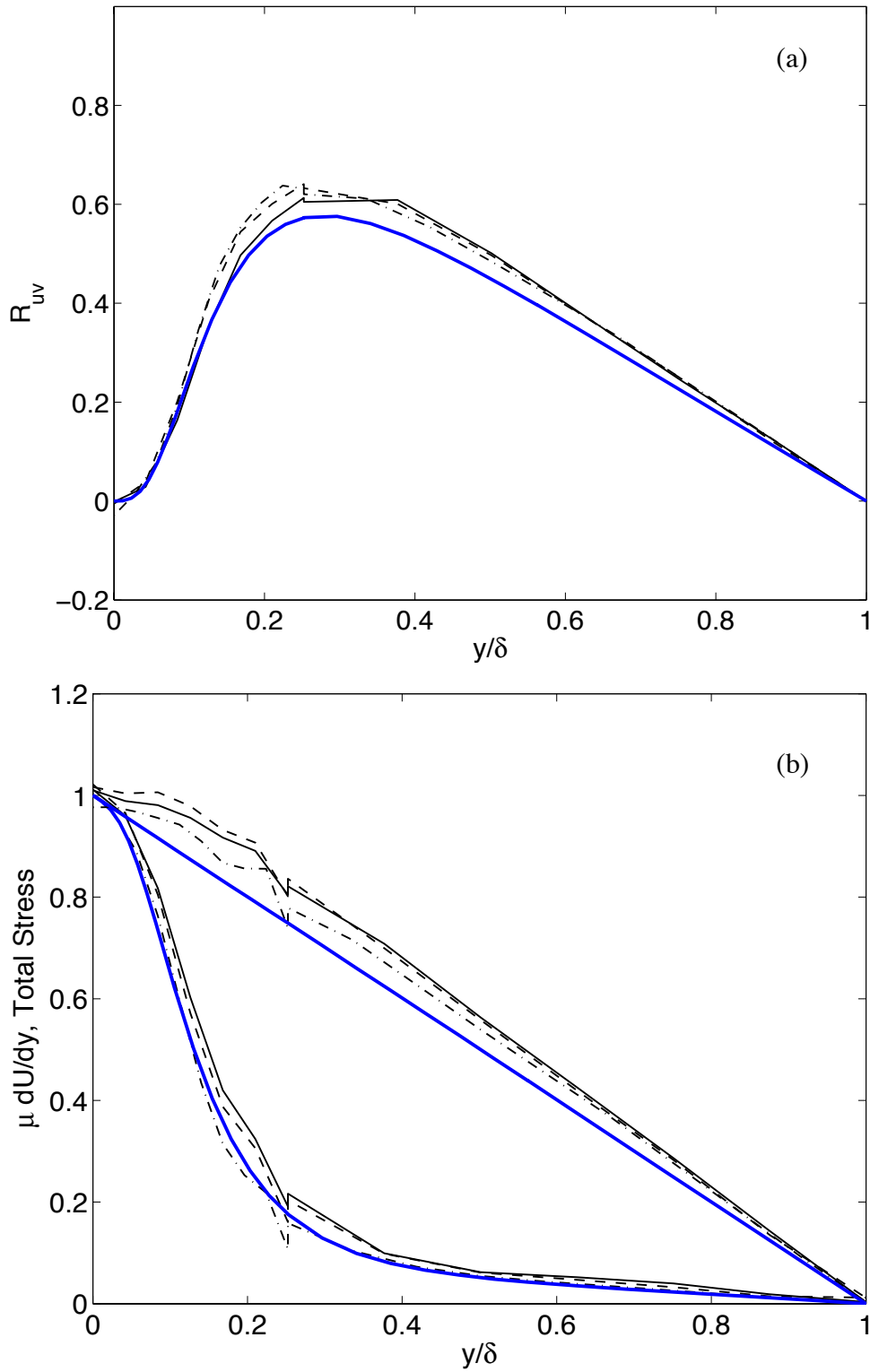


Figure 5.4: Reynolds, viscous, and total stress profiles for $Re_\tau = 100$ computed using a $4 \times 4 \times 4$ mesh using $p = 5$ with SF [61] and PD [67]: — DNS; — $s = 1$; ---- $s = 3$; —·— $q = 10$.

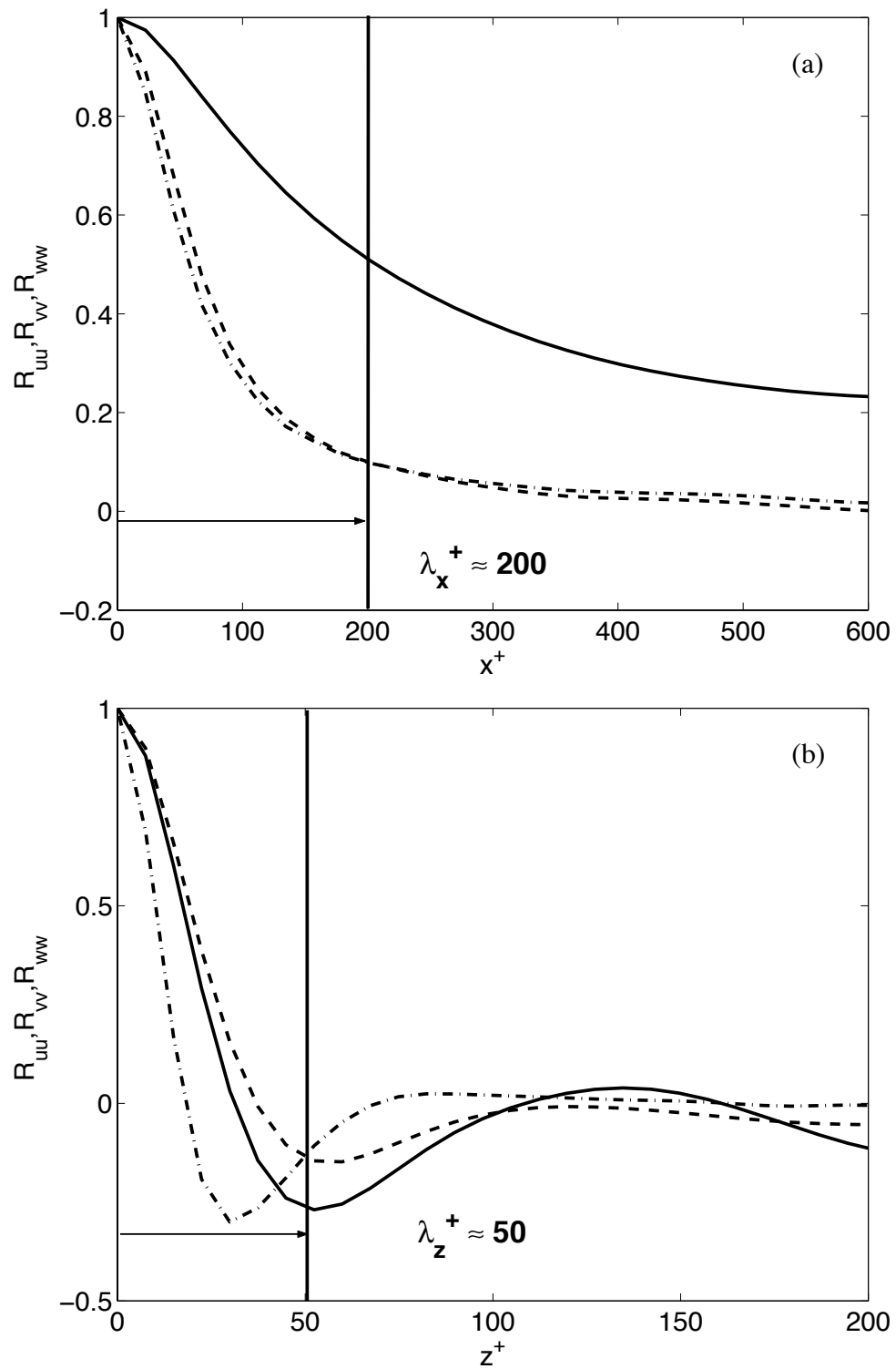


Figure 5.5: Important length scales for partition selection (L_e) in ℓ VMS for the turbulent channel flow [76]. Velocity correlation obtained from a $8 \times 8 \times 8$ mesh using $p = 6$ for $Re_\tau = 100$ at $y^+ \approx 10$: (a) Streamwise direction. (b) Spanwise direction.

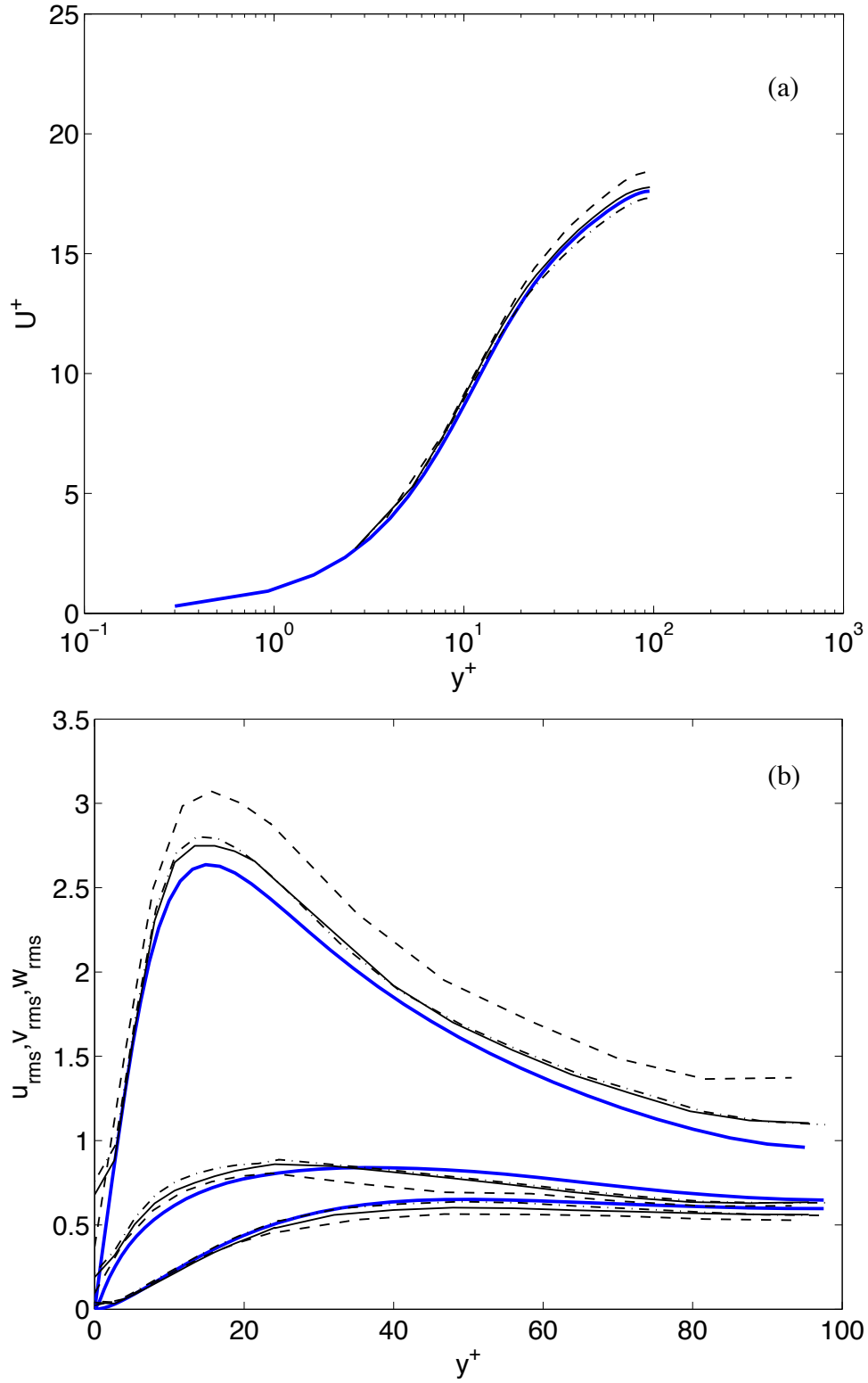


Figure 5.6: Meanflow and rms profiles for $Re_\tau = 100$ obtained with a $4 \times 4 \times 4$ mesh using $p = 5$ with SF, PD, and ℓVMS employing PD: — DNS; — ℓVMS , $L_e = 2$, and $q = 10$; ---- SF, $s = 3$; - - - PD, $q = 10$.

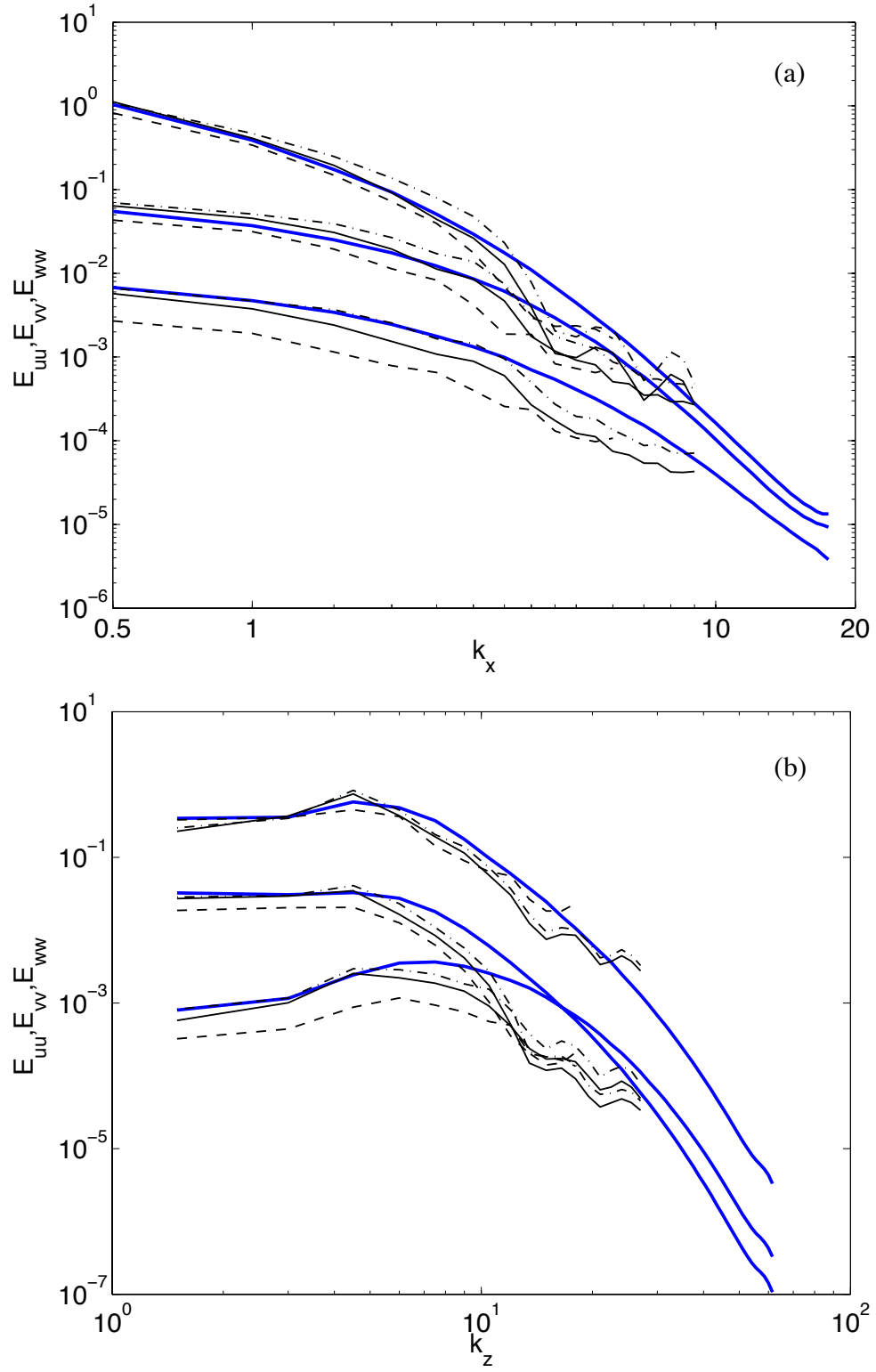


Figure 5.7: 1-D energy spectrum in the x - and z - directions at $y^+ \approx 12$ wall units for $Re_\tau = 100$ obtained with a $4 \times 4 \times 4$ mesh using $p = 5$ with SF, PD, and ℓ VMS employing PD: — DNS; — ℓ VMS, $L_e = 2$, and $q = 10$; ---- SF, $s = 3$; — PD, $q = 10$.

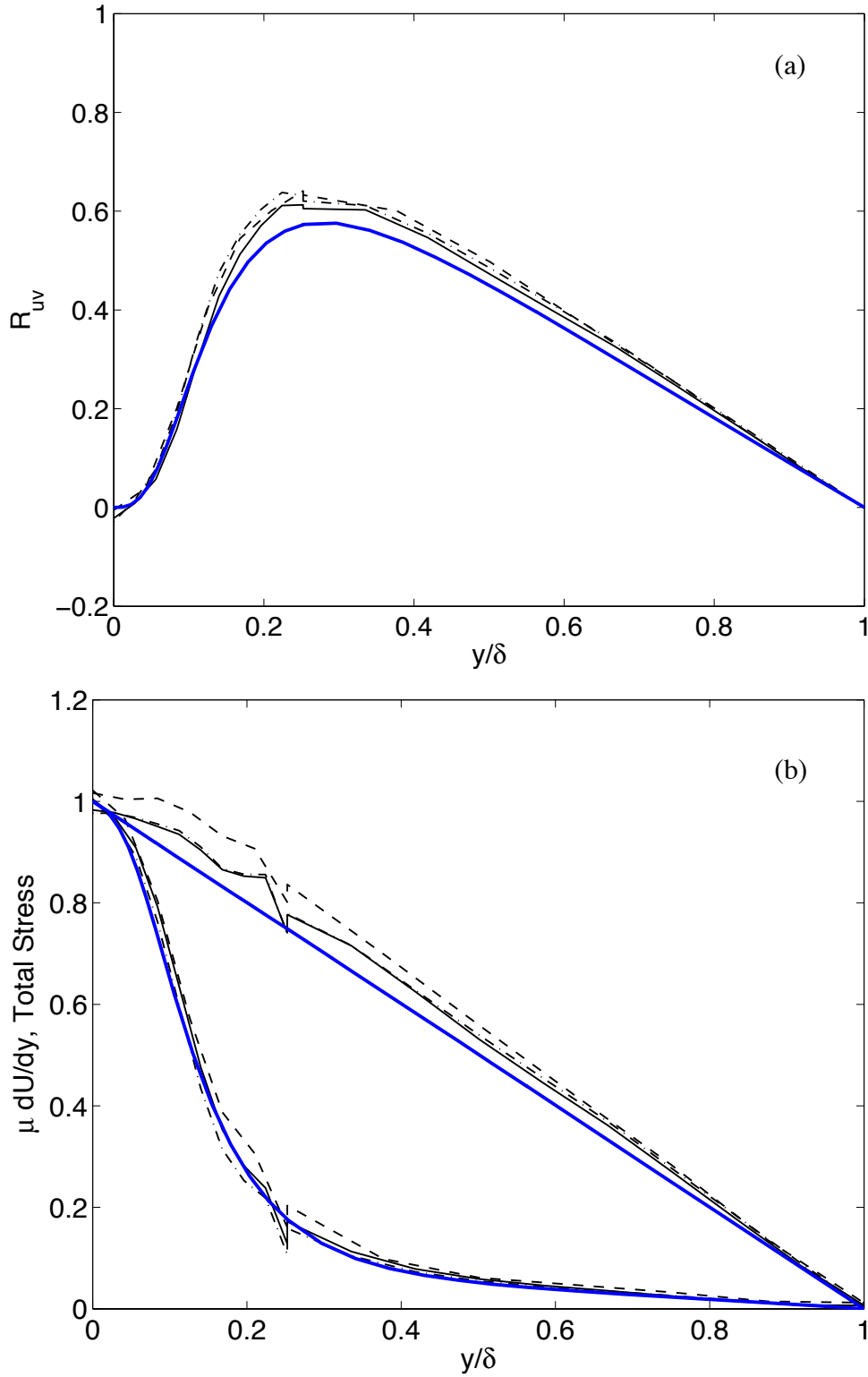


Figure 5.8: Reynolds, viscous and total stress profiles for $Re_\tau = 100$ obtained with a $4 \times 4 \times 4$ mesh using $p = 5$ with with SF, PD, and ℓVMS employing PD: — DNS; — ℓVMS , $L_e = 2$, and $q = 10$; ---- SF, $s = 3$; — PD, $q = 10$.

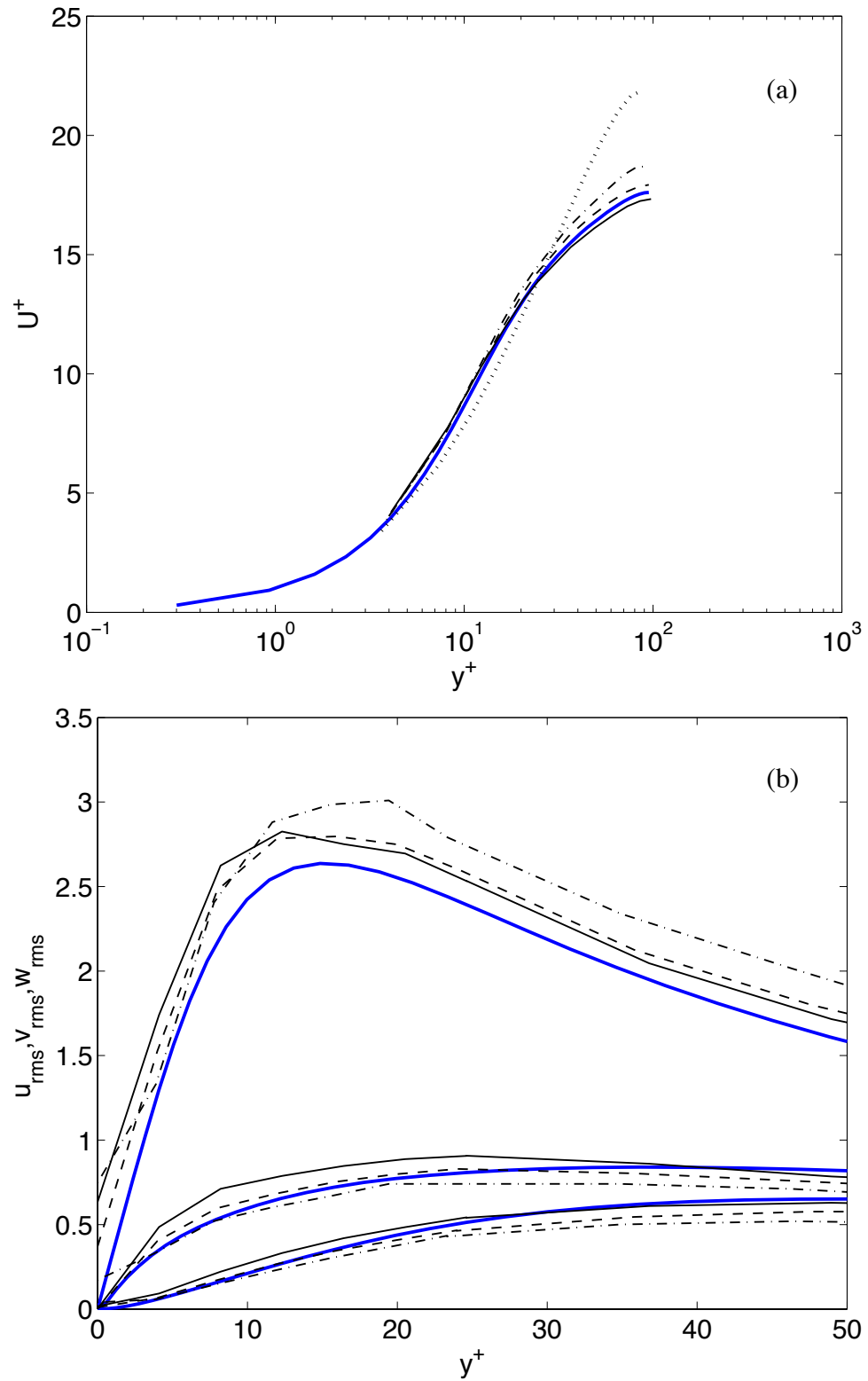


Figure 5.9: Illustration of issues involved in ℓ VMS modeling. Meanflow and rms profiles for $Re_\tau = 100$ obtained with a $4 \times 4 \times 4$ mesh using $p = 5$: — DNS; — SBLDG, $L_e = 2$; ---- SBLDG, $L_e = 2, s = 4$; - - - BR, $L_e = 1$; BR, Smagorinsky ($L_e = 0$).

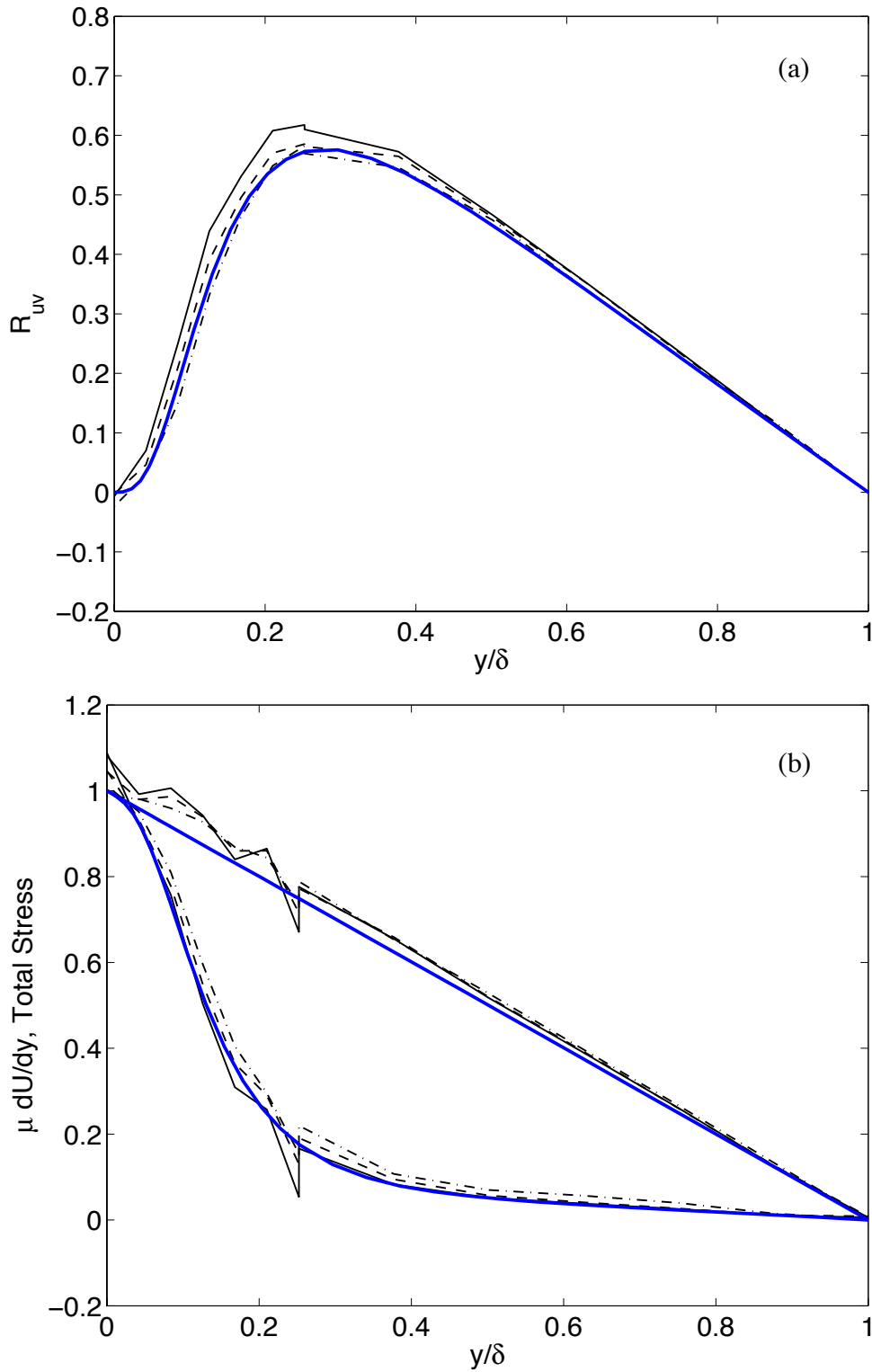


Figure 5.10: Illustration of issues involved in ℓVMS modeling. Reynolds, viscous and total stress profiles for $Re_\tau = 100$ obtained with a $4 \times 4 \times 4$ mesh using $p = 5$: — DNS; — SBLDG, $L_e = 2$; ---- SBLDG, $L_e = 2$, $s = 4$; -.- BR, $L_e = 1$.

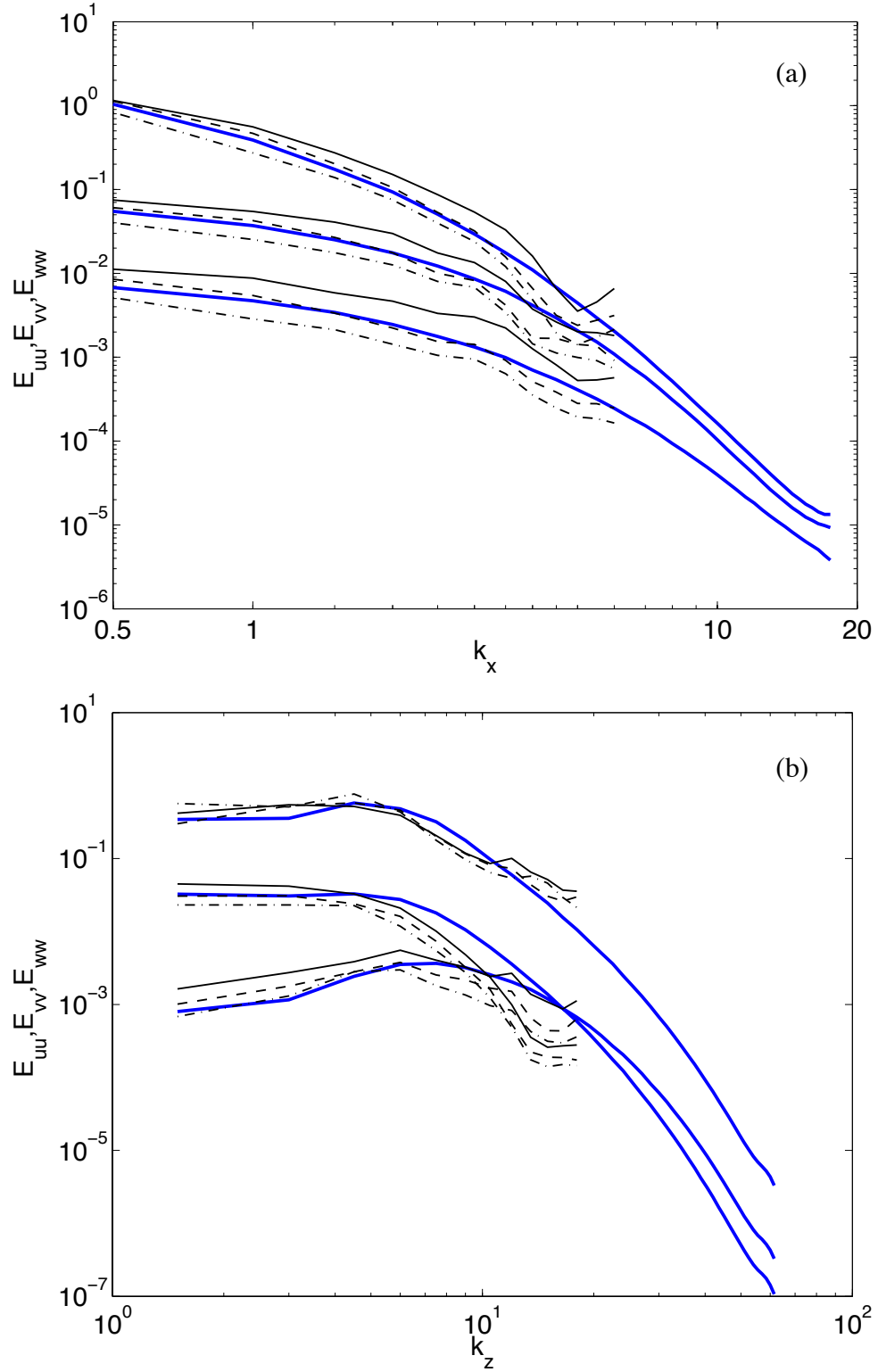


Figure 5.11: Illustration of issues involved in ℓ VMS modeling. 1-D energy spectrum in the x - and z - direction evaluated at $y^+ \approx 12$ for $Re_\tau = 100$ obtained with a $4 \times 4 \times 4$ mesh using $p = 5$: — DNS; — SBLDG, $L_e = 2$; ---- SBLDG, $L_e = 2, s = 4$; —·— BR, $L_e = 1$.

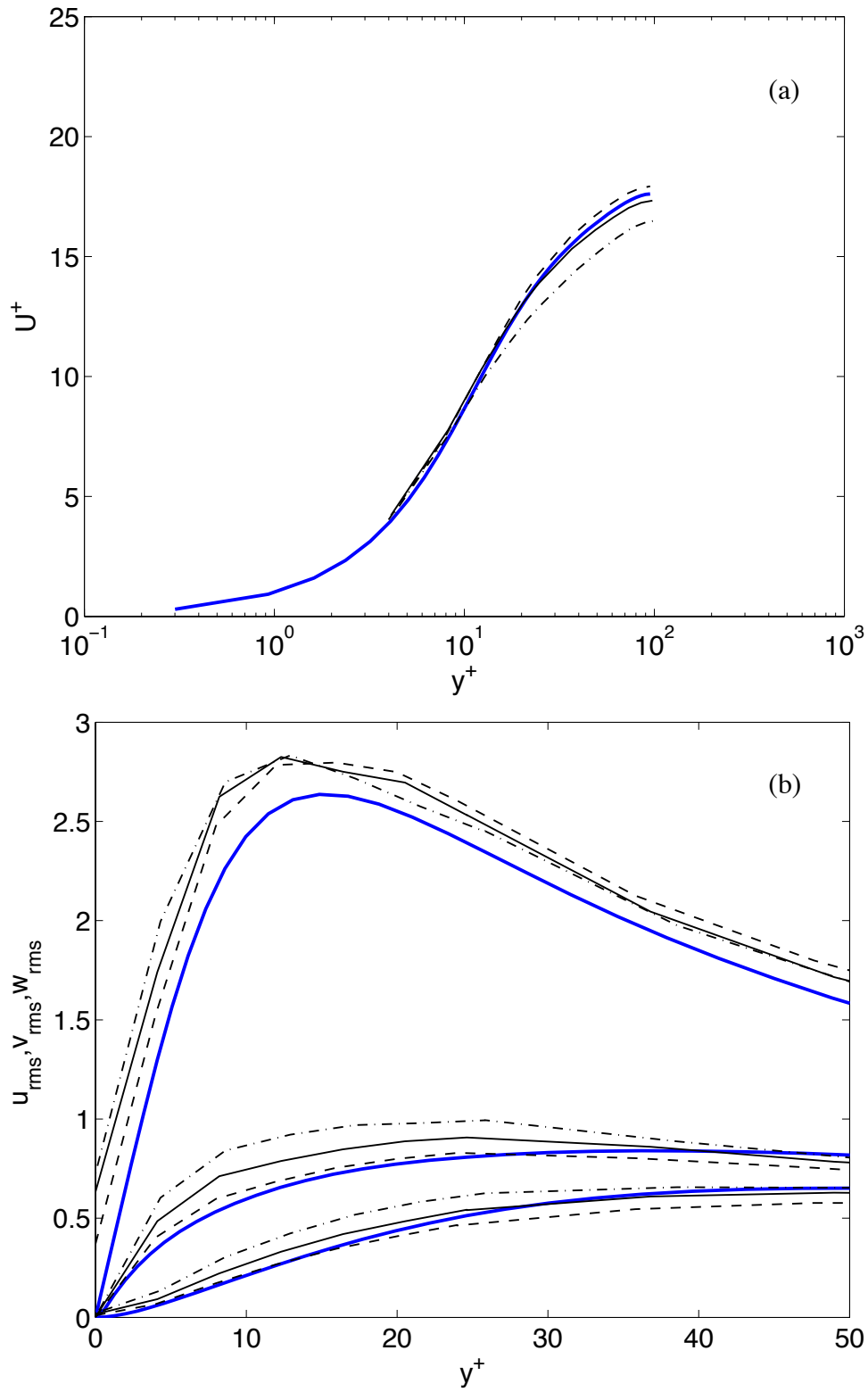


Figure 5.12: Role of partition (L_e) in ℓ VMS. Meanflow and rms profiles for $Re_\tau = 100$ obtained with a $4 \times 4 \times 4$ mesh with $p = 5$ and SBLDG: — DNS; — $L_e = 2$; --- $L_e = 3$; -.- $L_e = 2$ and $s = 4$.

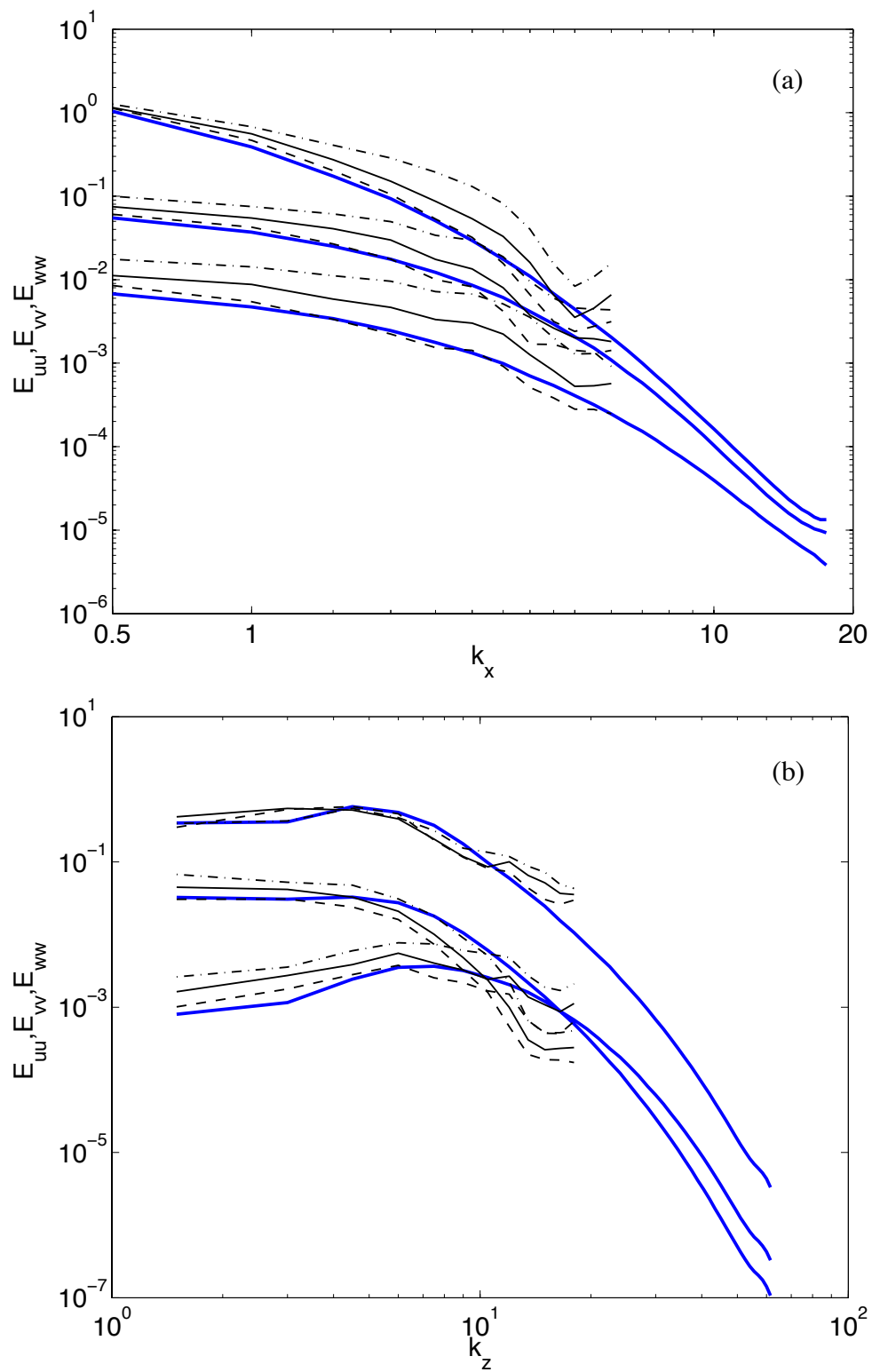


Figure 5.13: The role of partition (L_e) in ℓ VMS. 1-D energy spectrum in the x - and z -direction evaluated at $y^+ \approx 12$ for $Re_\tau = 100$ obtained with a $4 \times 4 \times 4$ mesh with $p = 5$ and SBLDG: — DNS; — $L_e = 2$; -·- $L_e = 3$; ---- $L_e = 2$ and $s = 4$.

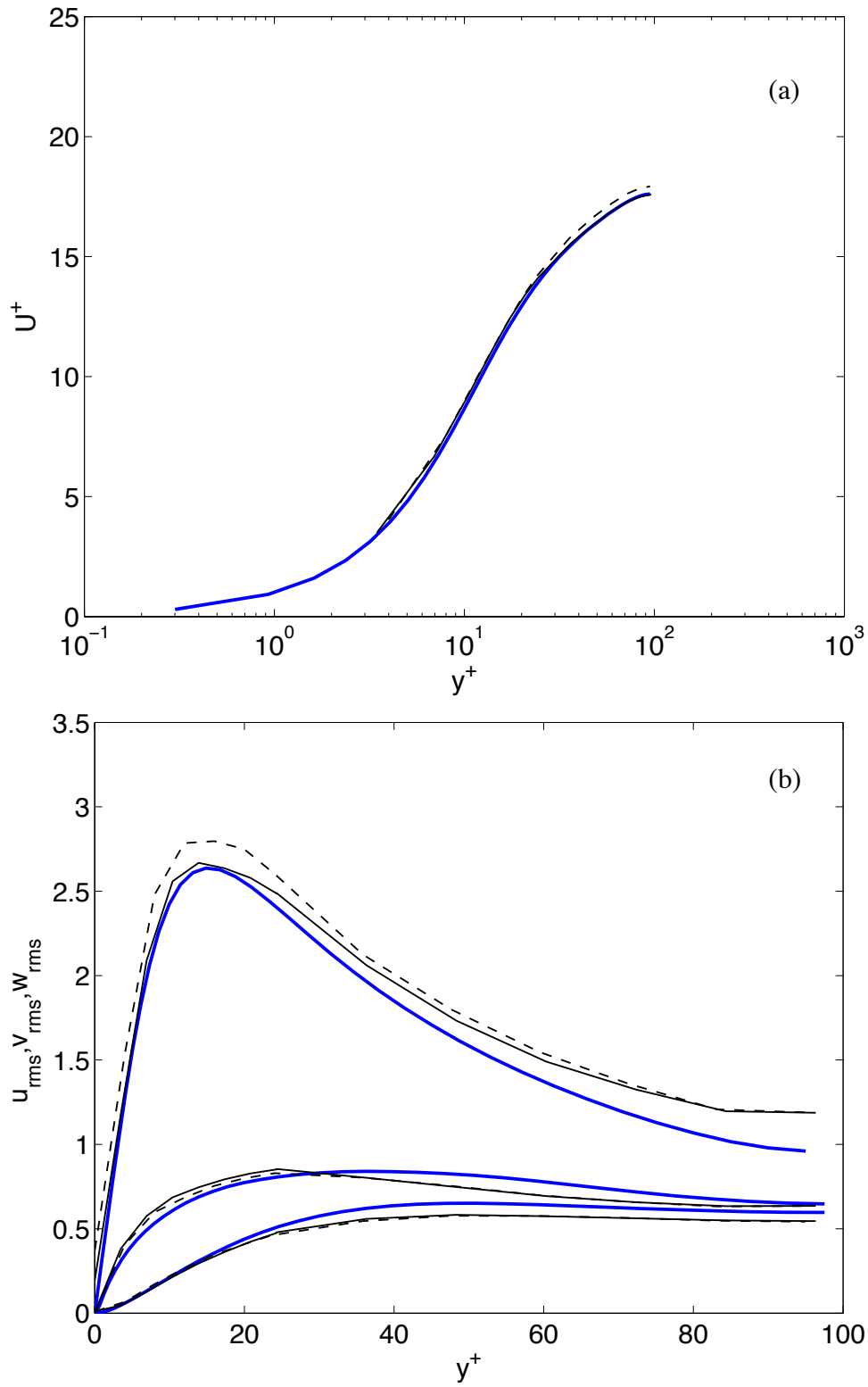


Figure 5.14: The effect of local polynomial refinement in ℓVMS . Meanflow and rms profiles for $Re_\tau = 100$ obtained with a $4 \times 4 \times 4$ mesh with $L_e = 2$, $s = 4$, and SBLDG: — DNS; — $p = \{6, 5, 5, 6\}$; ---- $p = 5$.

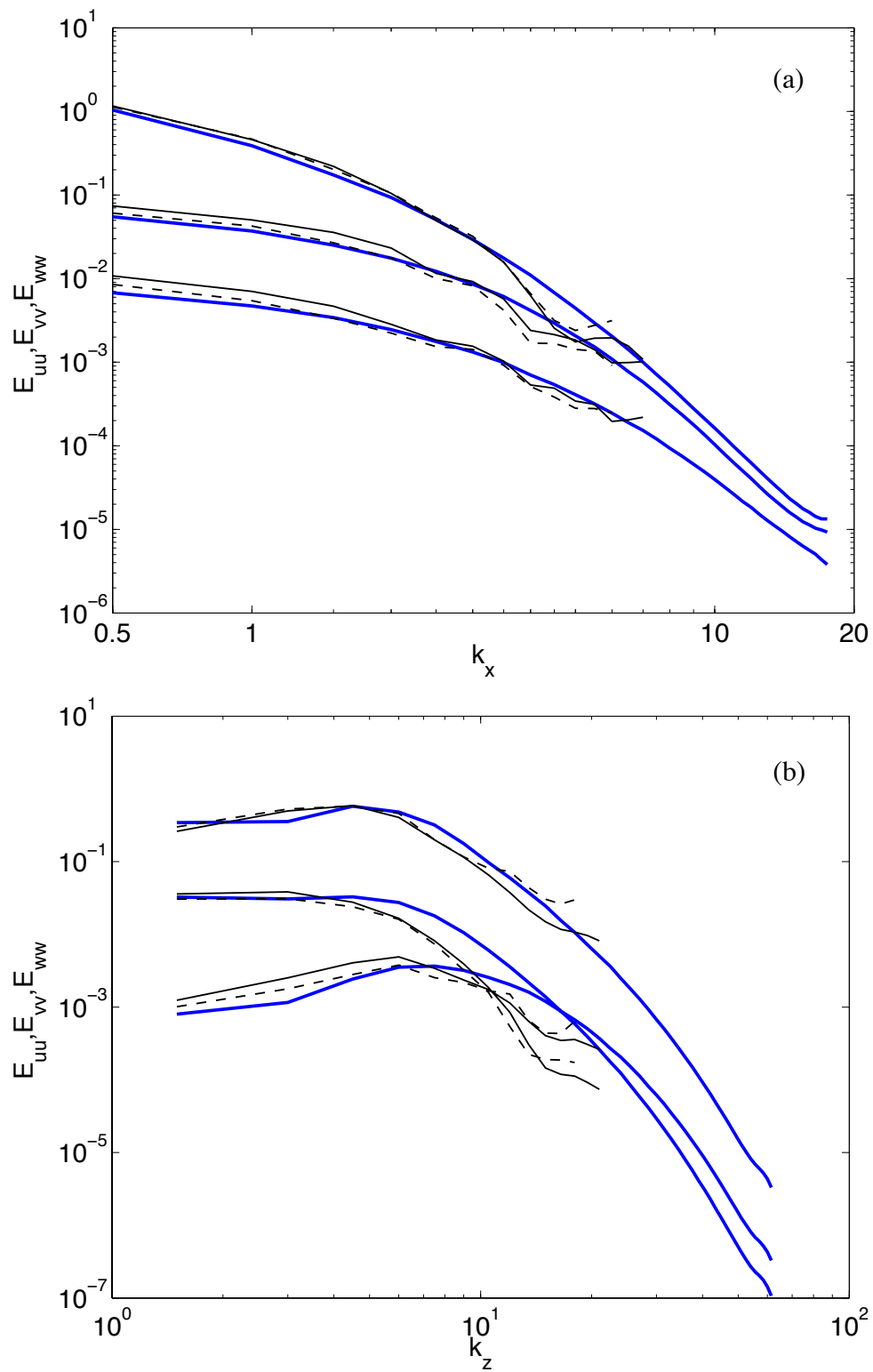


Figure 5.15: The effect of local polynomial refinement in ℓ VMS. 1-D energy spectrum in the x - and z - direction evaluated at $y^+ \approx 12$ for $Re_\tau = 100$ obtained with a $4 \times 4 \times 4$ mesh with $L_e = 2$, $s = 4$, and SBLDG: — DNS; — $p = \{6, 5, 5, 6\}$; ---- $p = 5$.

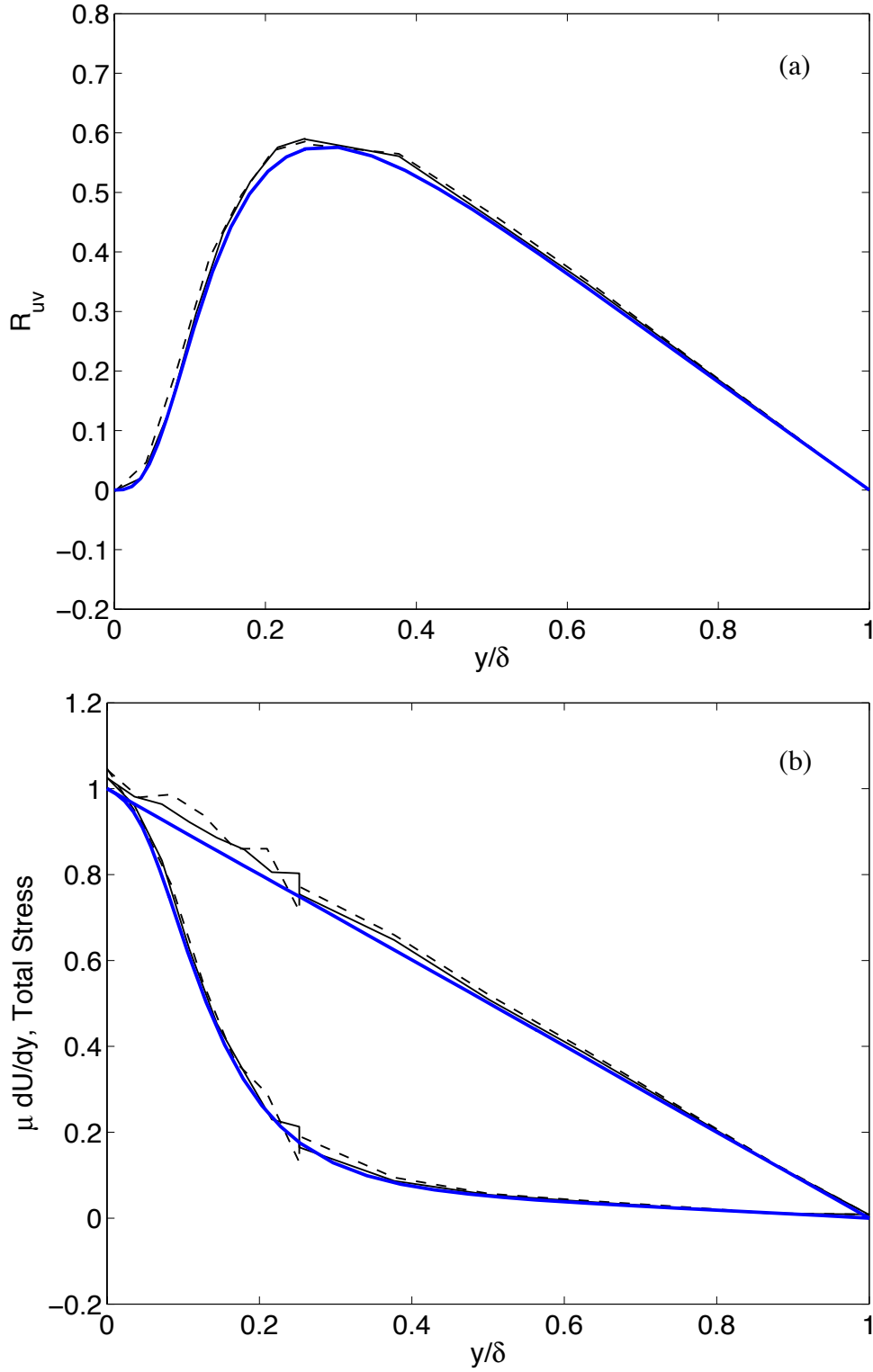


Figure 5.16: Local polynomial refinement in ℓVMS . Reynolds, viscous and total stress profiles for $Re_\tau = 100$ obtained with a $4 \times 4 \times 4$ mesh with $L_e = 2$, $s = 4$, and SBLDG: — DNS; — $p = \{6, 5, 5, 6\}$; ---- $p = 5$.

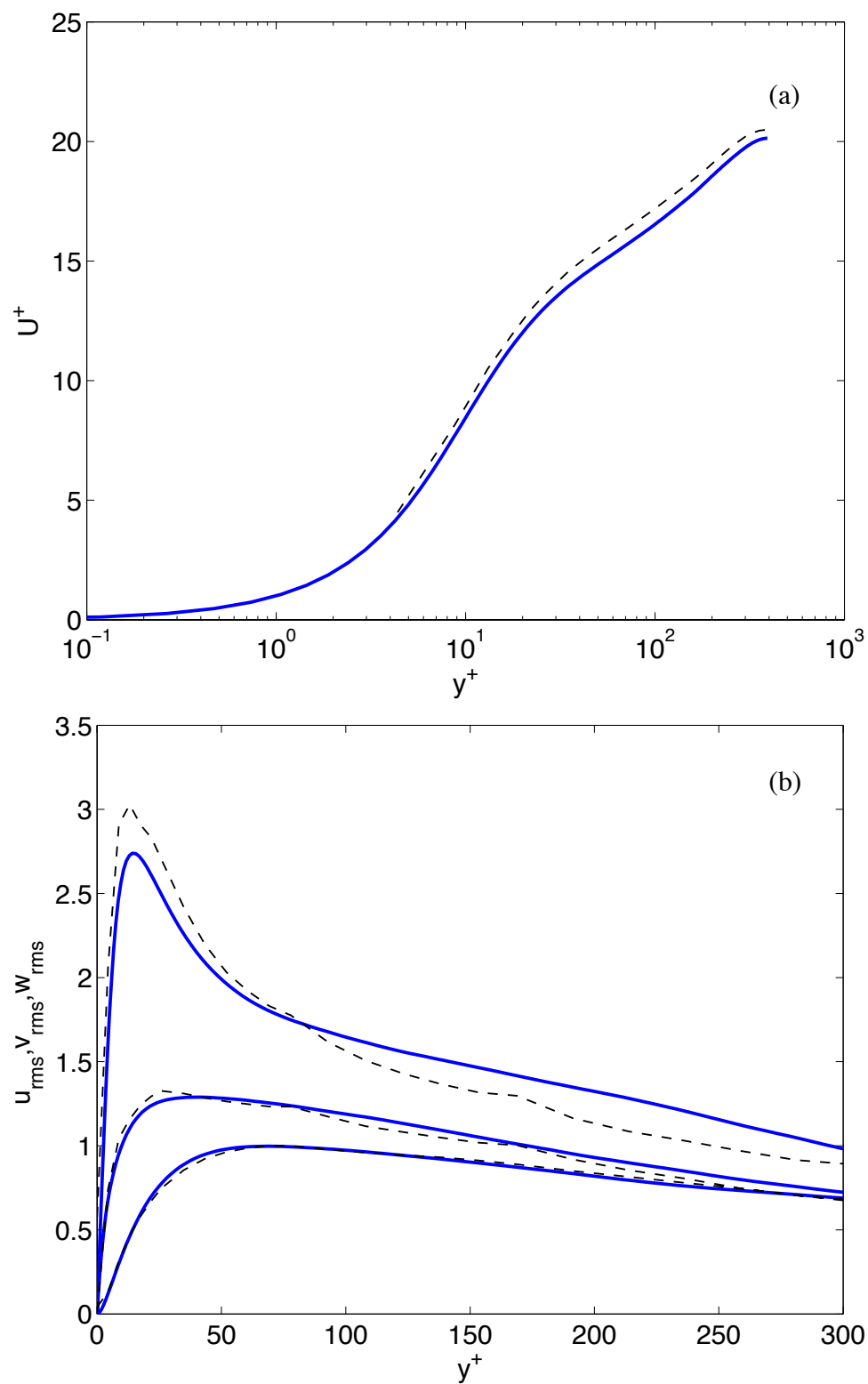


Figure 5.17: Meanflow and rms profiles for $Re_\tau = 395$ obtained using a relative resolution that matches a lower Reynolds number case. Simulation parameters are listed in Table 5.3: — DNS; ---- SBLDG.

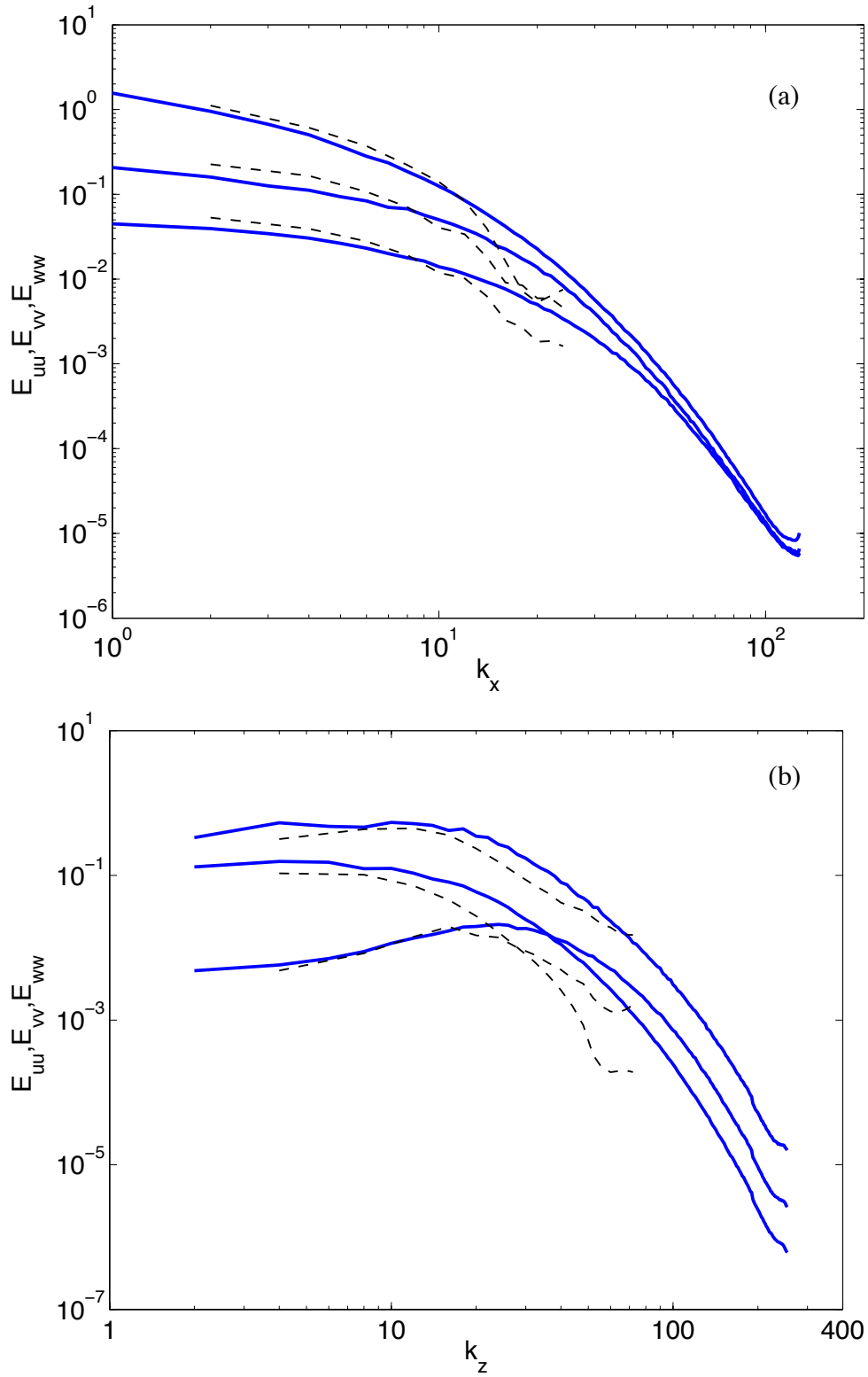


Figure 5.18: 1-D energy spectrum in the x - and z - directions at $y^+ \approx 20$ wall units for $Re_\tau = 395$ obtained using a relative resolution that matches a lower Reynolds number case. Simulation parameters are listed in Table 5.3: — DNS; ---- SBLDG.

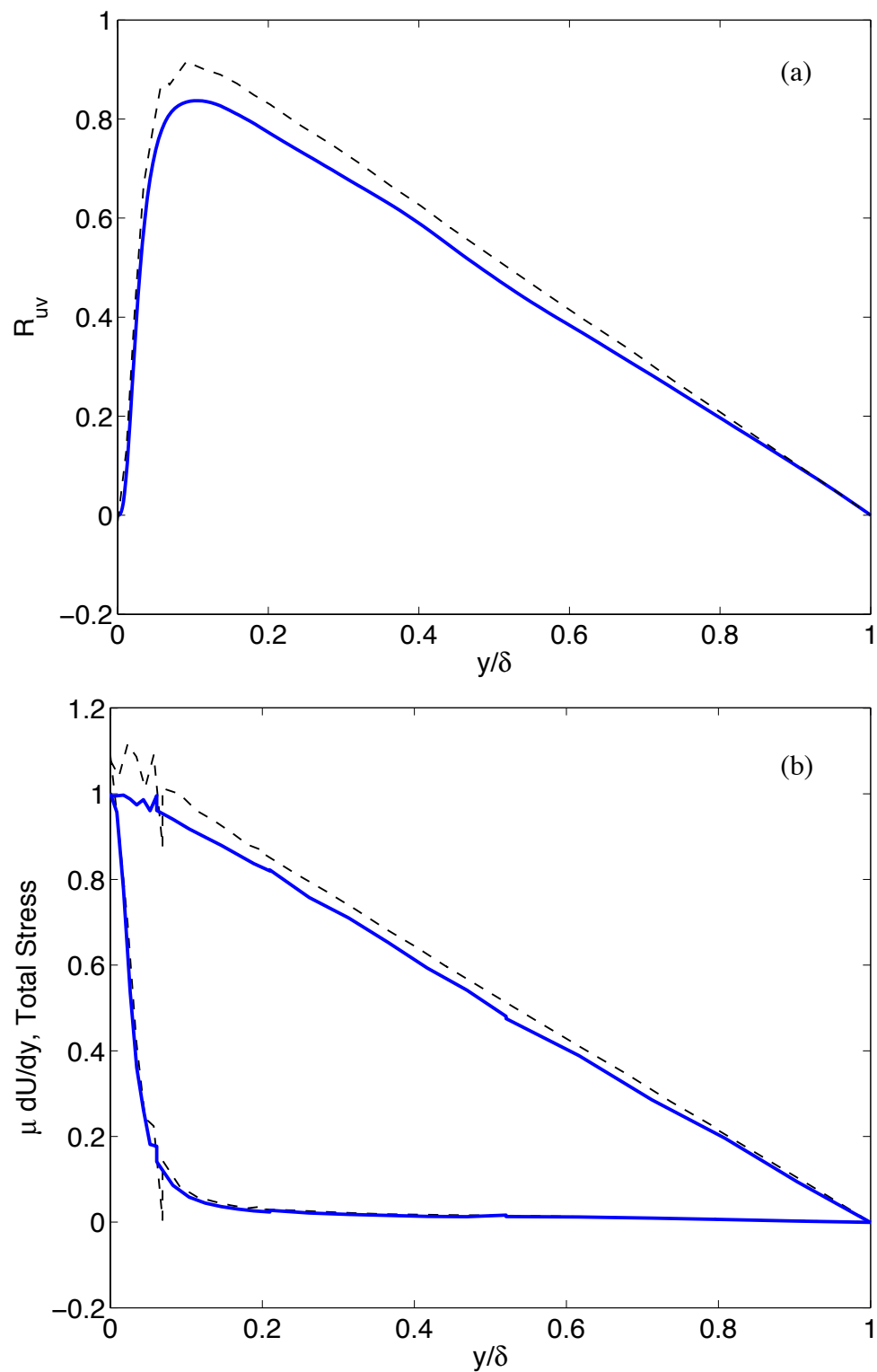


Figure 5.19: Reynolds, viscous and total stress profiles for $Re_\tau = 395$ simulation obtained using a relative resolution that matches a lower Reynolds number case. Simulation parameters are listed in Table 5.3: — DNS; ---- SBLDG.

Chapter 6

Discussion and Future Work

We conclude with a summary of the principal findings of the current research and present our recommendations for future research based on this work.

6.1 Conclusions

We have implemented and studied the efficacy of multi-scale modeling in a DG spatial discretization that we term local Variational Multi-Scale – ℓ VMS. Specifically, the current work focussed on evaluation of this framework for wall-bounded turbulence using a fully-developed turbulent channel flow.

The results of the spatial resolution study, undertaken in Chapter 3, may be categorised into two major components – resolution effects in the planar directions and wall-normal direction. The planar resolution effects may be further subdivided into streamwise and spanwise effects. The non-linear stability of the simulation is found to depend critically on the resolution in the spanwise direction. Meanwhile, we find that the level of numerical dissipation in the simulation is inversely proportional to the resolution in the streamwise direction.

Meanwhile, the y -direction resolution is found to control the degree of momentum slip at the solid walls that directly affects the accuracy of τ_w predictions. For large Δy_w^+ , the magnitude of slip are significantly high leading to poor τ_w predictions. Simultaneously, enforcement of wall boundary conditions weakly through numerical viscous fluxes is found to mitigate near-wall resolution requirements, compared with traditional discretizations [14], in the y direction. In fact, by allowing the flow to slip at the wall, part of the boundary layer is captured in the solution jump. Thereby, the influence of the wall commensurate with the local resolution is simulated. Further, regulating the slip at the solid walls, through a solution jump penalty in the numerical viscous flux, is found to improve τ_w predictions even at relatively large Δy_w^+ . Additionally, the introduction of the penalty appears to have a stabilizing influence on the solution, and thereby, enhancing non-linear stability properties of the simulation.

Overall, without explicit modeling, reasonable low-order statistics are obtained using $\Delta x^+ \approx 150$, $\Delta z^+ \approx 50$, and $\Delta y_m^+ \approx 10$ with $p \geq 3$ that gives $\Delta y_w^+ \leq 2$. Below these resolutions, the errors are dominated by the presence of numerical dissipation. Thereafter, aliasing and SGS effects become increasingly important. The minimization of these effects requires relatively high polynomial orders ($p > 5$) with the above mesh guidelines.

Now, in the context of reduced order modeling, the low resolution in the spanwise direction likely exacerbate the aliasing and SGS effects that adversely affects non-linear stability. Therefore, Spectral Filtering (SF) [61] and Polynomial Dealiasing (PD) [67] were explored as strategies for improving the non-linear stability of the simulation. Although both approaches are successful in ensuring non-linear stability, PD may be better suited to SGS modeling. Further, while solutions obtained using a combination of SF [61] and SBLDG offer a computationally efficient alternative, a proper selection of additional parameters (s, ϵ) may require extensive numerical experimentation in general flow configurations. Meanwhile, PD [67] is found to be both an effective as well as a simple strategy that simultaneously minimizes aliasing while isolating SGS effects.

Finally, the introduction of multi-scale modeling, where the scale separation is related to the physical structures in the flow [76, 77], successfully accounts for the SGS effects. Further, improved results obtained using local polynomial refinement demonstrate the efficacy of ℓ VMS for both accurate and efficient wall-bounded turbulence simulation.

6.2 Future Work

The locality of the DG spatial discretization and the ability of specify model parameters individually on each element in ℓ VMS holds promise for surgical modeling of a wide range of flows. Thus, a natural extension of the current work is to test the capabilities of ℓ VMS for flows in complex geometries.

In fact, VMS is a hybrid method that combines DNS and LES on adjacent scale ranges. Thus, an appropriate selection of the partition parameter (L_e) provides a natural mechanism to toggle the SGS model. Thus, in addition to coupling of solutions of different fidelities (hp -refinement) on adjacent elements, different models may be introduced in different regions of the flow (see Figure 2.3). Here, the issues related to the choice of the partition parameter L_e , the location of the boundaries between different ℓ VMS modeling zones, and appropriate SGS models need to be addressed.

Meanwhile, the DG spatial discretization also provides a practical means to integrate RANS and VMS through the numerical fluxes. The combination of ℓ VMS and RANS has the potential to produce very efficient computations. Thus, providing a unified framework for efficient and accurate turbulence simulation.

The exploration of the weak wall boundary conditions enforcement through numerical fluxes, using a general three-dimensional boundary layer, could potentially lead to a mathematically consistent approach for robust wall-modeling.

Now, the explicit time advancement scheme imposes a severe restriction on the timestep size, especially at the higher polynomial orders. An efficient implicit time-advancement scheme/strategy that allows larger timesteps is important to reduce the *overall* computational expense of turbulence simulations.

Thus far, VMS [47, 48, 78] implementations have generally been restricted to incompressible flows. Meanwhile, there has been a steady development of LES to flows where compressibility effects are important. Therefore, one can expect the success of the multi-scale modeling strategy with incompressible flows to extend to compressible flows [57]. Therefore, the development of multi-scale modeling for such flows, building on prior research efforts, will allow ℓ VMS to tackle an additional class of high speed flows.

Bibliography

- [1] K. Akselvoll and P. Moin. *Large Eddy Simulation of Turbulent Confined Coannular Jets and Turbulent Flow Over A Backward Facing Step*. PhD thesis, Stanford University, 1995.
- [2] D. N. Arnold. An interior penalty finite element method with discontinuous elements. *SIAM J. Numer. Anal.*, 19:742–760, 1982.
- [3] D. N. Arnold, F. Brezzi, B. Cockburn, and L. D. Marin. Unified analysis of discontinuous Galerkin methods for elliptic problems. *SIAM J. Numer. Anal.*, 39(5):1749–1779, 2002.
- [4] H. L. Atkins. Continued development of the discontinuous Galerkin method for computational aeroacoustic applications. *AIAA Paper 97-1581*, 1997.
- [5] N. Aubry, P. Holmes, J. Lumley, and E. Stone. The dynamics of coherent structures in the wall region of a turbulent boundary layer. *J. Fluid Mech.*, 192:115–173, 1988.
- [6] F. Bassi and S. Rebay. A high-order accurate discontinuous finite element method for the numerical solution of the compressible Navier–Stokes equations. *J. Comp. Phys.*, 131:267–279, 1997.
- [7] F. Bassi and S. Rebay. Numerical evaluation of two discontinuous Galerkin methods for the compressible Navier–Stokes equations. *Inter. J. Num. Meth. Fluids*, 40:197–207, 2002.
- [8] F. Bassi, S. Rebay, G. Mariotti, S. Pedinotti, and M. Savini. A high-order accurate discontinuous finite element method for inviscid and viscous turbomachinery flows. In R. Decuyper and G. Dibelius, editors, *2nd European Conference on Turbomachinery Fluid Dynamics and Thermodynamics*, pages 99–108, Technologisch Instituut, 1997.
- [9] C. E. Baumann and J. T. Oden. A discontinuous hp finite element method for the Euler and Navier–Stokes equations. *Inter. J. Num. Meth. Fluids*, 31:79–95, 1999.
- [10] K. S. Bey and J. T. Oden. hp– version discontinuous galerkin methods for hyperbolic conservation laws. *Computer Methods in Applied Mechanics and Engineering*, 133:259–286, 1996.

- [11] A. N. Brooks and T. J. R. Hughes. Streamline upwind/Petrov–Galerkin formulations for convection dominated flows with particular emphasis on the incompressible Navier–Stokes equations. *Comp. Meth. in Appl. Mech. Eng.*, 32:199–259, 1982.
- [12] G. L. Brown and A. Roshko. On density effects and large structure in turbulent mixing layers. *J. Fluid Mech.*, 64:775–816, 1974.
- [13] C. Canuto, M. Y. Hussaini, A. Quarteroni, and T. A. Zang. *Spectral Methods in Fluid Dynamics*, page 69. Springer-Verlag, 1988.
- [14] Y. Chang. *Reduced Order Methods for Optimal Control of Turbulence*. PhD thesis, Rice University, Mechanical Engineering and Materials Science, 2000.
- [15] Y. Chang, S. S. Collis, and S. Ramakrishnan. Viscous effects in control of near-wall turbulence. *Phys. Fluids*, 14(11):4069–4080, 2002.
- [16] C.-J. Chen and S.-Y. Jaw. *Fundamentals of Turbulence Modeling*. Taylor & Francis, 1998.
- [17] H. Choi, P. Moin, and J. Kim. Active turbulence control for drag reduction in wall-bounded flows. *J. Fluid Mech.*, 262(75):75–110, 1994.
- [18] B. Cockburn, editor. *High-order methods for computational applications, Lecture Notes in Computational Science and Engineering*, chapter Discontinuous Galerkin methods for convection-dominated problems, pages 69–224. Springer, Berlin, 1999.
- [19] B. Cockburn. Discontinuous Galerkin methods. *ZAMM - Journal of Applied Mathematics and Mechanics / Zeitschrift für Angewandte Mathematik und Mechanik*, 83(11):731–754, 2003.
- [20] B. Cockburn, G. Kanschat, I. Perugia, and D. Schotzau. Superconvergence of the local discontinuous Galerkin method for elliptic problems on cartesian grids. Technical Report 2000/71, UMSI, 2000.
- [21] B. Cockburn, G. Karniadakis, and C.-W. Shu, editors. *Discontinuous Galerkin Methods: Theory, Computation, and Applications*. Springer, 2000.
- [22] B. Cockburn and C.-W. Shu. TVD Runge–Kutta local projection discontinuous Galerkin finite element method for scalar conservation laws II: General framework. *Math. Comp.*, 52:411–435, 1989.

- [23] B. Cockburn and C.-W. Shu. TVD Runge–Kutta local projection discontinuous Galerkin finite element method for scalar conservation laws IV: The multidimensional case. *Math. Comp.*, 54:545–581, 1990.
- [24] B. Cockburn and C.-W. Shu. The local discontinuous Galerkin method for time-dependent convection-diffusion systems. *SIAM J. Numer. Anal.*, 35:2440–2463, 1998.
- [25] B. Cockburn and C.-W. Shu. The Runge–Kutta discontinuous Galerkin method for conservation laws v. *J. Comp. Phys.*, 141:199–224, 1998.
- [26] B. Cockburn and S. Y. L. C.-W. Shu. TVD Runge–Kutta local projection discontinuous Galerkin finite element method for scalar conservation laws III: One dimensional systems. *J. Comp. Phys.*, 84:90–113, 1989.
- [27] G. N. Coleman, J. Kim, and R. D. Moser. A numerical study of turbulent supersonic isothermal-wall channel flow. *J. Fluid Mech.*, 305:159–83, 1995.
- [28] S. S. Collis. Monitoring unresolved scales in multiscale turbulence modeling. *Phys. Fluids*, 13(6):1800–1806, 2001.
- [29] S. S. Collis. The DG/VMS method for unified turbulence simulation. *AIAA Paper 2002-3124*, 2002.
- [30] S. S. Collis. Discontinuous Galerkin methods for turbulence simulation. In *Proceedings of the 2002 Center for Turbulence Research Summer Program*, pages 155–167, 2002.
- [31] S. S. Collis and Y. Chang. On the use of LES with a dynamic subgrid scale model for the optimal control of wall bounded turbulence. In D. Knight and L. Sakell, editors, *Recent Advances in DNS and LES*, pages 99–110. Kluwer Academic Publishers, 1999.
- [32] S. S. Collis, Y. Chang, S. Kellogg, and R. D. Prabhu. Large eddy simulation and turbulence control. *AIAA Paper 2000-2564*, 2000.
- [33] J. W. Deardorff. A numerical study of three-dimensional turbulent channel flow at large Reynolds number. *J. Fluid Mech.*, 41:453–480, 1970.

- [34] J. Douglas Jr. and B. L. Dupont. *Interior penalty procedures for elliptic and parabolic Galerkin methods*, chapter Lecture Notes in Physics, vol. 58. Springer-Verlag, Berlin, 1976.
- [35] M. Dubiner. Spectral methods on triangles and other domains. *J. Sci. Comp.*, 6:345, 1991.
- [36] J. H. Ferziger. Large eddy simulation. In T. B. Gatski, M. Y. Hussaini, and J. L. Lumley, editors, *Simulation and Modeling of Turbulent Flows*, ICASE/LaRC Series in Computational Science and Engineering, chapter 3. Oxford University Press, 1996.
- [37] C. Fureby and F. Grinstein. Large eddy simulation of high-reynolds-number free and wall-bounded flows. *J. Comp. Phys.*, 181:68–97, 2002.
- [38] M. Germano, U. Piomelli, P. Moin, and W. H. Cabot. A dynamic subgrid-scale eddy viscosity model. *Phys. Fluids A*, 3(7):1760–1765, 1991.
- [39] S. Ghosal and P. Moin. The basic equations for the large-eddy simulation of turbulent flows in complex-geometry. *J. Comp. Phys.*, 118:24–37, 1995.
- [40] E. P. Hammond, T. R. Bewley, and P. Moin. Observed mechanisms for turbulence attenuation and enhancement in opposition-controlled wall-bounded flows. *Phys. Fluids*, 10(9):2421–2423, 1998.
- [41] C. Hirsch. *Numerical Computation of Internal and External Flows, Vol. I: Fundamentals of Numerical Discretization*. Wiley, New York, 1988.
- [42] J. Holmen, T. J. R. Hughes, A. A. Oberai, and G. N. Wells. Sensitivity of the scale partition for variational multiscale large-eddy simulation of channel flow. *Phys. Fluids*, 16(3):824–827, 2004.
- [43] P. Holmes, J. L. Lumley, and G. Berkooz. *Turbulence, Coherent Structures, Dynamical Systems and Symmetry*. Cambridge University Press, 1996.
- [44] F. Q. Hu, M. Y. Hussaini, and P. Rasetarinera. An analysis of the discontinuous Galerkin method for wave propagation problems. *J. Comp. Phys.*, 151:921–046, 1999.
- [45] T. J. R. Hughes, G. R. Feijoo, L. Mazzei, and J. B. Quincy. The variational multiscale method – a paradigm for computational mechanics. *Comp. Meth. in Appl. Mech. Eng.*, 166(1–2):3–24, 1998.

- [46] T. J. R. Hughes, L. Mazzei, and K. E. Jansen. Large eddy simulation and the variational multiscale method. *Comp Vis Sci*, 3:47–59, 2000.
- [47] T. J. R. Hughes, L. Mazzei, A. A. Oberai, and A. A. Wray. The multiscale formulation of large eddy simulation: Decay of homogeneous isotropic turbulence. *Phys. Fluids*, 13(2):505–512, 2001.
- [48] T. J. R. Hughes, A. A. Oberai, and L. Mazzei. Large eddy simulation of turbulent channel flows by the variational multiscale method. *Phys. Fluids*, 13(6):1755–1754, 2001.
- [49] T. J. R. Hughes and J. R. Stewart. A space-time formulation for multiscale phenomena. *Journal of Computational and Applied Mathematics*, 74:217–29, 1996.
- [50] K. Jansen. The effect of element topology on variational multiscale methods for les. *Bull. Am. Phys. Soc.*, 45(9):56, 2000.
- [51] C. Johnson and J. Pitkäranta. An analysis of the discontinuous galerkin method for a scalar hyperbolic equation. *Mathematics of Computation*, 46(173):1–26, 1986.
- [52] S. Kang and H. Choi. Active wall motions for skin-friction drag reduction. *Phys. Fluids*, 12(12):3301–3304, 2000.
- [53] G. E. Karniadakis and S. J. Sherwin. *Spectral/hp Element Methods for CFD*. Oxford University Press, 1999.
- [54] J. Kim, P. Moin, and R. Moser. Turbulence statistics in fully developed channel flow at low Reynolds number. *J. Fluid Mech.*, 177:133–166, 1987.
- [55] S. J. Kline, W. C. Reynolds, F. A. Schraub, and P. W. Runstadler. The structure of turbulent boundary layers. *J. Fluid Mech.*, 1967.
- [56] A. N. Kolmogorov. The local structure of turbulence in incompressible viscous fluid for very large reynolds number. *Dokl. Akad. Nauk SSSR*, 30:301–305, 1941.
- [57] B. Koobus and C. Farhat. A variational multiscale method for the large eddy simulation of compressible turbulent flows on unstructured meshes-applications to vortex shedding. *Computer Methods in Applied Mechanics and Engineering*, 193:1367–1383, 2004.

- [58] A. G. Kravchenko and P. Moin. On the effect of numerical errors in large eddy simulation of turbulent flows. *J. Comp. Phys.*, 131:310–322, 1996.
- [59] P. LeSaint and P. A. Raviart. On a finite element method for solving the neutron transport equation. In C. de Boor, editor, *Mathematical Aspects of Finite Element Methods in Partial Differential Equations*, pages 89–145. Academic Press, 1974.
- [60] M. Lesieur and O. Métais. New trends in large-eddy simulations of turbulence. *Ann. Rev. Fluid Mech.*, 28:45–82, 1996.
- [61] J. G. Levin, M. Iskandarani, and D. B. Haidvogel. A spectral filtering procedure for eddy-resolving simulations with a spectral element ocean model. *J. Comp. Phys.*, 137:130–154, 1997.
- [62] D. K. Lilly. A proposed modification of the Germano subgrid-scale closure method. *Phys. Fluids A*, 4(3):633–635, 1992.
- [63] D. P. Lockard and H. L. Atkins. Efficient implementations of the quadrature-free discontinuous Galerkin method. *AIAA 99-3309*, 1999.
- [64] I. Lomtev, C. B. Quillen, and G. E. Karniadakis. Spectral/hp methods for viscous compressible flows on unstructured 2D meshes. *J. Comp. Phys.*, 144:325–357, 1998.
- [65] M. P. Martin, U. Piomelli, and G. V. Candler. Subgrid-scale models for compressible large-eddy simulations. *Ther. Comp. Fluid Dyn.*, 13:361–376, 2000.
- [66] W. Meng and P. Moin. Computation of trailing-edge flow and noise using large-eddy simulation. *AIAA J.*, 38(12):2201–9, 2000.
- [67] R. M. Kirby and G. E. Karniadakis. De-aliasing on non-uniform grids: algorithms and applications. *J. Comp. Phys.*, 191:249–264, 2003.
- [68] P. Moin and K. Mahesh. Direct numerical simulation: A tool in turbulence research. *Ann. Rev. Fluid Mech.*, 30:539–78, 1998.
- [69] R. D. Moser, J. Kim, and N. N. Mansour. Direct numerical simulation of turbulent channel flow up to $Re_\tau = 590$. *Phys. Fluids*, 11:943, 1999.
- [70] N. V. Nikitin, F. Nicoud, B. Wasistho, K. D. Squires, and P. R. Spalart. Approach to wall modeling in large-eddy simulations. *Phys. Fluids*, 12(7):1629–1632, 2000.

- [71] A. A. Oberai and T. J. R. Hughes. The variational multiscale formulation of LES: Channel flow at $Re_\tau = 590$. *AIAA 2002-1056*, 2002.
- [72] J. T. Oden, I. Babuska, and C. E. Baumann. A discontinuous hp finite element method for diffusion problems. *J. Comp. Phys.*, 146:491–519, 1998.
- [73] U. Piomelli and E. Balaras. Wall-layer models for large eddy simulations. *Ann. Rev. Fluid Mech.*, 34:349–374, 2002.
- [74] S. B. Pope. *Turbulent Flows*. Cambridge University Press, 2000.
- [75] R. D. Prabhu, S. S. Collis, and Y. Chang. The influence of control on proper orthogonal decomposition of wall-bounded turbulent flows. *Phys. Fluids*, 13(2):520–537, 2001.
- [76] S. Ramakrishnan. Variational multiscale methods for turbulence control. Master’s thesis, Rice University, 2002. Available electronically at <http://mems.rice.edu/~collis>.
- [77] S. Ramakrishnan and S. S. Collis. Partition selection in multi-scale turbulence modeling. *Submitted to Physics of Fluids*, 2004.
- [78] S. Ramakrishnan and S. S. Collis. Turbulence control simulations using the variational multiscale method. *AIAA J.*, 42(4):745–753, 2004.
- [79] W. H. Reed and T. R. Hill. Triangular mesh methods for the neutron transport equation. Technical Report LA-UR-73-479, Los Alamos Scientific Laboratory, 1973.
- [80] G. R. Richter. An optimal-order error estimate for the discontinuous galerkin method. *Mathematics of Computation*, 50:75–88, 1988.
- [81] R. S. Rogallo and P. Moin. Numerical simulation of turbulent flows. *Ann. Rev. Fluid Mech.*, 16:99–137, 1984.
- [82] P. Sagaut. *Large Eddy Simulation for Incompressible Flows: An Introduction*. Scientific Computing. Springer, Berlin, 1998.
- [83] M. Shur, P. R. Spalart, M. Strelets, and A. Travin. Detached-eddy simulation of an airfoil at high angle of attack. In W. Rodi and D. Laurence, editors, *Fourth International Symposium on Engineering Turbulence Modeling and Experiments, Corsica, 24–26 May 1999*. Elsevier, New York, 1999.

- [84] J. Smagorinsky. General circulation experiments with the primitive equations. I. The basic experiment. *Mon. Weather Rev.*, 91:99–165, 1963.
- [85] C. R. Smith and S. P. Metzler. The characteristics of low-speed streaks in the near-wall region of a turbulent boundary layer. *J. Fluid Mech.*, 129:27, 1983.
- [86] M. Strelets. Detached eddy simulation of massively separated flows. *AIAA 2001-0879*, 2001.
- [87] H. Tennekes and J. L. Lumley. *A First Course in Turbulence*. MIT Press, 1972.
- [88] E. F. Toro. *Riemann Solvers and Numerical Methods for Fluid Dynamics*. Springer, 1999.
- [89] M. van Dyke. *An Album of Fluid Motion*. Parabolic Press, 1982.
- [90] M. F. Wheeler. An elliptic collocation-finite element method with interior penalties. *SIAM J. Numer. Anal.*, 15:152–161, 1978.
- [91] F. M. White. *Viscous Fluid Flow*, page 29. McGraw–Hill, Inc., second edition, 1991.
- [92] D. C. Wilcox. *Turbulence Modeling for CFD*. DCW Industries, Inc., third edition, 1998.